The Physical Chemistry of Gaseous Protonated and Metal Cation-Coordinated Proline Containing Complexes Studied by Tandem Mass Spectrometry Methods

by

© Yasaman Jami-Alahmadi

A dissertation submitted to the School of Graduate Studies

in partial fulfillment of the requirements for the degree of

Doctor of Philosophy

in

Department of Chemistry

Memorial University

St. John's, Newfoundland, Canada

September 2017

Abstract

Studying protonated or metal cationized amino acids and small peptides in the gas phase offers an opportunity to better understand these systems on a molecular level, not often afforded for macromolecules in solution. In the current thesis, proline containing complex ions were electrosprayed and isolated in an FTICR cell where their unimolecular chemistries, structures, and kinetics were explored using sustained off-resonance irradiation collision-induced dissociation (SORI-CID), infrared multiple photon dissociation (IRMPD) spectroscopy and blackbody infrared radiative dissociation (BIRD). These experiments were augmented by computational methods such as electronic structure, simulated annealing, master equation modeling and atoms in molecules (AIM) calculations.

The purpose of the present study is to examine the gas phase structures of the proton- and sodium-bound proline amino acids. Later the unimolecular chemistries of the complexes of proline containing doubly charged first row transition and alkaline earth metals were explored. Finally, the structures and the energetics of the complexes containing isomeric ProLeu and LeuPro dipeptides bound alkali metal cations were discussed. Reasonable agreements between the experimental data obtained from IRMPD spectroscopy and BIRD results with the theoretical calculations for the lowest energy forms were achieved. In the following sections the influence of the size and identity of the metal cation, the gas-phase basicity of the amino acid, anchor site of each ligand and peptide sequence on the structures and energetics of molecules were considered.

Acknowledgments

The research presented in this dissertation would not have been possible without the help and support from many wonderful people who have inspired me over the five years of my Ph.D at Memorial University. I wish to express my gratitude first and foremost to my PhD supervisor, Prof. Travis D. Fridgen, who inspired me to accomplish my goals. I am greatly indebted to Prof. Travis D. Fridgen for his endless patient guidance throughout this research. My research time was immensely valuable, and without Prof. Travis D. Fridgen the success of this project could not have been possible. He was always very positive and let me share my thoughts without worrying that I might have wrong opinions. He was not only encouraging me about my research, but his friendly and cheerful nature have made the last four years of my studying enjoyable times of learning. He has actively given me plenty of opportunities to present my work at international conferences over the world. Through these trips, I was able to get in touch with a lot of well-known people in the mass spectrometry research community worldwide.

I am also thankful to have worked with all wonderful people in Prof. Travis. D Fridgen ‘s research group for providing helpful comments and discussions about the research in a very friendly environment. I would also like to thank my committee members, Prof. Peter G. Pickup and Prof. Christopher M. Kozak for all their time, guidance, and advice. I would also like to acknowledge my internal examiners, Prof. Ray Poirier and Prof. Robert Davis and my external examiner, Prof. Scott Hopkins from University of Waterloo,

for their valuable feedback on my thesis. I would love to emphasize on my special thanks to Prof. Robert Davis who encouraged me to continue pursuit of my way toward the completion of this work.

I definitely could not make it to this point without the never-ending love of my parents, who have kept me motivated in challenging times to get a better education and life and I am very grateful to them.

My gratitude is also extended to a number of wonderful people in the general office in the chemistry department, Ebony, Rosalind, Mary, Debbie and Melissa for making this a great work place.

At the end, my deepest thanks go to Saleh Riahi, my life best friend for carrying far more than his fair share.

Table of Contents

List of Figures

Chapter 1

Chapter 2

Chapter 3

Chapter 4

Chapter 5

Chapter 6

List of Tables

Chapter 6

List of Schemes

Chapter 4

List of Abbreviations and Symbols

ΔE_{el}	electronic energy
$\Delta_{rel}G$	relative Gibbs energy
$\Delta_{rel}H$	relative enthalpy
$\nabla^2\rho$	Laplacian of electron density
A	Arrhenius pre-exponential factor
Å	Ångströms
ACEnet	Atlantic Computational Excellence network
AIM	Atoms in Molecules
AlaPro	alanineproline
B	magnetic field strength
ß	geometrical factor
B3LYP	Becke, 3-parameter, Lee-Yang-Parr density functional theory
BCP	bond critical point
BIRD	blackbody infrared radiative dissociation
CFI	Canada Foundation for Innovation
CID	collision induced dissociation
CLIO	Centre Laser Infrarouge d'Orsay
CRM	charge residue model
Ω	collision cross section
CC-PVTZ	correlation-consistent polarized valence triple-zeta basis set
cm^{-1}	wavenumbers; inverse centimeters

CI	configuration interaction
CS	charge solvated
d	diameter
Def2SVP	Karlsruhe basis sets split valence polarization
Def2TZVP	Karlsruhe basis sets valence triple-zeta polarization
D_0	0 K dissociation energy
DFT	density functional theory
DNA	deoxyribonucleic acid
ε	ellipticity
ECF	extracellular fluids
ECP	effective core potentials
ENaC	epithelial sodium channel
E_0	critical dissociation energy
E_a	Arrhenius activation energy
E_a^{∞}	limiting rapid-exchange Arrhenius activation energy
E_{elec}	electronic energy
E_{rot}	rotational energy
E_{trans}	translational energy
E_{vib}	vibrational energy
E_{ZP}	zero-point energy
ESI	electrospray ionization
f_c	cyclotron frequency
FAIMS	high field asymmetric waveform ion mobility spectrometry

FEL	free electron laser
FT-ICR	Fourier transform ion cyclotron resonance
FTICR-MS	Fourier-transform ion cyclotron resonance mass spectrometry
FWHM	full width at half maximum
GAFF	General AMBER force field
GlyHis	glycinehistidine
GTF	Gaussian type functions
h	Planck's constant
HDMS	hydrogen–deuterium exchange mass spectrometry
HF	Hartree-Fock
HisGly	histidineglycine
I	intensity
ICR	ion cyclotron resonance
IEM	ion evaporation model
IMS	ion mobility spectrometry
IR	infrared
IRMPD	infrared multiple photon dissociation
IVR	intramolecular vibrational energy redistribution
J	total angular momentum
$k_{1,rad}$	rate constant for radiative absorption
$k_{-1,rad}$	rate constant for radiative emission
k_d	unimolecular dissociation rate constant
k_{ij}	rate constants for all state-to-state transitions

k_{obs}	observed (measured) rate constant
k_{uni}	thermal unimolecular dissociation rate constant
K	temperature; Kelvin
k_B	Boltzmann constant
kJ mol^{-1}	kilojoules per mole
KTP	potassium titanyl phosphate, $KTiOPO_4$
Leu	leucine
LeuPro	leucineproline
LDT	linear drift tube
m	mass
M	molarity; moles per liter
M06-2X	Minnesota density functionals
MALDI	matrix-assisted laser desorption ionization
MD	molecular dynamics
MEM	master equation modeling
μL h^{-1}	microliters per hour
mmol L^{-1}	millimoles per liter
m/z	mass-to-charge ratio
MP	Møller-Plesset
MP2	Møller–Plesset second order perturbation theory
MS	mass spectrometry
N	number of atoms in a molecule
Na_vMs	Na^+ channel from *Magnetococcus marinus*

Nd:YAG	neodymium-doped yttrium aluminum garnet, $Nd:Y_3Al_5O_{12}$
NZ	non-zwitterionic
NSERC	Natural Sciences and Engineering Research Council of Canada
OPO	optical parametric oscillator
PES	potential energy surface
Pro	proline
ProLeu	prolineleucine dipeptide
QqTOF	quadrupole/time of flight
ω_c	angular velocity
ρ	electron density
REX	rapid exchange
RF	radio frequency
s	seconds
SB	salt-bridge
SA	simulated annealing
SORI-CID	sustained off-resonance irradiation collision induced dissociation
STO	Slater type orbitals
T	tesla
TOF	time of flight
TWIG	travelling wave ion guide
TWIMS–MS	traveling wave ion mobility–mass spectrometry
V	velocity
Z	charge

ZW	zwitterionic
μ	transition dipole moment

List of Appendices

Co-authorship Statement and Status of Manuscripts

The research presented in Chapters 3-6 of this thesis has been conducted by the author for the degree of Doctor of Philosophy under the supervision of Prof. Travis D. Fridgen.

1. Jami-Alahmadi, Y.; Gholami, A.; Fridgen, T. D.: **The Protonated and Sodiated Dimers of Proline by IRMPD Spectroscopy in the N-H and O-H Stretching Region and Computational Methods**. *Phys. Chem. Chem. Phys.*, 2014, 16, 26855-26863. This published work forms the basis for the work described on Chapter 3. The two experimental IRMPD spectra reported were recorded by Dr. Ameneh Gholami at Memorial University. Data analysis, theoretical calculations and preparation of the manuscript were done by Yasaman Jami-Alahmadi. Manuscript was edited by Prof. Travis D. Fridgen.

2. Jami-Alahmadi, Y.; Fridgen, T. D.: **Structures and Unimolecular Chemistry of M(Pro2-H)$^+$ (M = Mg, Ca, Sr, Ba, Mn, Fe, Co, Ni, Cu, Zn) by IRMPD Spectroscopy, SORI-CID, and Theoretical Studies.** *Phys. Chem. Chem. Phys.*, 2016, 18, 2023-2033. This published work forms the basis for the work described on Chapter 4. All the experimental design, data collection/analysis, theoretical calculations and manuscript preparation were done by Yasaman Jami-Alahmadi. Edits to the manuscript were done by Yasaman Jami-Alahmadi and Prof. Travis D. Fridgen.

3. Jami-Alahmadi, Y.; Linford, B. D.; Fridgen, T. D: **Distinguishing Isomeric Peptides: The Unimolecular Reactivity and Structures of (LeuPro)M$^+$ and (ProLeu)M$^+$ (M = Alkali Metal).** *J. Phys. Chem. B.*, 2016, 120, 13039-13046. This published work forms the

basis for the work described on Chapter 5. Experimental design, data collection in 2700-3800 cm^{-1} region and analysis, theoretical calculations and manuscript preparation were done by Yasaman Jami. The IRMPD spectra in the range of 900-1800 cm^{-1} were collected by Prof. Travis D. Fridgen, and Mr. Bryan D. Linford at the CLIO facility in Paris, France. Edits to the manuscript were done by Yasaman Jami-Alahmadi and Prof. Travis D. Fridgen.

4. Jami-Alahmadi, Y.; Fridgen, T. D.: **Distinguishing Complexes of Isomeric Peptides: Structures, Energetic, and Reactions of Sodium Cation-Coordinated ProLeu or LeuPro Trimers in The Gas Phase.** (Just accepted) This work that was just published forms the basis for the work described on Chapter 6. All the experimental design, data collection/analysis, theoretical calculations and manuscript preparation were done by Yasaman Jami. Edits to the manuscript were done by Yasaman Jami-Alahmadi and Prof. Travis D. Fridgen.

Chapter 1
Introduction

1.1. Studying Biological Molecules. Molecular level knowledge about the intrinsic structures of small to large biological molecules such as amino acids, peptides, and proteins is the starting point for a detailed understanding of their functionality under physiological conditions. Details regarding protein–ligand interactions, where the ligand could be any other species such as enzymes, water molecules, or even another protein, reveal the nature of the various activities happening within the living cells.[1] A lot of unknown processes causing diseases in living cells are identified in more detail by understanding the structures and reactivities of these molecules which may be related to their abnormal functionality.[2,3,4,5]

The very first proposed concept of the interactions between atoms resulting from their tendency to equally share electrons forming a covalent bond, or the electrostatic interaction between very polar bonds and electronegative atoms resulting in hydrogen bonding, refers back to 1919[6] and 1936,[7] respectively. Although covalent bonding is the strongest interaction between atoms, the importance of non-covalent interactions in molecular associations cannot be neglected.[8] Metal cation interactions in complexes involving amino acids, peptides, and proteins through strong inter- and intramolecular interactions are key components controlling many chemical processes in living things. Identification of the nature of these interactions has had an important impact in understanding much of the chemistry of life at the molecular level.

Since each protein has a unique amino acid sequence, the details of many protein interactions with other biologically important molecules such as enzyme active sites, metal cations, other proteins, peptides, and amino acids are still unknown. The presence of a metal cation can change the structural properties of these systems resulting in different biological functionalities. Understanding the structures and thermodynamics of metal cation chelation to macromolecules helps in identifying the details of interactions between these species. For example, the selectivity of the epithelial sodium channel (ENaC) to Na^+ is important in the regulation of sodium ion in the extracellular fluids (ECF) and hence controlling blood pressure. Since sodium channels contain a proline side chain in ENaC, structural changes caused by mutation of channel subunits result in abnormal binding sites and consequently cause diseases such as kidney or Liddle's syndrome.[9,10,11,12] Interestingly, the structures of the voltage-gate Na^+ channel from *Magnetococcus marinus* (Na_vMs) shows high selectivity of the channel to create a pore and discriminate between certain ions. Coordination of hydrogen-bonded water molecules in sodium channels prevents the direct interaction of ions with the side chains of sodium channels. In contrast, in potassium channels, ions can directly interact with the side chain of the polypeptide rather than coordinate to water molecules (see Figure 1.1).[13]

Metal ion coordination can stabilize the zwitterionic (ZW) form of amino acids, but depends on factors such as the size and valency of the metal ion and the gas-phase basicity of the amino acids, or even on the presence of a solvent such as water.[15,16,17,18] Brief details of amino acids and peptides, along with their possible structures, are discussed in later sections.

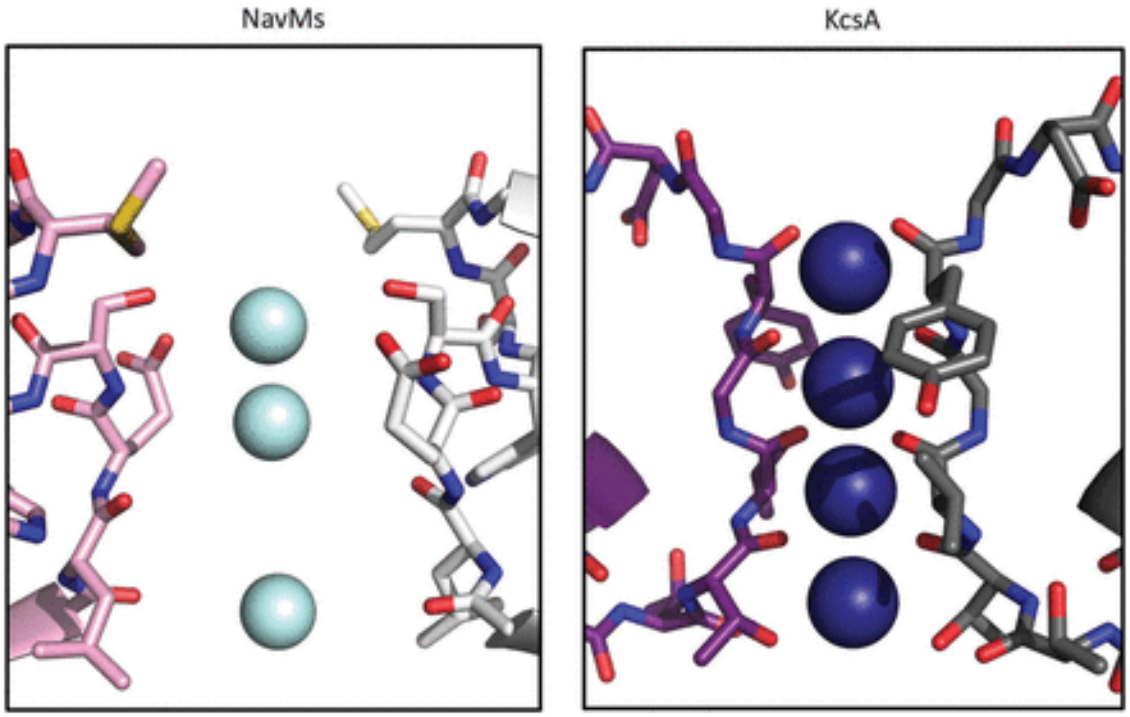

Figure 1.1. Comparison of ion binding in a sodium (left) and potassium (right) channel. Left: Selectivity of Na_vMs channel to sodium ions (cyan color). Right: Selectivity filter of KcsA channel to potassium ions (dark blue color). For clarity, only two monomers are shown. Figure adapted with permission from *EMBO*, **2016**, 1-11.[14]

The rest of this chapter describes the purpose of studying biomolecular ions in the gas phase and how mass spectrometric techniques provide detailed insights into the gas phase chemistry of ionic complexes involving biologically-relevant molecules. In Chapter 2, the instrumentation and in Chapters 3-6, applications of mass spectrometric techniques in the characterization of non-covalent interactions and thermodynamics of protonated and metal cation-bound proline and proline containing peptide complexes are discussed. Several experimental techniques such as infrared multiple photon dissociation (IRMPD) spectroscopy, sustained off-resonance irradiation collision induced dissociation (SORI-

CID), and blackbody infrared radiative dissociation (BIRD) were used in this research and are discussed in these chapters. In addition, details about how gas phase mass spectrometric techniques are combined with theoretical methods to help in deducing the most probable gas-phase structures are revealed. Computational methods such as density functional theory (DFT) and simulated annealing (SA) help to determine the dominant structures of different complexes in the gas phase. The current thesis can serve as an example of research on gas-phase ion-molecule reactions that provides wider understanding into molecular properties such as, structure, thermochemistry, and reactivity of these interesting molecules.

1.2. The Purpose of Studying Biomolecular Ions in the Gas Phase. The detailed structures and the reactivity of biologically interesting molecules can be obtained when the disrupting effects induced by other chemical agents such as solvent molecules are at a minimum. Research on gas-phase ions and ion-molecule reactions provides information on their intrinsic physical properties in the absence of solvent. In addition, under low pressure conditions, the time between collisions is long enough to slow down rates of reactions which would, under normal conditions, be too fast to follow. Since the pressure is so low, ions can be stored for a long time and spectroscopic studies of mass selected ions are possible for these typically reactive species.

Interestingly, the effect of solvation can be studied systematically by generating and studying a series of ions of the type $(M(solvent)_k)^n$, where k is the number of neutral solvent molecules such as water or alcohol and M is the ion of interest with the charge, n.[19,20,21,22] For example, by increasing the number of solvent molecules, the intrinsic properties can be compared with solution phase properties that can help us understand the role of solvent.

This cooperation explains why we believe gas phase investigations allow us to gain some insight into the physical chemistry of these complexes that, in principle, may be useful to rationalize the behavior of more complicated systems which present similar basic sites but, are too complicated to study in the solution phase. Gas phase studies of protonated or metal cationized amino acids or peptides offers an opportunity to better understand these systems on a molecular level, not often afforded for macromolecules in solution. Gas phase studies provide a good understanding of non-covalent interactions and useful structural information on biomolecular and other gaseous ions. These fundamental intrinsic properties lead to an understanding of how non-covalent interactions stabilize biomolecules in living organisms.

1.3. A Brief History of Important Early Scientific Advancements Leading to the Development of the Study of the Physical Chemistry of Gas-Phase Ions. In 1906,[23] J. J. Thomson was awarded the Nobel prize in physics for the development of a way to conduct electricity in gases and separating isotopes. In 1913 Thompson and F. W. Aston created a "mass spectrograph" for the very first time. Aston was awarded the Nobel prize in chemistry in 1922 for development of the mass spectrograph which was able to differentiate between the isotopes of large numbers of naturally occurring elements by expressing that the atomic mass of isotopic elements is a whole number multiple of hydrogen atomic mass.[24,25,26]

In 1961, John Charles Polanyi discovered infrared chemiluminescence based on the idea that when molecules are excited, they emit infrared light. He was able to measure the emitted light through chemical reactions, and differentiate between vibrational and

rotational energies. The importance of his work had a significant impact in the discovery of the sources of infrared radiation lasers. Along with Dudley Herschbach and Yuan T. Lee, the three were awarded the Nobel Prize in chemistry in 1986 for their work related to the dynamics of chemical reactions.

German physicist, Wolfgang Paul, conducted pioneering work on developing electric quadrupole fields to trap charged particles in three dimensions. The quadrupole ion trap was nicknamed a Paul trap in honor of his work in this field. He invented the ion trapping mass analyzer and was awarded the physics Nobel prize[27] in 1989 together with Norman Ramsay and Hans Dehmelt who developed ion-cyclotron resonance spectrometers.

John B. Fenn and Koichi Tanaka received one-quarter of the Nobel prize for chemistry in 2002, for the invention of soft ionization methods (ESI and MALDI).[28] This brief review of the history of science reveals that the genesis of the advanced instruments in MS is built on the earlier work by others.[29]

1.4. Determining the Structures of Biomolecules Using Mass Spectrometric Techniques. A mass spectrometer is typically composed of three main parts: the ion source, the analyzer and the detector. However, the proper choice of ion source and analyzer type depends on the nature of the sample and the desired information, respectively. Many different types of mass spectrometers have been developed using different types of ionization sources, mass analyzers, and mass analyzer configuration.

The ion source is an essential part of every mass spectrometer where ions are formed by a wide range of methods. In the present work, electrospray ionization (ESI) was used exclusively as the method of ionization and is described in more detail in the next chapter. The mass analyzer is the heart of every mass spectrometer since the mass of ionized species is determined in this part of the MS instrument. In all mass analyzers, ions are essentially organized according to their mass–to–charge ratio (*m/z*). Mass analyzers are characterized by a few parameters, including resolving power, mass range, mass accuracy, and coupling compatibility. They can generally be categorized into two classes: (1) beam type mass analyzers and (2) ion trapping mass analyzers. In beam type mass analyzers, such as time of flight (TOF), after their formation, ions travel continuously through a path from the source to the detector. On the other hand, trapping analyzers like the Fourier transform ion cyclotron resonance mass analyzer (FTICR–MS) can isolate and store ions for long periods of times giving more control of ions. Ions of interest can be isolated based on mass and stored inside the ion trapping instrument for further desired manipulations and experimental activation processes, such as photodissociation experiments.[30]

The FTICR mass spectrometer has found a wide range of applications. This mass analyzer is known as an ultra-high resolution mass analyzer with great mass accuracy that is able to resolve isotopic fine structures of proteins with masses up to 100 kDa. The FTICR has many advantages, such as a high upper mass limit. The theoretical upper mass limit is the mass in which the radius of the ion cyclotron achieves the radius of the trap. For example, using a 7 Tesla ICR in a trap size of one-inch cross-sectional radius, for a singly-charged ion at room temperature, this theoretical upper mass is around 5.89 MDa.[31,32] Other

advantages are the mass resolving power, the number of ions trapped, and trapping duration. The FTICR mass spectrometer is an excellent mass analyzer especially when using slow activation techniques like low energy CID and BIRD is desired. Some of these benefits and limitations are discussed in the activation technique section (next section).

On the other hand, there are other ion trapping mass analyzers such as quadrupole ion traps, orbitraps,[31] and high order linear traps such as the 22-pole ion trap[33] that are valuable tools for investigating ion-molecule reactions.[34] All these trapping instruments are used in conjunction with techniques such as CID and IRMPD in which the fragmentation of ions is required.[35] 22-Pole ion traps are particularly useful for collision processes and when chemical reactions are to be studied at low temperatures. In the 22-pole[36,37] ion trap, twenty two rods with lengths of 50 mm and 1 mm diameters are used to generate an electric radio frequency field with opposite phases. In the axial direction, ions are trapped using electrostatic voltages applied to the two cylindrical electrodes. Therefore, in a 22-pole ions are confined by oscillating electric fields which excite the ions translationally, whereas in an ICR cell the ion translational energy is in thermal equilibrium with the surroundings and trapped with a high-field magnet. The 22-poles are capable of performing experiments at low temperatures in which ions are cooled using a buffer gas (down to a nominal 3.8 K). However, under multiple collisions with the gas molecules in the trap, ions are well thermalized and trapped for a long period of time.[38,39]

1.5. Mass Spectrometric Fragmentation Techniques of Gas Phase Non-Covalently-Bound Complexes. Mass spectrometry provides useful information such as the mass-to-charge ratio of the ion, but to obtain further information, it is necessary to employ

fragmentation techniques. Fragmentation methods are used to determine structural characteristics as well as thermochemical quantities. To fragment an ion, the energy of that ion is increased above its dissociation threshold by one of many methods such as collisions, laser absorption, electron attachment, or absorption of ambient blackbody infrared radiation. Besides fragmentation patterns, appearance and disappearance rates of species can be determined to obtain useful information about their structures.

As mentioned earlier, proteins and peptides function through non–covalent interactions with metals, other peptides or proteins, or even cofactors.[40,41] Due to the larger number of structural conformations in larger molecules compared to simple amino acids, the identification of macromolecular structures is more difficult. Therefore, gas phase studies are appropriate models to understand the physical properties of the amino acids, peptides and proteins.[42] For example, low energy CID is a useful characterization technique to slowly activate lower energy dissociation channels of large peptides and proteins.

For this work, gas phase fragmentation techniques such as CID, IRMPD, and BIRD are used to study the properties of proline and proline-containing dipeptide complexes.

1.5.1. CID. CID is one of the earliest activation techniques used in mass spectrometry and it is the most common. During the CID process, the translational energy of an ion is increased and it is collided into an inert target gas, converting a portion of its translational energy to internal energy. The ion dissociates as the amount of energy deposited surmounts the dissociation threshold. CID can be coupled to any mass spectrometer including beam type instruments and ion trapping mass spectrometers, but its performance and applications are highly dependant on the type of mass analyzer. There are two regimes of translational

energy that are used, depending on the mass spectrometer. For example, in TOF or sector instruments, the kinetic energies of the ions can be in the kV range so that only one collision is necessary to induce dissociation. In ion trapping devices, the collision energies are on the order of a few tenths of an eV up to about 100 eV so that multiple collisions are necessary to affect fragmentation. Low energy is useful to slowly activate (or heat) the ion of interest, resulting in only the lower energy dissociation channels being accessed.

As shown Figure 1.2, when a protonated peptide undergoes fragmentation, the cleavage typically occurs from either the C-terminus, producing b ions, or N-terminus, producing y ions. Bleiholder and co–workers[43] used collision induced dissociation to discover the fragmentation patterns of protonated peptides that contain proline and alanine, (Ala-Ala-Xxx-Pro-Ala when Xxx = Ala, Ser, Leu, Val, Phe, and Trp,). The results showed that the higher proton affinity at the C-terminus of a peptide is due to the existence of proline possessing high proton affinity, which favors the production of y_2 species in the fragmentation pattern. In order to perform the experiment, an electrospray/quadrupole/time of flight (QqTOF) mass spectrometer was used. As shown in Figure 1.2, the cleavage of the amide bond N-terminus to proline residues results in y-ion formation. The most dominant peak in the main fragmentation channel of Ala-Ala-Xxx-Pro-Ala peptides, when Xxx = Leu, Val, Phe, and Trp, is the y_2 product ion (depicted in Figure 1.2 top). The dominating y_2 product ion in the Pro-Ala sequence, formed by cleavage of the amide bond, is the result of the existence of proline residue in the peptide backbone. As indicated in Figure 1.2 top, the production of the y_2 ion is followed by a less abundant b_3 peak. In addition, the y_3 fragment due to protonated Xxx-Pro-Ala that is generated from loss of C-

terminus Ala residue. The very weak peaks shown in the CID spectrum correspond to the b_3 and b_4 ions that reveal the b_3 ion is produced from the cleavage of the Xxx-Pro amide bond instead of $b_4 \rightarrow b_3$ pathway. In order to rationalize the observed pathways, computational techniques were applied to calculate the relative energies of different backbone protonation sites and transition structures of the amide bond cleavage.

The obtained threshold energies of the mechanistic channel of transition structures for the cleavage of amide bonds of the backbone N-terminus to the proline were measured to be the lowest pathway. The N-terminus amide bond cleavage of the proline residues is preferred. This is due to the existence of this amino acid in the peptide backbone which stabilizes the protonation of the amide nitrogen position in Ala-Pro. The reason for the observed cleavage was the high proton affinity of proline as a result of this bond breakage. This cleavage increases the proton affinity of the generated C-terminus fragment and therefore, the formation of the y_2 fragment.

1.5.2. IRMPD. IRMPD is performed by taking advantage of the fact that ions can reach the dissociation threshold through sequential absorption of photons from a high intensity infrared laser, typically a CO_2 laser. IRMPD activation is a slow process, like CID, and the lowest energy dissociation pathways are observed. IRMPD is affected by an intense source of light that is used to simply dissociate ions, much like in the collisional activation method. Using a tunable infrared laser, one can also do spectroscopy experiments by determining which wavelengths of the laser are resonant with vibrational modes of the ion, causing dissociation.

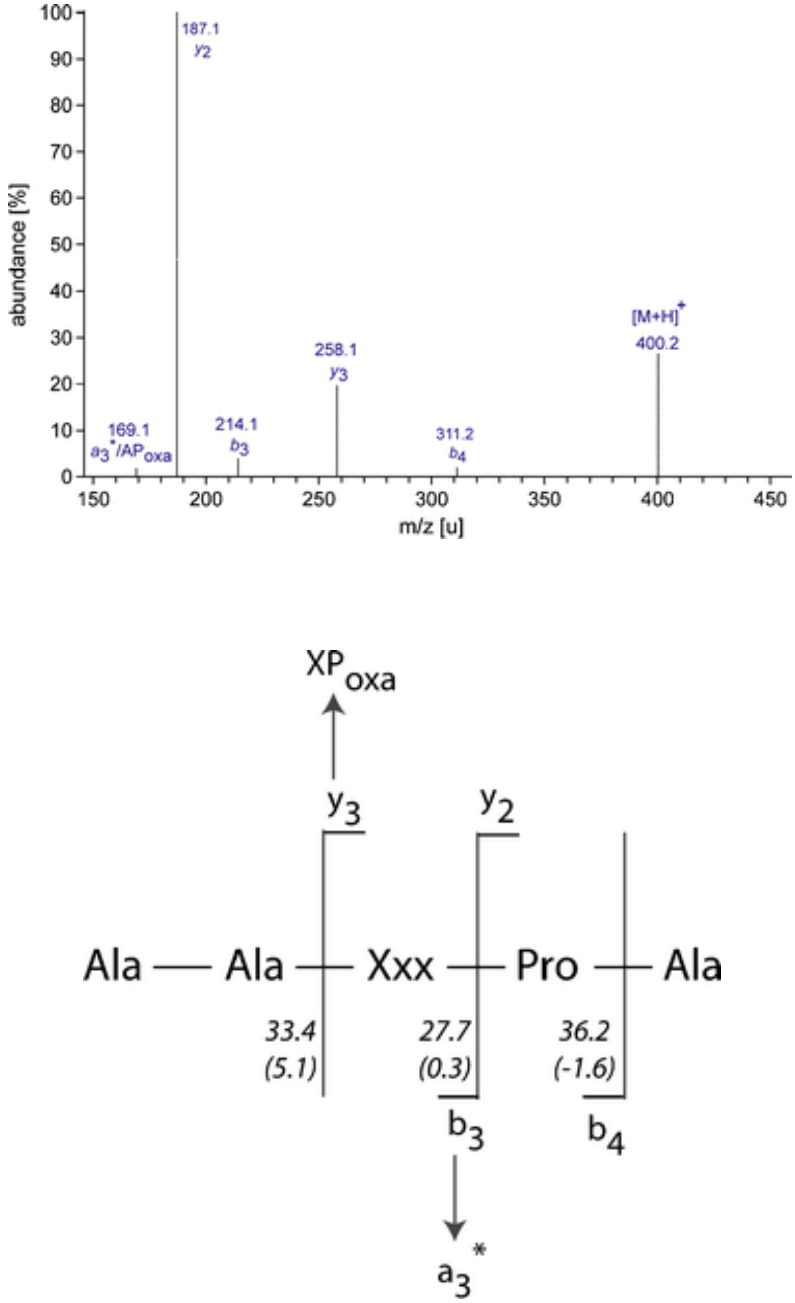

Figure 1.2. (Top) Fragmentation pathway and dominant peaks obtained for cleavage of protonated Ala-Ala-Ala-Pro-Ala, upon 16 eV collision energy. (Bottom) Fragmentation pathways correspond to the protonated Ala-Ala-Xxx-Pro-Ala. Along with computed threshold energies (kcal mol^{-1}) as well as the activation entropies (cal mol^{-1} K^{-1}) for the cleavage of amide bond for the protonated Ala-Ala-Ala-Pro-Ala. Figure adapted with permission from *Journal of the American Society for Mass Spectrometry*. **2011**, 22, 1032–1039.[43]

An IRMPD spectrum can be obtained by recording ion fragmentation as a function of laser wavelength. IRMPD spectroscopy is considered a consequence spectroscopy since the consequence of multiphoton absorption dissociation is detected.[44,45] More details of this fragmentation technique are discussed in the next chapter.

Williams and coworkers[46] combined IRMPD with DFT calculations to investigate the effects of hydrogen bonding on the structures of anionic glycine dimers. They recorded the IRMPD spectra in the 600 to 1800 cm^{-1} region as shown in Figure 1.3. The results showed that the formation of intramolecular hydrogen bonding stabilizes the zwitterionic form of the complex. Previous gas phase studies of the cationic protonated dimers of glycine using IRMPD[47,48] and BIRD[49] techniques showed the non-zwitterionic form of glycine dimers to be the predominant form. The ZW form, also known as salt bridge (SB) form, is different from the non-zwitterionic (NZ) form in which the proton has been transferred toward NH_2 to form NH_3^+ on one side and the CO_2^- group on the other side of glycine. It was found that, in the anionic complex, the intramolecular hydrogen bonding and the Coulombic attraction stabilize the ZW form. As shown in Figure 1.3, in the non-zwitterionic form, the deprotonated glycine is attached to the O–H group of the carboxylic acid in the intact glycine which forms a strong ionic hydrogen bond (O···H–O). The N–H bond in each NH_2 group is also involved in an intramolecular hydrogen bond to an oxygen atom of a carboxyl/carbonyl group. In the ZW form, shown in Figure 1.3, both oxygen atoms of the deprotonated anionic glycine are attempting to form two hydrogen bonds with hydrogen atoms located in the NH_3^+ group. There are also two intramolecular hydrogen bonding N–H···O between N–H bonds and the carboxylate groups. In the experimental

spectrum, the positions of prominent modes, such as, NH_2, CH_2 wagging, and NH_3^+ umbrella vibrations agree with the computed spectrum of the SB form.

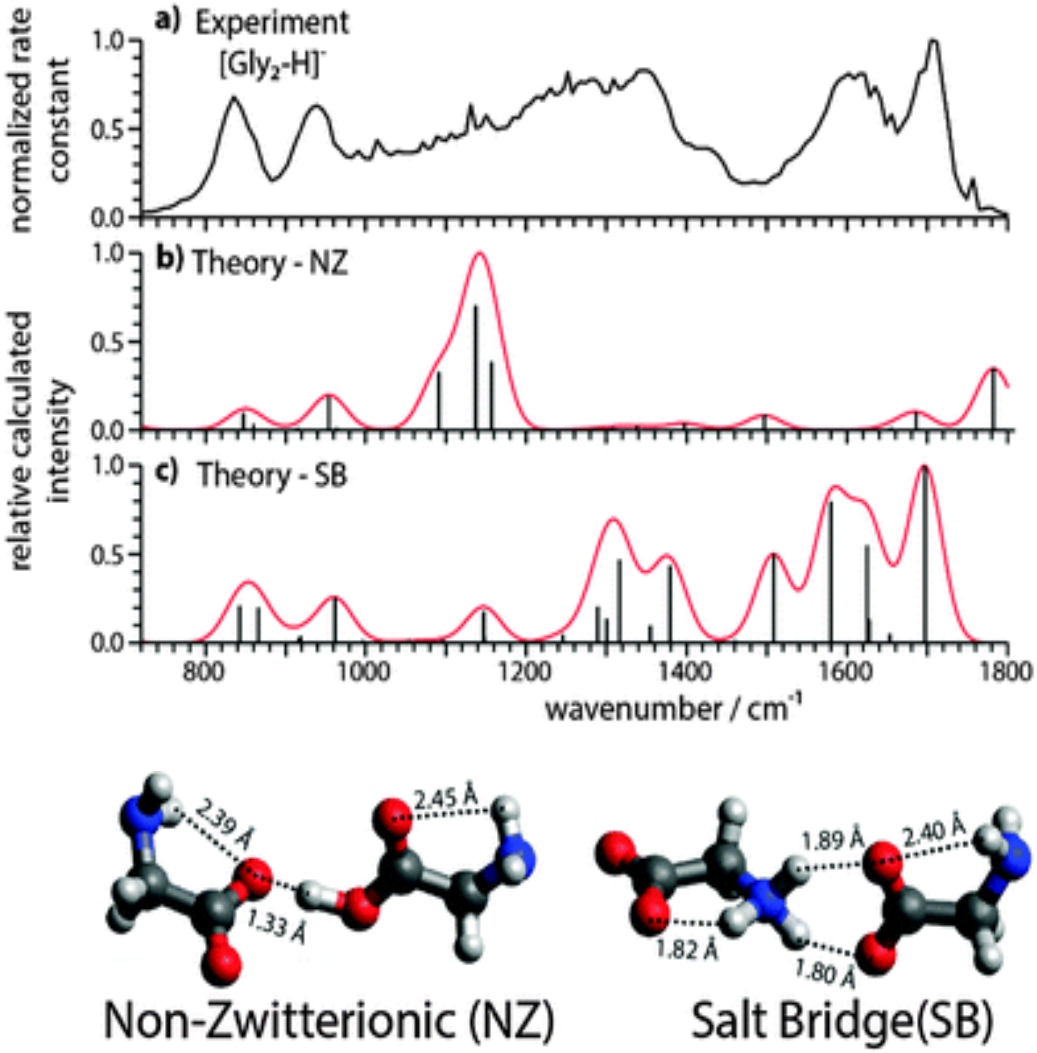

Figure 1.3. Comparison of (a) the experimental IRMPD spectrum and calculated IR spectra for the lowest energy structures of each form of the NZ and SB isomers of $[Gly_2–H]^-$ complex, at the B3LYP/6-311++G(d,p) level of theory using scaling factor of 0.985. Figure adapted with permission from *Phys. Chem. Chem. Phys.* **2015**, 17**,** 30642–30647.[46]

More importantly, the existence of a sharp experimental band at 1704 cm^{-1} is in agreement with the computed IR spectrum for the SB isomer and indicates that this is a possible form of this complex. It should be noted that in this study, the theoretical results showed a difference of 16 kJ mol^{-1} in the Gibbs energies of the two lowest energy forms. Altogether, the computed IR spectra of the anionic zwitterion complex, which is the best matched with the IRMPD spectrum, reveals the ZW form as the possible structure.

1.6. Other Mass Spectrometric Techniques for Studying Structures and Dynamics of Biological Complexes. There are other spectrometric techniques to study the physical chemistry of gas phase ion-molecules such as ion mobility spectrometry (IMS)[50,51] and H/D exchange[52,53,54,55] These techniques are not used in this thesis but, it is worth briefly mentioning some of their functionalities.

1.6.1. Ion Mobility Spectrometer (IMS). IMS is a gas phase spectrometric technique in which ions are essentially separated according to their mobilities through a higher pressure region followed by mass analysis. This method has the ability to identify species not only based on their mass-to-charge ratio, but also according to their collision cross section (Ω).

IMS has a lot of applications, ranging mainly from the structural identification of biological ions and conformational dynamics of species[56] to chemical detectors that are used in security and drug detection.[57,58] An important advantage of this method over other techniques is that two ions with the same mass but different shapes are separable due to their differing speed through a buffer gas. In this method, under the influence of an electric field, the movements of molecules under study are dictated by their mobility. A drift gas

such as helium, neon, nitrogen, argon or carbon dioxide that impedes the ion of interest's motion is also present.[59,60] In IMS, ions are generated in an ionization region using various ionization techniques and then enter a drift region where they can be pulsed into a drift tube. Figure 1.4 shows a block diagram of an ion mobility spectrometer. Because ions have different sizes, the time required to traverse the drift tube varies. Larger ions with higher collision cross section (Ω) undergo more collisions with the inert buffer gas and take longer to reach the detector. Therefore, in IMS, ion separation is based on both *m/z* and the mobility of ions. Coupling ESI or MALDI with IMS increases the efficiency of this method for conformational analysis in the millisecond time scale.[61] There are three main types of IMS, linear drift tube (LDT), travelling wave ion guide (TWIG), and high field asymmetric waveform ion mobility spectrometry (FAIMS).[62,63] Details about the functionality of each of the types are beyond the scope of this thesis. But, it should be stated that in order to have a complete understanding of molecular structure, computational methods are typically required. IMS has advantages of high sensitivity and precision, being very fast and having a very low detection limit. In addition to the advantages described above, a lot of capabilities of IM-MS have been achieved through the speed of this method, such as the investigation of the dynamics of protein folding process.[56]

Previous structural investigations of metal cationized 4-substituted proline diastereomers have been conducted by Bartberger and coworkers[64] using a traveling wave ion mobility–mass spectrometry (TWIMS–MS). Since these isomers have the same *m/z*, they cannot be identified by only their *m/z*, hence, IMS was employed to differentiate between isomers.

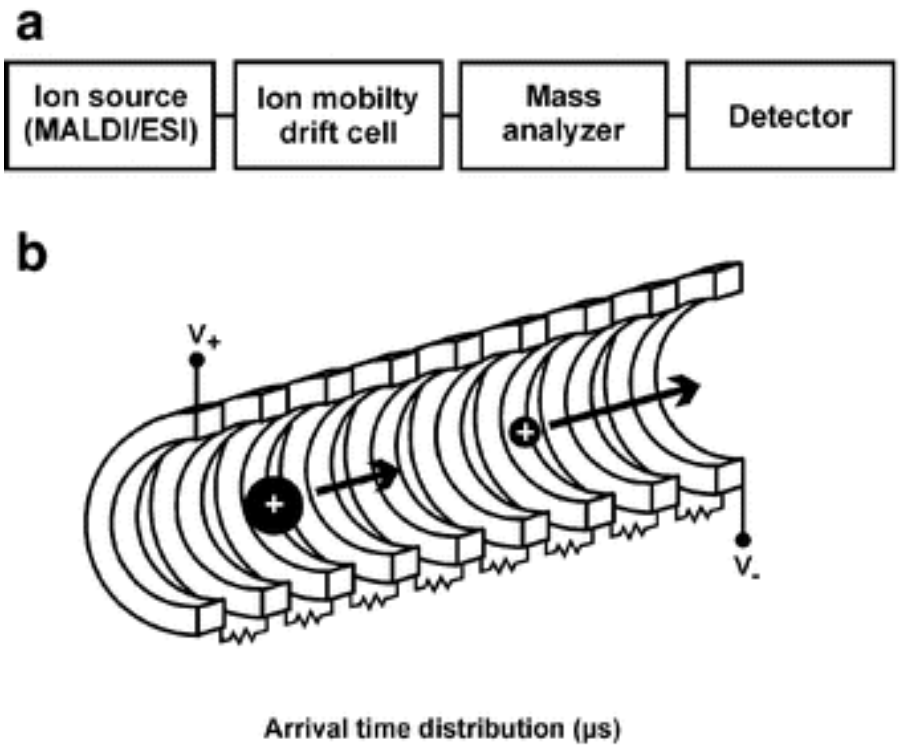

Figure 1.4. (a) A block diagram of key computational steps of an ion mobility mass spectrometry (IM–MS) (b) Schematic diagram of a drift cell along with detector electrodes. Figure adapted with permission from *Anal. Bioanal. Chem.* **2008**, 391, 905–909.[65]

As a result of change in chirality of the substituents on proline, the metal cations adopt different binding sites. Results of TWIMS-MS spectra are shown in Figure 1.5 and revealed that the measured collisional cross sections for N_2 (Ω_{N2}) of [trans-hydroxyproline + Na]$^+$ was larger than that of the [cis-hydroxyproline + Na]$^+$. In addition to this, the Ω_{N2} of [M + Na]$^+$ for both cis- and trans-hydroxyproline was larger than the Ω_{N2} of the protonated complexes. Comparison of the TWIMS spectra for the protonated hydroxyprolines, Figure 1.5. (a) and [M + X]$^+$, where X = Li, Na, K, and Cs, Figure 1.5. (b-e), indicates the effect of the metal cation size on the gas phase structure of cis- and trans-

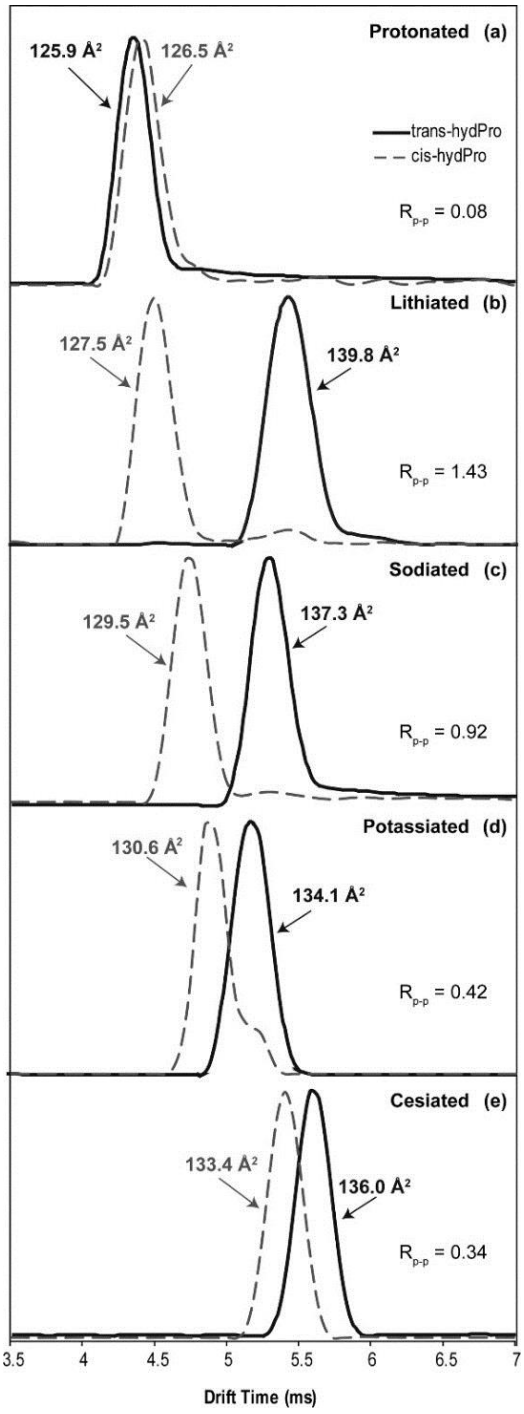

Figure 1.5. Comparison of TWIMS spectra of (a) protonated and $[M + X]^+$, where X = (b) Li, (c) Na, (d) K, or (e) Cs, for cis- and trans-hydroxyproline using N_2 as drift gas. Figure adapted with permission from *Journal of the Anal. Chem.* **2015**, 87, 3300–3307.[64]

hydroxyproline. In general, by increasing the metal size, the measured Ω_{N2} difference between diastereomers decreases.Therefore, this method was able to distinguish between the structures of the diastereomers. In order to compare the experimentally obtained Ω_{N2} results, theoretical calculations were done with the aim of finding the values of Ω_{N2}, theoretically. In the lowest energy structures of these complexes (Figures 1.6 and 1.7) the position of the proton is on the nitrogen atom of the pyrrolidine ring in both cis- and trans-hydroxyproline. There are also small differences in the orientation of the hydroxyl substituent of the ring. Generally, the experimentally observed Ω_{N2} values for the protonated cis and trans forms agree with the theoretical results. As shown in Figures 1.6 (a) and 1.7 (a), both cis/trans protonated structures have similar conformations (charge-solvated, or CS), while the cis/trans conformation differs when a metal cation is present. In the experimental data, as the size of the metal cation increases, in the alkali metal groups of elements from Li^+ to Cs^+, the resolution of both cis/trans isomers decreases. Based on the obtained results, the metallated cis-hydroxyproline was found to be in the CS form. The experimental data also indicate a smaller Ω_{N2} value for the cis-hydroxyproline isomer which is in a compact CS form.

According to the theoretical results, the larger metal cations with higher steric effects contribute in a weaker interaction, hence destabilizing the compact CS cis-proline structure. On the other hand, theoretical calculations showed that the metal cation bound trans-hydroxyproline form adopts a SB conformation that is also consistent with the Ω_{N2} values as shown in Figure 1.7. Therefore, combination of both theoretical methods

and experimental IM-MS technique helped them to determine both the cis/trans and the SB/CS forms of the cationized 4-substituted proline diastereomers.

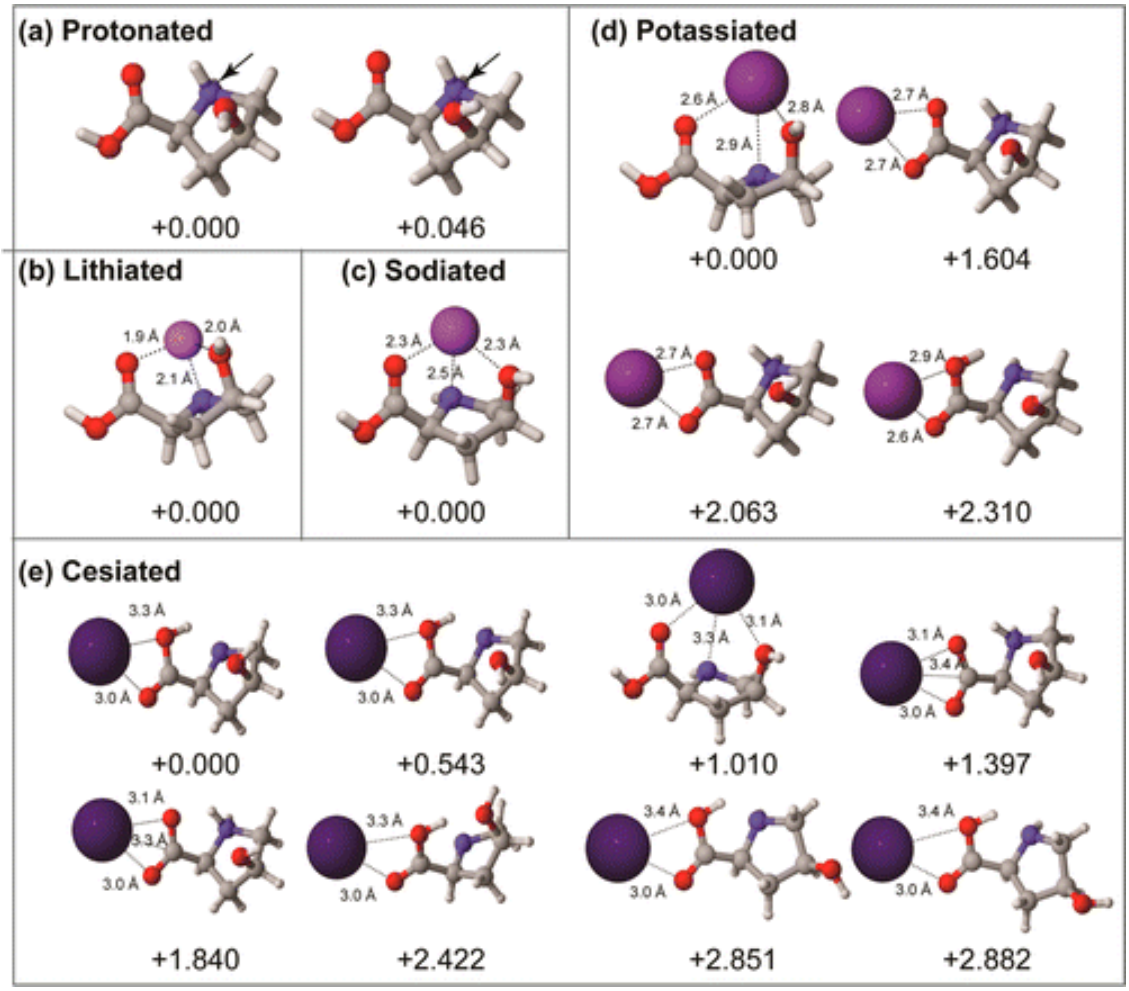

Figure 1.6. Illustration of the lowest energy structures for (a) protonated and $[M + X]^+$, where X = (b) Li, (c) Na, (d) K, or (e) Cs, for *cis*-hydroxyproline. Energies are in B3LYP level of theory and 6-31++G(d,p) basis set for all atoms except for Cs for which the pseudopotential-corrected SVPD basis was used. Reported energies are in kcal mol^{-1} and the arrow shown in (a) indicates the protonation site. Figure adapted with permission from *Journal of the Anal. Chem.* **2015**, 87, 3300–3307.[64]

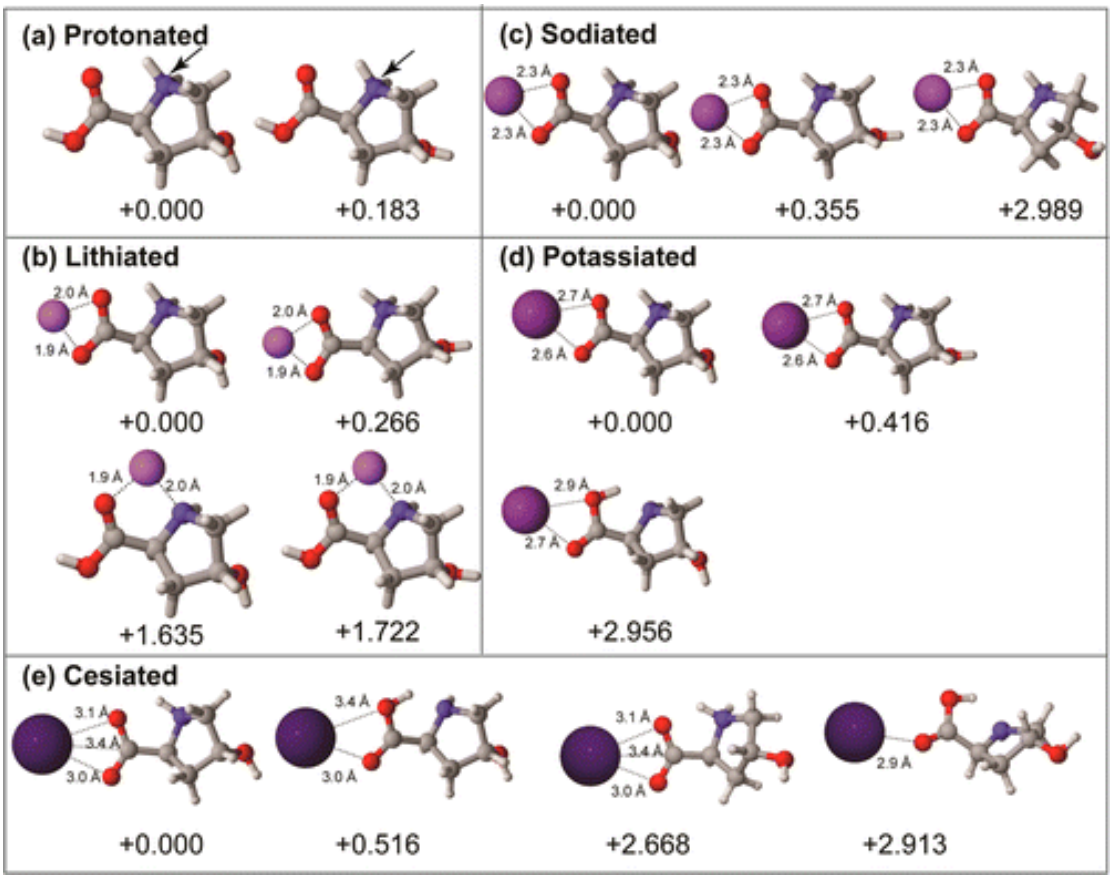

Figure 1.7. Illustration of the lowest energy structures for (a) protonated and $[M + X]^+$, where X = (b) Li, (c) Na, (d) K, or (e) Cs, for *trans*-hydroxyproline. Energies are in B3LYP level of theory and 6-31++G(d,p) basis set for all atoms except for Cs for which the pseudopotential-corrected SVPD basis was used. Reported energies are in kcal mol^{-1} and the arrow shown in (a) indicates the protonation site. Figure adapted with permission from *Journal of Anal. Chem.* **2015**, 87, 3300–3307.[64]

1.6.2. Hydrogen–Deuterium Exchange Mass Spectrometry (HDMS). In this technique, the rate that the amide hydrogen of a peptide or protein undergoes exchange with a deuterated reagent in the gas- or solution-phase, is measured. The availability of the amide hydrogen in each residue, (except for proline which does not have an amide hydrogen), depends on the backbone environment of the residues. Therefore, the rate of this exchange

is significantly influenced by the structure and the dynamics of the specific residue of the peptide or protein due to its involvement in intramolecular hydrogen bonds.[66]

For example, if an amide participates in an intramolecular hydrogen bond, its hydrogen exchange rate will be slower than an amide hydrogen which is exposed to the solvent molecules on the surface of the protein. Until a few years ago, hydrogen exchange was observed by NMR in solution in order to understand the conformations and dynamics of protein folding.[67] Some types of hydrogens within peptides or proteins undergo very rapid exchange with the solvent to be measured. These hydrogens are the ones located on the side chains, such as —NH_2, —OH, —SH, —$CONH_2$, —COOH. Hydrogens that are covalently bonded to the aliphatic and aromatic carbons, are very hard to exchange. Backbone amide hydrogens do exchange with varying rates depending on their environment as mentioned above. When a protein is in its folded form, due to the intramolecular interactions, some hydrogens are tightly shielded, therefore these backbone amide hydrogens are harder to be replaced than those from an unfolded protein. Since the mass of hydrogen differs from the mass of deuterium by one unit, introducing a mass spectrometer gives the capability to record this increase of one mass unit for the entire protein.

H/D exchange is a very good technique to study conformational changes associated with processes such as the protein folding,[68] due to the high sensitivity of amide hydrogens in the folded stage. Besides, the conditions around the side chain amide hydrogen, the rate of HD exchange depends on factors such as, pH, temperature and solution components. In general, a decrease in both temperature and pH will decrease the rate of H/D exchange so

these factors can be adjusted accordingly.[69,70] HDMS in both the solution– and gas–phase provides useful information about the intramolecular hydrogen bonding or van der Waals interactions vs interactions with solvent molecules.[71,72,73] Comparison of the results obtained from the gas and solution phase reveals the importance of intramolecular interaction and solvent contribution to protein structure. A combination of hydrogen/deuterium (H/D) with electrospray ionization as the ionization source[74] and tools such as ion mobility separation[75,76,77] or other techniques[78] has facilitated the study of biomolecules in the gas phase. More details regarding the instrumentation and procedure of how to dilute the solutions of proteins of interest, or the labeling methods will not be discussed here.

1.7. Motivation for Studying Proline and Proline Containing Dipeptides. Proline is different than all other 19 DNA-encoded amino acids because it is the only one that has a secondary amine, involved in a five-membered ring, giving uncommon rigidity to this amino acid and locally in peptides in which it is involved. Since proline does not provide any amide hydrogen,[79] it is not able to participate in hydrogen bonding stabilization and, therefore, breaks α-helices. However, it is frequently found in the first residue of alpha helices and in the edge strands of beta sheets, where the hydrogen bond to the imino nitrogen does not play a key role in the stabilization of polypeptide. Proline's rigidity, due to its cyclic form, allows the peptide backbone to adopt a suitable angle in a beta turn. Proline's high basicity and proton affinity make it a good proton acceptor and, therefore, under physiological conditions it is one of the most soluble amino acids.[80] The rigidity of the proline ring makes proline very suitable in stabilizing hydrogen bonding interactions.[81]

It induces a lot of important functionalities in plants such as, osmoprotective functionality,[82] or behaving as a signaling molecule in order to modulate mitochondrial functions in peptides.[83] Proline also plays a critical role in the recovery of plants under environmental water stress.[84,85] One of the rate-limiting steps in the protein folding is the cis/trans isomerization of the proteins that contain proline.[86,87,88]

1.8. Contents of This Thesis. In this thesis, applications of mass spectrometric studies to protonated and metal cationized proline and the ProLeu or LeuPro peptides are presented. In Chapter 2 the instrumentation required to perform the experiments and computational techniques are described in more detail. In Chapter 3 the structures of proline proton–bound complexes are investigated using IRMPD spectroscopy in the 3200 to 3800 cm^{-1} and in the 1000 to 2000 cm^{-1} regions.

In Chapter 4, the unimolecular chemistry and structures of $M(Pro_2\text{-}H)^+$ where M = Mg, Ca, Sr, Ba, Mn, Fe, Co, Ni, Cu, Zn, using different MS methods, such as CID and IRMPD spectroscopy are described. In both Chapters 3 and 4, the naming system is simplified with the use of the word dimer for proline complexes. But in fact, in Chapter 3 one proline is protonated or sodiated, while in Chapter 4 one proline is deprotonated and the other one is in its intact form. Chapter 5 examines the application of IRMPD as a useful technique in determining peptide sequences and demonstrating structural differences in different peptide sequencing when bounded to alkali metals. In Chapter 6 it is shown that BIRD kinetic measurements in combinations with the IRMPD spectroscopy can be used to differentiate between the binding energies and structures of the $[Na(ProLeu)_3]^+$ vs the $[Na(LeuPro)_3]^+$ complexes in the gas phase.

1.9. References

1. De Las Rivas, J.; Fontanillo, C. *PLoS Comput Biol*, **2010**, *6***,** 1-8.
2. Dulla, C. G.; Coulter, D. A.; Ziburkus, J. *Neuroscientist*. **2016**, *3*, 295-312
3. Shimojo, M.; Higuchi, M.; Suhara, T.; Sahara, N. *Front. Neurosci.* **2015**, *9***,** 1-12.
4. Saria, A.; Prast, J.; Schardl, A.; Kummer, K. *Springerplus*, **2015**, *4*, 1–32.
5. Steimer, T. *Dialogues Clin Neurosci*, **2002**, *4*, 231-249.
6. Langmuir, I. *J. Am. Chem. Soc.* **1919**, *41*, 868–934.
7. Smith, D. A. ACS Symposium Series. American Chemical Society, Washington. **1994**, 569**,** 300.
8. Desiraju, G. R. *Angew. Chemie Int. Ed.* **2011**, 50**,** 52–59.
9. Ronzaud, C.; Staub, O. *Physiology*. **2014**, *29*, 16–26.
10. Staub, O.; Dho, S.; Henry, P.; Correa, J.; Ishikawa, T.; McGlade, J.; Rotin, D. *EMBO J.* **1996**, *15*, 2371–80.
11. Kashlan, O. B.; Kleyman, T. R. *Exp. Cell Res.* **2012**, *318*, 1011–1019.
12. Tamura, H.; Schild, L.; Enomoto, N.; Matsui, N.; Marumo, F.; Rossier, B. C. *J. Clin. Invest.* **1996**, *97*, 1780–1784.
13. Payandeh, J.; Scheuer, T.; Zheng, N.; Catterall, W. A. *Nature*, **2011**, *475*, 353–358.
14. Naylor, C. E.; Bagnéris, .C.; DeCaen, P. G.; Sula. A.; Scaglione, A.; Clapham, D. E.; Wallace, B. A. *EMBO J.* **2016**, *35*, 820-830.
15. Kapota, C.; Lemaire, J.; Maître, P. *J. Am. Chem. Soc.* **2004**, *126*, 1836–1842.
16. Remko, M.; Fitz, D.; Broer, R.; Rode, B. M. *J. Mol. Model.* **2011**, *17*, 3117–3128.
17. Bush, M. F.; Oomens, J.; Saykally, R. J.; Williams, E. R. *J. Am. Chem. Soc.* **2008**, *130*, 6463–6471.
18. Armentrout, P. B.; Rodgers, M. T.; Oomens, J.; Steill, J. D. *J. Phys. Chem. A.* **2008**, *112*, 2248–2257.
19. Wende, T. Heine, N.; Yacovitch, T. A; Asmis, K. R.; Neumark, D. M.; Jiang, L. *Phys. Chem. Chem. Phys.* **2016**, *18*, 267–277.
20. Freiser, B. S. *J. Mass Spectrom.* **1996**, *31*, 703–715.
21. DiTucci, M. J.; Heiles, S.; Williams, E. R. *J. Am. Chem. Soc.* **2015**, *137*, 1650–1657.
22. Rorrer, L. C.; Yost, R. A. *Int. J. Mass Spectrom.* **2015**, *378*, 336–346.
23. Downard, K. M. *J. Mass Spectrom.* **2012**, *47*, 1034–1039.
24. Budzikiewicz, H.; Grigsby, R. D. *Mass Spectrom. Rev.* **2006**, *25*, 146–157.
25. Thomson J. J. *Philosophical Magazine.* **1912**, *24*, 209–253.
26. Bainbridge, K. T. *J. Franklin Inst.* **1933** *215*, 509–533.
27. March, R. E. *J. Mass Spectrom.* **1997**, *32*, 351–369.

28. Nobelprize.org. Retrieved. **2008**-10-06.
29. Griffiths, J. A. *Anal. Chem.* **2008**, *80,* 5678–5683.
30. Laskin, J.; Futrell, J. H. *Mass Spectrom. Rev.* **2003**, *22,* 158–181.
31. Scigelova, M.; Hornshaw, M. P.; Giannakopulos, A.; Makarov, A. *Mol. Cell. Proteomics*. **2011**, *10,* M111.009431-1-19.
32. Marshall, A. G.; Hendrickson, C. L.; Jackson, G. S. *Mass Spectrom. Rev.* **1998**, *17,* 1–35.
33. Schlemmer, S.; Kuhn, T.; Lescop, E.; Gerlich, D. *J. Am. Soc. Mass Spectrom.* **2002**, *13,* 589–596.
35. Wang, Y. S.; Tsai, C. H.; Lee, Y. T.; Chang, H. C. *J. Phys. Chem. A.* **2003**, 4217–4225.
36. Asvany, O.; Bielau, F.; Moratschke, D.; Krause, J.; Schlemmer, S. *Rev Sci Instrum,* **2010**, *81*, 076102, 1–4
37. Gerlich, D. *Phys. Scr*. **1995,** *59*, 256-263.
38. Svendsen, A.; Lorenz, U. J.; Boyarkin, O. V.; Rizzo, T. R. *Rev. Sci. Instrum.* **2010**, *81*, 073107-1-7
39. Schlemmer, S.; Kuhn, T.; Lescop, E.; Gerlich, D. *Int. J. Mass Spectrom.* **1999**, *185,* 589–602.
40. Han, X.; Aslanian, A.; Yates, J. R. *Curr. Opin. Chem. Biol.* **2008**, *12,* 483–490.
41. Yates, J. R.; Ruse, C. I.; Nakorchevsky, A. *Annu. Rev. Biomed. Eng.* **2009**, *11,* 49–79.
42. Chait, B. T.; Cadene, M.; Olinares, P. D.; Rout, M. P.; Shi, Y. *J. Am. Soc. Mass Spectrom.* **2016**, *27,* 952-965.
43. Bleiholder, C.; Suhai, S.; Harrison, A. G.; Paizs, B. *J. Am. Soc. Mass Spectrom.* **2011**, *22,* 1032–1039.
44. Eyler, J. R. *Mass Spectrom. Rev.* **2009**, *28,* 448–467.
45. Polfer, N. C.; Oomens, J. *Mass Spectrom. Rev.* **2009**, *28,* 468–494.
46. Heiles, S.; Cooper, R. J.; Berden, G.; Oomens, J.; Williams, E. R. *Phys. Chem. Chem. Phys.* **2015**, *17,* 30642–30647.
47. Wu, R.; McMahon, T. B. *J. Am. Chem. Soc.* **2007**, *129,* 4864–4865.
48. Atkins, C. G.; Rajabi, K.; Gillis, E. A. L.; Fridgen, T. D. *J. Phys. Chem. A.* ***2008,*** *112,* 10220–10225.
49. Price, W. D.; Schnier, P. D.; Williams, E. R. *J. Phys. Chem. B.* **1997**, *101,* 664–673.
50. Allen, S. J.; Giles, K.; Gilbert, T.; Bush, M. F. *Analyst*, **2016**, *141,* 884–891.
51. Manard, M. J.; Kemper, P. R. *Int. J. Mass Spectrom.* **2016**, *402,* 1–11.
52. Vadas, O.; Burke, J. E. *Biochem. Soc. Trans.* **2015**, *43,* 773–786.
53. Pan, J.; Zhang, S.; Chou, A.; Hardie, D. B.; Borchers, C. H. *Anal. Chem.* **2015**, *87,* 5884–5890.

54. Cumeras, R.; Figueras, E.; Davis, C. E.; Baumbach, J. I.; Gràcia, I. *Analyst.* **2015**, *140*, 1376–90.
55. May, J. C.; McLean, J. A. *Anal. Chem.* **2015**, *87*, 1422–1436.
56. Lanucara, F.; Holman, S. W.; Gray, C. J.; Eyers, C. E. *Nat Chem*, **2014**, *6*, 281–294.
57. May, J. C.; Goodwin, C. R.; McLean, J. A. *Curr. Opin. Biotechnol.* **2015**, *0*, 117–121.
58. Jeanne Dit Fouque, K.; Afonso, C.; Zirah, S.; Hegemann, J. D.; Zimmermann, M.; Marahiel, M. A.; Rebuffat, S.; Lavanant, H. *Anal. Chem.* **2015**, *87*, 1166–1172.
59. Jurneczko, E.; Kalapothakis, J.; Campuzano, I. D. G.; Morris, M.; Barran, P. E. *Anal. Chem.* **2012**, *84*, 8524–8531.
60. May, J. C.; Russell, D. H. *J. Am. Soc. Mass Spectrom.* **2011**, *22*, 1134–1145.
61. Gidden, J.; Ferzoco, A.; Baker, E. S.; Bowers, M. T. *J. Am. Chem. Soc.* **2004**, *126*, 15132–15140.
62. Wright, V. E; Reynolds, J. C.; Christie, S. D. R.; Creaser. C. S.; Castro-Gómez, F. Bo, C.; Jurneczko, E.; Barran, P.; Poulton, A. *Int. J. Ion Mobil. Spectrom.* **2013**, *16*, 61–67.
63. Rajabi, K.; Ashcroft, A. E.; Radford, S. E. *Methods* **2015**, *89*, 13–21.
64. Flick, T. G.; Campuzano, I. D. G.; Bartberger, M. D. *Anal. Chem.* **2015**, *87*, 3300–3307.
65. Fenn, L. S.; McLean, J. A. *Anal. Bioanal. Chem.* **2008**, *391*, 905–909.
66. Konermann, L.; Pan, J.; Liu, Y. H. *Chem. Soc. Rev.* **2011**, *40*, 1224–1234.
67. Morrison, E. A.; DeKoster, G. T.; Dutta, S.; Vafabakhsh, R.; Clarkson, M. W.; Bahl, A.; Kern, D.; Ha, T.; Henzler-Wildman, K. A. *Nature.* **2011**, *481*, 45-50.
68. Guttman, M. Wales, T. E.; Whittington, D.; Engen, J. R.; Brown, J. M.; Lee, K. K. *J. Am. Soc. Mass Spectrom.* **2016**, *27*, 662–668.
69. Wales, T. E.; Engen, J. R. *Mass Spectrom. Rev.* **2006**, *25*, 158–170.
70. Majumdar, R.; Middaugh, C. R.; Weis, D. D.; Volkin, D. B. *J. Pharm. Sci.* **2015**, *104*, 327–345.
71. Mistarz, U. H.; Brown, J. M.; Haselmann, K. F.; Rand, K. D. *Structure*. **2016**, *24*, 310–318.
72. Duc, N. M.; Du, Y.; Zhang, C.; Lee, S. Y.; Thorsen, T. S.; Kobilka, B. K.; Chung, K. Y. *J. Am. Soc. Mass Spectrom.* **2015**, *26*, 808–817.
73. Bohrer, B. C.; Atlasevich, N.; Clemmer, D. E. *J. Phys. Chem. B.* **2011**, *115*, 4509–4515.
74. Evans, S. E.; Lueck, N.; Marzluff, E. M. *Int. J. Mass Spectrom.* **2003**, *222*, 175–187.
75. Mistarz, U. H.; Brown, J. M.; Haselmann, K. F.; Rand, K. D. *Anal. Chem.* **2014**, *86*, 11868–11876.

76. Beeston, H. S.; Ault, J. R.; Pringle, S. D.; Brown, J. M.; Ashcroft, A. E. *Proteomics.* **2015**, *15*, 2842–2850.
77. Khakinejad, M.; Kondalaji, S. G.; Tafreshian, A.; Valentine, S. J. *J. Am. Soc. Mass Spectrom.* **2015**, *26*, 1115–1127.
78. Rand, K. D.; Pringle, S. D.; Morris, M.; Brown, J. M. S. *Anal. Chem.* **2012**, *84*, 1931–1940.
79. Woolfson, D. N.; Williams, D. H. *FEBS Lett.* **1990**, *277*, 185–188.
80. Theillet, F. X.; Kalmar, L.; Tompa, P.; Han, K. H.; Selenko, P.; Dunker, A. K.; Daughdrill, G. W.; Uversky, V. N. *Intrinsically Disord. Proteins,* **2013**, *1*, e24360.
81. Fuchs, S.; Nguyen, H. D,; Phan, T. T. P,; Burton, M. F.; Nieto, L.; De Vries-van, I. J.; Leeuwen; I. J. V.; Schmidt, A.; Goodarzifard, M.; Agten, S. M.; Rose, R.; Ottmann, C.; Milroy, L. G.; Brunsveld, L. *J. Am. Chem. Soc.* **2013**, *135*, 4364–4371.
82. Zaprasis, A.; Brill, J.; Thüring, M.; Wünsche, G.; Heun M.; Barzantny, H.; Hoffmann, T.; Bremer. E. *Appl. Environ. Microbiol.* **2013**, *79*, 576–587.
83. Szabados, L.; Savour. *Trends Plant Sci.* **2010**, *15*, 89–97.
84. Verslues, P. E.; Sharp, R. E. *Plant Physiol.* **1999**, *119*, 1349–1360.
85. Sharma, S.; Verslues, P. E. *Plant. Cell Environ.* **2010**, *33*, 1838–1851.
86. Lee, B. C.; Hoff, W. D. *Protein Sci.* **2008**, *17*, 2101–2110.
87. Lowe, A. R.; Itzhaki, L. S. *J. Mol. Biol.* **2007**, *365*, 1245–1255.
88. Wedemeyer, W. J.; Welker, E.; Scheraga, H. A. *Biochemistry*, **2002**, *41*, 14637–14644.

Chapter 2
Methods of Study

The purpose of this chapter is to introduce the experimental and theoretical methods that have been used to study the intrinsic properties of ion-molecule complexes in the gas phase.

2.1. Experimental Methods. The experimental results were conducted in the Laboratory for the Study of the Energetics, Structures, and Reactions of Gaseous Ions at Memorial University which houses a Bruker Apex Qe7 Fourier transform ion cyclotron resonance (FTICR) mass spectrometer. A photograph of this instrument is shown in the top of Figure 2.1. The basic principles of FTICR instrumentation, electrospray ionization, and gas phase fragmentation techniques will be introduced in this section. A schematic of the FTICR coupled with an Apollo II electrospray ionization source is depicted in the bottom of Figure 2.1 and shows the ionization source, quadrupole/hexapole region, ion transfer optics and ICR cell. The low-pressure environment of the FTICR facilitates the incorporation of ion dissociation techniques such as collision induced dissociation (CID), infrared multiphoton dissociation (IRMPD), and blackbody infrared radiative dissociation (BIRD). The mechanism of fragmentation involved in each method will also be discussed below.

2.1.1. Principles of FTICR Mass Spectrometry. The mass analyzer used in this work was an FTICR mass analyzer. The FTICR mass spectrometer allows ions to be isolated and stored for long times with minimal collisions.[1,2,3]

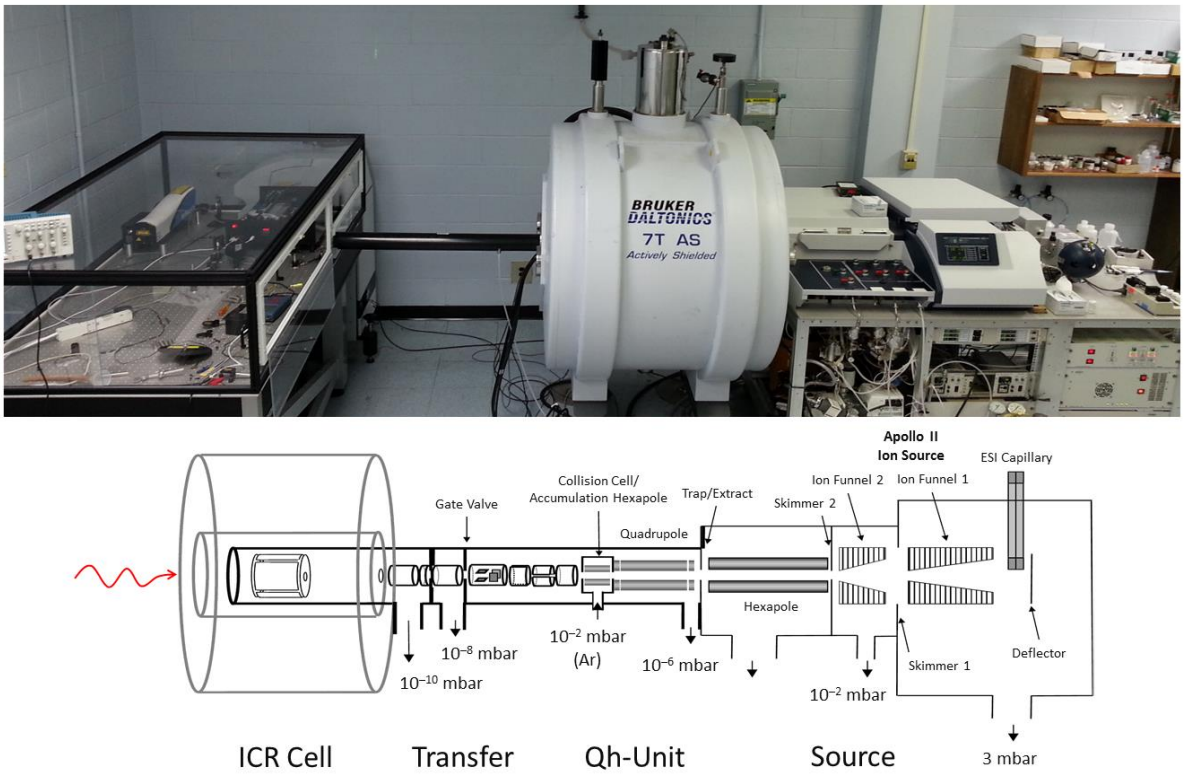

Figure 2.1. Top: The OPO lasers/Bruker Apex Qe 70 FTICR-MS located at Memorial University. Bottom: The schematic describes the Apollo II included, ion source, Qh (quadrupole/hexapole) collision cell, ion transfer optics and ICR cell at Memorial University of NL.

According to equation 2.1 and as shown in Figure 2.2, once ions of mass, *m*, moving with velocity, $\vec{v}$, and charge, *q*, enter into a uniform magnetic field, $\vec{B}$, they are influenced by the magnetic component of the Lorentz force.

$$\vec{F} = q\vec{v}\, x\vec{B} \tag{2.1}$$

When an ion is introduced into a uniform magnetic field that is perpendicular to its velocity, the particle will undergo a circular motion.[45] Because the Lorentz force is equal to the centrifugal force, the following can be written,

$$qvB = \frac{mv^2}{r} \tag{2.2}$$

The frequency of an ion in a magnetic field orbiting perpendicular to the direction of $\vec{B}$ is called the cyclotron frequency, ω_c, and is related to the velocity of the ion by equation 2.3.

$$\omega_c = \frac{v}{2\pi r} \qquad or \qquad 2\omega_c \pi r = v \tag{2.3}$$

Rearranging equation 2.2 for *v* yields

$$v = \frac{qrB}{m} \tag{2.4}$$

and equating to equation 2.3 yields

$$\frac{m}{q} = \frac{B}{\omega} \tag{2.5}$$

According to equation 2.5, ω is directly proportional to the strength of the magnetic field *B*, as well as the reciprocal of *m/q* of ion.[6,7,8] As a result, when *B* is constant, all ions of a given *m/q* ratio rotate with the same cyclotron frequency which is independent of ion velocity. Because $q=ze$, where *z* is the charge number and *e* is the elementary charge, in a uniform magnetic field, the *m/z* ratio of an ion can be determined by measuring the cyclotron frequency,

$$\frac{m}{z} = \frac{Be}{\omega} \tag{2.6}$$

The strength of the magnetic field is sufficient to trap ions in the xy or radial direction (Figure 2.2, right). To trap ions in the third dimension, an electric field is applied at both ends of the ICR cell.

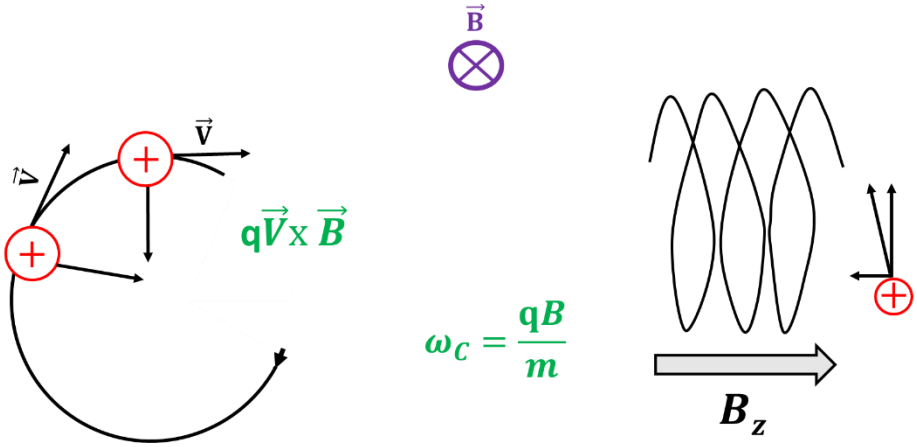

Figure 2.2. Left: Circular trajectory of charged ion in a uniform magnetic field. Right: How magnetic field confine ions only in xy direction.

The configuration, depicted in Figure 2.3 where ions are trapped both in the radial and axial dimensions using a magnetic and an electric field, respectively, is known as a Penning trap. As depicted in Figure 2.3, a cylindrical ICR is composed of two trapping, two excitation, and two detection plates. Figure 2.4 shows the excitation and detection plates and their position with respect to each other. Before detection, a radio frequency, RF, electric field is applied to the two excitation plates, and if the ion's cyclotron frequency is

in resonance with this RF potential, the trapped ions start accelerating and their radius of orbit and velocity increases, leaving the frequency of orbit unchanged (Figure 2.4).

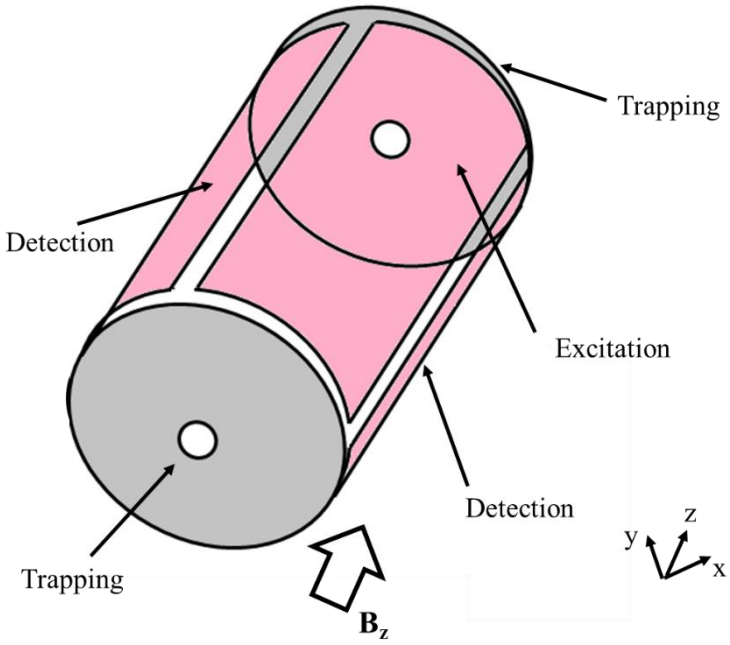

Figure 2.3. A schematic of the side view of a cylindrical geometric FTICR mass analyzer located within a strong magnetic field generated by a superconducting magnet in which an RF potential is applied to the excitation electrodes.

During excitation, all RF frequencies are swept to excite all masses of ions to a detectable radius. In the cross section view of the ICR cell shown in Figure 2.3, the excitation plates are the top and bottom plates. As depicted in the left of Figure 2.4, the excitation event is a critical step to convert the incoherent orbital motion of the ion packet to a detectable coherent motion (Figure 2.4 right side).

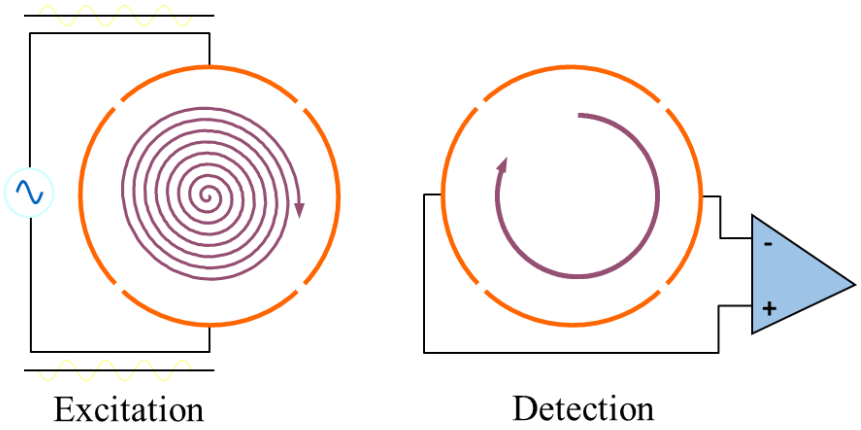

Figure 2.4. A schematic of the cross section view of an FTICR mass analyzer located within a strong magnetic field generated by a superconducting magnet in which an RF potential is applied to the excitation electrodes. The purple trace shows the excitation of ion packets.

As the ions orbit the centre of the ICR, they pass the detection plates. The electric fields of the coherently orbiting ion packets induce an image charge in the two detection plates depicted on the left and right sides in the cross section view of the ICR cell in Figure 2.3. For example, if positive ions pass close by the detection plate, electrons are drawn toward the surface of the plate. As they continue to orbit and pass the second detection plate, the image charge is drawn through a circuit to the second plate. This sinusoidal oscillation of the image charge is known as the image current. The image current contains the frequency and abundance information for all the ions present in the ion trap (also called transient sinusoidal signal or transient for short) which is measured as a function of time. The transient is converted to the frequency domain using a mathematical procedure known as a Fourier transform, and finally the frequencies are converted to *m/z* using equation 2.6 (Figure 2.5).

Details about the description of Fourier transform algorithms is beyond the scope of this work and are unnecessary to describe here.

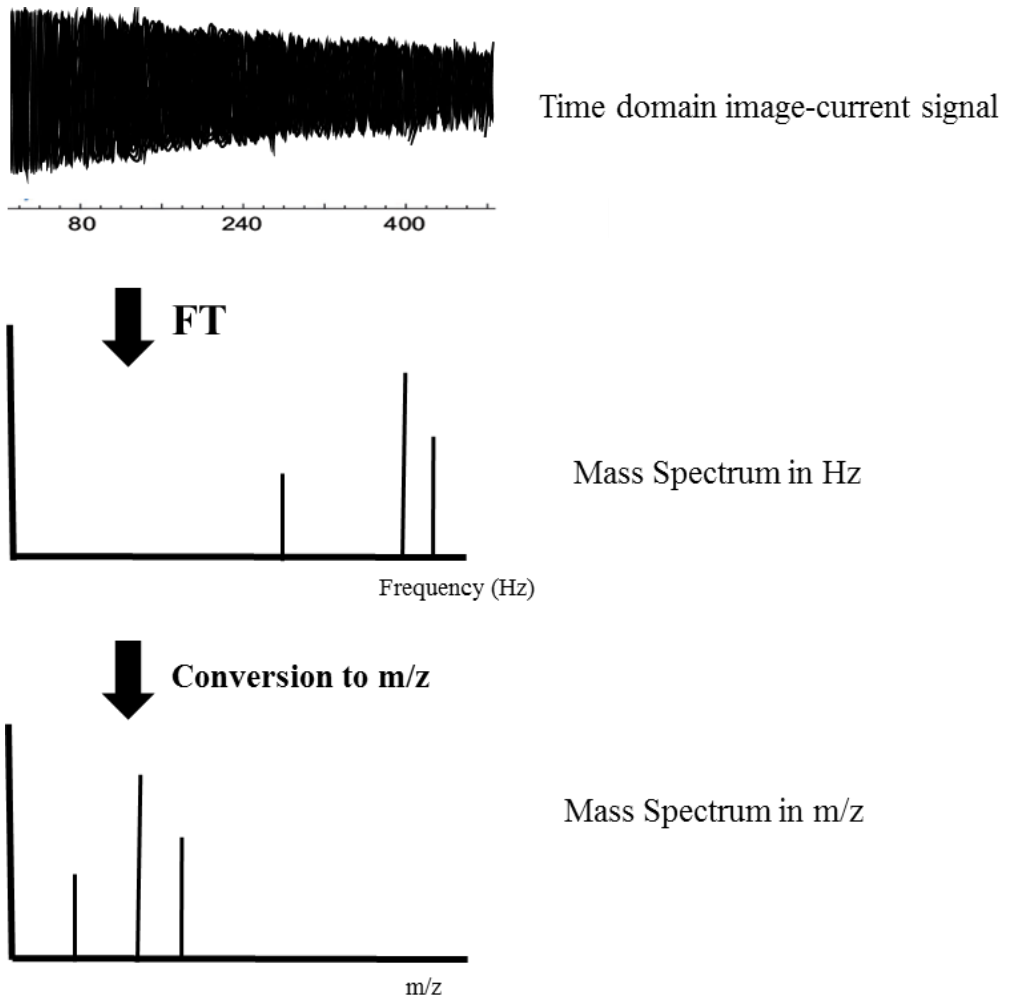

Figure 2.5. Illustration of the processing of transformation of the time domain transient of raw data to the frequency domain, and this resulting spectrum is then calibrated in terms of m/z.

The trapping allows ions to be stored long enough (order of second to hours) to determine the cyclotron frequencies with high precision. Trapping ions for extended periods of time provides plenty of time for the ions to experience desirable interactions with neutral molecules or to undergo unimolecular decompositions, or be irradiated with a laser. In addition, by isolating only the desired ion, all other ions can be excited and removed from the ICR cell guaranteeing that the products of dissociation originate from only the parent ion. Hence, the ICR cell is a very suitable mass analyzer for extracting the information about structure, thermochemistry, reactivity, and kinetics of ionic complexes.[9]

2.1.2. Electrospray Ionization (ESI). Since 1968, when Malcolm Dole[10] used the first ESI source coupled with mass spectrometry, the combination of ESI and MS has significantly broadened the application of MS for the characterization of biomolecules.[11,12,13,14,15] ESI is used to softly transfer ions from solution to the gas phase under atmospheric pressure. First, the sample is dissolved in a proper solvent, and then passed through a thin conducting capillary at high voltage. Under the influence of a strong electric field, around 10^6 V m^{-1}, at the tip of the capillary, the assemblage of charge near the droplet surface is converted to a cone, known as the Taylor cone.[16,17,18,19,20] Charged droplets containing analyte, with a strong potential applied across the capillary, are emitted from the Taylor cone apex. In a heated glass capillary, the droplets undergo evaporation and are stressed due to repulsive Coulombic forces, the charged droplets will begin splitting into smaller droplets. Eventually, the desolvated ions are released to the gas phase and enter the high vacuum region of the mass spectrometer, Figure 2.6.

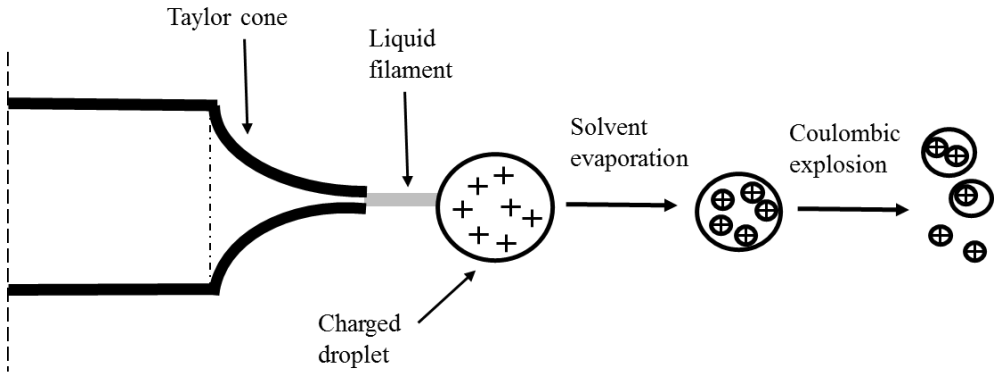

Figure 2.6. Schematic depiction of an electrospray ionization process for a positive ionization mode.

There are two proposed mechanisms that explain the formation of gas phase charged analyte which very briefly will be discussed here.[19,21,22,23] The first mechanism is called the charge residue model (CRM), and second one is the ion evaporation model (IEM), shown in Figure 2.7.

Depending on the size, geometry, and polarity[24] of the analyte, either of the two mechanisms are at play. The IEM, which is depicted in the top of Figure 2.7, explains the electrospray process for relatively small analytes containing high charge density. In the IEM, once the droplet has shrunk to around 20 nm size, as a result of Coulombic repulsion of the ions in the droplet, the small analyte ion is emitted from the surface directly to the gas phase before complete evaporation of the solvent molecules.

The CRM is used to explain the electrospray process for large biomolecular ions. As depicted in the bottom of Figure 2.7, in CRM some droplets contain as few as one

analyte ion. In this model, the analyte ion is left behind when the solvent molecules evaporate resulting in multiply charged ions. In the CRM only one analyte owning a part of the charge of the initial droplet remains, whereas in IEM when the droplet size decreases close to the Rayleigh limit to reduce the Columbic repulsion at the surface, singly or less multiply charged ions are directly desorbed from the droplet to the gas phase.[25]

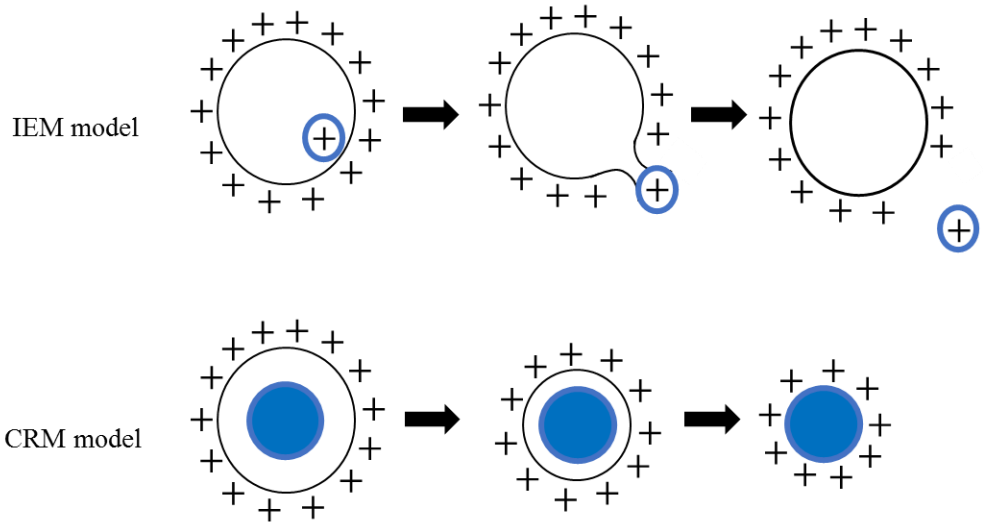

Figure 2.7. Schematic depiction of the IEM and CRM models to produce gas phase ions.

It is worth mentioning that the reason the ICR cell is separated from the ion source is that different pressures are needed for the operation of the ion source (high pressure, ~mbar) and the mass analyzer which works in high vacuum, ~10^{-10} mbar. After ESI is completed, and ions are transferred to the gas phase, they enter sequentially lower pressures until they reach the ICR cell.

2.1.3. Ion Dissociation Techniques. Once the ions are trapped in the ICR cell, a mass spectrum can be generated as discussed above. On the other hand, by similar RF excitation techniques, all ions except a particular *m/z* ion can be ejected from the ICR, thereby isolating an ion of interest. Once trapped and isolated, ions can be further studied by a number of activation techniques. Three activation techniques; collision induced dissociation (CID), infrared multiple photon dissociation (IRMPD), and blackbody infrared radiative dissociation (BIRD), will be explained here.

2.1.3.1. Sustained Off-Resonance Irradiation Collision Induced Dissociation (SORI-CID). In CID experiments in general, the information about the structure of the mass-selected precursor ion is determined by collisionally activating the ions and observing the fragmentation. In high (keV), low (10-100 eV), or very low (<10 eV) energy CID, collision with an inert target gas (Ar, N_2, CO_2 or He) converts a portion of an ion's translational energy to internal energy resulting in fragment ions that can be analyzed. SORI-CID is considered a very low energy activation process.

The maximum kinetic energy converted into internal energy is called the centre of mass collision energy, E_{com}, equation 2.7. E_{com} depends on the lab frame kinetic energy, E_{lab}, and the molar mass of the target gas and parent ion, represented by N and m_p, respectively:

$$E_{com} = E_{lab}\left(\frac{N}{m_p + N}\right) \tag{2.7}$$

In SORI-CID the trapped ions are irradiated with a 250 ms radio-frequency pulse off-resonance with the ion's cyclotron frequency by about 500 Hz during which they undergo translational excitation. In order to surpass the dissociation threshold, in SORI-CID, many 100's of collisions are required.[26] In SORI, the kinetic energy varies during the activation time. The maximum kinetic energy that ions obtain during SORI, E_{lab}, can be obtained from equation 2.8

$$E_{lab} = \left(\frac{ß^2 q^2 V_{p-p}}{32\pi^2 m d^2 \Delta v^2} \right) \tag{2.8}$$

where *ß* is a geometrical factor (0.92 for our instrument), *d* is the diameter of the ICR cell (0.06 m), q is the charge on the ion, V_{p-p} is the peak to peak excitation voltage, *m* is the mass of the ion, and Δv is the difference between the ion natural cyclotron frequency and RF excitation frequency (500 Hz).

SORI-CID can be performed to explore the fragmentation pathways of both precursor and fragment ions which is due to the ability of the FTICR mass spectrometer to act as a tandem-in-time instrument. In the first stage of tandem mass spectrometry, the parent ion is isolated using an rf pulse ejecting all but the ion of interest. A second stage is then used by isolating one of the products of primary fragmentation. This procedure can be repeated on all fragment ions as well as the products of secondary, tertiary, etc. fragmentation.

2.1.3.2. Infrared Multiple Photon Dissociation (IRMPD). IRMPD is a slow activation process, like CID, due to the absorption of small amounts of energy equal to the photon

energy, between 10 and 40 kJ mol^{-1} with the lasers used in this thesis. As such, the lowest energy dissociation pathways are typically observed.[27–32] For IRMPD to occur, there must be a vibrational mode belonging to the ion of interest in resonance with the IR laser frequency allowing the laser photons to be absorbed ($\nu = 0 \rightarrow 1$ transition). After the first absorption, subsequent absorptions of a monochromatic laser are strictly non-resonant with a subsequent transition due to anharmonicity, as depicted in Figure 2.8. However, in the absence of collisions, the energy of the absorbed photon can be distributed throughout the ion in a process known as intramolecular vibrational energy redistribution (IVR). Following IVR, the original mode, resonant with the laser, is free to absorb another photon. The repeating process of absorption followed by IVR, slowly increases the total internal energy of the ion until it exceeds the threshold for dissociation.[33] Figure 2.9 shows how the IR laser photons are sequentially absorbed to activate bonds.

IRMPD spectroscopy is a special case of IRMPD activation performed with a tunable infrared laser. By observing fragmentation due to IRMPD as a function of laser wavelength, an IRMPD spectrum can be obtained. IRMPD spectroscopy is a useful technique in determining structures of species in the range of small complexes, such as amino acids[34–43] or nucleic acid bases[44–48] peptides,[49–52] proteins and other interesting biomolecules.[27–32,53–61] The intensity in an IRMPD spectrum, the IRMPD efficiency, is determined from the relative intensities of the parent ion and fragment, I_p and I_f, respectively, according to the following equation:

$$IRMPD\ Efficiency = -ln\left(\frac{I_p}{I_p + \sum_i I_{f(i)}}\right) \tag{2.9}$$

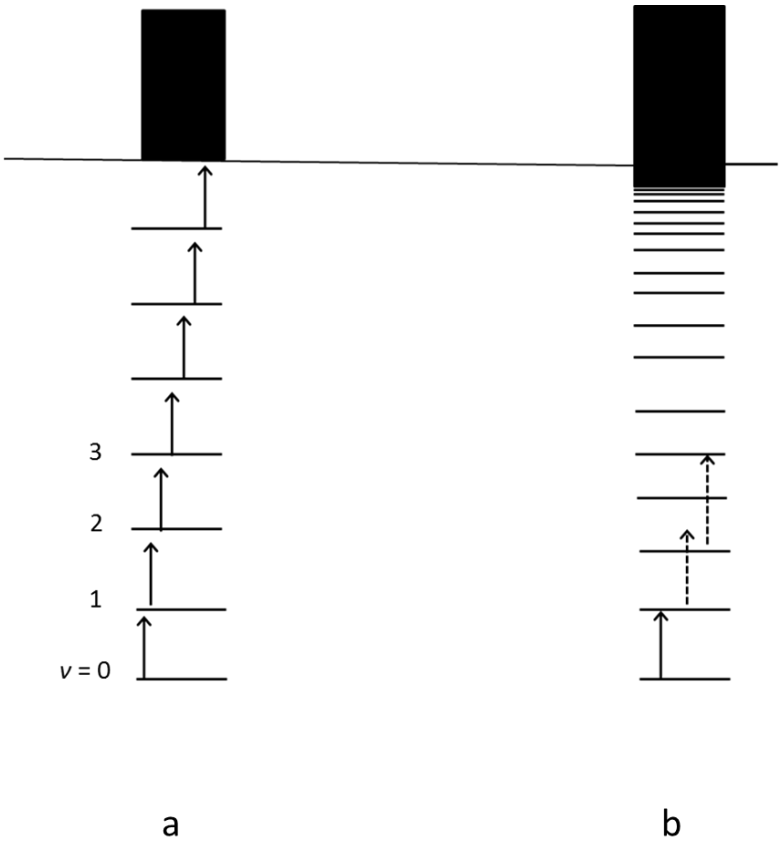

Figure 2.8. Schematic of the comparison of a) Harmonic vibrational energy levels and b) Anharmonic vibrational energy levels. The arrows depicted in figure show the transitions that are in resonance with the laser photons.

In this thesis, two sources of tunable infrared radiation were used in two different wavelength regions. A free electron laser (FEL) at the Centre Laser Infrarouge d'Orsay (CLIO) just outside Paris, France covers the fingerprint region (~900 – 2000 cm^{-1}) and an optical parametric oscillator (OPO) at Memorial University of Newfoundland covers the C-H/N-H/O-H stretching region (2700 – 3800 cm^{-1}).

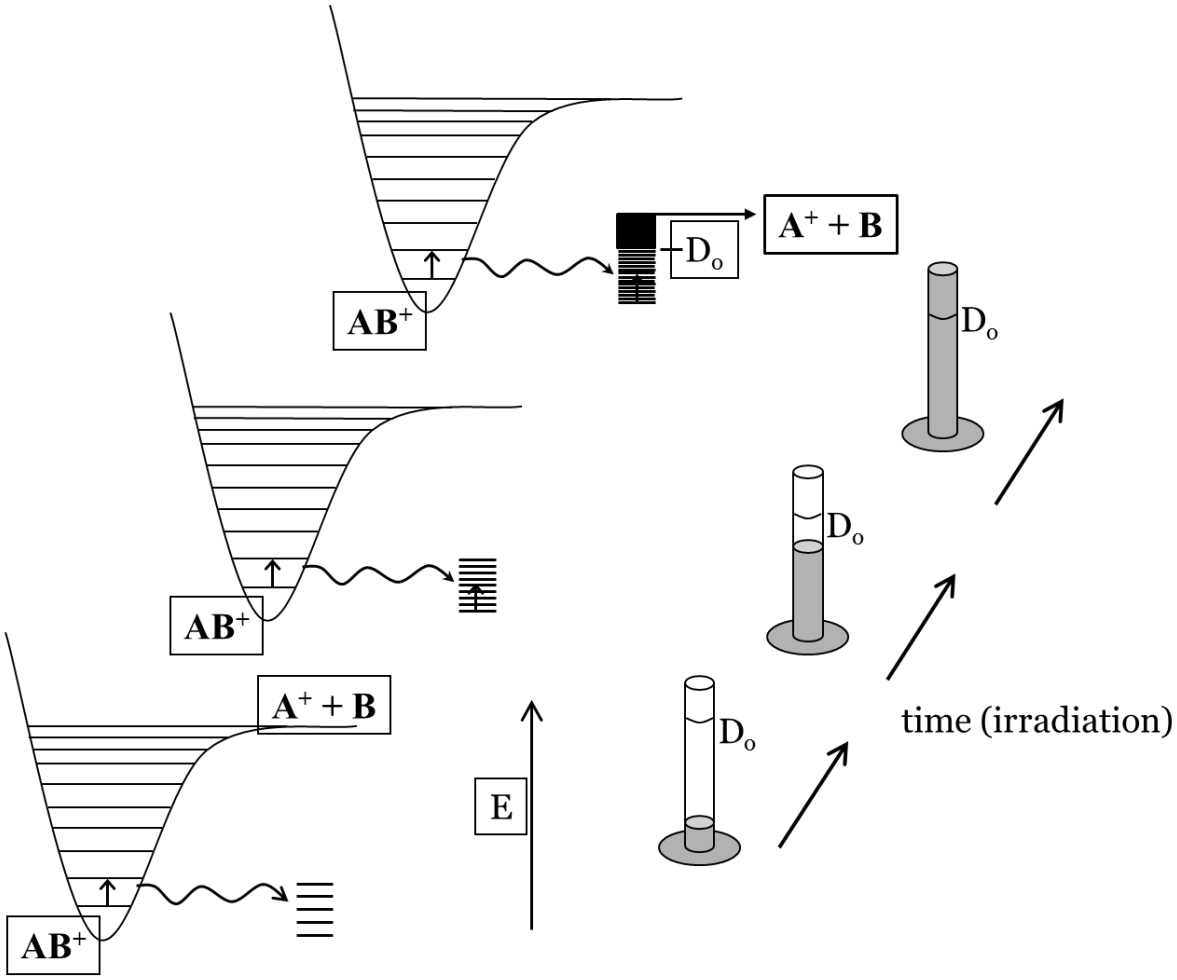

Figure 2.9. Schematic of the mechanism of IVR process in IRMPD. IVR, leads to an increase in the internal energy of the molecule which increases in the density of the vibrational states. The IVR continues till the dissociation threshold of the interested ion is reached.

A detailed description of laser operation is not discussed in this thesis. The application of IRMPD to determine structures of ionic complexes, particularly for systems composed of amino acid and peptides, will be discussed in Chapters 3, 4, 5 and 6.

2.1.3.3. Blackbody Infrared Radiative Dissociation (BIRD). In BIRD, ions undergo a very slow unimolecular dissociation, the rate of which is increased via absorption of a single infrared photon provided by the vacuum chamber acting as a blackbody emitter. The

first hypothesis of the activation of unimolecular dissociation by blackbody radiation absorption was introduced by Perrin in 1919.[62] However, Perrin's radiation hypothesis was discredited by Langmuir.[63] who showed that the radiation field was not intense enough, or of high enough energy to cause dissociation of strongly-bound molecules. The subsequently accepted Lindemann collision theory of unimolecular activation,[64] was that energy exchange occurs through bimolecular collisions.

However, the radiation hypothesis was reinstituted after the first observation of unimolecular dissociation of very weakly bound ion-molecule complexes, in the absence of collisions, in an FTICR by the McMahon group in 1994.[65] McMahon was the first to use an FTICR for trapping weakly bound ions in an extremely low-pressure environment, in the absence of collisions. In these experiments, the energy required for the dissociation of weakly-bound complex ions is achieved through the exchange of blackbody radiation with the ion's surroundings.

2.1.3.3.1. BIRD Mechanism. Since BIRD is a very slow process, observation of ion decay times on the order of seconds or even 100's of seconds is required. Because of the long trapping timescale required under thermal conditions, these experiments are typically conducted in an FTICR.[66] An important factor in BIRD is that the trapped ions are thermalized and the internal energy distribution of the trapped ions can be described by a Boltzmann distribution. The mechanism for activation and dissociation of $AB^{\pm}$ under BIRD conditions is shown in equation 2.10.

$$AB^{\pm} \underset{k_{em}}{\overset{k_{abs}}{\rightleftarrows}} AB^{\pm *} \xrightarrow{k_d} A + B^{\pm} \qquad (2.10)$$

Here, k_{abs} and k_{em} are the rate constants for absorption and emission, respectively, and k_d is the dissociation rate constant. Using the steady-state approximation, the apparent rate constant for unimolecular decomposition, k_{uni}, is given in by equation 2.11.

$$k_{uni} = \left(\frac{k_{abs} k_d}{k_{em} + k_d} \right) \tag{2.11}$$

From the slope of the logarithmic plot of precursor ion abundance as a function of reaction time, the corresponding observed unimolecular dissociation rate constant, k_{uni}, is determined.[67] If I is the normalized intensity, and t is the time, k_{uni} can be determined using equation 2.12.

$$[I] = e^{-k_{uni} t} \tag{2.12}$$

By plotting $log k_{uni}$ as a function of inverse temperature, T, according to equation 2.12, the Arrhenius activation energy of the dissociation, E_a, and pre-exponential factor, A, are obtained where k_B is the Boltzmann constant,

$$k_{uni} = A\, e^{-E_a / k_B T} \tag{2.13}$$

The entropy of activation (ΔS†) can be determined using equation 2.14,

$$A = \frac{k_B T}{h} e^{\left(1 + \left(\frac{\Delta S\dagger}{k_B}\right)\right)} \tag{2.14}$$

If the molecules are large they have many vibrational degrees of freedom and emission and absorption rate constants are expected to be large. Furthermore, at the threshold for dissociation for larger molecules, the dissociation rate constant is expected to be smaller because the energy randomized throughout the molecule must find itself in the

correct modes to undergo dissociation. For large molecules, the rate of dissociation is expected to be significantly smaller than the rate of emission and the observed k_{uni}, can be simplified from equation 2.11 to 2.15.

$$k_{uni} = \left(\frac{k_{abs} k_d}{k_{em}} \right) \qquad k_d \ll k_{em} \tag{2.15}$$

For large molecules, in the absence of collisions, thermal equilibrium can be reached through the rapid exchange (REX) of radiation.[68,69,70,71,72] At the REX limit, also known as the high-pressure limit due to the similarity of reaching thermal equilibrium, k_{abs}=k_{em} therefore, equation 2.15 simplifies to:

$$k_{uni} = k_d \tag{2.16}$$

In this large molecule limit, the ions have reached thermal equilibrium and the Arrhenius analysis of the temperature dependence of the rate constants, k_{uni}, is expected to yield the true energy threshold for dissociation.

If the size of the system is smaller, however (less than about 100 degrees of freedom) then the dissociation may be too fast compared to the absorption and emission rate constants so that the above assumptions cannot be made, and thermal equilibrium of the ions with their surrounding may not fully be reached. Here, the rate of dissociation is larger than the rate of emission, therefore the E_a values underestimate the true dissociation threshold, E_0. Because of this, the experimentally obtained values differ from the true high pressure limit values and a proper kinetic modeling method must be used.[73,74,75] Dunbar's regime for hydrocarbon-derived molecules depicted in Figure 2.10 provides an overview of unimolecular dissociation kinetics of small or medium to large size ions based on specific

variables. The relation between the number of degrees of freedom, entropy of activation, and the reaction rate reveals whether the dissociation process is in the REX limit or not. In general, the number of degrees of freedom and the temperature dependent dissociation rate constants in which the reaction takes place are not sufficient to describe the minimum size necessary for REX behaviour of systems. The third variable that needs to be considered is the entropy of activation based on the information about the nature of the transition state of the reaction. (loose or tight transition state)

The detailed analysis of the relative size regimes of ions is not discussed here, but a solution, when the REX limit is not attained, is that the dissociation energies can be extracted using master equation analyses. The systems in Chapter 6 have 321 vibrational degrees of freedom and are expected to be strongly absorbing in the infrared. However, the room temperature BIRD rate constants for these complexes, in the 10^{-3} s^{-1} regime, are on the border between small and large molecule kinetics. As such, master equation modeling of the Arrhenius plots is required to obtain true thermal dissociation thresholds.

2.1.3.3.2. Master Equation Modeling in BIRD Kinetics. One solution to obtain quasi-experimental thermodynamic parameters from experimental BIRD dissociation of ions is to use master equation modeling (MEM). For small molecules that do not obey the REX limit, the correct thermodynamic factors can be obtained using MEM. MEM simulates the changes in population of the internal energy levels of the system over time. In simple terms, it simulates all of the processes occurring in the BIRD mechanism and evaluates all of the rate constants composing equation 2.11.

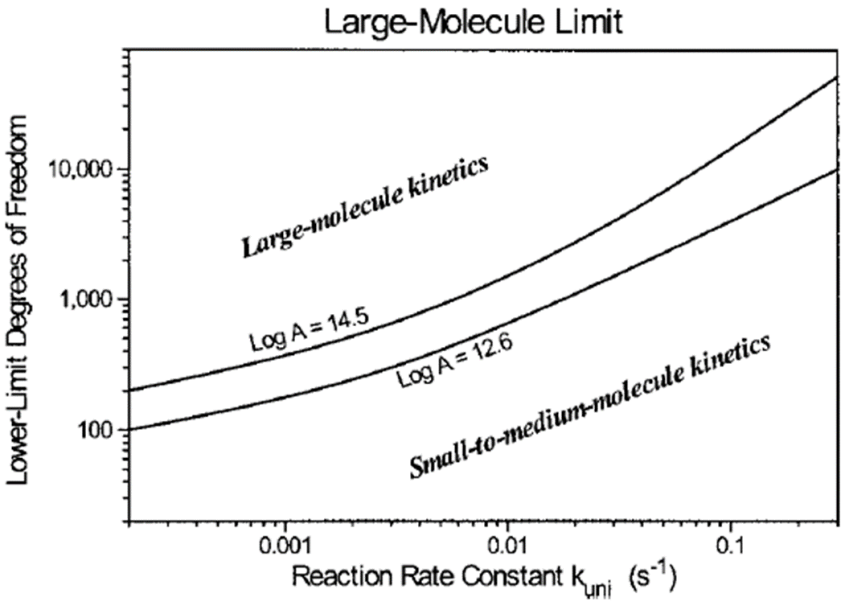

Figure 2.10. The number of degrees of freedom necessary for the Arrhenius activation energy E_a to lie within 10% of the limiting high-pressure E_a^{∞} corresponding to the same dissociation reaction. Figure adapted with permission from John Wiley and Sons. Mass Spectrom. Rev., 2004, 23, 127.[76]

This model uses a set of coupled linear first-order ordinary differential equations which take into consideration all possible energy transfer processes, including radiative absorption, emission, and dissociation. If *i* and *j* are the two-energy levels, $N_i(t)$ and $N_j(t)$, show the energy population of the corresponding levels, respectively. The coupled equations are equal to

$$\frac{dN_i(t)}{dt} = \sum_{j \neq i} k_{i,j} N_j(t) - k_d N_i(t) \qquad (2.17)$$

In the equation 2.17, $k_{i,j}$ and k_d are the rate constants for radiative exchange and dissociation processes, respectively. The first term in equation 2.17 is called the radiative exchange rate which, in the zero-pressure environment of BIRD experiments, is calculated using equation 2.18.

$$k_{i,j} = k_{1,rad} - k_{-1,rad} \quad (2.18)$$

$k_{1,rad}$ and $k_{-1,rad}$ are the radiative absorption and emission rates, respectively. There are a few adjustable parameters in the modeling process including E_0, which is selected in a range that fits better based on the specificity of the reaction. Two other factors are transition dipole moment (μ), and the high-pressure pre-exponential (A^{∞}) which are varied over a range of reasonable E_0 values, to give acceptable fits of the model to the experimentally measured results.

In the modeling process, once a Boltzmann distribution has reached a steady-state at a desired temperature, from the linear BIRD kinetics, the unimolecular decomposition rate constant can be obtained. The defined MEM rate constants at the highest and lowest temperatures are compared with the values of the BIRD experiment and the threshold activation energies are calculated.

2.2. Computational Methods. In this thesis, theoretical methods are used to determine structures and thermochemistries to compare to the experimentally obtained results. Described here are the details of the computational techniques that were used.

2.2.1. *Ab Initio* Methods. *Ab initio* techniques are methods in which the Born-Oppenheimer approximations are used to simplify the Schrödinger equation for many electron systems. Based on the Born-Oppenheimer approximation, the nuclear motion is decoupled from electronic motion.[77] This allows *ab initio* methods to be applied for a fixed nuclear configuration to systematically vary nuclear degrees of freedom to obtain the electronic energy of the ground state. The obtained electronic energy as a function of the reaction coordinate determines the potential energy surface (PES).

The Hartree-Fock (HF) scheme is one of the *ab initio* methods used to solve the Schrödinger equation, a form of a single determinant type, which is popular since it is a computationally fast method. The post-Hartree-Fock methods, such as Møller-Plesset (MP)[78,79] and configuration interaction (CI), were developed and account for the correlation energy to a certain extent. However, these calculations become computationally expensive and require significantly more computational time. Second order perturbation MP2 is also a post-Hartree-Fock method which applies the effects of electron correlation to the total energy.

2.2.2. Density Functional Theory (DFT) Methods. The computationally expensive nature of post Hartree–Fock wave function methods, like MP2 was an incentive to the development of methods based on the electron density, density functional theory (DFT). DFT methods are based on the Hohenberg--Kohn theorem that states existence of a unique one--to--one map between the electron density and energy of the system. Kohn--Sham theory provided a scheme/method to obtain energy of the system from the electron density. Using this theory, the energy is expressed as a functional of the electron density which is obtained from the molecular orbitals. In this thesis, DFT methods are the main ones that are used to predict the minimum energy structure of given molecules in the gas phase. Using this theory (kohn-sham) the energy is expressed as a functional of the electron density which is obtained from the molecular orbitals. In this thesis, DFT methods are the main ones that are used to predict the minimum energy structure of given molecules in the gas phase.

2.2.3. Basis Sets. All the above calculations are performed using a number of functions known as basis sets. A basis set is a finite set of functions called basis functions to make molecular orbitals. Gaussian type functions (GTF) are extensively used.[80,81,82,83,84] Depending on the type of the basis set one or more basis functions might be assigned to describe the core and the valence shell orbitals. The split-valence basis set represented as K-LMG nomenclature, is a popular class of basis set and the basis set used in this thesis. The K part represents the number of core Gaussian functions (G) and the LM part corresponds to the valence shell atomic orbitals which may include extensions with optional polarization and diffuse functions to them.

Polarization functions, which are functions of higher angular momentum quantum number, unoccupied in the atom, can be added to the basis sets to add more flexibility and gain better results. They are, for example, shown as (d or *), meaning that a d-function is added to the heavy atoms in the selected basis set, or (d,p or **) in which polarization functions are also added to light atoms (a p orbital). In addition to the polarization functions, the proper diffuse function, shown as plus sign + or aug, might be added to the basis set. The use of polarization and diffuse functions depend on the type of atoms in the molecule. For instance, in the case of anions and excited states, basis sets with diffuse functions should be used to obtain more reliable results.[85] For larger atoms containing many electrons, such as the complexes studied in Chapters 4 and 5, effective core potentials (ECP) are used. ECP is a method in that a pseudopotential is used instead of Gaussian functions for core electrons. For example, in Chapter 4 and 5, the Def2TZVP basis set is applied for Sr, Ba, Rb and Cs atoms.

The calculations usually start with an initial guess of the geometry constructed from chemical intuition which is done using the Gauss view program followed by the geometry optimization and the frequency calculations. A full geometry optimization is an iterative process based on geometry convergence criteria, which is continued until the minimum geometry is achieved. In the frequency analysis based on the forces applied to each nucleus (from the second derivative/gradient of potential energy) the normal mode calculation is performed.

By determining the second derivatives of the energy with respect to the Cartesian nuclear coordinates, the vibrational frequency, v of each of the n normal modes is calculated. Generally, in a molecule with N atoms, the vibrational energy, E_{vib} is the sum of the energy of each normal vibrational mode which is calculated using equation 2.19 where h is Planck's constant.

$$\mathrm{E_{vib}} = \sum_{i} \left(\frac{1}{2} h\nu_i\right) \tag{2.19}$$

After the normal mode analysis, the frequency of each vibrational normal mode is defined. The energy of each mode is used to account for the zero-point energy and this energy is added to the electronic energy. From the frequency calculations and their contributions to the enthalpy (H) and entropy of the molecule, the enthalpy and Gibbs energy (G) of the system is computed. Therefore, the frequency analysis on the optimized structure yields the thermochemistry and the obtained IR spectrum could be compared with the spectrum resulted from the IRMPD experiment.

If the E_{tot} represent the total internal energy of the molecule which is the sum of the electronic, vibrational, rotational, translational, and zero-point energies in based on equation 2.20

$$\mathrm{E}_{tot} = \mathrm{E}_{\mathrm{elec}} + \mathrm{E}_{\mathrm{vib}} + \mathrm{E}_{\mathrm{rot}} + \mathrm{E}_{\mathrm{trans}} + \mathrm{E}_{\mathrm{zp}} \quad (2.20)$$

H, and G, can be calculated from the internal energy by the following thermochemical relations

$$H = \mathrm{E}_{tot} + RT \quad (2.21)$$

$$G = \mathrm{E}_{tot} + RT - T\mathrm{S}_{tot} = H - T\mathrm{S}_{tot} \quad (2.22)$$

In most computational parts of this thesis, depending on the type of system, different basis sets and level of theory were selected. Single point calculations are then carried out in a higher level using a geometry which was optimized at a lower level of theory.

In this research, all *ab initio* and density functional calculations were done with the Gaussian 09[86] program. For the purposes of this thesis, the selected computational methods, mainly density functional methods, are used to obtain the geometry optimization, enthalpies and Gibbs energies. The final comment is about including dispersion correction to DFT methods. The dispersion correction mainly considers the short–range and London dispersion interactions between molecules and improves the performance of DFT methods. B3LYPD3 is a modified version of the DFT methods with extension to more elements using Grimme's version with the original D3 damping function[87] which was applied to optimizations.

Determining the global minimum is difficult and it is highly dependent on the starting structure. Molecular dynamics simulations are powerful tools that are used in Chapters 3, 4 and 5 to overcome the global minimum problems. To more fully explore the potential energy surface and as many possible structures and conformations as possible, methods such as simulated annealing (SA), have been developed. Simulated annealing is a method implemented in molecular dynamics packages, is designed to solve this problem.

2.2.4. Molecular Dynamics (MD) Methods. MD is a computer simulation technique that is based on integrating Newton's second law of motion to obtain trajectories of particle interactions through classical potentials between them. In MD, particles propagate in time based on the bonding and nonbonding forces that are applied to them. In order to find the structures of molecules, the laws of classical physics are used. In MD, a proper force field is used for simulation of biological and organic systems to calculate the intermolecular and intramolecular interactions. Since the MD techniques alone might not be computationally efficient, a combination of molecular dynamics simulation and DFT methods can be used as a powerful complementary tool. For instance, MD is used to do the conformational search of a given molecule. Afterward, a number of minimum energy structures obtained by MD are selected as initial structures of DFT calculations. In MD, a force field has been used to calculate the intermolecular and intramolecular interactions. For example, for the conformational search in SA, GAFF[88] force fields are carried out. A successful force field should work for both biological and organic molecules. Several general force fields such as AMBER, MMFF94, MM3, MM4, CHARMM, and OPLS have been developed. MMFF94, MM4, MM3 and OPLS force fields can not be widely used in studying

biological systems, but AMBER and CHARMM are used for both biological and organic systems. In General AMBER force field (GAFF) potential energy is;

$$E_{pair} = \sum_{bonds} k_r(r - r_{eq})^2 + \sum_{angles} k_\theta(\theta - \theta_{eq})^2 + \sum_{d} \frac{Vn}{2}[1 + Cos(n\phi - \gamma)] + \sum_{i<j} \left[\frac{A_{ij}}{R_{ij}^{12}} - \frac{B_{ij}}{R_{ij}^{6}} + \frac{q_i q_j}{\varepsilon R_{ij}}\right] \quad (2.23)$$

This equation consists of two parts, bonded and nonbonded. The bonded part includes, bond and angle harmonic vibrations, shown as r_{eq} and θ_{eq} that are equilibration bond length and angle and k_θ and k_r that are force constants. The next bonded interaction in the equation 2.23 is corresponded to the dihedral energy. The nonbonded part includes the Van der Waals and electrostatic interaction. A_{ij} and B_{ij} Lennard-Jones parameters and q_i, q_j are partial charges. More details about the force fields and molecular dynamics is beyond the scope of this thesis and is not described here.[34]

2.3. References.

1. Marshall, A. G.; Hendrickson, C. L.; Jackson, G. S. *Mass Spectrom. Rev.* **1998**, *17*, 1-35.
2. Laskin. J.; Futrell, J. H. *Mass Spectrom. Rev.* **2003**, *22*, 158-181.
3. Cho, Y.; Ahmed, A.; Islam, A.; Kim, S. *Mass Spectrom Rev.* **2015**, *34*, 248-263.
4. Nikolaev, E. N.; Kostyukevich, Y. I.; Vladimirov, G. N.; *Mass Spectrom. Rev.* **2016**, *35*, 219-258.
5. Kujawinski, E. B. *Environ Forensics*. **2002**, *3*, 207-216.
6. Amster. I. J. *J. Mass Spectrom.* **1996**, *31*, :1325-1337.
7. Scigelova, M.; Hornshaw, M.; Giannakopulos, A.; Makarov. *Mol Cell Proteomics*. **2011**, *10*, M111.009431.
8. Qi, Y.; O'Connor, P. B. *Mass Spectrom. Rev.* **2014**, *33*, 333-352.
9. Barrow, M. P.; Burkitt, W. I.; Derrick, P. J. *Analyst*. **2005**, *130*, 18-28.
10. Dole, M.; Mack, L. L, Hines, R. L.; Mobley, R. C, Ferguson, L. D.; Alice, M. B. *J Chem. Phys*. **1968**, *49*, 2240-2249.

11. Loo, J. A. *Mass Spectrom. Rev*. **1997**, *16*, 1-23.
12. Aebersold, R, Goodlett, D. R. *Chem. Rev*. **2001**, *101*, 269-296.
13. Fenn, J. B.; Mann, M.; Meng, C. K.; Wong, S. F.; Whitehouse, C. M. *Science,* **1989**, *246*, 64-71.
14. Cech, N. B.; Enke, C. G. *Mass Spectrom. Rev*. **2001**, *20*, 362-387.
15. Griffiths, W. J.; Brown, A.; Reimendal, R.; Yang, Y.; Zhang, J.; Sjovall J. *Rapid Commun. Mass Spectrom*. **1996**, *10*, 1169-1174.
16. Nemes, P.; Marginean, I.; Vertes, A. *Anal. Chem*. **2007**, *79*, 3105-3116.
17. Morad, M. R.; Rajabi, A.; Razavi, M. Sereshkeh, S. R. *Sci. Rep*. **2016**; *6*, 38509-38519.
18. Yamashita, M.; Fenn, J. B. *J. Phys. Chem*. **1984**, *88*, 4451-4459.
19. Konermann, L. A. *J. Am. Soc. Mass Spectrom*. **2009**, *20*, 496-506.
20. Steen, H.; Mann, M. *Nat. Rev. Mol. Cell Biol*. **2004**, *5*, 699-711.
21. Kebarle, P.; Peschke, M. *Anal. Chim. Acta*. **2000**, *406*, 11-35.
22. Kebarle, P.; Verkerk, U. H. *Mass Spectrom. Rev*. **2009**, *28*, 898-917.
23. Fenn, J. B.; Mann, M.; Meng, C. K.; Wong, S. F.; Whitehouse, C. M. *Mass Spectrom. Rev*. **1990**, *9*, 37-70.
24. Nguyen, S.; Fenn, J. B. *Proc. Natl. Acad. Sci*. **2007**, *104*, 1111-1117.
25. Wilm, M. *Mol. Cell Proteomics*. **2011**, *10*, M111.009407-1-8.
26. Herrmann, K. A.; Somogyi, A.; Wysocki, V. H.; Drahos, L.; Vékey, K. *Anal. Chem*. **2005**, *77*, 7626-7638.
27. Carl, D. R.; Cooper, T. E.; Oomens, J. Steill, J. D.; Armentrout, P. B. *Phys. Chem. Chem. Phys*. **2010**, *12*, 3384-3398.
28. Dunbar, R. C.; Steill, J. D.; Polfer, N. C.; Oomens, J. *J. Phys. Chem. A*. **2009**, *113*, 845-851
29. Piatkivskyi, A.; Osburn, S.; Jaderberg, K.; Grzetic, J.; Steill, J. D.; Oomens, J.; Zhao, J.; Kai-Chi Lau, J.; Verkerk, U. H.; Hopkinson, A. C.; Siu, K. W. M.; Ryzhovet, V. *J. Am. Soc. Mass Spectrom*. **2013**, *24*, 513-523.
30. Dunbar, R. C.; Hopkinson, A. C.; Oomens, J, Siu, C. K.; Siu, K, W. M, Steill, J. D.; Verkerk, U. H.;Zhao, J. *J. Phys. Chem. B*. **2009**, *113*, 10403-10408.
31. Heiles, S.; Cooper, R. J.; Berden, G.; Oomens, J.; Williams, E. R. *Phys. Chem. Chem. Phys*. **2015**, *17*, 30642-30647.
32. Bush, M. F.; Saykally, R. J.; Williams, E. R. *J. Am. Chem. Soc*. **2008**, *130*, 15482-15489.
33. Grant, E. R.; Schulz, P. A.; Sudbo, A. S.; Shen, Y. R.; Lee, Y. T. *Phys. Rev. Lett*. **1978**, *40*, 115-118.
34. Jami-Alahmadi, Y.; Gholami, A.; Fridgen, T. D. *Phys. Chem. Chem. Phys*. **2014**, *16*, 26855-26863.
35. Wu, R.; McMahon, T. B. *ChemPhysChem*. **2008**, *9*, 2826-2835.

36. Dunbar, R. C.; Steill, J. D.; Oomens, J. *Phys. Chem. Chem. Phys*. **2010**, *12*, 13383-13393.
37. Zhao, J.; Lau, J. C.; Grzetic, J.; Verkerk, U. H.; Oomens, J.; Siu, K. W. M.; Hopkinsonet, A. C. *J. Am. Soc. Mass Spectrom*. **2013**, *24*, 1957-1968.
38. Semrouni, D.; Balaj, O. P.; Calvo, F.; Correia, C. F.; Clavaguéra, C.; Ohanessian, G. *J. Am. Soc. Mass Spectrom*. **2010**, *21*, 728-738.
39. Jami-Alahmadi, Y.; Fridgen, T. D. *Phys. Chem. Chem. Phys*. **2016**, *18*, 2023-2033.
40. Drayß, M. K.; Armentrout, P. B.; Oomens, J.; Schäfer, M. *Int. J. Mass Spectrom*. **2010**, *297*, 18-27.
41. Kamariotis, A.; Boyarkin, O. V.; Mercier, S. R.; Beck, R. D.; Bush, M. F.; Williams, E. R.; Rizzo, T. R. *J. Am. Chem. Soc*. **2006**, *128*, 905-916
42. Drayss, M. K.; Blunk, D.; Oomens, J.; Schäfer, M. *J. Phys. Chem. A.* **2008**, 112, 11972-11974.
43. Schmidt, J.; Kass, S. R. *J. Phys. Chem. A.* **2013**, *117*, 4863-4869.
44. Van Stipdonk, M. J.; Patterson, K.; Gibson, J. K.; Berden, G.; Oomens, J. *Int. J. Mass. Spectrom*. **2015**, *379*, 165-178.
45. Gillis, E. A. L.; Rajabi, K.; Fridgen, T. D. *J. Phys. Chem. A*. **2009**, *113*, 824-832.
46. Rajabi, K.; Gillis, E, A. L.; Fridgen, T. D. *J. Phys. Chem. A*. **2010**, *114*, 3449-3456.
47. Yang, B.; Wu, R. R.; Polfer, N. C.; Berden, G.; Oomens, J.; Rodgers, M. T. *J. Am. Soc. Mass Spectrom*. **2013**, *24*, 1523-1533.
48. Dunbar, R. C; Polfer, N. C.; Berden, G.; Oomens, J. *Int. J. Mass Spectrom.* **2012**, *332*, 71-77.
49. Prell, J. S.; Flick, T. G.; Oomens, J.; Berden, G.; Williams, E. R. *J. Phys. Chem. A.* **2009**, *114*, 854-860.
50. Dunbar, R. C.; Berden, G.; Oomens, J. *Int. J. Mass Spectrom*. **2013**, *354*, 356-364.
51. Polfer, N. C.; Oomens, J.; Dunbar, R. C. *ChemPhysChem*. **2008**, *9*, 579-589.
52. Moghaddam, M. B.; Fridgen, T. D. *J. Phys. Chem. B*. **2013**, *117*, 6157-6164.
53. Martens, J. K; Grzetic, J.; Berden, G.; Oomens, J. *Int. J. Mass Spectrom*. **2015**, *377*, 179-187.
54. Piccirillo, S.; Ciavardini, A.; Bodo, E.; Rondino, F.; Scuderi, D.; Steinmetz, V.; Paladini, A. *Inorg. Chem.* **2013**,*52*, 103-112
55. Sannes-Lowery, K. A.; Hofstadler, S. A. *J. Am. Soc. Mass Spectrom*. **2003**, *14*, 825-833.
56. Lanucara, F.; Chiavarino, B.; Scuderi, D.; Maitre, P.; Fornarini, S.; Crestoni, M. E. *Chem. Commun*. **2014**, *50*, 3845-3848.
57. Paciotti, R.; Coletti, C.; Re, N.; Scuderi, D.; Chiavarino, B.; Fornarini, S.; Crestoni, M. E. *Phys. Chem. Chem. Phys*. **2015**;*17*, 25891-25904.

58. Wu, R.; Marta, R.; Martens, J.; Eldridge, K.; McMahon, T. *J. Am. Soc. Mass Spectrom*. **2011**, *22*, 1651-1659.
59. Yin, H.; Kong, X. *J. Am. Soc. Mass Spectrom*. **2015**, *26*, 1455-1461.
60. Armentrout, P. B.; Rodgers, M. T.; Oomens, J.; Steill, J. D. *J. Phys. Chem. A.* **2008**, *112*, 2248-2257.
61. Polfer, N. C.; Oomens, J. *Mass Spectrom. Rev*. **2009**, *28*, 468-494.
62. Perrin, J. jgkj. *J. Ann. Phys*. **1919**, *11*, 1-5.
63. Langmuir, I. *J. Am. Chem. Soc*. **1920**, *42*, 2190-2205.
64. Lindemann, F. A.; Arrhenius, S.; Langmuir, I.; Dhar, N. R.; Perrin, J.; Lewis, W. C. M. *Trans. Faraday Soc*. **1922**, *17*, 598-606.
65. Thoelmann, D.; Tonner, D. S.; McMahon, T. B. *J. Phys. Chem*. **1994**, *98*, 2002-2004.
66. Rodriguez-Cruz, S. E, Jockusch, R. A, Williams, E. R. *J. Am. Chem. Soc*. **2006**, *121*, 1986-1987.
67. Jockusch, R. A.; Williams, E. R. *J. phys. chem. A.* **1998**, *5639*, 4543-4550.
68. Price, W. D.; Schnier, P. D.; Jockusch, R. A.; Strittmatter, E. F.; Williams, E. R. *J. Am. Chem. Soc*. **1996**, *118*, 10640-10644.
69. Schnier, P. D.; Price, W. D.; Jockusch, R. A, Williams, E. R. *J. Am. Chem. Soc*. **1996**, *118*, 7178-7189.
70. Price, W. D.; Schnier, P. D.; Williams, E. R. *Anal Chem*. **1996**, *68*, 859-866.
71. Price, W. D.; Williams, E. R. *J. Phys. Chem. A*. **1997**, *101*,8844-8852.
72. Jockusch, R. A.; Schnier, P.D.; Price, W. D.; Strittmatter, E. F.; Demirev, P. A.; Williams, E. R. *Anal. Chem*. **1997**, *69*, 1119-1126.
73. Gillis, E. A. L,; Demireva, M.; Sarwar, M. G,; Chudzinski, M. G.; Taylor, M. S.; Williams, E. R.; Fridgen, T. D. *Phys. Chem. Chem. Phys*. **2013**, *15*, 7638-7647.
74. Gillis, E. A. L.; Demireva, M.; Nanda, K.; Beran, G.; Williams, E. R, Fridgen, T. D. *Phys. Chem. Chem. Phys*. **2012**, *14*, 3304-3315.
75. Burt, M. B.; Decker, S. G. A.; Fridgen, T. D. *Phys. Chem. Chem. Phys*. **2012**, *14*, 15118-15126.
76. Dunbar, R. C. *Mass Spectrom. Rev*. **2004**, *23*, 127-158.
77. Brunk, E.; Rothlisberger, U. *Chem. Rev*. **2015**, *115*, 6217-6263.
78. Head-Gordon, M.; Pople, J. A.; Frisch, M. J. *Chem. Phys. Lett*. **1988**, *153*, 503-506.
79. Møller, C.; Plesset, M. S. *Phys. Rev*. **1934**, *46*, 618-622.
80. Boys, S. F. *Proc. Roy. Soc*. **1950**, *200*, 542-554.
81. O-Ohata, K.; Taketa, H.; Huzinaga, S. *J. Phys. Soc. Japan*. **1966**, *21*, 2306-2313.
82. Huzinaga, S. *J. Chem. Phys*. **1965**, *42*, 1293-1302.
83. Jensen, F. *WIREs Comput. Mol. Sci*. **2013**, *3*, 273-295.
84. Mcweeny, R. *Nature*. 1950, *166*, 21-22.

85. Davidson, E. R.; Feller, D. *Chem. Rev*. **1986**, *86*, 681-696.
86. Frisch, M. J.; Trucks, G. W.; Schlegel, H. B.; Scuseria, G. E.; Robb, M. A.; Cheeseman, J. R.; Scalmani, G.; Barone, V.; Mennucci, B.; Petersson, G. A.; Nakatsuji, H.; Caricato, M.; Li, X.; Hratchian, H. P.; Izmaylov, A. F.; Bloino, J.; Zheng, G.; Sonnenberg, J. L.; Hada, M.; Ehara, M.; Toyota, K.; Fukuda, R.; Hasegawa, J.; Ishida, M.; Nakajima, T.; Honda, Y.; Kitao, O.; Nakai, H.; Vreven, T.; Montgomery, J. A. Jr.; Peralta, J. E.; Ogliaro, F.; Bearpark, M.; Heyd, J. J.; Brothers, E.; Kudin, K. N.; Staroverov, V. N.; Kobayashi, R.; Normand, J.; Raghavachari, K.; Rendell, A.; Burant, J. C.; Iyengar, S. S.; Tomasi, J.; Cossi, M.; Rega, N.; Millam, J. M.; Klene, M.; Knox, J. E.; Cross, J. B.; Bakken, V.; Adamo, C.; Jaramillo, J.; Gomperts, R.; Stratmann, R. E.; Yazyev, O.; Austin, A. J.; Cammi, R.; Pomelli, C.; Ochterski, J. W.; Martin, R. L.; Morokuma, K.; Zakrzewski, V. G.; Voth, G. A.; Salvador, P.; Dannenberg, J. J.; Dapprich, S.; Daniels, A. D.; Farkas, O.; Foresman, J. B.; Ortiz, J. V.; Cioslowski, J.; Fox, D. J. Gaussian 09, Revision A.01; Gaussian, Inc.: Wallingford, CT, 2009
87. Grimme, S.; Antony, J.; Ehrlich, S.; Krieg, H. A. *J. Chem. Phys*. **2010**, *132*, 15.
88. Wang. J.; Wolf, R. M.; Caldwell, J. W.; Kollman, P. A.; Case, D. A. *J. Comput. Chem*. **2004**, *25*, 1157-1174.

Chapter 3

The Protonated and Sodiated Dimers of Proline Studied by IRMPD Spectroscopy in the N–H and O–H Stretching Region and Computational Methods

This chapter is reproduced with permission from

Jami-Alahmadi, Y.; Gholami, A.; Fridgen, T. D.

"The protonated and sodiated dimers of proline studied by IRMPD spectroscopy in the N–H and O–H stretching region and computational methods"

Phys. Chem. Chem. Phys., **2014**, *16*, 26855-26863.

3.1. Introduction

Research on gas-phase ions and ion–molecule reactions provides us with information on the intrinsic properties of ions. Mass spectrometric techniques are uniquely suited to determine the reactivity and thermochemical properties of gas phase ions and can even be used to elicit structural characteristics. These techniques include blackbody infrared radiative dissociation (BIRD),[1-4] high pressure mass spectrometry (HPMS),[5–9] collision induced dissociation (CID),[10,11] high energy CID,[7,12–14] and the kinetic method.[15–17]

The three dimensional structures of biological macromolecules such as proteins are governed by non-covalent interactions such as hydrogen bonding and ionic hydrogen bonding. Typical ionic hydrogen bonds can have energy higher than 130 kJ mol^{-1}, significantly higher than the normal hydrogen bond.[18–20] The strength of these ionic

hydrogen bonds and their ubiquitousness in biomacromolecules make their fundamental study of utmost importance. Over the last decade, infrared multiple dissociation (IRMPD) spectroscopy[21–24] has been providing much more direct information on the subtleties of bonding, allowing for elucidation of the detailed structures of gaseous ions involving, for example, amino acids[21,22,25–32] and peptides.[22,33–40] IRMPD spectroscopy combined with electronic structure calculations is indeed a powerful combination of tools to help determine the structures of gas phase ions. Protonated amino acid dimers have been the topic of several recent IRMPD spectroscopic studies due to the existence of strong intermolecular ionic hydrogen bonding in these species as well as strong intramolecular hydrogen bonding interactions.[25,29,41–44] For example IRMPD spectroscopic studies on glycine, alanine, valine,[25] and serine[43] protonated dimers showed that the non-protonated amino acid in the dimer was canonical (i.e. non-zwitterionic) but in the proline protonated dimer, neutral proline is predominantly zwitterionic.[42] Due to a band observed at 1733 cm^{-1} which could not be ascribed to the zwitterionic protonated dimer, Wu and McMahon[42] also concluded that an isomer where the neutral proline was in its canonical form was also present in the gas-phase mixture. These small proton-bound dimers can be models for larger systems where strong ionic hydrogen bonding exists, such as proteins. Metal ions also play a huge role in stabilizing biological polymers. Metal ion complexation can stabilize zwitterionic structures of amino acids depending on the size and valency of the metal atom and gas-phase basicity of the amino acids.[30,45,46]

Proline is one of the twenty common amino acids that comprise proteins and obviously plays an important role in human biology. Proline and its post-translationally

modified analogue, hydroxyproline, are secondary amines and are among the main structural materials of fibrous proteins from which bones, tendons, ligaments, and skin are composed, owing to the rigidity of the cyclic structure.[47] Proline helps tissue repair following injuries such as burns, and after surgery.[48,49]

The present work is focused on the structural characterization of the protonated and sodiated dimers of proline using IRMPD spectroscopy in the N–H and O–H stretching region, 3200–4000 cm^{-1}. We also augment the experimental results with electronic structure calculations. Due to the existence of an immense number of possible structures of the gas phase ions under study, using only chemical intuition to come up with starting structures may not be a robust method to determine the global minimum. In order to fully explore the potential energy surface, different methods such as simulated annealing (SA) have been developed and used.[33,50,51]

3.2. Methods

3.2.1. Experimental Methods.

The protonated proline dimers, $[(Pro)_2H]^+$, were electrosprayed from 100 micromolar aqueous solutions of proline to which a few drops of 100 micromolar aqueous formic acid were added. Similarly, the sodiated proline dimers, $[(Pro)_2Na]^+$, were electrosprayed from solutions to which a few drops of 100 micromolar NaCl were added. The laboratory for the study of energetics, reactions, and structures of gaseous ions at Memorial University houses an ApexQe Bruker FTICR mass spectrometer to which a tunable IR laser (OPO) has been mated. The coupling of these two instruments and their

details have been published previously.[21,52,53] Briefly, the laser power is at a maximum of 60 mJ at about 3800 cm^{-1} and decreases smoothly to about 10 mJ at 3100 cm^{-1}. Spectra presented in this paper have not been corrected for power fluctuations. Electrosprayed ions were stored in the hexapole storage cell for about 2 s before being transferred to the ICR cell where they were isolated by standard FTICR techniques. Ions were irradiated for 3 s at each wavenumber value between about 3820 and 3180 cm^{-1} at 2 cm^{-1} intervals. The IRMPD efficiency is the negative of the natural logarithm of the ratio of the precursor ion intensity over the sum of the precursor and fragment ion intensities. The IRMPD spectrum is a plot of the IRMPD efficiency vs. wavenumber.

3.2.2. Computational Methods.

The AMBER9[54] suite of programs with the Generalized AMBER force field (GAFF)[55] was used to explore the conformational space of $[(Pro)_2H]^+$ and $[(Pro)_2Na]^+$. For the $[(Pro)_2Na]^+$ complexes Na was positioned in chemically relevant positions between the organic components and assigned an integer charge. Minimized energy conformations of the complexes were equilibrated for 10 ps at time steps of 0.5 fs at 300 K before undergoing 2000 cycles of simulated annealing (each 31 ps total, 0.5 in fs time step) starting with drastic heating from 300 K to 750 K over 3.00 ps and equilibrated for 1 ps. This was followed by cooling increments of 50 K over 2 ps with 1 ps of equilibration at each temperature until 300 K. The lowest energy structure from each annealing cycle was used to begin the subsequent round of simulated annealing. After each cycle the low energy conformation was cooled to 0 K over 5 ps, minimized, and the potential energy calculated.

Simulated annealing resulted in many different structures for $[(Pro)_2H]^+$ and $[(Pro)_2Na]^+$. For example, 8000 structures were obtained for $[(Pro)_2H]^+$ from four different simulated annealing runs, two for protonated proline complexed to zwitterionic proline, and two for protonated proline complexed with canonical proline. A potential energy vs. simulated annealing cycle plot is shown in Figure A1.1. Rearrangement of these data in the order of energy along the abscissa reveals groups of structures with similar energies as can be seen in Figure A1.2. From the 8000 structures produced from the simulated annealing runs, about 120 unique structures were chosen for geometry optimization and frequency calculations using B3LYP/6-31+G(d,p). These optimized structures were then subjected to single point calculations using B3LYP in conjunction with the 6-311+G(3df,3pd) basis set. All ab initio and density functional calculations were done with the Gaussian 09[56] suite of programs. To compare the computed IR spectra with the experimental IRMPD spectra, the former were scaled by 0.964 along the wavenumber axis.[57] The relative enthalpies, $\Delta_{rel}H$, and 298 K Gibbs energies, $\Delta_{rel}G$, denoted as B3LYP/6-311+G(3df,3pd)//B3LYP/6-31+G(d,p) are the electronic energies from the single-point calculations combined with the thermal corrections to the enthalpy and Gibbs energy from the B3LYP/6-31+G(d,p) calculations and are reported relative to the lowest energy structure found. All relative energies are provided in kJ mol^{-1} and were calculated using a temperature of 298 K. For comparison, geometry optimizations were done at the B3LYP/6-311+G(3df,3pd) and MP2/6-31+G(d,p) levels and basis sets and $\Delta_{rel}H$ and 298 K $\Delta_{rel}G$ were computed with these electronic energies with thermal corrections from the B3LYP/6-31+G(d,p) frequency calculations. MP2/6-311+G(3df,3pd) single point calculations were also done on the MP2/6-31+G(d,p) optimized geometries. Finally, for comparison, dispersion corrected

B3LYP (B3LYPD3) calculations using Grimme's D3 version with the original D3 damping function[58] were done with optimizations and frequency calculations using the 6-31+G(d,p) basis set and single point calculations using the 6-311+G(3df,3pd) basis set. All the thermochemistries from these calculations are reported in Tables A1.1 and A1.2.

3.3. Result and Discussion

Upon resonant absorption of the infrared OPO laser, the only dissociation pathway observed was loss of proline for both $[(Pro)_2H]^+$ and $[(Pro)_2Na]^+$. The IRMPD spectra of $[(Pro)_2H]^+$ and $[(Pro)_2Na]^+$ are compared in Figure 3.1 in the 3200–3800 cm^{-1} region. Both spectra contain a strong absorption at about 3600 cm^{-1} corresponding to an O–H stretching vibration of a carboxylic acid group. Both also contain a feature associated with what is most likely an N–H stretch at 3400 cm^{-1}. The IRMPD spectrum of $[(Pro)_2H]^+$ also contains a broad absorption spectrum centered at about 3260 cm^{-1} which most likely corresponds to N–H stretches that are red shifted due to hydrogen bonding. These IRMPD spectra can be compared with infrared spectra computed for various isomers in order to help determine their structure. The structures and spectra of both $[(Pro)_2H]^+$ and $[(Pro)_2Na]^+$ are discussed in turn below.

3.3.1. $[(Pro)_2H]^+$

$[(Pro)_2H]^+$ consists of a protonated proline bound to a neutral proline. It is fundamentally important to know whether the neutral proline is zwitterionic (ZW) or canonical. In the literature when the amino acid is canonical and bound to an ion the

structure has been coined “charge-solvated,” (CS) and we adopt this term for the present paper.

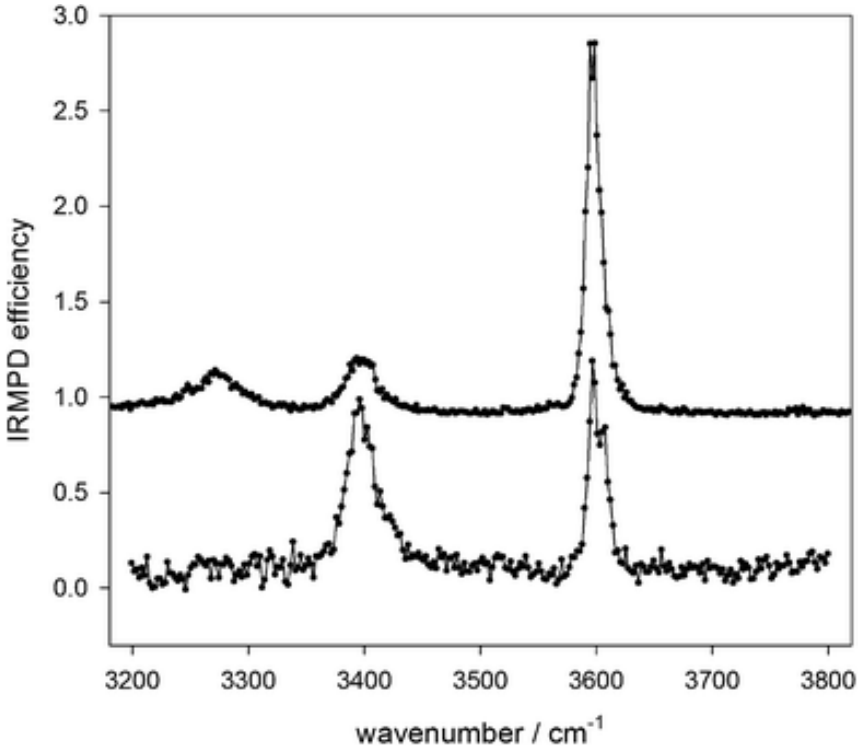

Figure 3.1. Comparison of the IRMPD spectra from 3200 to 3800 cm^{-1} for $[(Pro)_2H]^+$ (top) and $[(Pro)_2Na]^+$ (bottom).

A combination of simulated annealing and “chemical intuition” led to 42 unique structures for $[(Pro)_2H]^+$. Of these structures, 21 are within 16 kJ mol^{-1} in Gibbs energy based on MP2/6-311+G(3df,3pd)//B3LYP/6-31+G(d,p) calculations. There is good correlation in ordering and magnitude between the MP2 calculations and the B3LYP calculations as can be seen in Table A1.1. The ten lowest-energy structures are shown in Figure 3.2, and the remaining 11 below 16 kJ mol^{-1} are shown in Figures A1.3a and

A1.3b. Of the top 21 structures within 16 kJ mol^{-1}, two thirds are ZW, and 8 of the 10 lowest energy structures, in fact the six lowest, are ZW. The first two lowest energy structures differ only in ring puckering of the protonated proline (on the right side of each figure) and are separated by only 1.3 kJ mol^{-1} in Gibbs energy according to the MP2/6-311+G(3df,3pd)//B3LYP/6-31+G(d,p) calculations. The conformations of the protonated proline in ZW1 and ZW2 are identical to the first and second lowest-energy structures determined by Marino *et al.*[59] for bare protonated proline, exo and endo conformations, respectively, and with the carbonyl oxygen interacting with both the protonated amine and hydroxyl hydrogens. The zwitterionic prolines in both ZW1 and ZW2 are in endo conformations, similar to the lowest energy structure of neutral, non-zwitterionic proline.[59] ZW5 is similar to ZW1 except that the ring puckering of the zwitterionic proline is exo, and is almost 5 kJ mol^{-1} higher in Gibbs energy. The prolines in ZW3 have the same ring puckering as ZW1, but the two differ by what is effectively a rotation about the O–H^+–N. In all the zwitterionic structures, one of the carboxylate oxygens of the zwitterionic proline is involved in an intramolecular hydrogen bond to an amine hydrogen. In ZW1, 2, 3, 5 and 6 the zwitterionic proline is bound to the protonated amine by the other carboxylate oxygen. In ZW4 and ZW8, however, the zwitterionic proline is bound through the same carboxylate oxygen that is also hydrogen bonded to the amine hydrogen, leaving one carboxylate oxygen free from any hydrogen bonding interactions. This is important as the infrared spectra of these two sets of ZW structures may be expected to be different in the C=O stretching region, *vide infra*. ZW4 is only 3.7 kJ mol^{-1} higher in energy than ZW1 while ZW8, which differs in ring puckering of the protonated proline, is 8.1 kJ mol^{-1} relative to ZW1.

The lowest energy CS structure, CS7, is calculated to be 7.5 kJ mol^{-1} higher in Gibbs energy than ZW1. The conformations of the prolines are identical in CS7 and ZW2, the only difference is that the neutral proline in the latter is zwitterionic. In Figure 3.3, the computed spectra of the five lowest-energy ZW structures along with CS7 are compared to the experimental IRMPD spectrum. All the zwitterionic structures have virtually identical predicted spectra in the N–H/O–H stretching region, an O–H stretch at about 3600 cm^{-1}, and a free N–H stretch of the zwitterionic proline predicted at about 3390 cm^{-1}. A third vibration corresponds to the stretching of the N–H bond in protonated proline that is not bound to the neutral proline, but is involved in an intramolecular interaction with the carbonyl oxygen which is responsible for its red-shifting to between 3200 and 3300 cm^{-1} from a normal amine N–H stretch. The fluctuation in the position of this band in different structures is due to that mode being sensitive to hydrogen bond strength. All of the ZW structures agree well with the experimental spectrum. The breadth of the experimental band at about 3260 cm^{-1} is about 50 cm^{-1} (fwhm) significantly broader than the 3600 cm^{-1}band which is about 20 cm^{-1} (fwhm). The range of predicted positions for the N–H stretch responsible for the 3260 cm^{-1} feature is consistent with more than one structure being responsible for the observed infrared spectrum.

This is also consistent with so many (5) low-energy structures predicted to be within 5 kJ mol^{-1} in Gibbs energy of the lowest energy structure. The other N–H stretch for the zwitterionic proline in the ZW structures is predicted to occur below 2850 cm^{-1}, strongly red-shifted due to a strong hydrogen bonding interaction with the carboxylate oxygen and outside the range of our laser. The CS structures also have bands predicted at about 3600

cm^{-1} and between 3200 and 3300 cm^{-1}, which correspond to the same vibrational modes as discussed above for the ZW structures. The difference is the free N–H stretch of the neutral proline. For the CS structures this band is predicted to be ~50 cm^{-1} to the blue of that predicted for the zwitterionic structures. The predicted lower wavenumber N–H stretch for the ZW structure is due to a slight weakening of the free N–H bond due to protonation at the N. While this band is weak, there is no sign of it in the experimental IRMPD spectrum and this is consistent with the predicted thermochemistry, being 7.5 kJ mol^{-1} higher in energy corresponding to a population of only 4.9% relative to ZW1. It is concluded, based on the agreement of the IR spectra of the ZW structures with the IRMPD spectrum and the computed thermochemistries, that $[(Pro)_2H]^+$ is zwitterionic. Previous research has been conducted on the proton bound dimer of proline using IRMPD spectroscopy in the 1000–2000 cm^{-1} region in conjunction with electronic structure calculations.[42] Their calculations showed that the four lowest energy structures of $[(Pro)_2H]^+$ were zwitterionic and the next seven structures are CS structures, more than 8 kJ mol^{-1} higher in energy. The results presented here are perfectly consistent with Wu and McMahon in that the first CS structure is almost 8 kJ mol^{-1} higher in energy than the lowest energy structure.[42] Their IRMPD spectrum also better matched the IR spectrum of a ZW structure consistent with the results in the 3200–3800 cm^{-1} range presented here. However, none of their ZW structures had a predicted band that could account for a nicely resolved band observed at 1733 cm^{-1}. Their lowest energy CS structure, identical to CS7 in Figure 3.2 here, did have a predicted band matching the one observed at 1733 cm^{-1} due to the carbonyl of neutral proline, red shifted from the normal ~1800 cm^{-1} position due to interaction with protonated proline.

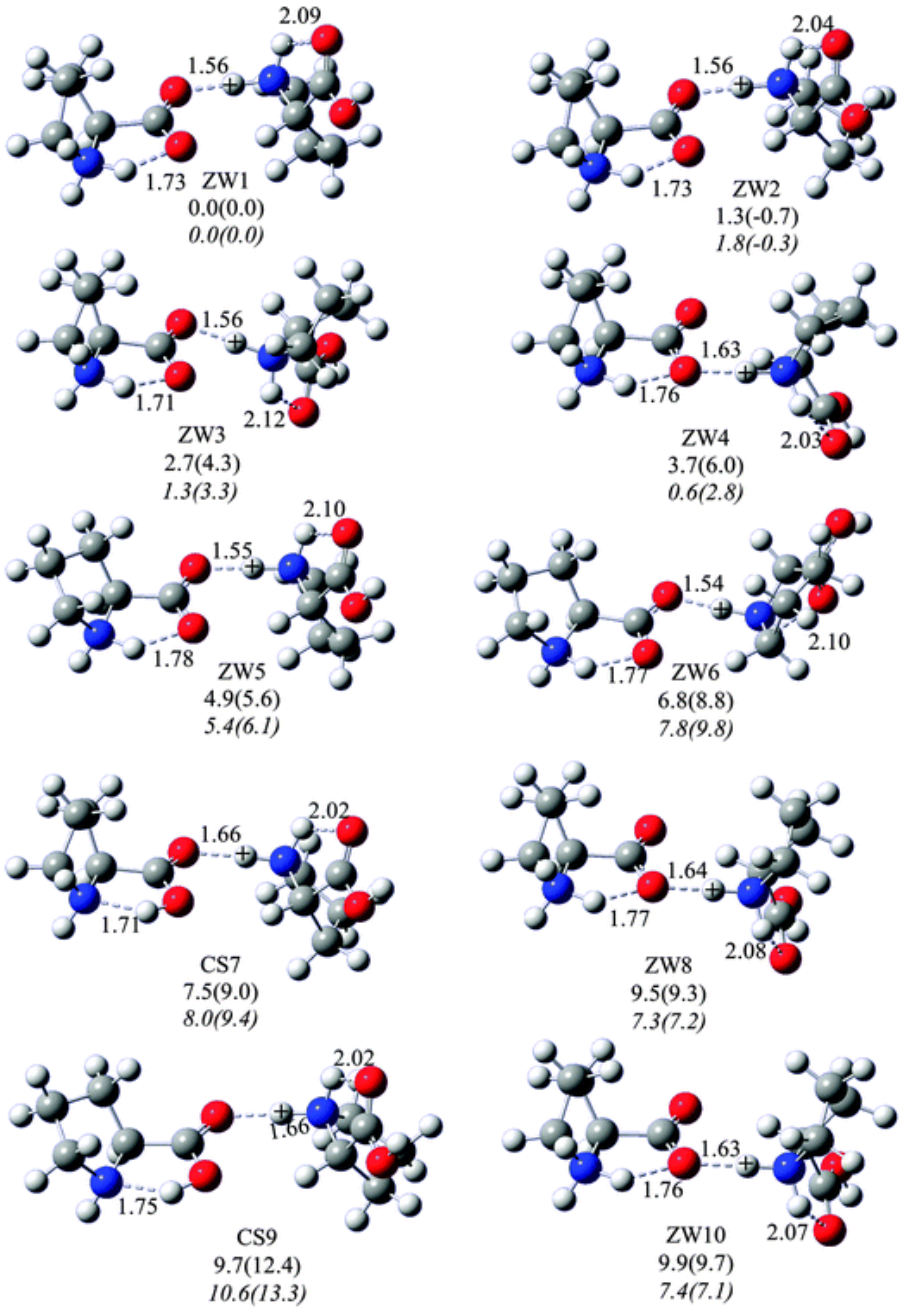

Figure 3.2. Ten lowest energy structures for $[(Pro)_2H]^+$. MP2/6-311+G(3df,3pd)// B3LYP/6-31+G(d,p) and MP2/6-311+G(3dp,3pd)//MP2/6-31+G(d,p); (italicized) 298 K relative Gibbs energies, $\Delta_{rel}G$, and enthalpies, $\Delta_{rel}H$, (parentheses). Energies are provided in kJ mol^{-1}.

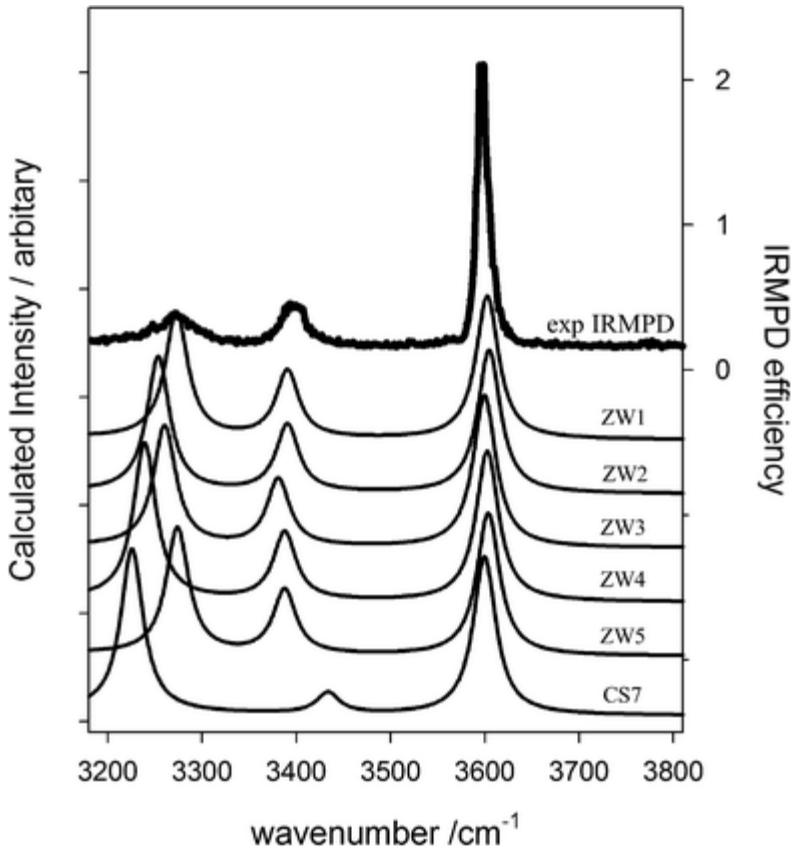

Figure 3.3. Comparison of the experimental IRMPD spectrum of $[(Pro)_2H]^+$ with calculated IR spectra of different isomers of the dimer.

They concluded that the species responsible for their IRMPD spectrum were a combination of zwitterionic structures and the high energy canonical structure. However, we present another explanation for this 1733 cm^{-1} band. ZW4 in Figure 3.2 is 3.7 kJ mol^{-1} lower in energy than CS7, and has a predicted C=O stretching vibration consistent with the 1733 cm^{-1} band in the Wu and McMahon spectrum[42] (see Figure A1.4). The C=O

stretch responsible for this band is the free carbonyl from zwitterionic proline which is blue shifted from the normal carboxylate C=O stretching position because it is not involved in a hydrogen bond; the other is involved in two hydrogen bonds.

The lowest energy structures for $[(Pro)_2H]^+$ were optimized using MP2/6-31+G(d,p) and the electronic energies were refined with MP2/6-311+G(3df,3pd) single point calculations. Dispersion corrected B3LYP calculations were also done for comparison. The thermochemistries computed for $[(Pro)_2H]^+$ structures are in Table A1.1 and are also included in Figure 3.2. It can be seen that the calculations using MP2/6-311+G(3df,3pd) on either the B3LYP/6-31+G(d,p) or MP2/6-31+G(d,p) geometries are consistent with a few minor differences. For example, structure ZW4 actually becomes the second lowest energy structure and higher in Gibbs energy than ZW1 by only 0.6 kJ mol^{-1}, corresponding to a ZW4 population 78% that of ZW1. A simulated spectrum constructed of a weighted average of ZW1 and ZW4 in the 900–2000 cm^{-1} region is provided in Figure A1.4 and shows an excellent match to the experimental spectrum. We conclude that the IRMPD spectra in both the 1000–2000 and 3200–3800 cm^{-1} regions, as well as the computed thermochemistries are most consistent with a mixture of ZW structures and the lowest energy CS structure is probably a minor, unobserved component.

3.3.2. $[(Pro)_2Na]^+$

$[(Pro)_2Na]^+$ consists of a sodium cation bound to two proline dimers. Unlike the proton in $[(Pro)_2H]^+$, the sodium ion is more evenly shared between the two monomers. Simulated annealing calculations combined with chemical intuition resulted in 36 unique structures of $[(Pro)_2Na]^+$. The B3LYP/6-311+G(3df,3pd)//B3LYP/6-31+G(d,p) thermochemistries

were used to rank the sodium bound dimer structures and it has been observed in the past that density functional theory provides better agreement with experimental thermochemistries for alkali and alkaline earth metal containing complexes.[60]

The eight lowest energy structures are shown in Figure 3.4. The rest of the structures that were identified computationally are available in Figures A1.5a, A1.5b and the thermochemistries are summarized in Table A1.2. Fifteen of these structures are within 10 kJ mol^{-1} of Gibbs energy and in all of these at least one of the prolines is ZW. The lowest energy structures are a mixture of ZW–ZW, where both prolines are zwitterionic, and ZW–CS, where one of the prolines is canonical. The lowest energy CS–CS structure is about 12 kJ mol^{-1} with respect to the lowest energy structure, ranked 18th of all the structures computed. This is consistent with previous research which shows that for the sodiated monomer, proline is zwitterionic,[45,61,62] so it would be expected that lower energy structures might have at least one of the prolines in its zwitterionic structure.

The O–H stretching band at 3600 cm^{-1} in the IRMPD spectrum of the sodium bound dimer (Figure 3.5), clearly suggests that at least part of the population of observed ions contains a structure in which there is at least one canonical proline with a non-hydrogen bonded—or free—O–H bond. The ZW–ZW structures do not have a hydroxyl group, and the O–H stretch is red-shifted out of the range of the laser for ZW–CS structures (*i.e.* ZW–CS1 which has an identical predicted spectrum to ZW–CS3 in the N–H/O–H stretching region) where the hydroxyl group is hydrogen bonded to the amine.

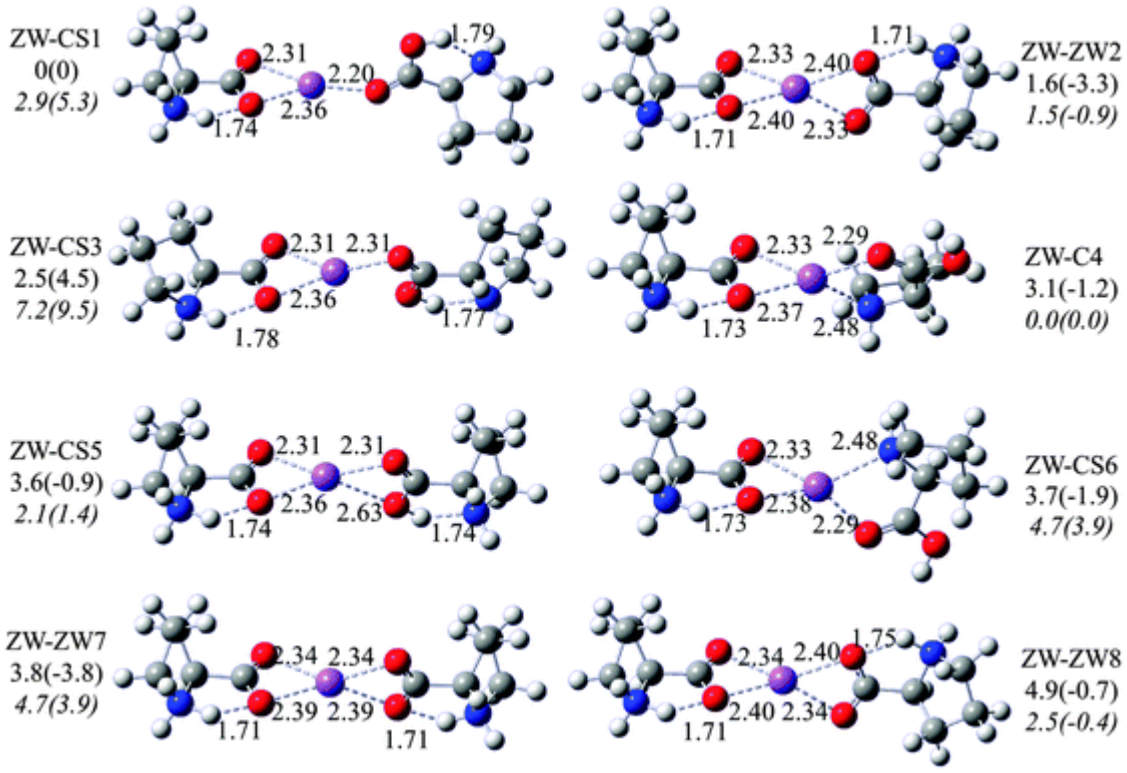

Figure 3.4. Eight lowest energy structures for $[(Pro)_2Na]^+$. B3LYP/6-311+G(3df,3pd)// B3LYP/6-31+G(d,p), B3LYP/6-311+G(3df,3pd)//B3LYPD3/6-31+G(d,p) (italicized), 298 K $\Delta_{rel}G$, and enthalpies, $\Delta_{rel}H$, (parentheses). Energies are provided in kJ mol^{-1}.

However, structures such as ZW–CS4 and ZW–CS6 (which have identical predicted spectra in the N–H/O–H stretching region which are only 3.1 and 3.7 kJ mol^{-1} higher in energy than the lowest energy structure, respectively) can account for the O–H stretching vibration with a free O–H moiety. In fact, ZW–CS4 is the lowest energy structure computed using dispersion corrected density functional theory (B3LYPD3, Table A1.2) with ZW–ZW2 and ZW–CS6 being 1.5 kJ mol^{-1} higher in Gibbs energy. The relative intensities of the experimental N–H stretch and O–H stretch are also most consistent with the predicted spectrum of ZW–CS4 (and ZW–CS6). It is concluded that $[(Pro)_2Na]^+$ is

predominantly composed of a zwitterionic proline bound to Na^+*via* the two carboxyl oxygens and the canonical proline is bound through the carbonyl O and the amine N with a free O–H bond that is observed to absorb at about 3600 cm^{-1}.

3.4. Conclusions

A combination of IRMPD spectroscopy and computational chemistry has been used to determine that the proton- and sodium-bound dimers of proline exist as a mixture of a number of different structures. Simulated annealing computations were also used to augment chemical intuition to determine the unique structures of the dimeric complexes. The proton-bound dimer structure exists as an N-protonated proline bound to zwitterionic proline. No spectroscopic evidence in the 3200–3800 cm^{-1} region was observed for a canonical structure. A well resolved C=O band at 1733 cm^{-1} from a previous spectroscopic study[42] was reassigned from a high energy canonical isomer to a lower energy zwitterionic structure.

Computationally, there are many low energy sodium bound dimers of proline computed to be within 10 kJ mol^{-1} in Gibbs energy and eight structures within 5 kJ mol^{-1}. None of the ZW–ZW structures can necessarily be ruled out based on the experimental spectrum. They all have an N–H stretching band predicted in the same position as that observed experimentally. However, only ZW–CS structures that have a free O–H bond can be responsible for the band at ~3600 cm^{-1}. The sodium-bound dimer may exist as a mixture of a number of different structures, but at least one of these must be a ZW–CS structure,

such as ZW–CS4 with a free hydroxyl group. Diffusion corrected B3LYP calculations predict this ZW–CS4 structure to be the lowest-energy structure.

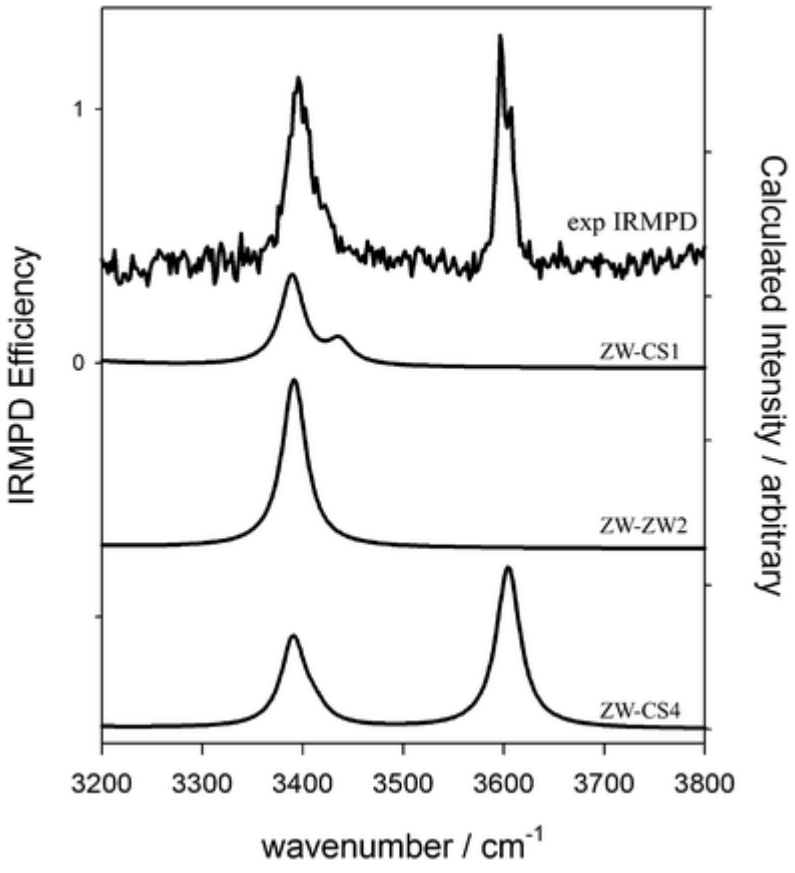

Figure 3.5. Comparison of the experimental IRMPD spectrum of $[(Pro)_2Na]^+$ with calculated IR spectra of different isomers of the dimer.

3.5. Acknowledgements

The authors acknowledge the financial contributions from the National Sciences and Engineering Research Council of Canada and the School of Graduate Studies at

Memorial University that made this research possible. Westgrid and HPCVL are also acknowledged for the computational resources. Finally, the generous contribution of time from Justin Renault, a former PhD Student from Paul Mayer's group at the University of Ottawa, in molecular dynamics calculation is greatly appreciated.

3.6. References

1. Burt, M. B.; Decker; S. G. A.; Fridgen, T. D. *Phys. Chem. Chem. Phys.* **2012,** *14*, 15118–15126.
2. Gillis, E. A. L.; Demireva, M.; Sarwar, M. G.; Chudzinski, M. G. Taylor, M. S.; Williams, E. R. Fridgen, T. D. *Phys. Chem. Chem. Phys.* **2013**, *15*, 7638–7647.
3. Dunbar, R. C. *Mass Spectrom. Rev.* **2004**, *23*, 127–158.
4. Gillis, E. A. L.; Demireva, M.; Nanda, K.; Beran, G.; Williams E. R.; Fridgen, T. D. *Phys. Chem. Chem. Phys.* **2012**, *14*, 3304–3315.
5. McMahon, T. B.; Wu, R.; *Mass Spectrom. Rev.* **2009**, *28*, 546–585.
6. Wincel, H. *J. Am. Soc. Mass Spectrom.* 2007, 18, 2083–2089.
7. Armentrout, P. B.; Heaton, A. *J. Am. Soc. Mass Spectrom.* **2012**, *23*, 632–643.
8. Wincel, H. *J. Phys. Chem. A.* **2007**, *111*, 5784–5791.
9. Wincel, H. *J. Am. Soc. Mass Spectrom*. **2009**, *20*, 1900–1905.
10. Piatkivskyi, A.; Osburn, S.; Jaderberg, K.; Grzetic, J.; Steill, J. D.; Oomens, J.; Zhao, J.; Lau, J. K. C.; Verkerk, U. H.; et al. *J. Am. Soc. Mass Spectrom.* **2013**, *24*, 513–523.
11. Mayer, P. M.; Poon, C. *Mass Spectrom. Rev*. **2009**, *28*, 608–639.
12. Yoo, J. S.; Park, T.; Bang, G.; Lee, C.; Rho, J. R.; Kim, Y. H. *J. Mass Spectrom.* **2013**, *48*, 164–171.
13. Carl, D. R,; Armentrout, P. B. *J. Phys. Chem. A.* **2012**, *116*, 3802–3815.
14. Yang, Z.; Rodgers, M. T. *Phys. Chem. Chem. Phys.* **2012**, *14*, 4517–4526.
15. Kuntz, A.; Boynton, A.; David, G.; Colyer K.; Poutsma, J. *J. Am. Soc. Mass Spectrom.* **2002**, *13*, 72–81.
16. Bouchoux, G. *Mass Spectrom. Rev*. **2012**, *31*, 391–435.
17. Webb, I. K.; Muetterties, C. E.; Platner, C. B.; Poutsma, J. C. *Int. J. Mass Spectrom.* **2012**, *316*, 126–132.
18. Fridgen, T. D.; MacAleese, L.; McMahon, T. B.; Lemaire, J. Maitre, P. *Phys. Chem. Chem. Phys*. **2006**, *8*, 955–966.
19. Burt, M. B.; Fridgen T. D. *J. Phys. Chem. A.* **2007**, *111*, 10738–10744.

20. Meot-Ner, M. *Chem. Rev.* **2012**, *112*, PR22–PR103.
21. Fridgen, T. D. *Mass Spectrom. Rev.* **2009**, *28*, 586–607.
22. Polfer, N. C. Oomens, J. *Mass Spectrom. Rev.* **2009**, *28*, 468–494.
23. Eyler, J. R. *Mass Spectrom. Rev.* **2009**, *28*, 448–467.
24. Burt, M.; Fridgen, T. D. *Eur. J. Mass Spectrom.*, **2012**, *18*, 235–250.
25. Rajabi, K.; Fridgen, T. D. *J. Phys. Chem. A*, **2007**, *112*, 23–30.
26. Bush, M. F.; Forbes, M. W.; Jockusch, R. A.; Oomens, J.; Polfer, N. C.; Saykally, R. J.; Williams, E. R. *J. Phys. Chem. A*, **2007**, *111*, 7753–7760.
27. Gholami, A.; Fridgen, T. D. *J. Phys. Chem. B*, **2013**, *117*, 8447–8456.
28. Schmidt, J.; Kass, S. R. *J. Phys. Chem. A*, **2013**, *117*, 4863–4869.
29. Atkins, C. G.; Rajabi, K.; Gillis, E. A. L,; Fridgen, T. D. *J. Phys. Chem. A*. **2008**, *112*, 10220–10225.
30. Armentrout, P. B.; Rodgers, M. T.; Oomens, J.; Steill, J. D. *J. Phys. Chem. A*, **2008**, *112*, 2248–2257.
31. Yang, B.; Wu, R. R.; Polfer, N. C.; Berden, G.; Oomens, J.; Rodgers, M. T. *J. Am. Soc. Mass Spectrom.* **2013**, *24*, 1523–1533.
32. Gholami, A. Fridgen, T. D. *Phys. Chem. Chem. Phys.* **2014**, *16*, 3134–3143.
33. Semrouni, D.; Balaj, O. P.; Calvo, F.; Correia, C. F.; Clavaguéra, C.; Ohanessian, G. *J. Am. Soc. Mass Spectrom.*, **2010**, *21*, 728–738.
34. Bythell, B. J.; Erlekam, U.; Paizs, B.; Maître, P. *ChemPhysChem*, **2009**, *10*, 883–885.
35. Prell, J. S., Flick, T. G.; Oomens, J.; Berden, G.; Williams, E. R. *J. Phys. Chem. A*, **2009**, *114*, 854–860.
36. Polfer, N. C.; Oomens, J.; Dunbar, R. C. *ChemPhysChem*, **2008**, *9*, 579–589.
37. Zhao, J.; Lau, J.C.; Grzetic, J.; Verkerk, U.; Oomens, J.; Siu, K. W. M.; Hopkinson, *J. Am. Soc. Mass Spectrom.*, **2013**, *24*, 1957–1968.
38. Lanucara, F.; Chiavarino, B.; Scuderi, D.; Maitre, P.; Fornarini, S.; Crestoni, M. E. *Chem. Commun.* **2014**, *50*, 3845–3848.
39. Turecek, F.; Moss, C. L.; Pikalov, I.; Pepin, R.; Gulyuz, K.; Polfer, N. C.; Bush, M. F.; Brown, J.; Williams, J.; Richardson, K. *Int. J. Mass Spectrom*. **2013**, 354–355, 249–256.
40. Dunbar, R. C.; Berden G.; Oomens, J.; *Int. J. Mass Spectrom.* **2013**, *354*, 356–364.
41. Wu, R.; Marta, R.; Martens, J.; Eldridge, K.; McMahon, T. *J. Am. Soc. Mass Spectrom.* **2011**, *22*, 1651–1659.
42. Wu, R.; McMahon, T. B. *J. Am. Chem. Soc.* **2007**, *129*, 4864–4865.
43. Kong, X.; Tsai, I. A.; Sabu, S.; Han, C.-C.; Lee, Y. T.; Chang, H.-C.; Tu, S.-Y.; Kung, A. H.; Wu, C.-C. *Angew. Chem., Int. Ed.* **2006**, *45*, 4130–4134.
44. Oh, H.-B., Lin, C.; Hwang, H. Y.; Zhai, H.; Breuker, K.; Zabrouskov, V.; Carpenter, B. K.; McLafferty, F. *J. Am. Chem. Soc.* **2005**, *127*, 4076–4083.

45. Kapota, C.; Lemaire, J.; Maître, P.; Ohanessian, G. *J. Am. Chem. Soc.* **2004**, *126*, 1836–1842.
46. Bush, M. F.; Oomens, J.; Saykally, R. J.; Williams, E. R. *J. Am. Chem. Soc.* **2008**, *130*, 6463–6471.
47. Lehninger, A.; Nelson, D.; Cox, and M. *Lehninger Principles of Biochemistry,* W. H. Freeman, 2008.
48. Stinnett, J. D.; Alexander, J. W.; Watanabe, C.; Macmillan, B. G.; Fischer, J. E.; Morris, M. J.; Trocki, O.; Miskell, P.; Edwards, L.; James, H. *Ann. Surg.* **1982**, *195*, 75–89.
49. Bergman, I.; Loxley, R. *Anal. Chem.* **1970**, *42*, 702–706.
50. Comeau, A. N.; Renaud, J. B.; Mironov, G. G.; Berezovski, M. V.; Mayer, P. M. *Int. J. Mass Spectrom.*, **2012**, *316*, 31–39.
51. Zou, S.; Oomens, J.; Polfer, N. C. *Int. J. Mass Spectrom.* **2012**, **316**, 12–17.
52. Burt, M. B.; Decker, S. G. A.; Atkins, C. G.; Rowsell, M.; Peremans, A.; Fridgen, T. D.*J. Phys. Chem. B.* **2011**, *115*, 11506–1151.
53. Rajabi, K.; Easterling, M.; Fridgen, T. D. *J. Am. Soc. Mass Spectrom*. **2009**, *20*, 411–418.
54. Case, D.; Darden, T. A.; Cheatham, T. E.; Simmerling, C.; Wang, J.; Duke, R.; Luo, R.; Crowley, M.; Walker, R.; Zhang, W.; et all. *Amber 11 OR*, University of California, San Francisco.
55. Wang, J.; Wolf, R. M.; Caldwell, J. W.; Kollman, P. A.; Case, D. A. *J. Comput. Chem.* **2004**, *25*, 1157–1174.
56. Frisch, M. J.; Frisch, M. J.; Trucks, G. W.; Schlegel, H. B.; Scuseria, G. E.; Robb, M. A.; Cheeseman, J. R.; Scalmani, G.; Barone, V.; Mennucci, B.; Petersson, G. A.; Nakatsuji, H.; Caricato, M.; Li, X.; Hratchian, H. P.; Izmaylov, A. F.; Bloino, J.; Zheng, G.; Sonnenberg, J. L.; Hada, M.; Ehara, M.; Toyota, K.; Fukuda, R.; Hasegawa, J.; Ishida, M.; Nakajima, T.; Honda, Y.; Kitao, O.; Nakai, H.; Vreven, T.; Montgomery, J. A. Jr.; Peralta, J. E.; Ogliaro, F.; Bearpark, M.; Heyd, J. J.; Brothers, E.; Kudin, K. N.; Staroverov, V. N.; Kobayashi, R.; Normand, J.; Raghavachari, K.; Rendell, A.; Burant, J. C.; Iyengar, S. S.; Tomasi, J.; Cossi, M.; Rega, N.; Millam, J. M.; Klene, M.; Knox, J. E.; Cross, J. B.; Bakken, V.; Adamo, C.; Jaramillo, J.; Gomperts, R.; Stratmann, R. E.; Yazyev, O.; Austin, A. J.; Cammi, R.; Pomelli, C.; Ochterski, J. W.; Martin, R. L.; Morokuma, K.; Zakrzewski, V. G.; Voth, G. A.; Salvador, P.; Dannenberg, J. J.; Dapprich, S.; Daniels, A. D.; Farkas, O.; Foresman, J. B.; Ortiz, J. V.; Cioslowski, J.; Fox, D. J. Gaussian 09, Revision A.01; Gaussian, Inc.: Wallingford, CT, 2009.
57. Moghaddam, M. B.; Fridgen, T. D. *J. Phys. Chem. B*. **2013**, *117*, 6157–6164.
58. Grimme, S.; Antony, J.; Ehrlich, S.; Krieg, H. *J. Chem. Phys.* **2010**, *132*, 154104.
59. Marino, T.; Russo, N,; Tocci, E.; Toscano, M. *J. Mass Spectrom*. **2001**, *36*, 301–305.

60. Zhu, W.; Luo, X.; Puah, C. M.; Tan, X.; Shen, J.; Gu, J.; Chen, K.; Jiang, H. *J. Phys. Chem. A.* **2004**, *108*, 4008–4018.
61. Hoyau, S.; Norrman, K.; McMahon, T. B.; Ohanessian, G. *J. Am. Chem. Soc.* **1999**, *121*, 8864–8875.
62. Marino, T.; Russo, N.; Toscano, M. *J. Phys. Chem. B.* **2003**, *107*, 2588–2594.

Chapter 4

Structures and Unimolecular Chemistry of $M(Pro_2\text{-}H)^+$ (M = Mg, Ca, Sr, Ba, Mn, Fe, Co, Ni, Cu, Zn) by IRMPD Spectroscopy, SORI-CID, and Theoretical Studies

This chapter is reproduced with permission from

Jami-Alahmadi, Y.; Fridgen, T. D.

"Structures and unimolecular chemistry of $M(Pro_2\text{-}H)^+$ (M = Mg, Ca, Sr, Ba, Mn, Fe, Co, Ni, Cu, Zn) by IRMPD spectroscopy, SORI-CID, and theoretical studies"

Phys. Chem. Chem. Phys., **2016**, *18*, 2023-2033.

4.1. Introduction

Interactions between transition or alkaline earth metal dications and biomolecules are of great interest and have garnered much attention due to the important roles they play in biological processes. Furthermore, it is anticipated that the detailed fundamental chemistry that can be learned from studying these small complexes will be transferrable to larger, more biologically relevant systems. Transition metals are present in trace amounts in living organisms complexed by peptides, proteins, or nucleic acids. The effects of metal cations can be positive, in fact necessary, stabilizing or binding substrates or acting as redox centres in enzyme catalyzed reactions; their effects can also be negative, destabilizing proteins or helical structures and acting as poisons. The nature of their effect depends on factors such as the identity of the metal cation and its concentration.[1]

The coordination of amino acids to transition metal ions has been studied in solution using techniques such as, X-ray diffraction, electron paramagnetic resonance (EPR),[2] optical absorption and FTIR studies,[2] HNMR,[3] UV-Vis spectroscopy,[3] and computational chemistry.[4,5] Gas-phase studies of metal-bound amino acid complexes have the advantage that the effects of counter ions and solvent can be eliminated. A more detailed understanding of the intrinsic physical chemistry of the ion/molecule complex can be obtained in the gas phase, providing a baseline to which solvent-phase experiments can be compared and provide information for models of metal ion–biomolecule interactions. IRMPD spectroscopy has proven to be one excellent tool to probe of the structures of amino acid bound metal ion complexes.[6–20] The positions of prominent modes, such as the C=O, N–H, and O–H stretch can shift significantly with changes in their bonding environment making this technique especially useful for the structural investigation of ionic amino acid complexes.

Proline is one of the twenty DNA-encoded amino acids and is unique in that its amine group is bound to its side chain making it a highly basic, secondary amine. Due to the ring structure of proline, when incorporated into a peptide or protein, it imparts a rigidity in the peptide backbone. For example, it has been proposed that a rate-limiting step in the protein folding is the *cis*/*trans* isomerization of the proteins that contain proline.[21] Recently in our lab, IRMPD spectroscopy and theory were used to conclude that the structure of the $[Zn(Pro\text{-}H)]^+$ complex in the gas phase can be described as an N/C2 or N/C5 dehydrogenated proline molecule (*i.e.* Deprotonated at N and either C2 or C5 of proline) with ZnH^+ bound to the imine N and carbonyl O. It was also found to predominantly lose neutral Zn upon collisional or IRMPD activation leaving the protonated dehydrogenated

proline as the ionic product. Interestingly, the major fragmentation product for the "dimeric" $[Zn(Pro_2)\text{-}H]^+$ complex was found to be sequential double dehydrogenation unlike any of the primary amines studied. Sarcosine, another secondary amino acid, also underwent dehydrogenation.[22] To our knowledge this is the first report of dehydrogenation of a gas-phase amino acid complex and one of the motivations of this study was to determine whether Zn^{2+} is unique or whether other $[M(Pro)_2\text{-}H]^+$ complexes would also dehydrogenate in the gas phase. Dehydrogenation of amino acids in biological systems occurs under the influence of amino acid oxidases using FAD as an oxidizing agent to dehydrogenate the substrate amino acid to the imino acid form. Following oxidation, the imino acid is transaminated to the alpha-keto acid.[23,24]

Transition metals in complexes can differ in terms of the metal oxidation state. To determine the geometry of transition metal bound ligand complexes, the degree of splitting of the d orbitals is significant and directs how orbitals can be filled and whether the complex is high spin *vs.* low spin. Metals such as Mn, Fe, Co and Ni are capable of different d-orbital splitting and can adopt different possible spin states; this makes it more complicated to calculate all of the possible electronic geometries of these complexes.[25–29] The cooperation between mass spectrometry techniques and density functional theory (DFT) calculations would allow gaining some understanding on the structural information of amino acid bound metals that, in principle, may be useful to rationalize the behavior of more complicated systems which present similar basic sites.

In this work we explore the unimolecular fragmentation pathways of the $[M(Pro)_2\text{-}H]^+$ complexes initiated by sustained off-resonance irradiation collision-induced dissociation (SORI-CID) in a Fourier transform ion cyclotron resonance (FTICR) mass

spectrometer. We also present IRMPD spectroscopy in the 2700–3800 cm^{-1} region, and for some complexes, in the 1000–1800 cm^{-1} region which is backed by theory to help determine the structures of these $[M(Pro)_2\text{-}H]^+$ complexes.

4.2. Methods

4.2.1. Experimental

All mass spectrometry experiments were performed using a Bruker ApexQe 7.0 FTICR. $[M(Pro)_2\text{-}H]^+$ (M = Mn, Fe, Co, Ni, Cu, Zn, Mg, Ca, Sr, and Ba) ions were formed by electrospray ionization (ESI) of 1 mL of 10 mmol L^{-1} aqueous solution of proline to which 15 μL of 10 mmol L^{-1} aqueous transition metal salt or 5 μL of the aqueous alkaline earth metal salt were added. ESI was done with an Apollo II ESI source using a syringe pump operated at 100 μL h^{-1}. $MnCl_2$, $FeCl_2$, $Co(NO_3)_2$, $NiCl_2$, $CuCl_2$, $ZnCl_2$, $MgSO_4$, $CaCl_2$, $SrCl_2$, and $BaCl_2$ were the source of metal dications used in these experiments.

For SORI-CID experiments, the ions of interest were first isolated in the ICR cell then accelerated into argon gas under multiple collision SORI conditions. SORI/CID was completed inside the ICR cell which was followed by an Ar pulse to a pressure of $\sim 10^{-6}$ mbar. SORI powers were applied in the range of 0.19–1.40 eV for 250 ms.

IRMPD experiments were performed by using two setups. IRMPD spectra in the 2700–4000 cm^{-1} region were obtained in the Laboratory for the Study of the Energetics, Structures, and Reactions of Gaseous Ions at Memorial University using an FTICR coupled to an IR OPO, manufactured by LaserSpec. This laser is tuneable from 1.4 to 4.5 μm, with a bandwidth of 2 cm^{-1}. The OPO, built around a periodically poled $LiNbO_3$ crystal, is

pumped by a diode pumped solid state Nd:YAG laser. The OPO operates at 20 kHz, with pulse duration of few nanoseconds and generates output power near 3 W at 3 μm, however, the power was limited to 1 W in the present experiments. For IRMPD spectra in the fingerprint region an FTICR was coupled to a mid-infrared free electron laser (FEL)[30] with a 5 cm^{-1} bandwidth at the Centre Laser Infrarouge d'Orsay (CLIO). IRMPD irradiation times were between 1 and 2 s. The experimental IRMPD spectra were obtained by plotting the IRMPD efficiency (negative logarithm of the complex intensity divided by the total ion intensity) as a function of the radiation wavenumber. No attempts were made to correct the IRMPD spectra for fluctuations in laser power.

4.2.2. Computational Methods

All calculations were performed using Gaussian 09.[31] Since all the transition metals studied here, except zinc, have unpaired electrons in their valence shells, the unrestricted open shell version of the B3LYP method (UB3LYP) was used. For Zn, which is a full d-shell orbital, and the alkali metals the restricted B3LYP was used. Geometry optimizations and calculations of the infrared spectra for the optimized structures were carried out using the 6-31+G(d,p) basis set on all atoms except for Sr and Ba, for which the Def2SVP basis set was used. Empirical correction for dispersion was done using Grimme's D3 version with the original D3 damping function, B3LYPD3.[32] All harmonic frequencies were corrected using scaling factors of 0.980 and 0.955 in the fingerprint and C–H/N–H/O–H stretching regions, respectively. These scaling factors are typical for the complexes and regions studied. Computed IR spectra were convoluted using Gaussian functions with a 10 cm^{-1} width (fwhm). Electronic energies were refined with single point calculations using

B3LYPD3/6-311+G(3df,3pd) for all atoms except Sr and Ba for which the Def2TZVP basis set was used. Just for comparison, geometry optimizations and frequency calculations were done using B3LYPD3 in with the cc-pVTZ basis set on some of the Co, Mn, and Mg complexes.

The bonding within the lowest-energy structures was analyzed by locating the bond critical points (BCPs) using atoms-in-molecules (AIM) theory,[33] which is based on a topological analysis of the electronic density at the BCPs, and is a good descriptor of the bond strength or weakness. This analysis was conducted using AIMAll software.[34]

4.3. Results and Discussion

4.3.1. SORI/CID of $[M(Pro)_2\text{-}H]^+$

4.3.1.1. M = Mn, Fe, Co, Ni, and Cu. As depicted in Figure 4.1, all the $[M(Pro)_2\text{-}H]^+$ complexes containing doubly charged first row transition metals, except Cu, were found to lose H_2, H_2O, and CO_2 as the primary fragmentation pathways upon SORI activation. The Zn complex was found to undergo the same primary fragmentation processes.[22] The MS/MS spectra for the $[M(Pro)_2\text{-}H]^+$ complexes where M = Mn, Fe, Co, and Ni are in Figure A2.1–A2.4, respectively, and confirm the three primary fragmentation pathways. The SORI mass spectra and MS/MS spectra also reveal secondary fragmentations which include further H_2 losses. $[Mn(Pro)_2\text{-}H]^+$ and $[Fe(Pro)_2\text{-}H]^+$ also lose a second CO_2 molecule. Interestingly, $[Co(Pro)_2\text{-}H]^+$ and $[Ni(Pro)_2\text{-}H]^+$ seem to not lose a second CO_2, but formic acid, HCOOH, instead. While this loss of 46 Da could originate from a loss of CO_2 followed by H_2 loss, or *vice versa*, MS/MS experiments were not able

to reveal the ion resulting in two CO_2 losses. However, the MS/MS on some CO_2 loss products which were also dehydrogenated were indeed found to lose CO_2. For example, the ion at *m*/*z* 240 in the SORI spectrum of $[Co(Pro)_2\text{-}H]^+$ is the result of double dehydrogenation and loss of CO_2. When isolated and subjected to SORI-CID, *m*/*z* 240 was found to produce fragment ions resulting from loss of 44 and 46 Da (Figure A2.3). HCOOH is apparently a neutral loss, rather than loss of CO followed by loss of H_2O or *vice versa*. In Figure A2.1, for example, $Mn(Pro_2\text{-}H)^+$ loses H_2O to form 266 and also forms 238 with loss of 46 Da. However, 266 does not lose 28 Da, ruling out sequential H_2O + CO loss. No CO loss was observed for these complexes; this indicates but does not prove that CO loss followed by H_2O loss does not occur.

$[Cu(Pro)_2\text{-}H]^+$ (*m*/*z* 292) has a significantly different unimolecular chemistry—it was found to undergo loss of CO_2 as its sole primary dissociation producing *m*/*z* 248. MS/MS studies (Figure A2.5) show that this primary loss of CO_2 is followed mainly by loss of HNCO, forming *m*/*z* 205 as well as a minor loss of H_2O. The fragment ion at *m*/*z* 205 was found to lose HCOOH. It is worthwhile noting that none of these complexes lose proline, clearly due to very strong metal–proline interactions. Also, the fragmentation patterns and extent of fragmentations—no loss of N in any fragmentation except for secondary HNCO loss in $[Cu(Pro)_2\text{-}H]^+$—signifies strong metal–N binding in the complexes.

4.3.1.2. M = Mg, Ca, Sr, and Ba. The SORI-CID spectra for $[M(Pro)_2\text{-}H]^+$, where M are the alkaline earth metals are shown in Figure 4.2. The Sr and Ba complexes were found to

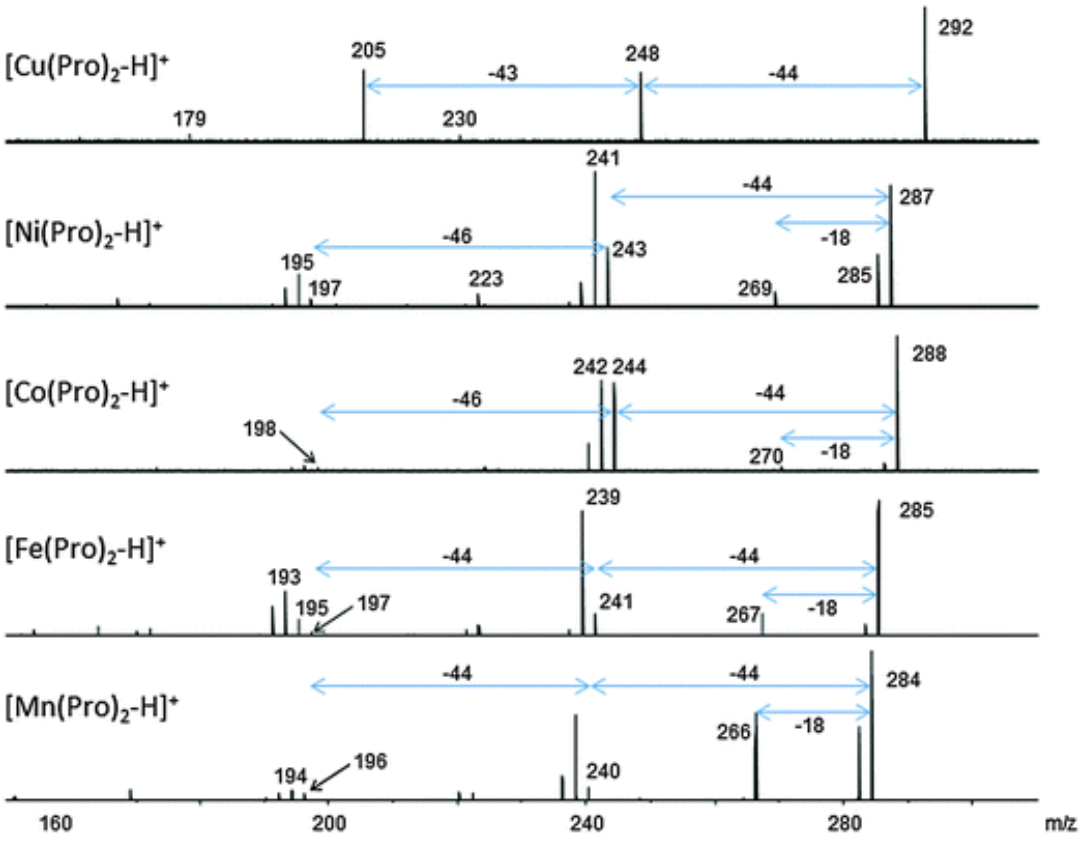

Figure 4.1. SORI/CID spectra obtained for $[Mn(Pro)_2\text{-}H]^+$, $[Fe(Pro)_2\text{-}H]^+$, $[Co(Pro)_2\text{-}H]^+$, $[Ni(Pro)_2\text{-}H]^+$and $[Cu(Pro)_2\text{-}H]^+$.

primarily undergo loss of proline as their main fragmentation, although $[Sr(Pro)_2\text{-}H]^+$ underwent a small amount of successive H_2O loss as seen by fragment ions at *m*/*z* 299 and 281. $[Ca(Pro)_2\text{-}H]^+$ also underwent a significant amount of proline loss, but loss of H_2O strongly competes. A small amount of HCOOH loss was also observed for $[Ca(Pro)_2\text{-}H]^+$. MS/MS (Figure A2.7) confirms that the ion at *m*/*z* 207 is due to a secondary loss of CO_2 following H_2O loss. Interestingly, following the loss of proline, $[Ca(Pro\text{-}H)]^+$ was seen to exhibit H_2 loss.

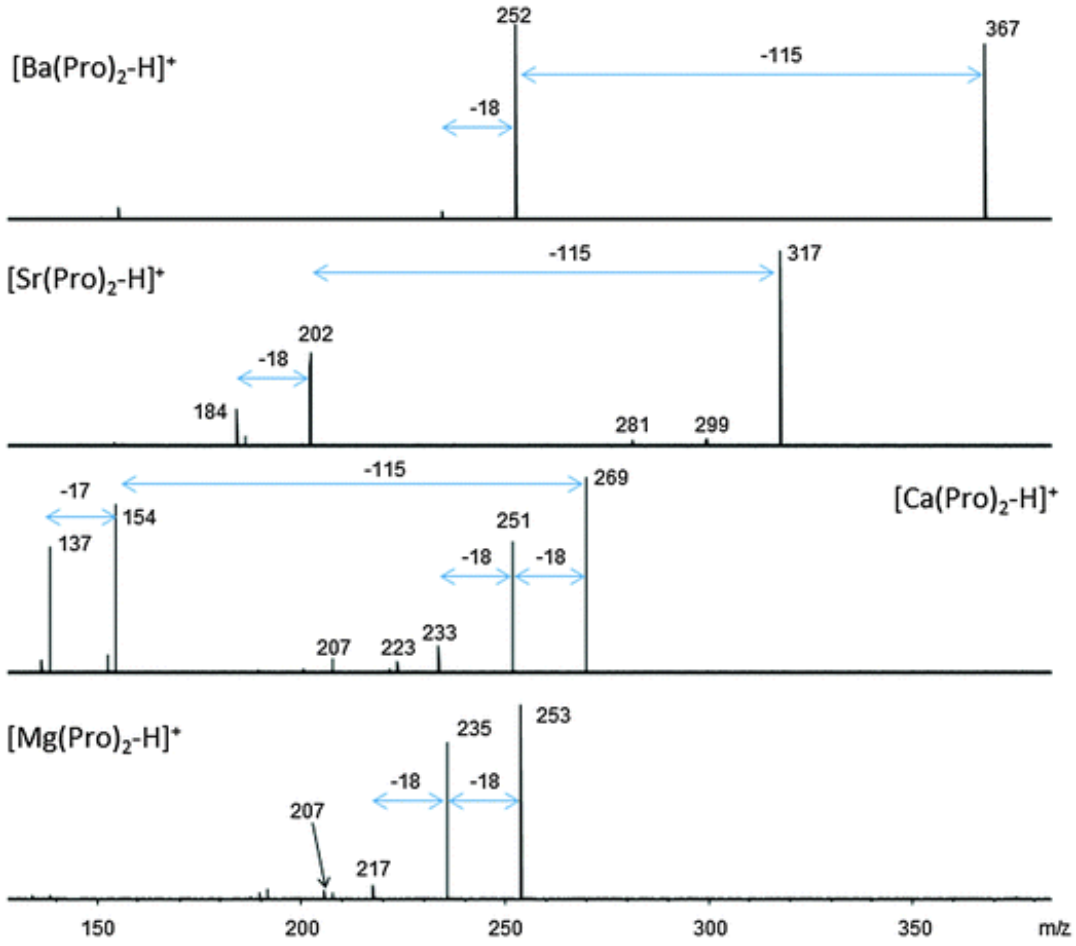

Figure 4.2. SORI/CID spectra obtained for $[Mg(Pro)_2\text{-}H]^+$, $[Ca(Pro)_2\text{-}H]^+$, $[Sr(Pro)_2\text{-}H]^+$, $[Ba(Pro)_2\text{-}H]^+$.

The main primary fragmentation observed for $[Mg(Pro)_2\text{-}H]^+$ (*m*/*z* 253) was loss of water with a small peak also observed for loss of HCOOH at *m*/*z* 207, as seen from the MS/MS data in Figure A2.6. The fragment ion at *m*/*z* 217 is due to a second water loss

from *m*/*z* 235. The small peaks at *m*/*z* 205, 191, and 189 are due to secondary losses of H_2CO, CO_2 and HCOOH, respectively.

The trend in the fragmentation patterns observed for the alkaline earth metals is expected if the binding to the metal cation is electrostatic. The larger Ba^{2+}, with less charge density, binds less strongly to proline resulting in its loss. The smaller the central cation, the higher the charge density and the stronger the metal to proline interaction, resulting in fragmentation of the proline ligand. The binding in $[Mg(Pro)_2\text{-}H]^+$ is so strong that, like the transition metal cation complexes, which have a similarly small size and high charge density, no loss of proline and only proline fragmentation is observed.

4.3.2. IRMPD Spectroscopy of $[M(Pro)_2\text{-}H]^+$

4.3.2.1. M = Mn, Fe, Co, Ni, Cu and Zn. The experimental IRMPD spectra in the 2700–3800 cm^{-1} and 1000–1850 cm^{-1} ranges for $[M(Pro)_2\text{-}H]^+$, (M = transition metal) are depicted in Figure 4.3a and b, respectively. The spectra for all transition metals contain absorptions at about 3550 cm^{-1} and about 3370 cm^{-1} corresponding to a carboxylic acid O–H stretch and a free N–H stretch, respectively. The presence of the O–H stretch in the IRMPD spectrum clearly indicates structures in which one of the prolines has an intact carboxylic acid group—not deprotonated and non-zwitterionic. Weak bands below 3000 cm^{-1} can be ascribed to C–H stretching. In the fingerprint region, 1000–1850 cm^{-1}, for the metals we have spectra for, each have two bands between 1650 cm^{-1} and 1800 cm^{-1} assigned to the C=O stretching of two different carbonyl groups, one free (~1780 cm^{-1}) and one that has been weakened by an interaction, probably with the metal cation

(~1660 cm^{-1}). Also there is a set of pronounced features at around 1230 cm^{-1} in the region corresponding to modes such as COH bending, as well as CH_2 rocking. The spectrum in the fingerprint region for $[Mn(Pro)_2\text{-}H]^+$ is clearly different than the rest. It contains an intense band at 1450 cm^{-1} that could correspond to C–COO stretching and HNC bending as well as a pronounced shoulder at about 1620 cm^{-1} that could be assigned to NH_2 scissoring motions. The intense 1330 cm^{-1} band is also unique to $[Mn(Pro)_2\text{-}H]^+$.

4.3.2.2. M = Mg, Ca, Sr and Ba. A comparison of the experimental IRMPD spectra in the 2800–3800 cm^{-1} region for the $[Mg(Pro)_2\text{-}H]^+$, $[Ca(Pro)_2\text{-}H]^+$, $[Sr(Pro)_2\text{-}H]^+$, and $[Ba(Pro)_2\text{-}H]^+$ complexes is displayed in Figure 4.3c.

The IRMPD spectra of the $[Mg(Pro)_2\text{-}H]^+$ complex is similar to the transition metal-bound complexes, containing absorptions corresponding to a free N–H stretch as well as an O–H stretching vibration, along with C–H stretching observed below 3000 cm^{-1}. Interestingly, the complexes where M = Ca, Sr or Ba do not have the O–H stretching band, and only show the free N–H stretching feature corresponding to the zwitterionic form of proline at 3370 cm^{-1}. There are also very strong and broad bands below 3200 cm^{-1}, that are indicative of hydrogen bonded N–H or O–H stretches.

4.3.3. $[M(Pro)_2\text{-}H]^+$ Structures and Comparison of Computed IR Spectra to IRMPD Spectra

Based on calculations, $[M(Pro)_2\text{-}H]^+$ complexes consist of a deprotonated proline and an intact proline, the latter of which could adopt either a canonical or zwitterionic form,

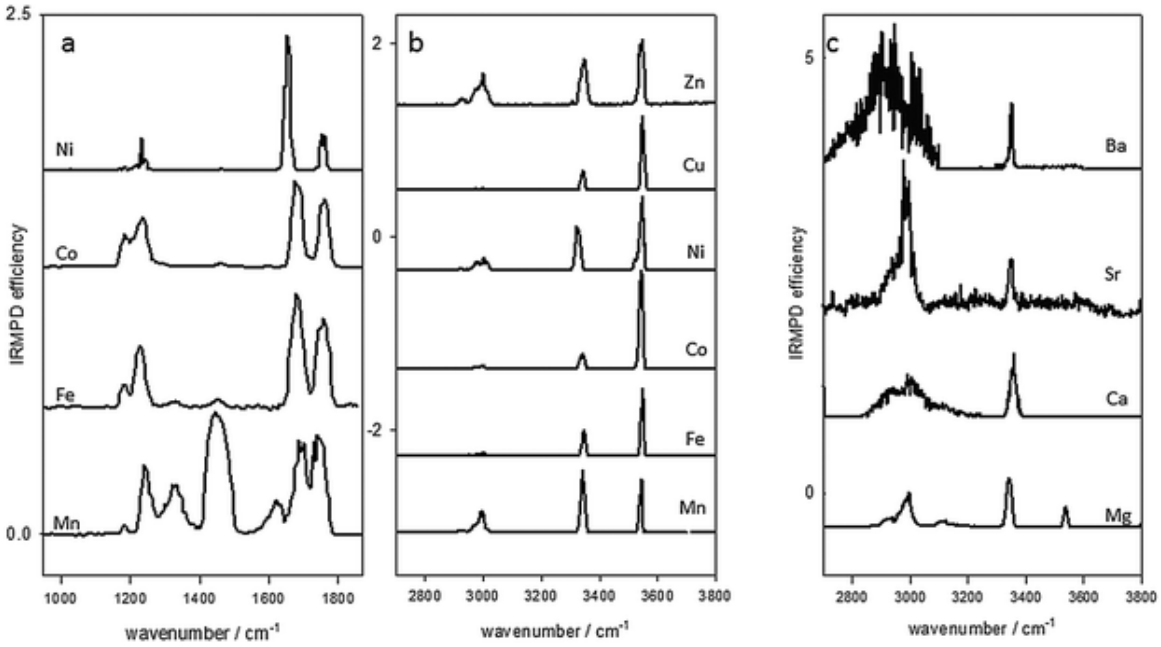

Figure 4.3. Comparison of the experimental IRMPD spectra (a) from 1000 to 1900 cm^{-1} where M = Mn, Fe, CO and Ni, (b) from 2700 to 3800 cm^{-1} where M = Mn, Fe, Co, Ni, Cu, Zn and (c) from 2800 to 3800 cm^{-1} where M = Mg, Ca, Sr and Ba.

both coordinated to the metal cation. The carboxylic acid is the most acidic site in proline and is the site of deprotonation in these $M(Pro_2\text{-}H)^+$ complexes. The $[M(Pro)_2\text{-}H]^+$ complexes can adopt one of four main groupings of structural isomers as depicted in Scheme 4.1. The first label (NO or OO) describes the coordination of the intact proline to the metal cation and the second corresponds to binding of the deprotonated proline. The third label, CS or ZW, corresponds to canonical (charge solvated) or zwitterionic intact proline. First, NO–NO–CS structures are those where the metal cation is coordinated to N and an O atom of the carboxylic acid group of both canonical intact proline and the N and one of the O atoms of the carboxylate group of deprotonated proline. In the NO–OO–CS structures the metal cation is also bound through N and carbonyl-O of the canonical proline

and both oxygens of the carboxylate group of deprotonated proline. In the third general group of structures, OO–OO–ZW, both zwitterionic proline and deprotonated proline are bound through the carboxylate oxygens. Finally, in OO–NO–ZW structures a zwitterionic proline is bound through both carboxylate oxygens and deprotonated proline is bound through one carboxylate O and N. As in a previous work on the protonated and sodiated dimers of proline,[20] the same expressions for the ring puckering type as outlined by Marino *et al.*[35] are used, E for endo, and X for exo puckering. The first label in the name corresponds to intact proline, and the second corresponds to deprotonated proline.

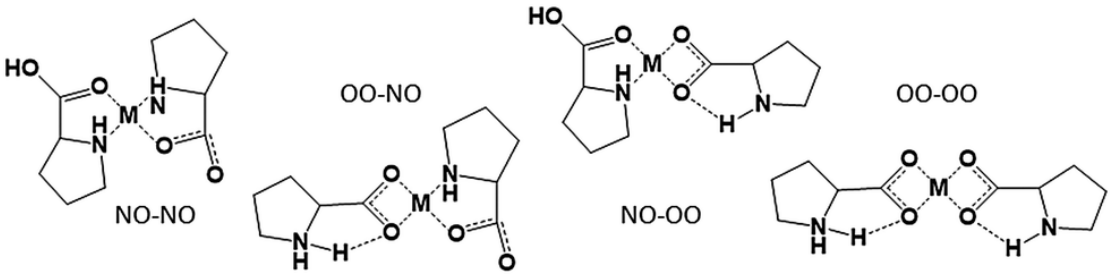

Scheme 4.1. The four main $[M(Pro)_2\text{-}H]^+$ structures.

4.3.3.1. M = Mn, Fe, Co, Ni, Cu and Zn. Cu^{2+} and Zn^{2+} each have one spin state, doublet and singlet, respectively. Cu^{2+} complexes are all four coordinate while Zn^{2+} structures all have tetrahedral coordination. Mn can potentially have a doublet, quartet, or sextet spin state, but the high spin sextet complexes are significantly lower in energy (Table A2.1). The lowest energy sextet complexes are tetrahedral whereas the doublets and quartet all optimized to be square planar. Similarly, for Fe, the high spin quintet complexes are the

lowest in energy (Table A2.2) and are all tetrahedral. In contrast, the lowest energy Co and Ni complexes are the low spin doublets and singlets, respectively (Tables A2.3 and A2.4), and form square planar complexes. For Co, the quartet OO–NO–ZW, NO–OO–CS, and OO–OO–ZW complexes are lower in energy than the doublet. For Ni, the triplet OO–NO–ZW structures are lower in energy than the singlet. All of the high spin Co and Ni complexes were computed to be tetrahedral and the low spin complexes were square planar. There is not as much difference in energy between the higher spin and lower spin states for the Co NO–NO–CS complexes as there is for the Ni, Mn, and Fe complexes, but the difference is enough (~10 kJ mol^{-1}) that only the lowest energy NO–NO–CS spin states, in fact the lowest energy spin states for each of the four general structural isomer groups, will be discussed further.

The lowest energy structures for all of the $[M(Pro)_2\text{-}H]^+$ complexes are NO–NO–CS and there is little difference in the energies of the different ring puckering conformers. As can be seen from Figure A2.10, for $[Cu(Pro)_2\text{-}H]^+$ and $[Ni(Pro)_2\text{-}H]^+$, the computed spectra for all four of the ring puckering conformers of the NO–NO–CS complexes are virtually identical and infrared spectroscopy could not be used to distinguish between them in either the N–H/O–H stretching or the fingerprint regions. In the discussions below we only compare the computed IR spectrum of the lowest energy conformer for each of the four structural isomer groups.

In Figure 4.4 the experimental spectra for both the $[Zn(Pro)_2\text{-}H]^+$ and $[Cu(Pro)_2\text{-}H]^+$ complexes in the 2700–3800 cm^{-1} range are compared to the computed IR spectra for the lowest energy structures of each of the four structural isomer groups. The positions of

the experimental O–H, N–H, and C–H stretching vibrations are well- and best-reproduced by the computed spectra for the lowest energy NO–NO–CS structures. Also, in Figure 4.5, Figure A2.17, and A2.18, the experimental spectra in both the fingerprint and 2700–3800 cm^{-1} regions are compared to computed IR spectra for $[Co(Pro)_2\text{-}H]^+$, $[Fe(Pro)_2\text{-}H]^+$, and $[Ni(Pro)_2\text{-}H]^+$, respectively. Once again, and in both regions of the infrared, the lowest energy NO–NO–CS structures best reproduced the experimental IRMPD spectrum.

As mentioned above, the experimental spectrum for $[Mn(Pro)_2\text{-}H]^+$ is more complex than the other transition metal complexes having intense bands at about 1330 and 1450 cm^{-1} and a strong shoulder at about 1620 cm^{-1}. In Figure 4.6, the experimental IRMPD spectrum is compared with the computed spectra for the lowest energy structure from each of the structural isomer groups. It is clear that the lowest energy NO–NO–CS structure does not account for the 1620, 1450, or 1330 cm^{-1} bands observed in the experimental spectrum. The NO–NO–CS structure also does not account for the observation that the N–H stretch is stronger than the O–H stretching band which is not observed for any of the other transition metal cation complexes. Calculations were done on each of the isomers shown in Figure 4.6, where two water molecules were added to the complex. The lowest energy structures found for each are shown in Figure A2.19 but most importantly, the energy of the solvated OO–OO–ZW structure is the lowest in energy, 13 kJ mol^{-1} lower than the NO–NO–CS structure. The grey spectrum underlying the experimental IRMPD spectrum in Figure 4.6 is a simple sum of the computed IR spectra for the NO–NO–CS and OO–OO–ZW structures and better reproduces the experimental spectrum than either of the two individual computed spectra. Admittedly, the hydrogen bonded N–H stretch region is not well reproduced by the OO–OO–ZW complex, but this

is expected for harmonic calculations. For comparison, the same solvation calculations were done on $[Cu(Pro)_2\text{-}H]^+$ (Figure A2.20) and while the energies of the zwitterionic structures did decrease slightly with respect to NO–NO–CS for the solvated complexes, they were still found to be significantly higher in energy, by 13 and 56 kJ mol^{-1}. The observation of both the charge solvated and zwitterionic structures for $[Mn(Pro)_2\text{-}H]^+$ can be attributed the zwitterionic structure being more stable when microsolvated. During the last stages of desolvation, the energy barrier for the zwitterionic to charge solvated structure is too high to surmount and the lowest energy, microsolvated zwitterionic $[Mn(Pro)_2\text{-}H]^+$ complex survives in the gas phase. It has been shown in the past that the last stages of desolvation during electrospray, as well as the amount of energy imparted during desolvation can influence the structure of the gas phase ions observed.[36]

4.3.3.2. M = Mg, Ca, Sr and Ba. All computed structures for the $[M(Pro_2\text{-}H)]^+$ complexes where M = Mg, Ca, Sr, and Ba are available in Figures A2.21–A2.24. All the Mg^{2+} complexes are tetrahedral about Mg^{2+}. The Ca^{2+} complexes are all tetrahedral except for the NO–OO–CS complexes which have a very distorted geometry for four coordinate species.

All four interactions of the Ca^{2+} with the prolines occur on one hemisphere allowing for an apparent weak interaction between H on C5 of the intact proline and N of the deprotonated proline (2.5 Å). Similar geometries for the Sr^{2+} and Ba^{2+} NO–OO–CS complexes were computed. The OO–OO–ZW structures for Sr^{2+} and Ba^{2+} take on an elongated tetrahedral shape.

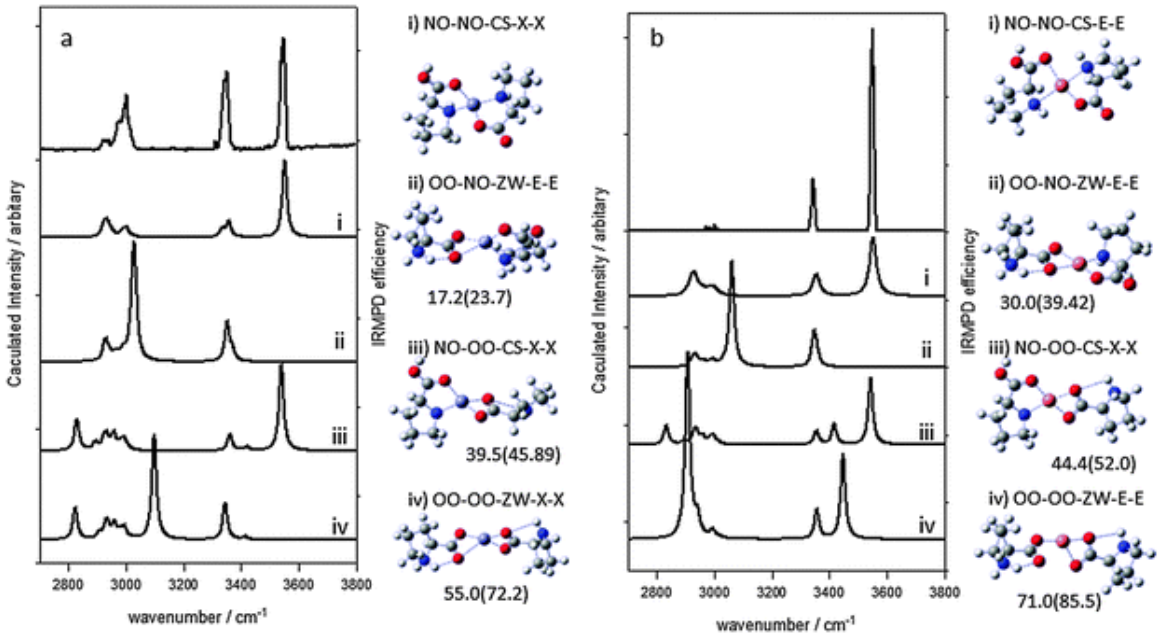

Figure 4.4. Comparison of the experimental IRMPD spectrum and calculated IR spectra of the lowest energy structures of each form of the (a) $[Zn(Pro)_2\text{-}H]^+$ and (b) $[Cu(Pro)_2\text{-}H]^+$ complexes in the 2700 to 3800 cm^{-1} region. Energies are B3LYPD3/6-311+G(3df,3pd)//B3LYPD3/6-31+G(d,p) 298 K Gibbs energies (and enthalpies) and in kJ mol^{-1} and are relative to the lowest energy structure shown as (i).

The OO–NO–ZW and NO–NO–ZW for both Sr^{2+} and Ba^{2+} and the NO–OO–CS for Ba^{2+} have a square pyramidal or distorted square pyramidal geometry with the metal cation at the apex, allowing the two prolines to interact with one another. Only for $[Mg(Pro_2\text{-}H)]^+$ is the NO–NO–CS structure the lowest in energy, as was the case for the transition metal complexes. The OO–NO–ZW complex is only ~8 kJ mol^{-1} higher in energy. The IRMPD spectrum for $[Mg(Pro_2\text{-}H)]^+$ is shown in Figure 4.7a and contains an O–H stretch, N–H stretch and C–H stretching bands, consistent with the computed spectrum for the NO–NO–CS structure. However, the broad band at about 3100 cm^{-1} and the significantly more intense N–H stretch compared to the O–H stretch is not reproduced.

The second highest energy structure, OO–NO–ZW, does not have an O–H stretch because it is zwitterionic and there is a band predicted to occur at 3100 cm^{-1} due to a hydrogen bonded N–H stretch. Solvation calculations (Figure A2.25), like those done for the Mn^{2+} and Cu^{2+} complexes, reveal that the zwitterionic structures are significantly stabilized with respect to the charge solvated structures. In fact, the addition of solvent decreases the energy of the OO–NO–ZW structure such that it is lower in energy by some 30 kJ mol^{-1}. As it was concluded for the Mn^{2+} complex, it is suggested that some of the solvent phase structure (OO–NO–ZW) survives the electrospray process and persists in the gas phase.

For $[Ca(Pro_2\text{-}H)]^+$, the lowest energy structure is the OO–OO–ZW structure. The IRMPD spectrum (Figure 4.7b) is consistent with that predicted for the OO–OO–ZW structure. The NO–OO–CS complex cannot be ruled out spectroscopically, but the absence of an O–H stretch in the IRMPD spectrum does rule out the charge-solvated structures. The intense broad band observed between 2800 and 3200 cm^{-1} is consistent with hydrogen bonded N–H stretching. The computed hydrogen bonded N–H and O–H stretching bands generally agree with the strong red shifting from the non-hydrogen bonded N–H and O–H stretches that is observed in the experimental spectra, but due to the harmonic nature of the calculations, they do not reproduce the broadness of the observed bands. For $[Sr(Pro_2\text{-}H)]^+$ and $[Ba(Pro_2\text{-}H)]^+$, the lowest energy structures are found to be OO–NO–ZW. The computed IR spectra for the zwitterionic complexes are consistent with the IRMPD spectra for both (Figures 4.7c and d). As was the case for $[Ca(Pro_2\text{-}H)]^+$ the charge solvated structures are not observed due to the absence of O–H stretching features in the IRMPD spectra.

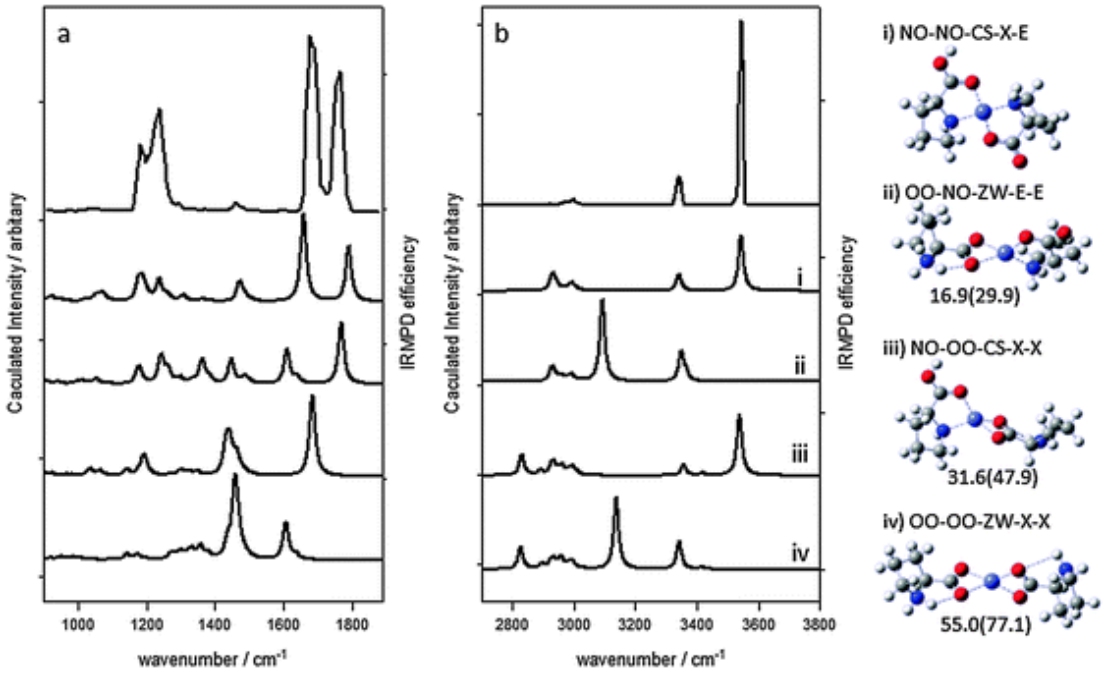

Figure 4.5. Comparison of the experimental IRMPD spectrum and calculated IR spectra of the lowest energy structures of each form of the $[Co(Pro)_2\text{-}H]^+$ in (a) 1000 to 2000 cm^{-1} region and (b) 2800 to 3800 cm^{-1} region. Energies are B3LYPD3/6-311+G(3df,3pd)//B3LYPD3/6-31+G(d,p) 298 K Gibbs energies (and enthalpies) and in kJ mol^{-1} and are relative to the lowest energy structure shown as (i).

The strong and broad features in the 3000 cm^{-1} region are consistent with N–H (or O–H) stretching vibrations that are strongly hydrogen bonded.[37,38] The behaviour, larger cations favouring the zwitterionic amino acid, have been observed before, for example in alkali metal cation complexes of histidine and threonine.[8,39]

4.3.3.3. 6-31+G(d,p) *vs.* cc-pVTZ Basis Set. In Figures A2.27–A2.29, Figure 4.5, 4.6, and 4.7a are reproduced only with the IRMPD spectra compared to spectra calculated using the cc-pVTZ basis. These two basis sets produce almost identical results for the four isomers

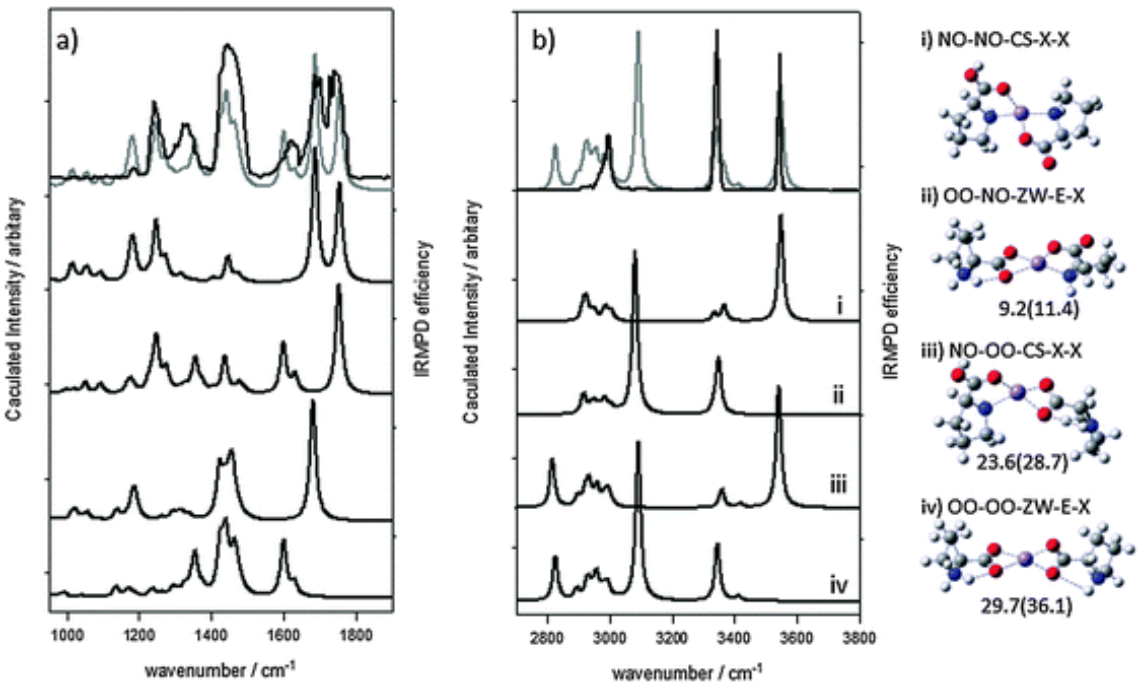

Figure 4.6. Comparison of the experimental IRMPD spectrum and calculated IR spectra for the lowest energy structures of each form of the $[Mn(Pro)_2\text{-}H]^+$ complex in the (a) 1000 to 2000 cm^{-1} region and (b) 2800 to 3800 cm^{-1} region. Energies are B3LYPD3/6-311+G(3df,3pd)//B3LYPD3/6-31+G(d,p) 298 K Gibbs energies (and enthalpies) and in kJ mol^{-1} and are relative to the lowest energy structure shown as (i). They grey line overlaying the experimental spectrum is a sum of complex (i) and (iv).

of the $M(Pro_2\text{-}H)^+$ (M = Co, Mn, Mg) complexes. Similarly, the relative energies are compared in Tables A2.15–A2.17. A comparison reveals no major differences in the computational methods used in this work for these complexes.

4.3.4. Metal-to-Proline Bonding: AIM Analysis

In Tables A2.5–A2.14 are a summary of the AIM analyses done for the complexes studied in this work. For all of the complexes, the Laplacian of the charge density ($\nabla^2\rho$) is positive for all the metal to proline (O or N) interactions. The positive value of $\nabla^2\rho$ means

a depletion of the charge density at the critical point suggesting closed shell or electrostatic interactions.

As discussed above, $[Mg(Pro_2\text{-}H)]^+$ behaves very much like the transition metals in both the CID and IRMPD spectroscopy experiments. Indeed, these experimental findings are also consistent with electrostatic metal cation-to-ligand interactions. The complexes of the larger and less-densely charged metal cations (Ca^{2+}, Sr^{2+}, and Ba^{2+}) exist as zwitterions and predominantly loose proline following collisional or IRMP activation. On the other hand, the smaller, and more densely charged transition metal and Mg^{2+} cations are more strongly bound to their ligands which are shown to fragment and the intact proline is predominantly in the charge solvated form in the complex. These findings are consistent with the results of the alkaline earth metal dication/tryptophan[40] and phenylalanine[41] complexes where the larger metal cations were found to favour the zwitterionic structure. Similarly, alkali metal cationized complexes of arginine,[42,43] serine,[18] and methionine[44] show a tendency toward zwitterionic structures as the metal cation increases in size. In contrast, the zwitterionic structures of aliphatic amino acids (including proline) were found to be stabilized by the smaller alkali metal cations.[45] This latter trend was convincingly explained using the principle of hard and soft Lewis acids and bases; the smaller, harder metal cations prefer to bind to the harder carboxylate base while the larger, softer metal cations prefer to bind to the softer carbonyl. The question, then, is how to explain the opposite trend in the present experiments where the zwitterionic proline structure is observed for the larger cations, Ca^{2+}, Sr^{2+}, and Ba^{2+} and the charge solvated structure is observed for the smaller cations.

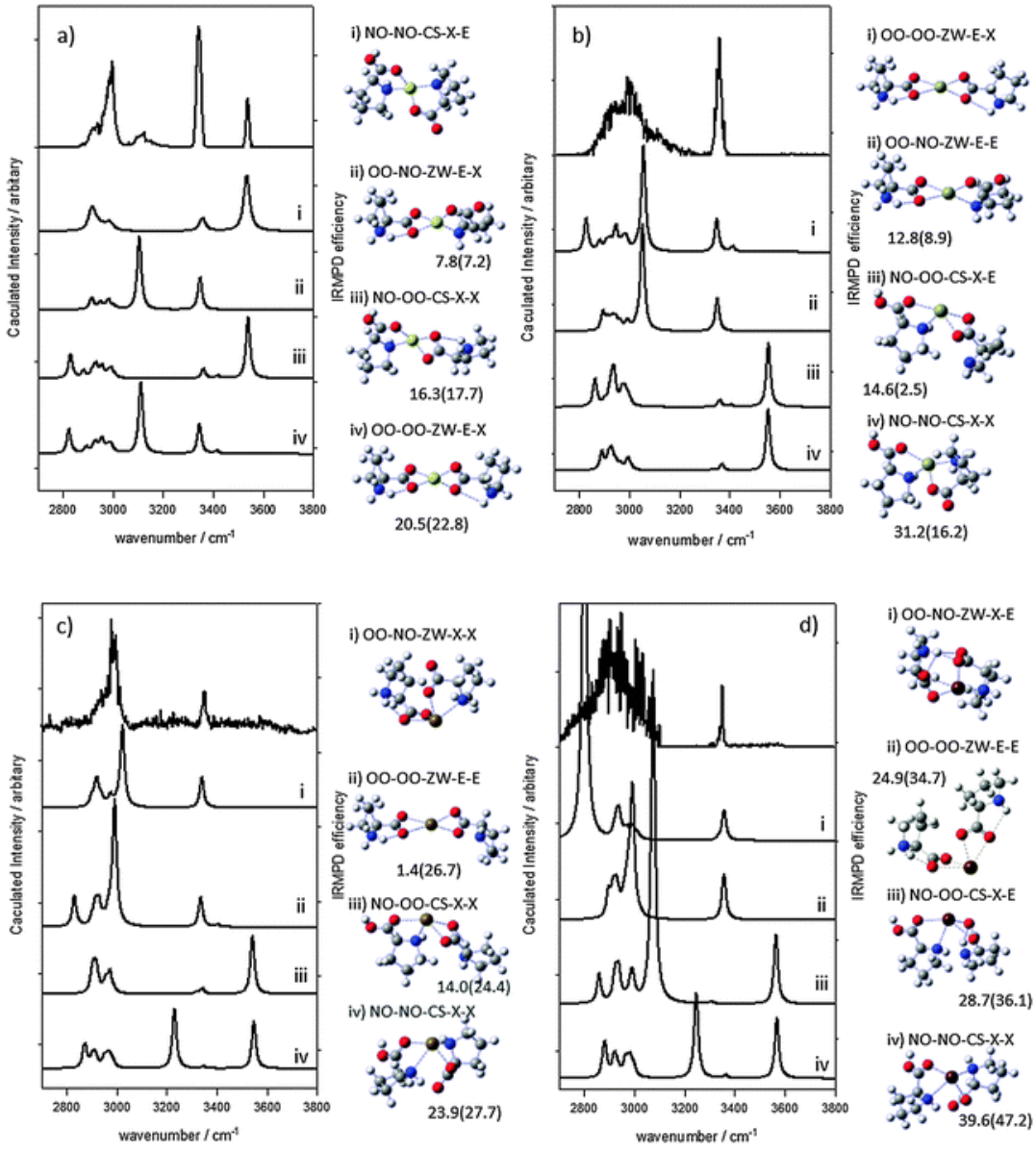

Figure 4.7. Comparison of the experimental IRMPD spectrum and calculated IR spectra for the lowest energy structures of each form of the (a) $[Mg(Pro)_2\text{-}H]^+$, (b) $[Ca(Pro)_2\text{-}H]^+$, (c) $[Sr(Pro)_2\text{-}H]^+$ and (a) $[Ba(Pro)_2\text{-}H]^+$ complexes in the 2700 to 3800 cm^{-1} region. Energies are B3LYPD3/6-311+G(3df,3pd)//B3LYPD3/6-31+G(d,p) 298 K Gibbs energies (and enthalpies) and in kJ mol^{-1}expect for Sr and Ba where the Def2TZVP basis sets were used and are relative to the lowest energy structure shown as (i).

The principles of hard and soft Lewis acids and bases were developed based on observations of chemical bonding in the condensed phase and included solvent contributions.[46] The results of the AIM analysis shows that the interaction between the metal cation and the ligands are all electrostatic in nature. Since the $M(Pro\text{-}H)^+$–Pro interactions are electrostatic, either ionic or ion–dipole interactions, the smaller more densely charged cations would favour an ion–dipole interaction between $M(Pro\text{-}H)^+$ and neutral proline which occurs in the charge-solvated complexes. Indeed, the $M(Pro\text{-}H)^+$ moiety is bound to canonical proline along its dipole. For the larger more polarizable cations, the ion–dipole complex is not as strong. So, to maximize bonding interactions and overall stablilization of the complex, the $M(Pro\text{-}H)^+$ cation interacts with the negative end of the zwitterionic neutral proline.

4.4. Conclusions

The unimolecular chemistries and structures of ten gas phase $[M(Pro_2)\text{-}H]^+$ complexes have been explored using a combination of SORI-CID, IRMPD spectroscopy, and computational methods. It was shown that the complexes containing the larger metal cations, Ca^{2+}, Sr^{2+}, and Ba^{2+} predominantly lose neutral proline. Furthermore, their structures are shown to have a zwitterionic neutral proline moiety. On the contrary, the complexes of Mg^{2+} and the transition metal dications tend to fragment losing small neutral molecules such as water and carbon dioxide. Furthermore, the neutral proline molecule in these complexes involving the smaller metal cations is canonical (or charge-solvated). The charge-solvation structures for the complexes involving the smaller cations are rationalized based upon the formation of strong ion–dipole complexes for these species.

The larger cations do not make as strong an ion dipole complex. To maximize bonding they form strong "ionic" interactions between $M(Pro\text{-}H)^+$ and the negative end of the zwitterionic structure.

As a final comment, it was also shown, that upon collisional or IRMPD activation, all complexes involving transition metal dications *except* the one with the Cu^{2+} lose H_2 upon collisional or IRMPD activation. This was first observed for $[Zn(Pro_2)\text{-}H]^+$,[22] and a mechanism was proposed involving H transfer from C5 to Zn, followed by eventual elimination of H_2 from Zn and N, and that H_2 originates from the intact (not deprotonated) proline. The surprising observation that the Zn^{2+} complex is not alone in its ability to undergo H_2 elimination but rather the Cu^{2+} complex is alone (among the transition metals studied) in its inability to produce H_2. It is important to speculate as to why this might be. Neither IRMPD spectroscopy, nor the calculations reveal any unique structure for the Cu complex, so the difference in reactivity is not due to a difference in the lowest energy structure. However, one unique property of copper, compared to the other transition metals explored in this study is its positive standard reduction potential (see Figure A2.26), meaning that compared to the other transition metals, copper prefers to keep its electrons. A comparable property in the gas phase is the ionization energy; copper has the highest second ionization energy of all the transition metals. It is reasonable to assume that at some point during H_2 elimination electron density is required by proline, and Cu^{2+}, with a very high affinity for its electrons, does not readily accommodate the need for electron density to allow for H_2 elimination.

4.5 Acknowledgements

The authors wish to express their gratitude for funding from the National Sciences and Engineering Research Council of Canada supporting this research. The authors also acknowledge funding from the Canada Foundation for Innovation for infrastructure (Laboratory for the Study of Gaseous Ion Energetics, Structures, and Reactions) and Memorial University for graduate research funding. The authors wish to thank the CLIO team (J. M. Ortega, C. Six, G. Perilhous, J. P. Berthet) as well as P. Maître and V. Steinmetz for providing their experimental facilities for this research. B. Power and B. Linford are acknowledged for their assistance in collecting some of the data. Finally, Westgrid and ACENET and their staff are acknowledged for providing the computational resources used for this work.

4.6. References

1. Duguid, J.; Bloomfield, V.; Benevides, J.; Thomas, G. J.; *Biophys. J.* **1993**, *65*, 1916–1928.
2. Rani, P. N. V. V. L. P.; Chandra, J. S.; Parvathi, V.; Sunandamma, Y. *Int. J. Mod. Eng. Res*. **2013**, *3*, 3615–3620.
3. Waheed, E. J. *Journal of Al-Nahrain University*. **2012**, *15*, 1–10.
4. Rulíšek, L.; Havlas, Z. *J. Am. Chem. Soc.* **2000**, *122*, 10428–10439.
5. Yang, G.; Zhu, R.; Zhou, L.; Liu, C. *J. Mass Spectrom.* **2012**, *47*, 1372–1383.
6. Ziegler, B. E.; Marta, R. A. Burt, M. B.; McMahon, T. B. *Inorg. Chem.* **2014**, *53*, 2349–2351.
7. Aguilar-Galindo, F.; Montero-Campillo, M. M.; Yáñez, M. Mó, O. *Chem. Phys. Lett.* **2014**, *598*, 91–95.
8. Citir, M.; Hinton, C. S.; Oomens, J.; Steill, J. D.; Armentrout, P. B. *J. Phys. Chem. A.* **2012**, *116*, 1532–1541.

9. Corral, I.; Lamsabhi, A. M; Mó, O.; Yáñez, M. *Int. J. Quantum Chem.* **2012**, *112*, 2126–2134.
10. Drayss, M. K.; Blunk, D.; Oomens, J.; Scha, M. *J. Phys. Chem. A.* **2008**, 11972–11974.
11. Yang, B.; Wu, R. R.; Polfer, N. C.; Berden, G.; Oomens, J.; Rodgers, M. T. *J. Am. Soc. Mass Spectrom.* **2013**, *24*, 1523–1533.
12. T. D. Fridgen. *Mass Spectrom. Rev.* **2009**, *28*, 586–607.
13. Polfer, N. C.; Oomens, J. *Mass Spectrom. Rev.* **2009**, *28*, 468–494.
14. Eyler, J. R. *Mass Spectrom. Rev.* **2009**, *28*, 448–467.
15. Bush, M. F.; Forbes, M. W.; Jockusch, R. A.; Oomens, J.; Polfer, N. C.; Saykally, R. J.; Williams, E. R. *J. Phys. Chem. A.* **2007**, *111*, 7753–7760.
16. Schmidt, J.; Kass, S. R. *J. Phys. Chem. A.* **2013**, *117*, 4863–4869.
17. Atkins, C. G.; Rajabi, K.; Gillis, E. A. L.; Fridgen, T. D. *J. Phys. Chem. A.* **2008**, *112*, 10220–10225.
18. Armentrout, P. B.; Rodgers, M. T.; Oomens J.; Steill, J. *J. Phys. Chem. A.* **2008**, *112*, 2248–2257.
19. Bush, M. F.; Oomens, J.; Saykally, R. J.; Williams, E. R. *J. Am. Chem. Soc.* 2008, **130**, 6463–6471.
20. Jami-Alahmadi, Y.; Gholami, A. Fridgen, T. D. *Phys. Chem. Chem. Phys.* **2014**, *16*, 26855–26863.
21. Pappenberger, G.; Aygun, H.; Engels, J. W.; Reimer, U.; Fischer, G.; Kiefhaber, T. *Nat. Struct. Mol. Biol.* **2001**, *8*, 452–458.
22. Gholami, A.; Fridgen, T. D. *Phys. Chem. Chem. Phys.* **2014**, *16*, 3134–3143.
23. Umhau, S.; Pollegioni, L.; Molla, G.; Diederichs, K.; Welte, W.; Pilone, M. S.; Ghisla, S. *Dehydrogenation*. **2000**, *97*, 0–5.
24. Bruice, P. Y. *Amino Acid Metabolism*, 7th edn, **1961**.
25. Glatzel, P.; Bergmann, U. *Coord. Chem. Rev.* **2005**, *249*, 65–95.
26. Dunbar, R. C.; Steill, J. D.; Polfer, N. C.; Oomens, J. *J. Phys. Chem. A*, **2009**, *113*, 845–851.
27. Turecek, F.; Jones, J. W.; Holm, A. I. S.; Panja, S.; Nielsen, S. B.; Hvelplund, P. *J. Mass Spectrom.* **2009**, *44*, 707–724.
28. Khodabandeh, M. H.; Davari, M. D.; Zahedi, M.; Ohanessian, G. *Int. J. Mass Spectrom.*, **2010**, *291*, 73–83.
29. Rimola, A.; Rodrı, L.; Sodupe, M. *J. Phys. Chem. B*, **2006**, *9*, 24189–24199.
30. Prazeres, R.; Glotin, F.; Insa, C.; Jaroszynski D. A.; Ortega, J. M. *Eur. Phys. J. D*, **1998**, *3*, 87–93.
31. Frisch, M. J.; Frisch, M. J.; Trucks, G. W.; Schlegel, H. B.; Scuseria, G. E.; Robb, M. A.; Cheeseman, J. R.; Scalmani, G.; Barone, V.; Mennucci, B.; Petersson, G. A.; Nakatsuji, H.; Caricato, M.; Li, X.; Hratchian, H. P.; Izmaylov, A. F.; Bloino, J.;

Zheng, G.; Sonnenberg, J. L.; Hada, M.; Ehara, M.; Toyota, K.; Fukuda, R.; Hasegawa, J.; Ishida, M.; Nakajima, T.; Honda, Y.; Kitao, O.; Nakai, H.; Vreven, T.; Montgomery, J. A. Jr.; Peralta, J. E.; Ogliaro, F.; Bearpark, M.; Heyd, J. J.; Brothers, E.; Kudin, K. N.; Staroverov, V. N.; Kobayashi, R.; Normand, J.; Raghavachari, K.; Rendell, A.; Burant, J. C.; Iyengar, S. S.; Tomasi, J.; Cossi, M.; Rega, N.; Millam, J. M.; Klene, M.; Knox, J. E.; Cross, J. B.; Bakken, V.; Adamo, C.; Jaramillo, J.; Gomperts, R.; Stratmann, R. E.; Yazyev, O.; Austin, A. J.; Cammi, R.; Pomelli, C.; Ochterski, J. W.; Martin, R. L.; Morokuma, K.; Zakrzewski, V. G.; Voth, G. A.; Salvador, P.; Dannenberg, J. J.; Dapprich, S.; Daniels, A. D.; Farkas, O.; Foresman, J. B.; Ortiz, J. V.; Cioslowski, J.; Fox, D. J. Gaussian 09, Revision A.01; Gaussian, Inc.: Wallingford, CT, 2009.

32. Grimme, S.; Antony, J.; Ehrlich, S.; Krieg, H. *J. Chem. Phys.* **2010**, *132*, 154104.
33. Bader, R. F. W. Atoms in Molecules: A Quantum Theory, Clarendon Press, Oxford Univ. Press, Oxford, New York, 1990.
34. AIMAll (Version 14.10.27), Todd A. Keith, TK Gristmill Software. Overl. Park KS, USA, 2014, 10708–10711.
35. Marino, T.; Russo, N.; Tocci, E.; Toscano, M. *J. Mass Spectrom.* **2001**, *36*, 301–305.
36. Rogalewicz, F.; Hoppilliard, Y.; Ohanessian, G. *Int. J. Mass Spectro.* **2003**, *227*, 439–451.
37. Gillis, E. A. L.; Rajabi, K.; Fridgen, T. D. *J. Phys. Chem. A*, **2009**, *113*, 824–832.
38. Burt, M. B.; Fridgen, T. D. *J. Phys. Chem. A*, **2013**, *117*, 1283–1290.
39. Rodgers, M. T.; Armentrout, P. B.; Oomens, J.; Steill, J. D. *J. Phys. Chem. A.* **2008**, *112*, 2258–2267.
40. Mino, W. K.; Szczepanski, J.; Pearson, W. L.; Powell, D. H.; Dunbar, R. C,; Eyler, J. R.; Polfer,N. C. *Int. J. Mass Spectrom.* **2010**, *297*, 131–138.
41. Dunbar, R. C.; Steill, J. D.; Oomens, J. *Phys. Chem. Chem. Phys.* **2010**, *12*, 13383–13393.
42. Bush, M. F.; O'Brien, J. T.; Prell, J. S.; Saykally, R. J.; Williams, E. R. *J. Am. Chem. Soc.* **2007**, *129*, 1612–1622.
43. Forbes, M. W.; Bush, M. F.; Polfer, N. C.; Oomens, J.; Dunbar, R. C.; Williams, E. R.; Jockusch, R. A. *J. Phys. Chem. A.* **2007**, *111*, 11759–11770.
44. Carl, D. R.; Cooper, T. E.; Oomens, J.; Steill, D.; Armentrout, P. B. *Phys. Chem. Chem. Phys.* **2010**, *12*, 3384–3398.
45. Drayß, M. K.; Armentrout, P. B.; Oomens, J.; Schäfer, M. *Int. J. Mass Spectrom.* **2010**, *297*, 18–27.
46. Pearson, R. G. *J. Am. Chem. Soc.* **1963**, *85*, 3533–3539.

Chapter 5

Distinguishing Isomeric Peptides: The Unimolecular Reactivity and Structures of $(LeuPro)M^+$ and $(ProLeu)M^+$ (M = Alkali Metal)

This chapter is reproduced with permission from

Jami-Alahmadi, Y.; Linford, B. D.; Fridgen, T. D.

"Distinguishing Isomeric Peptides: The Unimolecular Reactivity and Structures of $(LeuPro)M^+$ and $(ProLeu)M^+$ (M = Alkali Metal)"

J. Phys. Chem. B., **2016**, *120*, 13039-13046.

5.1. Introduction

While covalent bonding is regarded as the strongest interaction between atoms, the prevalence of noncovalent interactions in molecular associations makes their study of utmost importance.[1] In this regard, electrospray ionization tandem mass spectrometry techniques are powerful for characterizing noncovalent interactions such as intramolecular hydrogen bonding and metal cation−dipole interactions; these are paramount to the functionality of biomolecular species such as DNA, RNA, and proteins.[2−4] Different experimental and theoretical methods have been used in order to determine the binding sites of alkali metal cations to molecules such as amino acids or peptides.[5−9] Besides metal-ion binding strength and metal-ion size,[10−12] the amino acid sequence in peptides has an influential role in defining the structures, binding sites, and binding energies of metals.[13,14]

Leucine is one of the amino acids that factors in the development of Parkinson's disease (PD), a neurodegenerative disorder.[15,16] Mutations of an encoded gene called leucine-rich repeat kinase 2, or LRRK2, result in an abnormal assemblage of proteins in the brain which causes the progression of PD.[17−21] There is also considerable interest in studying proline which is an amino acid with a secondary amine containing a five membered ring. Proline induces in the first turn of α-helical secondary structures in protein folding processes.[22,23] Interestingly, it exhibits unusual properties in molecules containing proline residues. For example, the folding kinetics of a protein containing three prolines were investigated by Che and Clark[24] using fluorescence emission. Proline substitution showed that proline plays a critical role in stabilizing intermediates created during the unfolding stage of wild-type RICK-CARD, a small helical protein associated with many tissues, which consequently changes the kinetics of the refolding mutants. The role of proline containing peptides and proteins also cannot be neglected in defining the protein−protein interaction which results in changing the behavior of some proteins. An example is the SRC homology 3 domain, composed of 50−75 residues in certain proteins, which prefers to interact with proline-rich peptide ligand sequences, hence playing an important role in intermolecular protein−protein interactions in enzyme regulation.[25−27]

Moision and Armentrout[28] measured binding energies of four-, five-, and six-membered ring analogues of proline bound to Li^+, Na^+, and K^+ using a guided ion beam mass spectrometer. Comparisons of theoretical and experimental binding energies show that proline was most likely zwitterionic when bound to alkali metals. Analysis of the results shows that binding in metal−proline complexes is stronger even though the conformational mobility in the six-membered ring, having an additional carbon atom, is

increased related to the five-member proline ring. Other studies on proline−alkali metal complexes reveal the zwitterionic form of this complex as the preferred structure.[29] Interestingly, due to the formation of a strong N− H···O hydrogen bond, which apparently has no effect on the ring side distortion of proline, alkali metals are attached tightly to the proline in its zwitterionic form.[30]

Mass spectrometric techniques have become powerful tools in the field of proteomics by identifying different amino acid sequences of proteins.[31,32] More specifically, MS is also a predominant technique that is used to identify the sequences of specific peptides containing both proline and leucine residues[33,34] and has an important effect in the field of peptide research and all other connected fields in which the identification of protein structures is required. Work on two sequences of dipeptides revealed that the conformations they adopt depend on factors such as the amino acid sequence, the identity of the metal cation, and the anchor site of each dipeptide ligand.[14] The structures of divalent metal cations bound to isomeric peptides, GlyHis or HisGly and PheAla or AlaPhe, were investigated using IRMPD spectroscopy in combination with DFT methods.[14] Depending on binding strength, larger ions such as Ba^{2+} prefer the zwitterionic (ZW) form over the charge solvated (CS, also termed canonical) and iminol forms. In contrast, more strongly binding metals such as Mg^{2+} and Ni^{2+} preferentially adopt the CS and iminol forms, respectively, rather than the ZW. In addition to the metal binding strength, dipeptide sequence is also important in determining the form of the peptide bound to metal ions. For example, it was observed that Ba^{2+} and Ca^{2+} make the ZW form of the GlyHis the predominant form while being bound to the HisGly sequence makes the CS configuration the majority form of these dipeptides. The reason for this sequence depends

on the existence of an N-terminus side chain located in the histidine residue of the HisGly isomer which makes it able to wrap and interact properly with the metal cation and hence favor the charge solvated conformer. The absence of this interaction through the N-terminus side in the histidine residue in GlyHis favors the ZW for this dipeptide, unlike the GlyHis isomer.

Herein, we report on the investigations of the structures of the two isomeric dipeptides, ProLeu and LeuPro, bound to alkali metal ions using SORI-CID (MS/MS) and IRMPD spectroscopy in the gas phase combined with theoretical methods. Spectra in both the 1000−1800 and 2700−3800 cm^{-1} regions were recorded to determine the structures of alkali metal-cationized proline−leucine containing dipeptides.

5.2. Methods

5.2.1. Experimental Section. All experiments were performed using a Bruker Apex-Qe 7T FTICR. Ions were electrosprayed from 1 mL of 50 mmol L^{-1} aqueous solution of either ProLeu or LeuPro to which 5 μL of the 10 mmol L^{-1} aqueous alkali metal salt in a 50/50 mixture of 18 MΩ cm water and methanol were added. Solutions were sprayed at 100 μL h^{-1} using a syringe pump into an Apollo II ESI source in which 1 mL of 50 mmol L^{-1} aqueous solution of dipeptide to which 5 μL of the aqueous alkali metal salts was added. Alkali metal chlorides (LiCl, NaCl, KCl, RbCl, and CsCl) were the source of metal cations used in this study.

Multiple stages of sustained off-resonance irradiation collision induced dissociation (SORI-CID) on the alkali metal complexes with both peptides were done by exciting the

ion of interest in the presence of Ar gas to a pressure of $\sim 10^{-6}$ mbar. Infrared multiphoton dissociation (IRMPD) spectra were recorded from 2700 to 3800 cm^{-1} in the Laboratory for the Study of the Energetics, Structures, and Reactions of Gaseous Ions at Memorial University using an FTICR coupled to an IR OPO manufactured by LaserSpec which is tunable from 1.4 to 4.5 μm with a bandwidth of 2 cm^{-1}. The OPO is built around a periodically poled $LiNbO_3$ crystal which is pumped by a diodepumped solid state Nd:YAG laser. The OPO operates at 20 kHz, with pulse duration of a few nanoseconds, and generates output power near 3 W at 3 μm; however, the power was limited to 1 W in these experiments by limiting the pump laser power. For IRMPD spectra in the fingerprint region, the facility at Centre Laser Infrarouge d'Orsay (CLIO) was used. At CLIO, the FTICR is coupled to a mid-infrared free electron laser (FEL)[35] with a 5 cm^{-1} bandwidth. IRMPD irradiation times were between 1 and 2 s. The experimental IRMPD spectra were obtained by plotting the IRMPD efficiency, the negative logarithm of the precursor intensity divided by the sum of precursor and fragment ion intensities, as a function of the radiation wavenumber.

5.2.2. Computational Methods. Using Gaussian 09,[36] structures were optimized, and IR spectra were computed at the M06-2X/6-31+G(d,p) and B3LYP/6-31+G(d,p) levels of theory on all atoms except for Rb and Cs, for which the Def2SVP basis sets and effective core potentials were used. Unlike the 6-31+G(d,p) basis, the Def2SVP basis set on the cations does not include any diffuse functions. An empirical dispersion correction was done using Grimme's D3 version with the original D3 damping function, B3LYPD3[37] and M06-2XD3.[38] M06-2X methods have shown good results for the thermochemistry of systems

containing noncovalent interactions.[39–41] Previous research on various functionals has shown M06-2XD3[38] to yield better results than without the D3 functional. For calculated spectra, scaling factors of 0.95 in the fingerprint and 0.94 in the C−H/N−H/O−H stretching regions were used to correct the harmonic frequencies (for the M06-2XD3 calculations). The computed IR spectra were convoluted using Gaussian functions with a width of 15 cm^{-1} (fwhm). Electronic energies were refined with single point calculations using M06-2XD3/6-311+G(3df,3pd) for all atoms except Rb and Cs for which the Def2TZVP basis set[42] and effective core potential were used.

5.3. Results and Discussion.

5.3.1. SORI/CID of (LeuPro)M^+ and (ProLeu)M^+ Where M = Li, Na, Rb, and Cs.

Under CID conditions both (LeuPro)M^+ and (ProLeu)M^+, where M = Rb and Cs, lost ProLeu or LeuPro leaving only the metal cation as seen in Figures 5.1 and 5.2. While the intensity of (LeuPro)K^+ and (ProLeu)K^+ decreases dramatically during CID experiments, no fragmentation products were observed, indicating that the sole loss for both is the dipeptide as observed for the Rb and Cs complexes. When M = Li and Na, CID of both isomeric dipeptides resulted in losses of 113 and 97 Da as the main primary fragmentation pathways (Figures 5.1 and 5.2). The masses of the product ions correspond to either (Pro)Li^+ (m/z 122) and (Leu)Li^+ (m/z 138) or (Pro)Na^+ (m/z 138) and (Leu)Na^+ (m/z 154). When M is a smaller ion, as observed in earlier studies on proline[9,43] and uracil[44] dimers, due to the strong densely charged metal cation-to-proline interactions, these complexes fragment, breaking covalent bonds rather than the ion−amino acid interactions. Conversely, the larger Cs^+, Rb^+, and K^+ with less charge density bind less strongly to ProLeu and LeuPro

resulting in their cleavage from the metal cation. (ProLeu)Na^+, (LeuPro)Na^+, and (ProLeu)Li^+ also underwent a small amount of fragmentation to lose 18 Da (H_2O) and a loss of 62 Da (either H_2CO_3 or H_2O followed by CO_2 loss). The only differentiable features in the CID mass spectra for these metal-cationized dipeptide isomers were that (ProLeu)Li^+ lost 18 and 62 Da, whereas these fragmentations were completely absent in the (LeuPro)Li^+ CID spectra. Figures A3.1 and A3.2 show the MS/MS spectra of (ProLeu)Li^+ and (LeuPro)Li^+, respectively, which resulted in loss of water and ammonia from m/z 138 in both isomers. MS/MS on m/z 122 resulted in losses of 52, 46, and 18 Da as the major fragmentation pathways.

5.3.1.1. IRMPD Spectroscopy on the Major Fragment Products of (ProLeu)Li^+ and (LeuPro)Li^+. As shown above, CID of both (ProLeu)Li^+ and (LeuPro)Li^+ generated losses of 113 Da (m/z 122, presumably ProLi^+) and 97 Da (m/z 138, presumably LeuLi^+). The fragment ions were isolated, and IRMPD spectra in the 2700−3800 cm^{-1} region were recorded (Figure 5.3). The m/z 138 ions generated from both (ProLeu)Li^+ and (LeuPro)Li^+ are generally quite similar in that the same features are present in the IRMPD spectra. In both spectra there are strong absorptions due to a carboxylic acid O−H stretch (~3550 cm^{-1}), amine N−H stretching (~3350 cm^{-1}), and C−H stretching (centered ~2910 cm^{-1}). The computed spectrum for the lowest energy structure of (Leu)Li^+ (underlying gray trace in Figure 5.3a) agrees well with the experimental spectrum. The computed spectrum for the lowest energy zwitterionic structure, some 21 kJ mol^{-1} higher in energy, does not agree with the experimental IRMPD spectrum (Figure A3.3).

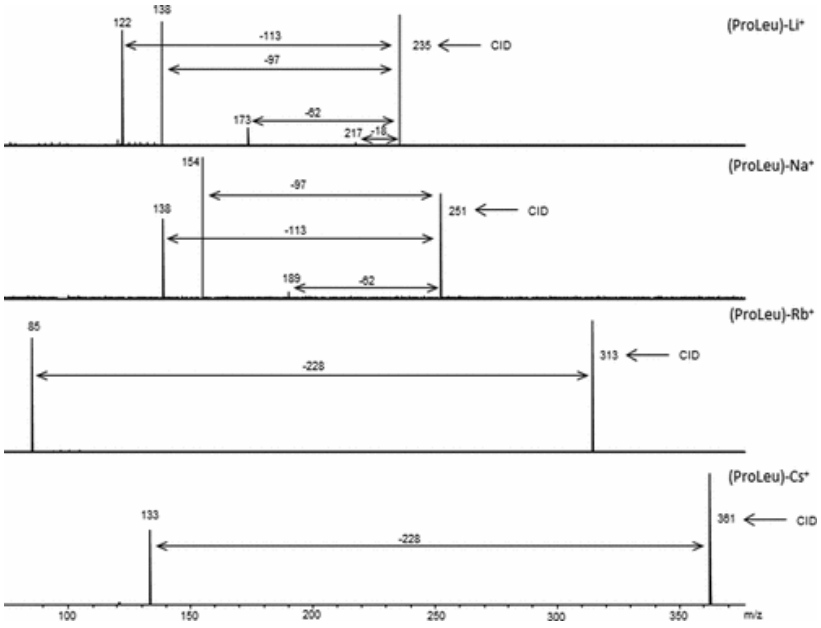

Figure 5.1. SORI/CID spectra obtained for (ProLeu)−M^+ where M = Li, Na, Rb, and Cs.

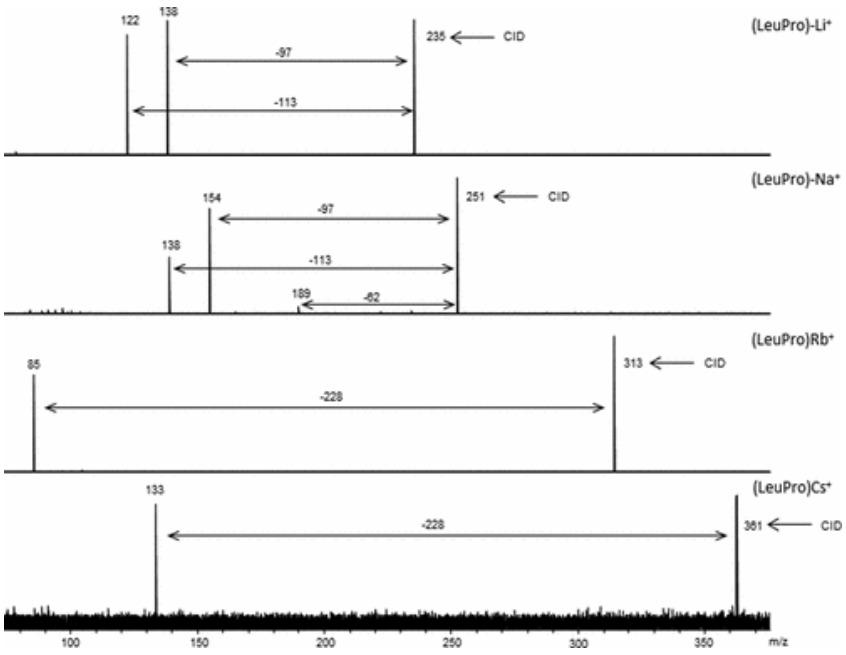

Figure 5.2. SORI/CID spectra obtained for (LeuPro)−M^+ where M = Li, Na, Rb, and Cs

For m/z 122 from both (ProLeu)Li^+ and (LeuPro)Li^+, the IRMPD spectra both generally agree well. There is a lower intensity O−H stretch (~3550 cm^{-1}), a stronger N−H stretching feature (~3330 cm^{-1}), and C−H stretching (centered at about 2990 cm^{-1}). Calculations for the lowest energy canonical and zwitterionic forms of lithiated proline are shown at the bottom of Figure 5.3b. Clearly, the zwitterionic (Pro)Li^+ cannot account for the experimental IRMPD spectrum since there is an O−H stretching feature present. However, this feature is less intense than the experimental N−H stretching feature.

An arithmetic average of the computed spectra for the lowest energy canonical and zwitterionic structures is compared to the experimental IRMPD spectra (underlying gray traces). In general, there is agreement between the experimental spectra and the average computed spectra for both the zwitterionic and canonical structures. Attempts to electrospray (Pro)Li^+ for comparison were not successful; even at the lowest concentrations of proline, only the lithiated proline dimers were present. Previous calculations using B3LYP/6-311++G(d,p) show that the lowest energy zwitterionic structure was very close in energy to the lowest energy canonical structure that we are showing. IRMPD spectroscopy experiments in the fingerprint region showed that there was zwitterionic (Pro)Li^+, but were inconclusive as to whether the canonical form was present.[45,46] On the basis of the infrared spectra in the 2700−3800 cm^{-1} region presented here, (Pro)Li^+ is concluded to be present in both zwitterionic and canonical forms, at least when generated by CID of (ProLeu)Li^+ and (LeuPro)Li^+. Interestingly, both (LeuPro)Li^+ and (ProLeu)Li^+ peptides form (Pro)Li^+ and (Leu)Li^+ when activated.

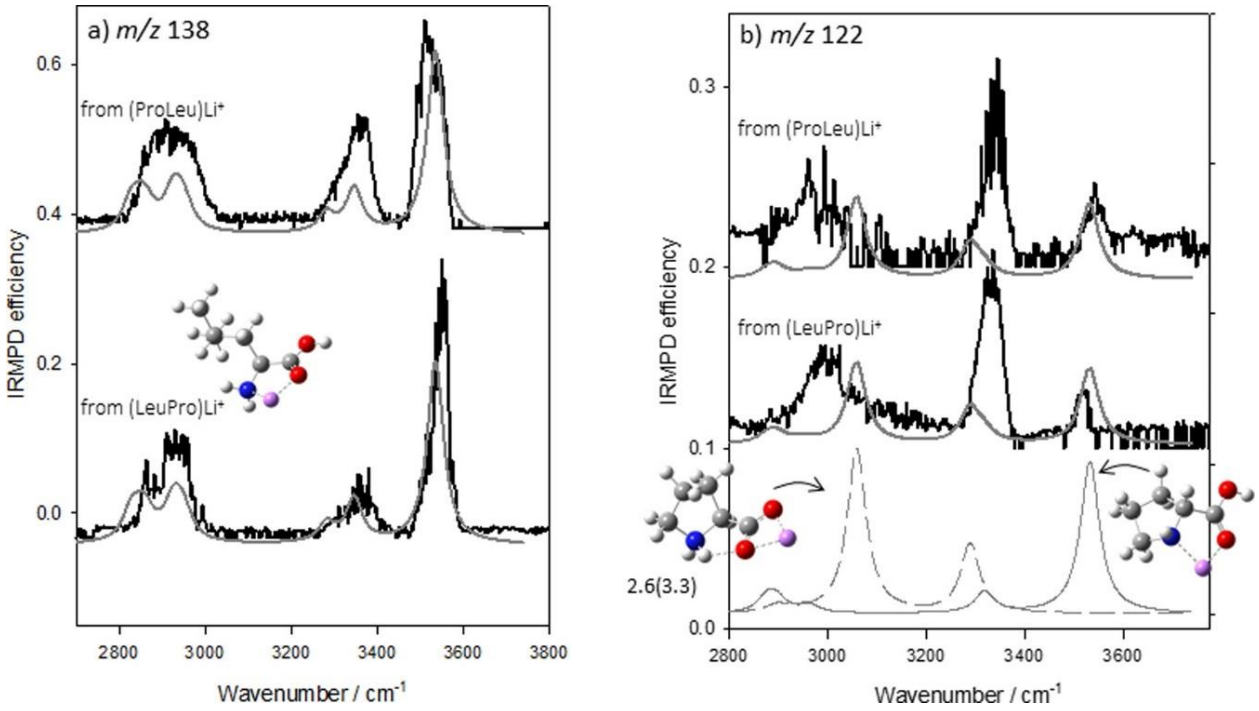

Figure 5.3. Comparison of the experimental IRMPD spectra (black traces) of the (a) m/z 138 and (b) m/z 122 fragment ions generated by CID of (ProLeu)Li^+ and (LeuPro)Li^+ with the calculated spectra of (Pro)Li^+ and (Leu)Li^+. Energies are M06-2XD3/6-311++G(3df, 3pd)//6-31+G(d,p), 298 K Gibbs energies (and enthalpies) and in kJ mol^{-1}.

A proposed mechanism for formation of the lithiated amino acids from both lithiated peptides is presented in Figure A3.4. To form (Pro)Li^+ from (ProLeu)Li^+, and (Leu)Li^+ from (LeuPro)Li^+, cleavage of the amide bond with a transfer of OH from the C-terminus to the N-terminus amino acid of the peptide is required. The formation of (Leu)Li^+ from (ProLeu)Li^+, and (Pro)Li^+ from (LeuPro)Li^+, can be thought of as a simple amide bond cleavage and transfer of an N-terminus proton to the C-terminus amino acid. In the latter cleavages, a double ring system is shown as the neutral product, there is likely a ring opening to form one six-membered ring, but there would also initially be charge separation. The final neutral product identities are unknown.

5.3.2. IRMPD Spectroscopy of Alkali Metal Cation Complexes of ProLeu or LeuPro. IRMPD of $M(ProLeu)^+$ and $M(LeuPro)^+$ produced the same photofragments as observed for SORI-CID.

5.3.2.1. (ProLeu)M^+. Figure 5.4 shows the experimental IRMPD spectra in the 1000−1900 and 2700−3800 cm^{-1} regions for metal-cationized ProLeu. The IRMPD spectra in the 2700− 3800 cm^{-1} region for all alkali metals (Figure 5.4b) have bands at about 3580 cm^{-1} corresponding to the O−H stretch of a free carboxylic acid group which clearly indicates the present structures in which proline is canonical rather than zwitterionic. When the metal cation is Rb or Cs, another intense band is observed centered at 3310 cm^{-1} which corresponds to hydrogen bonded amide N−H stretches.[47] Absorptions below 3000 cm^{-1} are assigned to C−H stretching.

In the fingerprint region, 1000−1900 cm^{-1} (Figure 5.4), each isomer has two strong bands between 1630 and around 1750 cm^{-1} assigned to the C=O stretching of the amide and carboxyl carbonyl groups. It is also interesting to note the pronounced blue shift of the C=O stretching band as the metal changes from Li^+ to Cs^+, indicating binding of the metal cation, at least in part, to the carbonyl. As the metal cation gets larger, its binding to the peptide is weaker which in turn weakens the C=O bond to a lesser extent. The strong band between 1500 and 1600 cm^{-1} corresponds predominantly with the HNC bending of the amide. Weak CH_2/CH_3 bending and CH_2 scissoring modes are observed between 1200 and 1600 cm^{-1}. Finally, there is a set of pronounced features below 1200 cm^{-1} corresponding with COH bending as well as CH_2 rocking.

5.3.2.2. (LeuPro)M$^+$. The IRMPD spectra in the 1000−1900 and 2700−3800 cm^{-1} regions of (LeuPro)M$^+$ where M = Li, Na, Rb, and Cs are depicted in Figure 5.5. Similar to (ProLeu)M$^+$, all four complexes contain a band at around 3580 cm^{-1} corresponding to the O−H stretch of the free carboxylic acid group in the proline residue indicating the canonical form of this peptide. In all the (LeuPro)M$^+$ spectra, the asymmetric NH_2 stretches show only very weak features between 3300 and 3400 cm^{-1}. There are also broad C−H stretching features observed between 2800 and 3000 cm^{-1}. In the fingerprint region each isomer has two bands between 1600 and 1800 cm^{-1}.

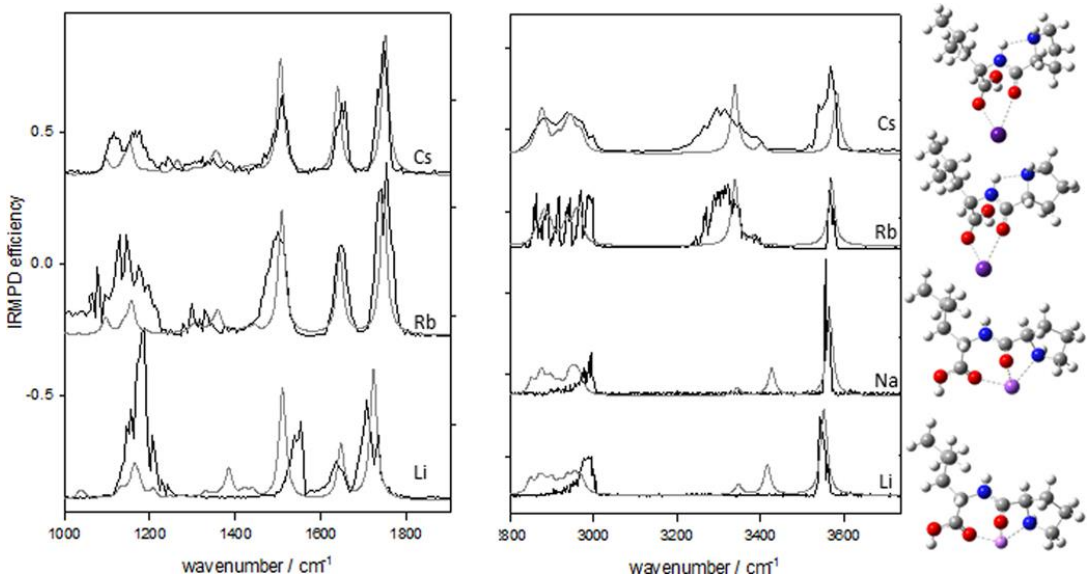

Figure 5.4. Comparison of the experimental (black traces) IRMPD spectra of (ProLeu)M$^+$ with the IR spectra for the lowest energy M06-2XD3/6-31+G(d,p) calculated structures (gray traces).

The higher energy one is the C=O stretching of the carboxylic acid, and the lower energy one is another C=O stretch of the amide. Like the (LeuPro)Li^+ complex, the C=O stretches in all other (LeuPro)M^+ complexes are also mixed with the NH_2 scissoring motions. Also, below 1200 cm^{-1} there are sets of pronounced features corresponding to COH bending and CH_2 rocking of these isomers. The absorptions between 1300 and 1500 cm^{-1} correspond to the combinations of all CH_2/CH_3 bending and CH_2 scissoring stretches as well as NH_2 wagging and twisting. One interesting feature about the IRMPD spectra that will be addressed more fully below is that the carboxylic acid C=O stretch position increases in the following order of metal cation complex: $Rb^+ < Na^+ \approx Cs^+ < Li^+$

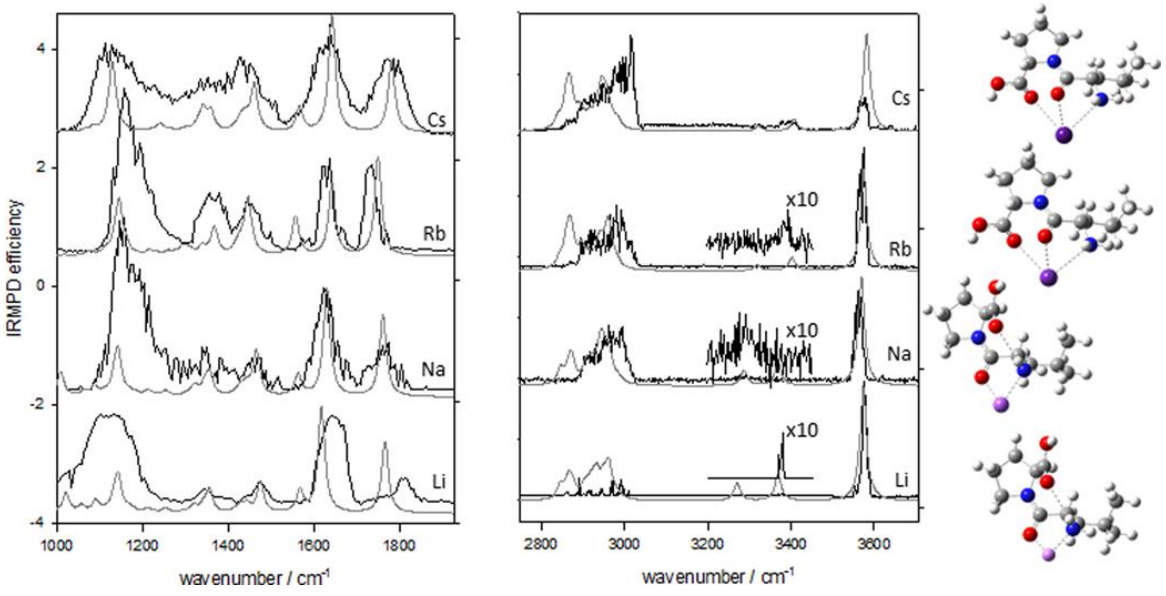

Figure 5.5. Comparison of the experimental (black traces) IRMPD spectra of (LeuPro)M^+ with the IR spectra for the lowest energy M06-2XD3/6-31+G(d,p) calculated structures (gray traces).

5.3.3. Structures, Energetics, and Comparison of Computed IR Spectra to IRMPD Spectra of Proline/Leucine Dipeptides. The gray traces in Figure 5.4 are the IR spectra computed for the lowest energy structures for each of the (ProLeu)M^+ complexes. For the Li^+ and Na^+ complexes, the metal cation is bound to both carbonyl oxygens and the very basic amine nitrogen. The computed spectra for these complexes agree very well with the experimental IRMPD spectra. In Figures A3.5 and A3.6, the computed IR spectra for some higher energy structures, including a zwitterionic structure, are compared to the experimental IRMPD spectrum. The best matches for the IRMPD spectra are the ones for the lowest energy structures.

For Rb^+ and Cs^+, the lowest energy structure is one where both carbonyls are bound to the metal cation, but the amine nitrogen is hydrogen bonded to the amide hydrogen. The IR spectra computed for these structures, including the amide N–H stretch centered about 3300 cm^{-1}, are in very good agreement with the IRMPD spectrum. While the structures where the metal is bound to both carbonyl oxygens and the amine nitrogen do not reproduce the amide N–H stretch, they cannot be ruled out completely on the basis of either spectroscopic or computational terms since they are computed to be virtually isoenergetic (see Figures A3.7 and A3.8). What is clear is that the structures with the larger and less acidic metal cations are stabilized by making an intramolecular hydrogen bond whereas the smaller, very acidic Na^+ and Li^+ prefer to bind directly to the amine N. In AlaGly and GlyAla, Na^+ was found to only bind to the two carbonyl oxygens, and there was an amide H to amine N hydrogen bond.[47] This shows that the identity of the metal cation is not the only factor to decide whether this type of intramolecular interaction occurs. The basicity of

the N-terminus amino acid, in the present case proline, plays a very important role in the structure, as expected.

For LeuPro, the computed IR spectra for the lowest energy structures agree very well with the experimental IRMPD spectra (Figure 5.5). In all complexes, the amide N has no hydrogen and therefore cannot be a hydrogen bond donor like in the ProLeu complexes, and hence, there is the absence of a strong hydrogen bonded amide N−H stretching band as observed in the Rb^+ and Cs^+ ProLeu complexes.

In the Li^+ and Na^+ complexes, the metal is bound to the amide O and amine N. In contrast to (ProLeu)Li^+ and (ProLeu)Na^+, in LeuPro the amine N–H is hydrogen bonded to the carbonyl oxygen of the carboxylic acid, and therefore, the carboxylic acid carbonyl is not bound to the metal. The Rb^+ and Cs^+ complexes have very similar computed spectra. The main difference is that the hydrogen bonded N−H stretch is predicted to be slightly red-shifted, but experimentally, the amine N−H stretching bands are too weak to be of any value in structure elucidation. Spectroscopically, the two types of structures cannot be distinguished.

The trend in the position of the carboxylic acid C=O stretch is very interesting. There is a red shift observed in going from Li^+ to Na^+. Purely on the basis of electrostatic interactions, it would be expected that the more acidic Li^+ would result in a longer N–H bond than that for the Na^+ complex. The computed geometry does show this to be the case, but not substantially so; the hydrogen bonded N–H is only slightly longer. It is 1.023 Å in the Li^+ complex and 1.022 Å in the Na^+ complex. It might be expected that there be a stronger hydrogen bonding interaction in the Li^+ complex which should result in a more

red-shifted C=O stretch. However, this is not observed; the C=O stretch in the Na^+ complex is observed to be significantly red-shifted compared to the one observed in the Li^+ complex. The reason for the red-shifted C=O stretch for (LeuPro)Na^+ must be because of the stronger hydrogen bond in that complex. The calculations show that the hydrogen bond in the Na^+ complex is significantly shorter, 2.358 Å compared to 2.483 Å for the hydrogen bond in the Li^+ complex. The reason for the weaker hydrogen bond in the Li^+ complex is because of the stronger interaction between Li^+ and the amine nitrogen and amide oxygen. Due to the inflexibility, inherent with the proline ring and that brought on by the strong metal binding, the hydrogen bond is constrained to a longer distance.

The further red shift in the C=O stretch for (LeuPro)Rb^+ compared to (LeuPro)Na^+ is due to a structure change. The lowest energy structure for the heavier metal cations is one where the metal is bound to both carbonyl oxygens and the amine nitrogen; therefore, the carboxylic acid C=O stretch is weaker than that in the Na^+ complex, and the absorption is observed to the red. A blue shift observed in the carboxylic acid C=O stretch for the Cs^+ complex compared to the Rb^+ is due to the lower acidity of Cs^+, resulting in a weaker interaction with the peptide.

Spectroscopically and by comparison with the computed spectra, the hydrogen bonded structures cannot be ruled out for the Rb^+ and Cs^+ complexes (Figures A3.11 and A3.12). However, the tridentate structures which are slightly higher in energy for the Li^+ and Na^+ complexes can be ruled out by comparison with the computed spectra (Figures A3.9 and A3.10).

5.4. Conclusions.

A combination of mass spectrometric and computational techniques has been used to identify the sequence and chemical differences of two proline−leucine residues containing dipeptides. Except in the case of the lithiated complexes, SORI-CID alone is not sufficient to distinguish between the two isomers; the use of IRMPD spectroscopy was quite useful to distinguish the two isomers and determine their structures. Interestingly, through IRMPD spectroscopy experiments, it was shown that both lithiated dipeptides fragmented to form both $(Pro)Li^+$ (m/z 122) and $(Leu)Li^+$ (m/z 138). This further exaggerates the difficulty in distinguishing these isomeric peptides by fragmentation-only methods.

IRMPD spectroscopy experiments on the metal-cationized dipeptides in the fingerprint and CH/NH/OH regions were conducted. Due to the O−H stretching features in all computed spectra, all complexes are in their canonical form rather than zwitterionic; the latter is computed to be significantly higher in energy. For rubidiated and cesiated ProLeu, the existence of a strong hydrogen bonded NH amine stretch reveals structures in which the metal is bound to both carbonyls and there is a hydrogen bond between the amide N−H and the amine nitrogen of proline. On the other hand, the lithiated and sodiated complexes have the metal bound to both carbonyls as well as the proline nitrogen. Rubidiated and cesiated LeuPro species also have the metal cation bound to both carbonyls and the amine nitrogen, whereas for lithiated and sodiated LeuPro, the metal is bound to the amide oxygen and amine nitrogen with the amine group also hydrogen bonded to the carboxylic acid carbonyl. The computed spectra agree very well with the IRMPD spectra for the computed

lowest energy structures. IRMPD spectra in the fingerprint region, especially the position of the carboxylic acid C=O stretch, are also very telling as to the nature of the interactions of these carbonyls.

This work shows the importance of both the sequence of the peptide and size of the metal cation in determining the structure of metal-cationized peptides.

5.5. Acknowledgements

The authors wish to thank the CLIO team (J. M. Ortega, G. Perilhous, J. P. Berthet) as well as P. Maître and V. Steinmetz for their support during the experiments conducted at CLIO. We are indebted to Mr. Samuel Atkinson for his help in collecting data at CLIO as well as Dr. Terry McMahon and his group for the collection of two of the CLIO IRMPD spectra in the fingerprint region that we required to complete the work. The authors also acknowledge the computational resources provided by ACENET and Westgrid. Finally, T.D.F. acknowledges the financial contributions from NSERC, CFI, and Memorial University.

5.6. References

1. Desiraju, G. R. *Angew. Chem., Int.Ed.* **2011**, *50*, 52−59.
2. Chen, F.; Gülbakan, B.; Weidmann, S.; Fagerer, S. R.; Ibanez, A. J.; Zenobi, R. *Mass Spectrom. Rev*. **2016**, *35*, 48−70.
3. Cui, X.; Lin, S.; Zhou, J.; Yuan, G. *Rapid Commun. Mass Spectrom*. **2012**, *26*, 1803−1809.
4. Brodbelt, J. S. *Rev. Anal. Chem.***2010**, *3*, 67−87.
5. Jafari-Chermahini, Z.; Najafi Chermahini, A.; Dabbagh, H. A.; Teimouri, *Struct. Chem*. **2015**, *26*, 675−684.

6. Armentrout, P. B.; Yang, B.; Rodgers, M. T. *J. Phys. Chem. B.* **2014**, *118*, 4300−4314.
7. Dilger, J. M.; Valentine, S. J.; Glover, M. S.; Ewing, M. A.; Clemmer, D. E. A. *Int. J. Mass Spectrom.* **2012**, *35*, 35−45.
8. Jami-Alahmadi, Y.; Gholami, A.; Fridgen, T. D. *Phys. Chem. Chem. Phys.* **2014**, *16*, 26855−26863.
9. Jami-Alahmadi, Y.; Fridgen, T. D. *Phys. Chem. Chem. Phys*. **2016**, *18*, 2023−2033.
10. Flick, T. G.; Campuzano, I. D. G.; Bartberger, M. D. *Anal. Chem.* **2015**, *87*, 3300−3307.
11. Dunbar, R. C.; Berden, G.; Oomens, *J. Int. J. Mass Spectrom*. **2013**, *354*, 356−364.
12. Dunbar, R. C.; Polfer, N. C.; Berden, G.; Oomens, J. *Int. J. Mass Spectrom*. **2012**, 332, 71−77.
13. Yin, Z.; Liu, R.; Sun, B.; Hang, W. *J. Anal. At. Spectrom*. **2015**, *30*, 1970−1979.
14. Dunbar, R. C.; Berden, G.; Martens, J. K.; Oomens, J. *J. Phys. Chem. A.* **2015**, *119*, 9901−9909.
15. Kalia, L. V.; Lang, A. E.; Hazrati, L. N.; Fajioka, S.; Wszolek, Z. K.; Dickson, D. W.; Ross, O. A.; Van Deerlin, V. M.; Trojanowski, J. Q.; Hurting, H. I.; et al. *JAMA Neurol*. **2015**, *72*, 100−105.
16. Tong, Y.; Shen, J. *Biochem. Soc. Trans*. **2012**, *40*, 1042−1046.
17. Bravo-San Pedro, J. M.; Gomez-Sa´ nchez, R.; Pizarro-Estrella, E.; Niso-Santano, M.; Gonzalez-Polo, R. A.; Fuentes Rodríguez, J. M. *Intimate Enemies. Parkinson's Dis*. **2012**, 1−9.
18. Berg, D.; Schweitzer, K. J.; Leitner, P.; Zimprich, A.; Lichtner, P.; Belcredi, P.; Brü
19. ssel, T.; Schulte, C.; Maass, S.; Nagele, T.; et al. *Brain*, **2005**, *128*, 3000−3011.
20. Duan, Y.; Li, F.; Li, Y.; Tang, Y.; Kong, X.; Feng, Z.; Anthony, T. G.; Watford, M.; Hou, Y.; Wu, G.; et al. *Amino Acids*, **2016**, *48*, 41−51.
21. Columbus, D. A.; Fiorotto, M. L.; Davis, T. A. *Amino Acids.* **2015**, *47*, 259−270.
22. Xu, Z. R.; Tan, Z. J.; Zhang, Q.; Gui, Q. F.; Yang, Y. M. *J. Nutr*. **2015**, *113*, 25−34.
23. MacArthur, M. W.; Thornton, J. M. *J. Mol. Biol*. **1991**, *218*, 397−412.
24. Vanhoof, G.; Goossens, F.; De Meester, I.; Hendriks, D.; Scharpe, S. *FASEB J.* **1995**, *9*, 736−744.
25. Chen, Y.-R.; Clark, A. C. *Protein Sci*. **2006**, *15*, 395−409.
26. Desrochers, G.; Lussier-Price, M.; Omichinski, J. G.; Angers. *Biochemistry*, **2015**, *54*, 7345−7354.
27. Kay, B. K.; Williamson, M. P. *FASEB J*. **2000**, *14*, 231−241.
28. Opitz, R.; Müller, M.; Reuter, C.; Barone, M.; Soicke, A.; Roske, Y.; Piotukh, K.; Huy, P.; Beerbaum, M.; Wiesner, B.; et al. *Proc. Natl. Acad. Sci. U. S. A.* **2015**, *112*, 5011−5016.
29. Moision, R. M.; Armentrout, P. B. *J. Phys. Chem. A.* **2006**, *110*, 3933−3946.

30. Kish, M.; Ohanessian, G.; Wesdemiotis, C. *Int. J. Mass Spectrom*. **2003**, *227*, 509−524.
31. Rodgers, M. T.; Armentrout, P. B. *Acc. Chem. Res.* **2004**, 37, 989−998.
32. Baker, E. S.; Burnum-Johnson, K. E.; Ibrahim, Y. M.; Orton, D. J.; Monroe, M. E.; Kelly, R. T.; Moore, R. J.; Zhang, X.; Theberge, R.; Costello, C. E.; et al. *Proteomics*. **2015**, *15*, 2766−2776.
33. Keough, T.; Youngquist, R. S.; Lacey, M. P. Proc. *Natl. Acad. Sci. U. S. A.* **1999**, *96*, 7131−7136.
34. Breci, L. A.; Tabb, D. L.; Yates, J. R.; Wysocki, V. H. *Mass Spectra. Anal. Chem.* **2003**, *75*, 1963−1971.
35. Cook, S. L.; Collin, O. L.; Jackson, G. P. *J. Mass Spectrom*. **2009**, *44*, 1211−1223.
36. Prazeres, R.; Glotin, F.; Insa, C.; Jaroszynski, D. A.; Ortega, J. M. *Eur. Phys. J. D*. **1998**, *3*, 87−93.
37. Frisch, M. J.; Trucks, G. W.; Schlegel, H. B.; Scuseria, G. E.; Robb, M. A.; Cheeseman, J. R.; Scalmani, G.; Barone, V.; Mennucci, B.; Petersson, G. A.; et al. Gaussian09, revision C.01; Gaussian, Inc. Wallingford, CT, 2010.
38. Grimme, S.; Antony, J.; Ehrlich, S.; Krieg, H. *J. Chem. Phys.* **2010**, *132*, 154104−154124.
39. Goerigk, L.; Kruse, H.; Grimme, S. *ChemPhysChem*. **2011**, *12*, 3421−3433.
40. Zhao, Y.; Truhlar, D. G. *Theor. Chem. Acc.* **2008**, *120*, 215−241.
41. Paciotti, R.; Coletti, C.; Re, N.; Scuderi, D.; Chiavarino, B.; Fornarini, S.; Crestoni, M. E. *Phys. Chem. Chem. Phys.* **2015**, *17*, 25891−25904.
42. Schmidt, J.; Kass, S. R. *J. Phys. Chem. A*. **2013**, *117*, 4863−4869.
43. Weigend, F. *Phys. Chem. Chem. Phys.* **2006**, *8*, 1057−1065.
44. Gholami, A.; Fridgen, T. D. *Phys. Chem. Chem. Phys.* **2014**, *16*, 3134−3143.
45. Ali, O. Y.; Randell, N. M.; Fridgen, T. D. *ChemPhysChem*. **2012**, *13*, 1507−1513.
46. Marino, T.; Russo, N.; Toscano, M. *J. Phys. Chem. B.* **2003**, *107*, 2588−2594.
47. Drayß, M. K.; Armentrout, P. B.; Oomens, J.; Schafer. *Int. J. Mass Spectrom*. **2010**, *297*, 18−27.
48. Moghaddam, M. B.; Fridgen, T. D. *J. Phys. Chem. B.* **2013**, *117*, 6157−6164.

Chapter 6

Distinguishing Complexes of Isomeric Peptides: Structures, Energetics, and Reactions of Sodium Cation-Coordinated ProLeu or LeuPro Trimers in The Gas Phase

This chapter is reproduced with permission from

Jami-Alahmadi, Y.; Fridgen, T. D.

"Distinguishing Complexes of Isomeric Peptides: Structures, Energetics, and Reactions of Sodium Cation-Coordinated ProLeu or LeuPro Trimers in The Gas Phase"

Int. J. Mass Spectrom., **2017** (Just accepted)

6.1. Introduction

Electrostatic interactions and hydrogen bonding are the two fundamental non-covalent forces that stabilize the structures of proteins that play key roles in regulating cellular activities. Proteins and peptides are responsible for many chemical reactions that take place under physiological conditions such as, cellular regeneration,[1] signal transduction,[2,3] enzymatic activities,[4] gene expression,[5] transportation of hemoglobin,[6] antibacterial activities,[7–9] and so on. On the other hand, sometimes due to the changes in 3D-conformation, instead of normal re-folding, proteins or peptides adopt a misfolded state which often results in peptide aggregation such as in amyloid assemblies.[10–12] Abnormal functionality of the peptide or protein through aggregation is associated with neurodegenerative diseases such as Alzheimer's, Parkinson's, and BSE (mad cow), as well as type II diabetes and cell death.[13,14] In the folding process, an aggregated peptide can

stabilize itself through intermolecular interactions with other peptides rather than the intramolecular forces within the protein or peptide itself.[15,16] For such reasons, the identification of the nature of non-covalent interactions and aggregation structures of peptides at the molecular level will help to understand their biological activities on a larger scale.

Proline-containing motifs show unique properties due in part to the steric effects induced by the proline side chain. The conformational restrictions cause unusual functionality in proline-containing proteins. Proline is known as a helix breaker,[17] since it lacks an amide hydrogen and cannot donate a hydrogen bond, it breaks the helical structure when it exists in an alpha helix. The existence of metal-cation interactions with the protein that impart important effects in molecular association also cannot be neglected. For example, Na^+-dependent proline rich motif transporters in humans are responsible for the regulation of sodium ion in the extracellular fluids (ECF) and hence controlling blood pressure.[18] Sodium transport through cell membranes via sodium channel regulation in the kidney shows high selectivity of the channel meaning that it greatly discriminates against other ions.[18,19,20,21,22] Indeed, understanding how amino acids or peptides bind with metal cations has an important impact in understanding much of the chemistry of life at the molecular level.

Gas phase fragmentation techniques in combination with tandem mass spectrometry, have helped to reveal vast amounts of information about the structures and dynamics of peptides in a solvent-free environment. Electron capture dissociation (ECD),[23,24] electron transfer dissociation (ETD),[25,26] collision induced dissociation

(CID),[27,28] infrared multiphoton dissociation (IRMPD),[29,27] electron detachment dissociation (EDD),[30] and surface-induced dissociation (SID)[31] are some fragmentation methods that have been used to provide information toward peptide identification.

Differentiation of isomeric peptides by mass spectrometry is important and methods such as ion-mobility are rather well-suited to this task.[32,33] Differential mobility spectrometry (DMS) is a special case of ion-mobility where an asymmetric radiofrequency field is applied between two parallel plates. In the presence of a chemical modifier such as water or methanol, etc. isomeric ions' mobilities are affected differently by the asymmetric field. Essentially, two isomers will cluster to a different extent with the chemical modifier and their mobilities then differ.[34,35] Blagojevic et al. studied different modifiers to significantly separate GlyAla from AlaGly and GlySer from SerGly by DMS.[36,37] Using multicomponent modifiers in DMS, Blagojevic and Bohme[38] were even able to separate conformational isomers of both Bradykinin and hexaglycine and were able to monitoring H/D exchange kinetics for the different exchangeable hydrogens of each of the isomers.

There has also been a significant amount of research in the recent past, to investigate the structures and energetic of biomolecules using a variety of mass spectrometric techniques such as IRMPD spectroscopy or BIRD kinetics.[39,40,41,42,43,44] To differentiate between two isomeric peptide complexes, $Na^+(ProLeu)_3$ and $Na^+(LeuPro)_3$, IRMPD spectroscopy is used to help shed light on the structures, and blackbody infrared radiation-induced dissociation (BIRD) is used to compare the relative dissociation energies. The present study provides insight into the understanding of the effects of sodium metal cation on the aggregated proline containing dipeptides using mass spectrometric techniques that

are backed by theoretical methods. The results reveal how the structure and dissociation energy of sodium cation bound peptide complexes are affected by the intramolecular hydrogen-bonding network, which varies as the peptide sequence differs.

6.2. Methods

6.2.1. Mass Spectrometry. All experiments were performed in the Laboratory for the Study of the Structures, Energetics, and Reactions of Gaseous Ions[45] at Memorial University, which houses a Bruker ApexQe7 Fourier transform ion cyclotron resonance mass spectrometer, FTICR-MS. Gaseous ions were transmitted from solution to the gas phase using an Appollo II electrospray ionization (ESI) source. $Na^+(ProLeu)_3$ or $Na^+(LeuPro)_3$ complexes were formed by electrospray ionization (ESI) of 1 mL of 50 mmol L^{-1} aqueous solution of ProLeu or 1 mL of 25 mmol L^{-1} aqueous solution of L-leucyl-L-proline (LeuPro) hydrochloride dipeptide to which 0.1 mL of 10 mmol L^{-1} aqueous sodium chloride in 50/50 solutions of water (nanopure) and methanol (99.8%, ACP Chemicals) were added. ESI was done with an Apollo II ESI source using a syringe pump operated at 0.14 mL h^{-1}.

6.2.2. BIRD Kinetic Measurements and Master Equation Modeling. At the University of Waterloo, McMahon[46] was the first to observe the unimolecular dissociation of weakly bound cluster ions by absorption of blackbody infrared radiation. These cluster ions were trapped in an FTICR under extremely low-pressure such that collisional activation was minimal; the process was originally called zero-pressure thermal radiation induced dissociation or ZTRID[47] which was later changed to BIRD.[42] In these experiments the

energy required for the dissociation of weakly-bound complex ions is achieved through the exchange of blackbody radiation with the ion's surroundings.[42,44,45,48]

Here, the BIRD rate constants for the unimolecular dissociation of $Na^+(ProLeu)_3$ and $Na^+(LeuPro)_3$ complexes were measured by first isolating them in the ICR cell at 10^{-10} mbar and measuring the intensities of the precursor ion and their dissociation products as a function of time until the precursor ion intensity is about 10% of the total ion abundance. Experiments were repeated at various temperatures over the temperature ranges of 292-357K for $Na^+(LeuPro)_3$ and 314-357K for $Na^+(ProLeu)$. According to equation 2.11, the unimolecular BIRD rate constant, k_{uni}, is determined by fitting the normalized intensity of the precursor ion, *I*, vs time, *t*. The temperature was adjusted and controlled using a water-cooled heating jacket placed around the entire vacuum chamber, which was controlled by an AC input voltage. The temperature of the walls of the vacuum chamber were measured using a J-type thermocouple and the temperature at the center of the ICR cell was determined using a previous calibration based on the vacuum chamber wall temperature.[49]

By plotting k_{uni} as a function of inverse temperature, *T*, according to equation 2.13, the Arrhenius activation energies, E_a, and pre-exponential factor, *A*, were obtained where *R* is the ideal gas constant, 8.314 J K^{-1} mol^{-1}. Errors in the reported Arrhenius activation energies and pre-exponential factor are based on the standard deviations of both the rate constant at each temperature and that of the linear fit to the Arrhenius equation.

In BIRD experiments, the experimentally obtained thermodynamic information can only be reliable if the rates of photon exchange are faster than the dissociation rates. If the

ions are not sufficiently large, this may not be the case the case, and true thermal dissociation energies can be extracted using a master equation analysis.[47,50] Master equation simulates the change in populations of the internal energy levels of system over a range of time. Briefly, this model uses a set of coupled linear first-order ordinary differential equations and the radiative absorption, emission and dissociation rate constants of all state-to-state transitions to find the probability of energy transfer between all possible energy states. In the modeling process, once a Boltzmann distribution of ion populations and a steady-state is reached at a, the unimolecular decomposition rate constants can be obtained. The dissociation thresholds, E_0, are varied to obtain a good fit to the temperature dependence of the experimental rate constants. The value E_0 is the one which is used in the modeling to best match the slope of the experimental Arrhenius plot as long as the modelled E_a is within a standard deviation of the experimental and the modelled rate constants are within a factor of five of the experimental rate constants.[44,49] To compute the dissociation and radiative rate constants, the computed vibrational frequencies and intensities were used for the lowest energy trimer complexes found. The pre-exponential factors depend on the nature of the transition state, loose or tight. In the present cases, we don't expect the dissociations to involve any rearrangements so the transition states are expected to be neutral to loose, with transition state entropies of about 0 to about 100 J K^{-1} mol^{-1}. To obtain these transition state entropies (or pre-exponential factors) the lowest energy complex vibration frequencies were scaled by an appropriate factor. The uncertainties in the extracted E_0 values were taken as the range of E_0 values used to model the Arrhenius plots with over a range of plausible A factors.

6.2.3. Infrared Multiphoton Dissociation (IRMPD) Spectroscopy. IRMPD spectroscopy experiments were performed in 2700–3800 cm^{-1} region using an IR optical parametric oscillator, OPO, manufactured by LaserSpec. This OPO laser is tunable from 7100 to 2200 cm^{-1}, with a bandwidth of 2 cm^{-1}. Built around a periodically-poled $LiNbO_3$ crystal, the OPO is pumped by a diode-pumped solid state Nd:YAG laser and operates at 20 kHz with pulse duration of few nanoseconds. The output power is near 1 W at 3300 cm^{-1}. The experimental IRMPD spectra were obtained by plotting the IRMPD efficiency as a function of the radiation wavenumber.

6.2.4. Electronic Structure Calculations. The lowest-energy structures of both complexes were computed using Gaussian 09.[51] Geometry optimizations and frequency calculations for the optimized structures were carried out at the B3LYP level of theory with the 6-31+G(d,p) basis set. Empirical corrections for dispersion were done using Grimme's D3 version with the original D3 damping function, B3LYPD3.[52] All harmonic frequencies were corrected using scaling factors of 0.95. Computed IR spectra were convoluted using Gaussian functions with a 25 cm^{-1} width (fwhm).

6.3. Results and Discussion

6.3.1. BIRD Kinetics. Within the temperature ranges used, the exposure of $Na^+(ProLeu)_3$ and $Na^+(LeuPro)_3$ to ambient blackbody photons resulted in the loss of a neutral ProLeu or LeuPro dipeptide, respectively. While the fragmentation pattern for both isomers is identical, the $Na^+(ProLeu)_3$ complex is observed to dissociate through the loss of a neutral dipeptide at a significantly slower rate. In fact, at 20 ^oC BIRD of $Na^+(ProLeu)_3$ was too

slow to observe with a reasonable time delay. To compare, the BIRD rate constant for $Na^+(ProLeu)_3$ at 66 °C was 5.1±0.4x10^{-3} s^{-1} whereas that for $Na^+(LeuPro)_3$ was found to be more than 5 times larger, 28.2±0.1x10^{-3} s^{-1}, at the same temperature. As expected, the BIRD rate constants increase with temperature and were observed to be 73±2x10^{-3} s^{-1} and 202±5x10^{-3} s^{-1} at 108 °C for $Na^+(ProLeu)_3$ and $Na^+(LeuPro)_3$, respectively. The first-order BIRD plots for $Na^+(LeuPro)_3$ and $Na^+(ProLeu)_3$ along with the BIRD rate constants are shown in Figures 6.1 and 6.2, respectively.

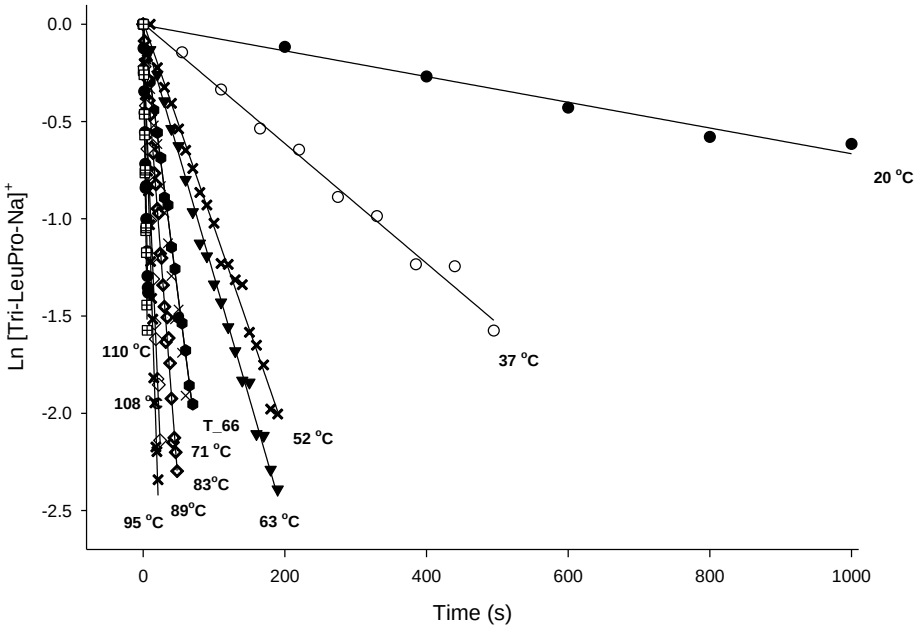

Figure 6.1. Blackbody infrared radiative dissociation first-order kinetics plots at various temperatures between 20–110 °C for the $Na^+(LeuPro)_3$.

From the temperature dependence of the dissociation rate constants, Figure 6.3, the Arrhenius activation energies and entropies were determined for dipeptide loss from each

isomeric complex. There is an excellent linear fit in both Arrhenius plots with r^2 values of 0.973 to 0.993 for $Na^+(LeuPro)_3$ and $Na^+(ProLeu)_3$, respectively.

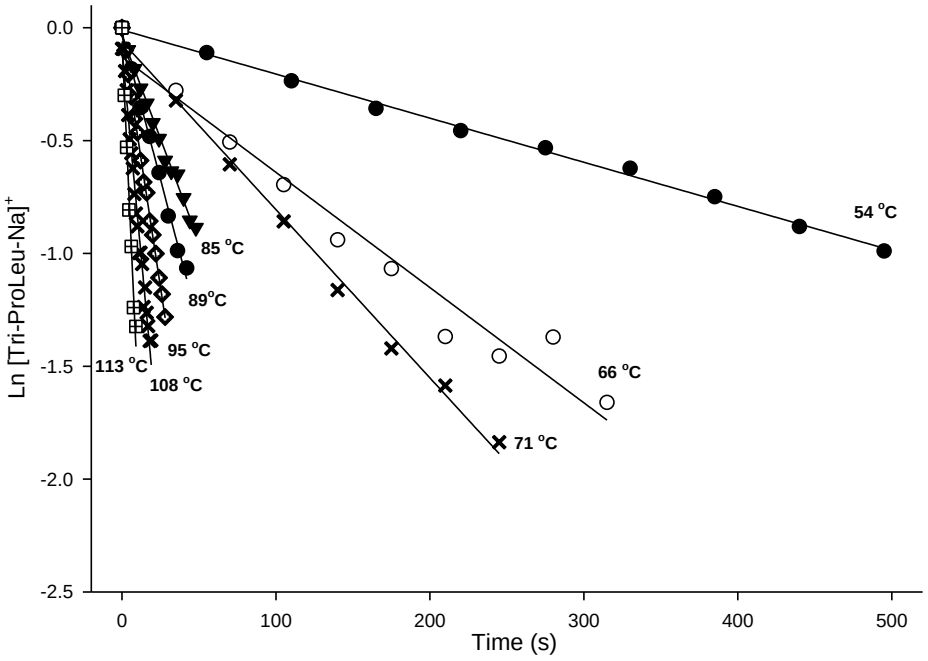

Figure 6.2. Blackbody infrared radiative dissociation first-order kinetics plots at various temperatures between 54–113 °C for the $Na^+(ProLeu)_3$.

The experimentally determined activation energies were found to be about 20 kJ mol^{-1} higher for $Na^+(ProLeu)_3$ than for $Na^+(LeuPro)_3$, 92±5 kJ mol^{-1} vs 73±4 kJ mol^{-1}, respectively. Evidently, the experimentally determined BIRD rate constants and BIRD activation energies for dissociation are able to be used to distinguish the LeuPro or ProLeu complexes. The measurements of the activation energies of the $Na^+(LeuPro)_3$ and $Na^+(ProLeu)_3$ are the first of their kind and there are no comparisons of sodiated trimers of

peptides. However, using high pressure mass spectrometry, Raspopov and McMahon did measure the binding energies of the protonated trimers of glycine to be in a similar range as the binding energies found here, 77 kJ mol^{-1}.[53] The experimental pre-exponential factors (lnA) were determined to be 28.9 and 23.4, for $Na^+(ProLeu)_3$ and $Na^+(LeuPro)_3$, respectively, yielding (298 K) entropies of activation of -13±2 J K^{-1} mol^{-1} and -59±5 J K^{-1} mol^{-1}, respectively, lower than expected for dissociation reactions that are expected to occur without a significant barrier. The $Na^+(ProLeu)_3$ and $Na^+(LeuPro)_3$ complexes have 321 vibrational degrees of freedom and are expected to be strongly absorbing in the infrared. However, the room temperature BIRD rate constants for these complexes, in the 10^{-3} s^{-1} regime, are on the border between small and large molecule kinetics (Figure A4.1).[48,49,52] As such, master equation modelling of the Arrhenius plots is required to obtain true thermal dissociation thresholds (see section 2.1.3.3.2).

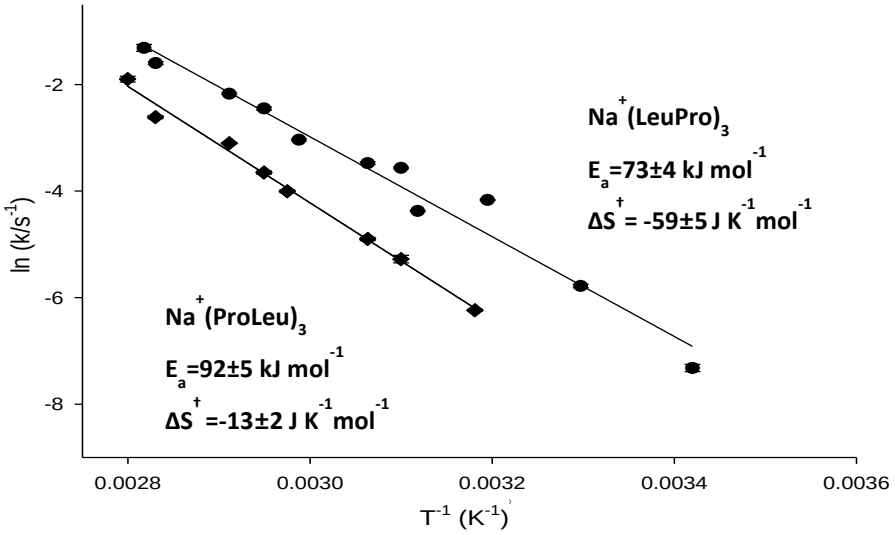

Figure 6.3. Arrhenius plots for the dissociation of the $Na^+(LeuPro)_3$ and $Na^+(ProLeu)_3$. The error bars are from the fitting of the first order kinetics plots in Figures 6.1 and 6.2.

6.3.2. IRMPD Spectroscopy and Structures of $Na^+(ProLeu)_3$ and $Na^+(LeuPro)_3$ Complexes. The lowest energy computed structures found for the $Na^+(ProLeu)_3$ and $Na^+(LeuPro)_3$ complexes are shown in Figure 6.4 a and b, respectively, and other unique structures are depicted in Figures A4.2 and A4.3 along with their relative thermochemistries. The lowest energy structure for $Na^+(ProLeu)_3$ adopts a distorted octahedral geometry in which the metal cation interacts with both carbonyl oxygens of all three ProLeu dipeptides. This structure is stabilized by intramolecular hydrogen bonding occurring between each of the amine nitrogens and amide hydrogens in all three dipeptides similar to those seen before in dipeptide-metal complexes.[54,27] There is also a hydrogen bond between one of the O-H groups and an amide oxygen of another dipeptide. The other two O-H groups are free of hydrogen bonding interaction. In contrast, the $Na^+(LeuPro)_3$ complex, which lacks an amide hydrogen, is stabilized through the interactions of the sodium cation with two of the amide oxygens and all three of the amine nitrogens. Interestingly, this structure is stabilized through the intramolecular interactions occurring between the carboxylate O-H and either the two carbonyl oxygens or an amide oxygen.

The experimental spectra for the $Na^+(ProLeu)_3$ and $Na^+(LeuPro)_3$ complexes are shown in Figures 6.5a and b. The spectra are dominated by broad absorptions between 2800 and 3500 cm^{-1} for $Na^+(ProLeu)_3$ and 2800 and 3300 cm^{-1} for $Na^+(LeuPro)_3$ the breadth of which is due predominantly to hydrogen bonded O-H stretching. The broad features are not completely featureless, however. For example, maxima are observed in both spectra at about 2890 and 2980 cm^{-1} corresponding to C-H stretching. Similarly, in the spectrum for $Na^+(ProLeu)_3$ there is a maximum at about 3330 cm^{-1} corresponding to hydrogen bonded

amide N-H stretching. Hydrogen bonded O-H stretching absorptions are predicted at about 3050 cm^{-1} for $Na^+(ProLeu)_3$ and at 3130 and 3300 cm^{-1} for $Na^+(LeuPro)_3$, the latter of which is observed at 3220 cm^{-1}. As expected, these very anharmonic hydrogen bonded O-H stretching vibrations are not well reproduced by the harmonic vibrational frequencies predicted by the electronic structure calculations. Finally, a distinguishing feature of the isomers, and also in agreement with the computed structures, are a pair of free (non-hydrogen bonded) carboxylic acid O-H stretching features centered at about 3550 cm^{-1}. Another distinguishing feature between spectra of the two complexes is the breadth of the broad band, encompassing the hydrogen bonded aminde N-H stretching band out to 3400 cm^{-1} for $Na^+(ProLeu)_3$.

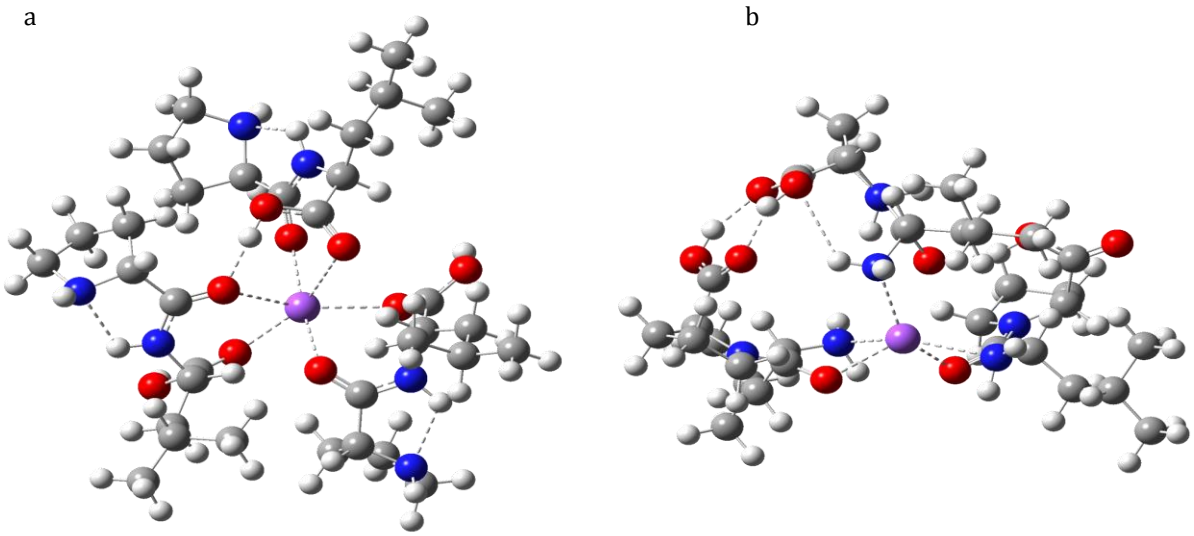

Figure 6.4. The B3LYPD3/6-31+G(d,p) computed lowest energy structures of a)$Na^+(ProLeu)_3$ and b)$Na^+(LeuPro)_3$.

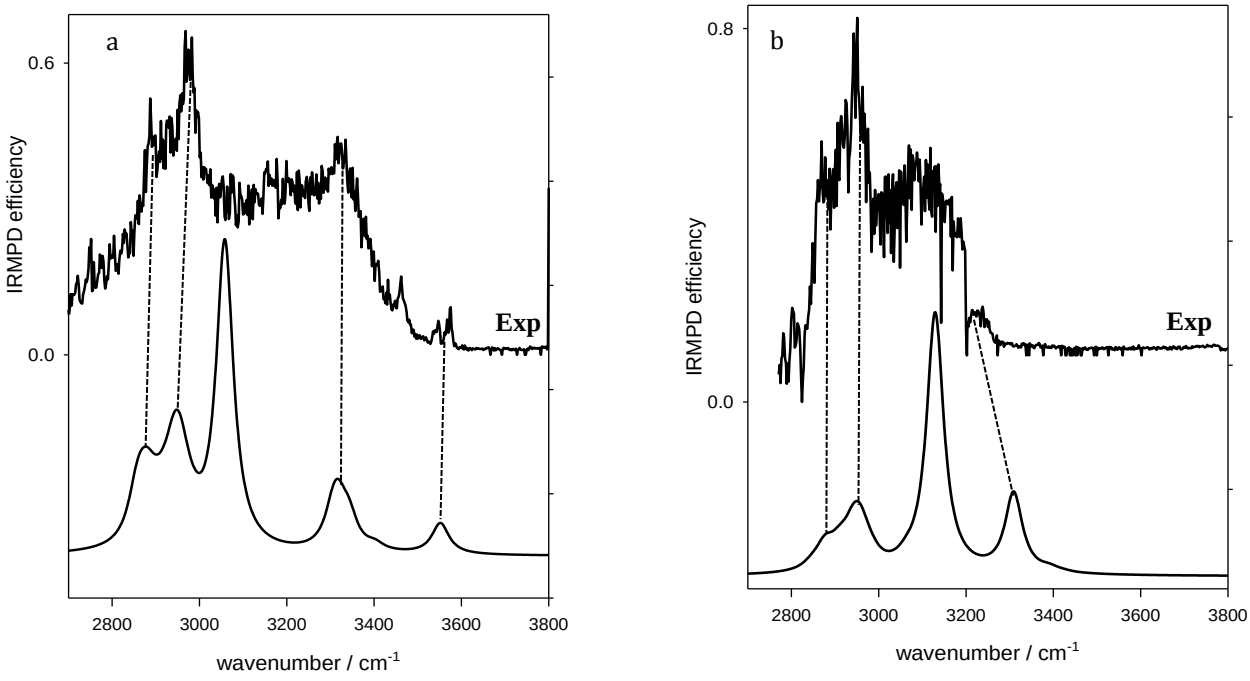

Figure 6.5. Experimental IRMPD spectra (top traces) and calculated IR spectra (lower trace) for the lowest energy structures of the a) $Na^+(ProLeu)_3$ and b) $Na^+(LeuPro)_3$ complexes in the 2800 to 3800 cm^{-1} region. The spectra were computed using B3LYPD3/6-31+G(d,p) at 298 K and scaled by 0.95.

It should be noted that experimentally, the amine N−H stretching bands are too weak to be of any value in structure elucidation. In a previous study on sodiated LeuPro and ProLeu monomeric complexes, it was observed that the amine N−H stretching bands are too weak to be experimentally observed.[55]

Comparison of the experimental IRMPD spectra with the computed IR spectra of the higher energy isomers are shown in Figures A3.4 and A3.5. While few of these can be ruled out by spectroscopic means, the computed lowest energy structures are indeed

consistent with the experimental IRMPD spectra. Furthermore, the very different IRMPD spectra of the two complexes, $Na^+(ProLeu)_3$ and $Na^+(LeuPro)_3$, clearly distinguishes them.

6.3.3. Dissociation Thresholds: Master Equation Analysis and Electronic Structure Calculations. In Table 6.1, the results of the master equation modeling are provided. Values of A ranging from 10^{14} to 10^{20} s^{-1}, corresponding to a $\Delta_r S^{\ddagger}$ of 10 to 130 J K^{-1} mol^{-1} as it is expected that the dissociations are neutral to loose. Over this range of A values, the E_0 values were determined to be between 97 and 123 kJ mol^{-1} for $Na^+(ProLeu)_3$ and 92 to 116 kJ mol^{-1} for $Na^+(LeuPro)_3$ and values of 110(±13) and 103(±13) kJ mol^{-1} seem to be best master equation estimates of the dissociation thresholds. The master equation estimates are slightly higher than the experimental activation energies (92 and 73 kJ mol^{-1}), but not excessively so, which is consistent with the size of the complex being borderline for large molecule BIRD kinetics.

The computed enthalpies for the loss of peptide, from $Na^+(ProLeu)_3$ and $Na^+(LeuPro)_3$ (see Table 6.1) are 120 and 113 kJ mol^{-1}, respectively, which are consistent with the master equation values and are also consistent with the higher stability to BIRD observed for $Na^+(ProLeu)_3$.

Master equation calculations were performed with A factors equal to the experimental ones. For $Na^+(ProLeu)$, the E_0 determined was 95 kJ mol^{-1}, however, the rate constants computed were between 5 and 10 times the experimental values. For $Na^+(LeuPro)$, the computed slopes did not compare well with any slope using E_0 values that produced rate constants within an order of magnitude of the experimental values. These

results are consistent with the clusters displaying small molecule BIRD kinetics and that the experimental E_a and ln A values are not the true values as would be obtained if the dissociating population were thermally equilibrated.

6.4. Conclusions

The structures and stabilities of the self-assembled $Na^+(ProLeu)_3$ and $Na^+(ProLeu)_3$ complexes have been studied in the gas phase using both experimental (BIRD and IRMPD spectroscopy) and theoretical methods (master equation and electronic structure calculations). Experimentally observed BIRD kinetics energies for both isomeric complexes were measured and are sufficient to distinguish between the complexes composed of isomeric peptides, showing the $Na^+(ProLeu)_3$ being more stable. A temperature dependence in the BIRD rate constants also resulted in a larger activation energy for $Na^+(ProLeu)_3$. Master equation modeling gave in slightly higher dissociation thresholds than the activation energies, but was also consistent with the greater stability observed for $Na^+(ProLeu)_3$. Computed enthalpies of dissociation also agreed well with the "experimental" dissociation thresholds. The complexes were also distinguished by IRMPD spectroscopy. The computed IR spectra for the lowest energy structures were consistent with the experimental IRMPD spectra.

Table 6.1. Table of master equation E_0 values calculated at different A factors, the best master equation estimate E_0 and $\Delta_r H$ for dissociation computed by B3LYPD3/6-31+G(d,p). All energies in kJ mol^{-1}.

A / s^{-1} / Species	1.2x10^{14}	1.3x10^{15}	1.1x10^{18}	1.2x10^{20}	E_0*	$\Delta_r H$
$Na^+(ProLeu)_3$	97	101	116	123	110(±13)	120
$Na^+(LeuPro)_3$	92	97	106	116	103(±13)	113

* best estimate from master equation modeling.

6.5. Acknowledgements

The authors acknowledge the computational resources provided by ACENET, Westgrid, and SharcNet for these studies. The authors wish to thank the financial contributions from NSERC, CFI, and Memorial University. The authors congratulate Dr. McMahon on many decades of excellent science and look forward to decades more.

6.6. References

1. Johnson, T.; Koria, P. *BioDrug.* **2016**, *30*, 117–127.
2. Zhou, R.; Yuan, Z.; Liu, J.; Liu, J. *Mol. Med. Rep.* **2016**, *13*, 4689-4696.
3. Richards, J. P.; Bowles, E. A.; Ellsworth, M. L.; Stephenson, A. H.; Sprague, R. S. *ISBT Sci. Ser.* **2016,** *11*, 325–331.
4. Musrati, A. A. Tervahartiala, T.; Gürsoy, M.; Könönen, E.; Fteita, D.; Sorsa, T.; Uitto, V. J; Gürsoy, U. K. Arch Oral Biol. **2016**, *66*, 1–7.
5. Svensson, D.; Nebel, D.; Nilsson, B. O. *Inflamm. Res.* **2015**, *65*, 25–32.
6. Thévenod, F.; Wolff, N. A. *Metallomics*. **2016**, *8*, 17-42.
7. Zhang, D. L.; Guan, R. Z., Huang, W. S.; Xiong, J. *Fish Shellfish Immunol.* **2013**, *35*,

625–31.
8. Belmonte, R.; Cruz, C. E.; Pires, J. R.; Daffre, S. *Peptides.***2012**, *37*, 120–127.
9. Nedjar-Arroume, N.; Dubois-Delval. V.; Adje, E. Y.; Traisnel, J.; Krier, F.; Mary, P.; Kouach, M.; Briand, G.; Guillochon, D. *Peptides.* **2008**, *29*, 969–977.
10. Tartaglia, G. G.; Pawar, A. P.; Campioni, S.; Dobson, C. M.; Chiti, F.; Vendruscolo, M. *J. Mol. Biol.* **2008**, *380*, 425–436.
11. Stefani, M.; Dobson, C. M. *J. Mol. Med.* **2003**, *81*, 678–699.
12. Aguzzi, A.; O'Connor, T. *Nat. Rev. Drug Discov.* **2010**, *9*, 237–248.
13. Chaudhuri, T. K.; Paul, S. *FEBS J.* **2006**, *273*, 1331–1349.
14. Ahmad, E.; Ahmad, A.; Singh, S.; Arshad, M.; Khan, A. H.; Khan, R. H. *Biochimie.* **2011**, *93*, 793–805.
15. Routledge, K. E.; Tartaglia, G. G.; Platt, G. W.; Vendruscolo, M.; Radford, S. E. *J. Mol. Biol.* **2009**, *389*, 776–786.
16. Stefani, M. *Biochim. Biophys. Acta - Mol. Basis Dis.* **2004**, *1739*, 5–25.
17. Vanhoof, G.; Goossens, F.; De Meester, I.; Hendriks, D.; Scharpé, S. *FASEB J.* **1995**, *9*, 736–744.
18. Eaton, D. C.; Malik, B.; Bao, H.-F.; Yu, L.; Jain, L. *Proc. Am. Thorac. Soc.* **2010**, *7*, 54–64.
19. Bröer, A.; Balkrishna, S.; Kottra, G.; Davis, S.; Oakley, A.; Bröer, S. *Mol. Membr. Biol.* **2009**, *26*, 333–346.
20. Ronzaud, C.; Staub, O. *Physiology*. **2014**, *29*, 16–26.
21. Brandsch, M. *Amino Acids*, **2006**, *31*, 119–136.
22. Takanaga, H.; Mackenzie, B.; Suzuki, Y.; Hediger, M. A. *J. Biol. Chem.* **2005**, *280*, 8974–8984.
23. Tsybin, Y.; Vvorobyev, A.; Zhurov, K.; Laskay, Ü. *Eur. J. Mass Spectrom.* **2015**, *21*, 451–458.
24. Medzihradszky, K. F.; Chalkley, R. J. *Mass Spectrom. Rev.* **2015**, *34*, 43–63.
25. Hunt, D. F.; Shabanowitz, J.; Bai, D. L. *J. Am. Soc. Mass Spectrom.* **2015**, *26*, 1256–1258.
26. Nardiello, D.; Palermo, C.; Natale, A.; Quinto, M.; Centonze, D. *Anal. Chim. Acta* **2015**, *854*, 106–117.
27. Moghaddam, M. B.; Jami-Alahmadi, Y.; Fridgen, T. D. *ChemPhysChem.* **2015**, *15*, 3190–3301.
28. Greer, S. M.; Parker, W. R.; Brodbelt, J. S. *J. Proteome Res.* **2015**, *14*, 2626-2632.
29. Van Stipdonk, M. J.; Patterson, K.; Gibson, J. K.; Berden, G.; Oomens, J. *Int. J. Mass Spectrom.* **2015**, 3*79*, 165–178.
30. Budnik, B. A.; Haselmann, K. F.; Zubarev, R. A. *Chem. Phys. Lett.* **2001**, *342*, 299–302.
31. Meroueh, O.; Hase, W. L. *J. Am. Chem. Soc.* **2002**, *124*, 1524–1531.

32. Lapthorn, C.,; Pullen, F.; Chowdhry, B. Z. *Mass Spectrom. Rev.* **2013**, *32*, 43–71.
33. Bleiholder, C.; Bowers, M. T. *Annu. Rev. Anal. Chem.* 2017, **10,** 365-386.
34. Campbell, J. L.; Zhu, M.; Hopkins, W. S. *J. Am. Soc. Mass Spectrom.* **2014**, *25*, 1583–1591.
35. Schneider, B. B. *Int. J. Ion Mobil. Spectrom.* **2013**, *16*, 207–216.
36. Blagojevic, V,; Koyanagi, G. K.; Bohme, D. K. *J. Am. Soc. Mass Spectrom.* **2014**, *25*, 490–497.
37. Blagojevic, V.; Chramow, A.; Schneider, B. B.; Covey, T. R.; Bohme, D. K. *Anal. Chem.* **2011**, *83*, 3470–3476.
38. Blagojevic, V. ; Bohme, D. K. *Int. J. Mass Spectrom.* **2015**, *378*, 180–185.
39. Dunbar, R. C.; Oomens, J.; Berden, G.; Kai-Chi Lau, J.; Verkerk, U. H.; Hopkinson, A. C.; Siu, K. W. M. *J. Phys. Chem. A.* **2013**, *117*, 5335–5343.
40. Dunbar, R. C.; Martens, J.; Berden, G.; Oomens, J. *Phys. Chem. Chem. Phys.* **2016**, *18*, 26923–26932.
41. Peckelsen, K.; Martens, J.; Berden, G.; Oomens, J.; Dunbar, R. C.; Meijer, A. J. H. M.; Schäfer, M. *J. Mol. Spectrosc.* **2017**, *332*, 38–44.
42. Mikhailov, V. A.; Liko, I.; Mize, T. H.; Bush, M. F.; Benesch, J.; Robinson, C. V. *Anal. Chem.* **2016**, *88*, 7060–7067.
43. Jami-Alahmadi, Y.; Gholami, A.; Fridgen, T. D. *Phys. Chem. Chem. Phys.* **2014**, *16*, 26855–26863.
44. Price, W. D.; Schnier, P. D.; Williams, E. R. *Anal. Chem.* **1996**, *68*, 859–866.
45. Rajabi, K.; Easterling, M.; Fridgen, T. *J. Am. Soc. Mass Spectrom.* **2009**, *20*, 411–418.
46. Thoelmann, D.; Tonner, D. S.; McMahon, T. B. *J. Phys. Chem.* **1994**, *98*, 2002–2004.
47. Dunbar, R. C.; McMahon, T. B.; Thoelmann, D.; Tonner, D. S.; Salahub, D. R.; Wei, D. *J. Am. Chem. Soc.* **1995**, *117*, 12819–12825.
48. Tonner, D. S.; Thölmann, D.; McMahon, T. B. *Chem. Phys. Lett.* **1995**, *233*, 324–330.
49. Gillis, E. A. L.; Demireva, M.; Nanda, K.; Beran, G.; Williams, E. R, Fridgen, T. D. Phys Chem Chem Phys. **2012**, *14*, 3304-3315.
50. Dunbar, R. C. *Mass Spectrom. Rev.* **2004**, *23*, 127–158 (2004).
51. Frisch, M. J.; Frisch, M. J.; Trucks, G. W.; Schlegel, H. B.; Scuseria, G. E.; Robb, M. A.; Cheeseman, J. R.; Scalmani, G.; Barone, V.; Mennucci, B.; Petersson, G. A.; Nakatsuji, H.; Caricato, M.; Li, X.; Hratchian, H. P.; Izmaylov, A. F.; Bloino, J.; Zheng, G.; Sonnenberg, J. L.; Hada, M.; Ehara, M.; Toyota, K.; Fukuda, R.; Hasegawa, J.; Ishida, M.; Nakajima, T.; Honda, Y.; Kitao, O.; Nakai, H.; Vreven, T.; Montgomery, J. A. Jr.; Peralta, J. E.; Ogliaro, F.; Bearpark, M.; Heyd, J. J.; Brothers, E.; Kudin, K. N.; Staroverov, V. N.; Kobayashi, R.; Normand, J.; Raghavachari, K.; Rendell, A.; Burant, J. C.; Iyengar, S. S.; Tomasi, J.; Cossi, M.; Rega, N.; Millam, J. M.; Klene, M.; Knox, J. E.; Cross, J. B.; Bakken, V.; Adamo, C.; Jaramillo, J.; Gomperts, R.; Stratmann, R. E.;

Yazyev, O.; Austin, A. J.; Cammi, R.; Pomelli, C.; Ochterski, J. W.; Martin, R. L.; Morokuma, K.; Zakrzewski, V. G.; Voth, G. A.; Salvador, P.; Dannenberg, J. J.; Dapprich, S.; Daniels, A. D.; Farkas, O.; Foresman, J. B.; Ortiz, J. V.; Cioslowski, J.; Fox, D. J. Gaussian 09, Revision A.01; Gaussian, Inc.: Wallingford, CT, 2009.
52. Grimme, S.; Antony, J.; Ehrlich, S.; Krieg, H. A. *J Chem Phys*. **2010**, *132*, 15.
53. Raspopov, S. A.; McMahon, T. B. A. *J. Mass Spectrom.* **2005**, *40*, 1536–1545.
54. Moghaddam, M. B.; Fridgen. T. D. *J. Phys. Chem. B.* **2013**, *117*, 6157–6164.
55. Jami-Alahmadi, Y.; Linford, B. D.; Fridgen, T. D. *J. Phys. Chem. B.* **2016**, *120*, 13039–13046.

Chapter 7

Summary and Outlook

In this work, the structures and energetics of non-covalent complexes were investigated using mass spectrometric methods. Sustained off-resonance irradiation collision-induced dissociation (SORI–CID), infrared multiple photon dissociation (IRMPD) spectroscopy in conjunction with computational techniques have been offering much more direct information on the subtleties of bonding, allowing for elucidation of the detailed structures of gaseous ions. The positions of prominent modes, such as the C=O, N–H, and O–H stretching can shift significantly with changes in their bonding environment making the IRMPD spectroscopy technique especially useful for the structural investigation of ionic complexes. The results were supported by comparing the IRMPD spectra with computed IR spectra obtained from the lowest energy isomers of each molecule. Furthermore, the blackbody infrared radiative dissociation (BIRD) technique, in an FTICR, has helped to quantitatively determine the dissociation kinetics and thermochemistry of these gas phase ions.

In the Chapter 3, mass spectrometric techniques have been applied to identify the unimolecular fragmentation pathways of protonated and metal cation-coordinated proline complexes. SORI–CID and IRMPD spectroscopy combined with simulated annealing (SA) have provided unique structural information. This cooperation explains why specially gas phase investigations allows one to gain some insight into the physical chemistry of these

complexes that, in principle, may be useful to rationalize the behavior of more complicated systems which present similar basic sites. Based on IRMPD spectroscopy and theoretical calculation, it was found that the structures of gaseous proton bound proline dimers exist as an N-protonated proline in which the intact amino acid is in the zwitterionic (ZW) form. Since there was no spectroscopic evidence in the 3200–3800 cm^{-1} region for a charge solvated (CS) structure, a well resolved C=O band at 1733 cm^{-1} from a previous spectroscopic study[1] was reassigned from a high energy CS isomer to a lower energy ZW form of the intact proline side. Comparison of experimental IRMPD spectra with computed spectra from computationally obtained structures of the sodium bound dimer of proline revealed a mixture of these species to exist in the gas phase. The presence of a free hydroxyl group may well be explained based on the existence of at least one CS form in the mixture of sodium bound prolines in the gas phase.

The research described in Chapter 3 opens several directions for further investigation of intramolecular interactions in stabilization of the ZW form of amino acids over the CS form, even in the gas phase. Gas phase addition of one water molecule at a time can imitate the role of water as a proton transfer in zwitterionic amino acids which may provide a better overall picture of the contribution of water in living organisms.

The importance of both the polarizability and size of the metal cation in determining the structure of metal-cationized peptides are the significant discoveries of Chapter 4. IRMPD spectroscopy in the 2700–3800 and 1000–1850 cm^{-1} regions combined with SORI-CID and computational methods have been used to determine the gas-phase structures of the $[M(Pro)_2\text{-}H]^+$ when M=Mn, Fe, Co, Ni, Cu, Zn, Mg, Ca, Sr and Ba. Under CID

conditions the unimolecular fragmentation pathways of $[M(Pro)_2\text{-}H]^+$ showed that all the complexes containing smaller metal dications tend to lose small neutral molecules such as water and carbon dioxide as main fragmentation pathways. When M was replaced by heavier metals, Ca, Sr and Ba, the loss of a proline was the main fragmentation pathway. With the exception of $Cu(Pro_2\text{-}H)^+$, all complexes involving transition metal dications and Mg lose H_2 upon collisional or IRMPD activation. IRMPD spectroscopy combined with the DFT calculations for $[M(Pro)_2\text{-}H]^+$ have revealed that all deprotonated transition metals, which are roughly the same size, have similar bands. The comparison of results reveals that the neutral proline forms strong ion–dipole complexes between the CS form of the intact proline and metal cation. On the contrary, the complexes containing larger metal cation, Ca^{2+}, Sr^{2+}, and Ba^{2+}, tend to maximize interaction between $M(Pro\text{-}H)^+$ and the negative end of the intact ZW proline in an ‘‘ionic’’ form. The IRMPD spectra for both $Mg(Pro_2\text{-}H)^+$ and $Mn(Pro_2\text{-}H)^+$ are concluded to have contributions from both CS and ZW structures. Interestingly, the calculations using both restricted open shell (ROB3LYP) and unrestricted (UB3LYP) DFT methods have shown that the lowest energy structure of $[Mn(Pro)_2\text{-}H]^+$ is a high spin complex with a sextet spin multiplicity, while in the $[Co(Pro)_2\text{-}H]^+$ and $[Ni(Pro)_2\text{-}H]^+$ complexes doublet and singlet states are the lowest energy structures, respectively.

Previous work[2] in our group has shown loss of H_2 from $[Zn(Pro_2\text{-}H)]^+$ which we decided to expand upon by replacing Zn with other first row doubly-charged transition metal ions. However, as mentioned, except copper, they all showed similar dissociation patterns. From this chapter, new insights into the reactivity of copper compared to the other

transition metals were obtained. Neither a difference in the lowest energy structure was observed based on the IRMPD spectroscopy, nor did the calculations revealed any unique structures for the Cu complex. However, copper has a positive standard reduction potential, meaning that compared to the other transition metals copper is difficult to oxidize. A comparable property in the gas phase is the ionization energy; copper has the highest second ionization energy of all the transition metals. It seems that at some point during H_2 elimination, electron density is pushed by a proline ring, but Cu^{2+} with a very high affinity for its electrons, does not readily accommodate the need for electron density to allow for H_2 elimination. It is of interest to consider this conclusion for future investigations using other secondary amino acids with similar basicity to better understand the role of proline as an important mechanistic factor in complexes containing Pro residues. It would be also beneficial to look into the complexes containing other metals, such as gold and thallium, that have similar second ionization energies as replacements for copper in proline clusters. Using the same approach would more strongly relate the standard reduction potential to the experimentally recorded dissociation pattern of this complexes.

The unimolecular fragmentation pathways and structures of the alkali metal ion-coordinated isomeric ProLeu/LeuPro dipeptides was investigated in Chapter 5. While CID of both isomers showed identical fragmentation pathways and could not differentiate between most isomers, the IRMPD spectroscopy in both the fingerprint and the CH/NH/OH regions has identified the structural differences of these isomers. In the ProLeu isomer, it was observed that if the metal cation is small, Li^+ and Na^+, it is bound to both carbonyl oxygens and the amine nitrogen. In contrast, for the larger Rb^+ and Cs^+ the amine nitrogen

is hydrogen bonded to the amide hydrogen, and metal cation is bounded to the two carbonyl groups. In the lithiated and sodiated LeuPro, the metal cation is bound to the amide carbonyl and the amine nitrogen while the amine nitrogen is hydrogen bonded to the carboxylic acid carbonyl. However, there is no hydrogen bond in the rubidiated and cesiated complexes; the metal cation is bound to both carbonyl oxygens and the amine nitrogen. The structures of metal cation bound dipeptides, therefore depend on several competing factors: non-covalent interactions; influence of peptide sequence on peptide-metal binding, and size of the metal cation.

The structures and stabilities of the self-assembled $Na^+(ProLeu)_3$ and $Na^+(LeuPro)_3$ have been studied in Chapter 6. In an attempt to differentiate between isomeric peptide complexes, IRMPD spectroscopy was used to help shed light on the structures, and BIRD is used to compare the relative dissociation energies of $Na^+(ProLeu)_3$ and $Na^+(LeuPro)_3$ complexes in the gas phase. According to the BIRD kinetics results, the rate constant for $Na^+(ProLeu)_3$ at, for example, 66 ^oC was 5.11 ± (0.36) x 10^{-3} s^{-1} whereas that for $Na^+(LeuPro)_3$ was found to be more than 5 times larger, 28.2 ± (0.04) x 10^{-3} s^{-1}. From the temperature dependence of the dissociation rate constants, the Arrhenius activation energies and entropies were determined for dipeptide loss from each isomeric complex. An excellent linear fit in both Arrhenius plots with r^2 values of 0.973 to 0.993 for $Na^+(LeuPro)_3$ and $Na^+(ProLeu)_3$ was found, respectively. The experimentally determined activation energies were compared with the energies obtained from master equation modeling (MEM). Comparison of the experimentally obtained binding energies with those computed

from electronic structure calculations and MEM are consistent with a larger binding energy for the $Na^+(ProLeu)_3$ complex.

Comparison of the experimental IRMPD spectra and the calculated spectra correspond to the lowest energy structures of both trimers in the 2750 – 3750 cm^{-1} region has supported the BIRD results. The proposed structures were found to be the best candidates for the interpretation of the experimental spectrum in CH/NH/OH region. Based on IRMPD results, the positions of prominent modes the IRMPD technique, useful for revealing the chemical differences of two proline−leucine residues containing dipeptides.

Finally, the current work addresses the applicability of the mass spectrometric techniques that can be used for both spectroscopic identification and the energetic approach of the complexes composed of amino acids and peptides. The simplicity of systems presented in this thesis may make it easier to grasp the concept of non-covalent interactions for future investigations in the fields in which the identification of behavior of larger structures is required.

7.1. References

1. Wu, R.; McMahon, T. B. *J. Am. Chem. Soc.* **2007**, *129*, 4864–4865.
2. Gholami, A. Fridgen, T. D. *Phys. Chem. Chem. Phys.* **2014**, *16*, 3134–3143.

Appendix A – Supporting Information for Chapter 3

Table A1.1. Table of relative Gibbs Energies and Enthalpies (298 K, in kJ mol^{-1}) for the different proton-bound proline dimer isomers.

Structure	$\Delta_{rel}G(\Delta_{rel}H)$ B3LYP/ 6-31+G(d,p)	$\Delta_{rel}G(\Delta_{rel}H)$ B3LYP/ 6-311+G(3df,3pd)// B3LYP/ 6-31+G(d,p)	$\Delta_{rel}G(\Delta_{rel}H)$ MP2/ 6-311+G(3df,3pd)// B3LYP/6-31+G(d,p)	$\Delta_{rel}G(\Delta_{rel}H)$ B3LYP/ 6-311+G(3df,3pd)	$\Delta_{rel}G(\Delta_{rel}H)$ MP2/ 6-31+G(d,p)	$\Delta_{rel}G(\Delta_{rel}H)$ MP2/ 6-311+G(3df,3pd)// MP2/6-31+G(d,p)	$\Delta_{rel}G(\Delta_{rel}H)$ B3LYP-D3/ 6-31+G(d,p)	$\Delta_{rel}G(\Delta_{rel}H)$ B3LYP-D3/ 6-311+G(3df,3pd)// B3LYP-D3/ 6-31+G(d,p)
ZW1	0.0(0.0)	0.0(0.0)	0.0(0.0)	0.0(0.0)	0.0(0.0)	0.0(0.0)	0.0(0.0)	0.0(0.0)
ZW2	1.9(-0.1)	1.7(-1.4)	1.3(-0.7)	1.7(-0.4)	2.6(0.5)	1.8(-0.3)	1.7(-0.1)	1.7(-0.1)
ZW3	2.1(3.7)	2.0(3.6)	2.7(4.3)	-0.3(1.7)	1.6(3.6)	1.3(3.3)	4.8(3.5)	4.9(3.7)
ZW4	7.3(9.6)	7.3(9.6)	3.7(6.0)	7.4(9.7)	0.8(3.1)	0.6(2.8)	9.9(5.6)	9.8(5.5)
ZW5	2.3(3.0)	2.4(3.1)	4.9(5.6)	2.4(3.1)	4.0(4.7)	5.4(6.1)	5.2(4.7)	4.9(4.4)
ZW6	3.4(5.4)	3.3(5.2)	6.8(8.8)	3.2(5.2)	6.6(8.6)	7.8(9.8)	6.5(7.5)	6.5(7.5)
CS7	7.2(8.6)	4.9(6.4)	7.5(9.0)	4.9(6.3)	13.6(15.1)	8.0(9.4)	9.6(9.2)	11.6(11.1)
ZW8	9.9(9.8)	10.6(10.4)	9.5(9.3)	10.5(10.4)	6.1(5.9)	7.3(7.2)	10.7(7.6)	10.2(7.1)
CS9	8.1(10.8)	5.6(8.3)	9.7(12.4)	5.5(8.2)	15.6(18.3)	10.6(13.3)	12.4(12.1)	14.7(14.3)
ZW10	9.9(9.7)	10.6(10.4)	9.9(9.7)	10.7(10.4)	6.1(5.8)	7.4(7.1)	10.7(7.6)	10.2(7.1)
CS11	8.4(10.3)	5.8(7.6)	10.0(11.9)					
ZW12	8.7(11.9)	9.4(12.6)	10.0(13.3)					
CS13	7.4(11.0)	5.1(8.7)	10.2(13.7)					
CS14	8.6(10.8)	6.0(8.2)	10.4(12.6)					
CS15	11.2(12.3)	11.7(12.8)	10.5(11.6)					
CS16	7.4(11.7)	4.9(9.2)	11.0(15.3)					
ZW17	14.4(15.9)	14.8(16.3)	12.4(13.9)					
ZW18	12.1(13.0)	12.9(13.9)	15.2(16.2)					
ZW19	13.7(15.0)	14.6(16.0)						
ZW20	18.0(16.9)	19.2(18.1)						
ZW21	12.9(19.6)	13.8(20.8)						
ZW22	15.0(14.8)							
CS23	18.4(24.8)							
CS24	21.9(27.0)							
CS25	21.6(27.9)							
ZW26	21.6(27.9)							
CS27	22.0(29.3)							
CS28	22.2(27.1)							
CS29	23.5(27.2)							
CS30	24.0(28.8)							
ZW31	25.3(26.1)							
CS32	25.7(30.5)							
ZW33	25.8(29.4)							
ZW34	26.9(29.2)							
ZW35	30.1(28.4)							
ZW36	32.1(29.8)							
CS37	32.3(37.9)							
ZW38	35.1(32.3)							
ZW39	40.5(38.4)							
ZW40	42.6(42.0)							
ZW41	49.1(52.0)							
ZW42	55.6(51.9)							

Table A1.2. Table of relative Gibbs Energies and Enthalpies (298 K, in kJ mol^{-1}) for the different sodium-bound proline dimer isomers.

Structure	$\Delta_{rel}G(\Delta_{rel}H)$ B3LYP/ 6-31+G(d,p)	$\Delta_{rel}G(\Delta_{rel}H)$ B3LYP/ 6-311+G(3df,3pd)// B3LYP/ 6-31+G(d,p)	$\Delta_{rel}G(\Delta_{rel}H)$ B3LYP/ 6-311+G(3df,3pd)	$\Delta_{rel}G(\Delta_{rel}H)$ MP2/ 6-31+G(d,p)	$\Delta_{rel}G(\Delta_{rel}H)$ MP2/ 6-311+G(3df,3pd)// MP2/6-31+G(d,p)	$\Delta_{rel}G(\Delta_{rel}H)$ B3LYP-D3/ 6-31+G(d,p)	$\Delta_{rel}G(\Delta_{rel}H)$ B3LYP-D3/ 6-311+G(3df,3pd)// B3LYP-D3/ 6-31+G(d,p)
ZW-CS1	0.0(0.0)	0.0(0.0)	0.0(0.0)	0.0(0.0)	0.0(0.0)	3.4(5.8)	2.9(5.3)
ZW-ZW2	-1.0(-5.9)	1.6(-3.3)	1.6(-3.3)	-9.0(-13.9)	2.2(-0.6)	4.4(2.0)	1.5(-0.9)
ZW-CS3	1.9(3.8)	2.5(4.5)	0.6(2.5)	2.2(4.1)	3.6(5.5)	7.8(10.0)	7.2(9.5)
ZW-CS4	3.5(-0.8)	3.1(-1.2)	3.1(-1.2)	1.0(-3.3)	4.9(0.6)	0.0(0.0)	0.0(0.0)
ZW-CS5	2.9(-1.6)	3.6(-0.9)	1.6(-3.3)	1.0(-3.5)	1.9(-2.6)	2.0(2.7)	1.4(2.1)
ZW-CS6	6.1(0.4)	3.7(-1.9)	7.7(2.1)	4.2(-1.4)	8.1(2.5)	1.3(1.9)	1.5(2.1)
ZW-ZW7	1.3(-6.5)	3.8(-3.8)	3.8(-3.9)	-6.6(-14.4)	0.8(-6.9)	6.6(1.3)	3.8(-1.6)
ZW-ZW8	6.1(0.4)	4.9(-0.7)	8.2(2.8)	-3.0(-8.4)	6.0(0.5)	7.8(7.0)	4.7(3.9)
ZW-ZW9	2.5(-3)	5.3(-0.2)	7.5(2.0)	-3.7(-9.2)	5.3(-0.2)	2.3(-0.6)	2.5(-0.4)
ZW-CS10	6.8(1.5)	6.2(0.9)				7.6(4.0)	4.5(3.0)
ZW-CS11	7.4(6.3)	6.8(5.7)					
ZW-CS12	8.2(2.7)	7.9(2.4)	10.1(4.6)	7.1(1.6)	12.5(6.9)		
ZW-CS13	8.3(3.7)	8.0(3.4)					
ZW-CS14	9.3(4.8)	8.9(4.3)					
ZWZW15	6.5(0.9)	9.4(3.9)					
ZWZW16	8.0(1.6)	10.9(4.5)	13.1(6.7)	3.5(-2.8)	14.1(7.7)		
ZW-CS17	12.0(0.8)	11.2(0.0)					
CS-CS18	12.4(11.1)	11.5(10.1)					
CS-CS19	14.2(13.4)	13.1(12.2)					
CS-CS20	19.8(16.1)	16.3(12.7)					
ZW-CS21	19.7(16.0)	19.3(15.7)					
ZW-CS22	20.0(15.9)	19.6(15.5)					
CS-CS23	23.9(18.2)	19.9(14.1)					
ZW-CS24	23.2(19.3)	23.0(19.1)					
ZW-CS25	19.5(19.2)	23.1(19.1)					
ZW-CS26	28.0(24.6)	23.6(20.2)					
ZW-CS27	27.9(24.5)	24.0(20.7)					
CS-CS28	28.9(27.7)	26.6(25.5)					
ZW-CS29	32.0(33.7)	30.2(31.5)					
ZW-CS30	33.9(33.9)	31.6(31.6)					
ZW-CS31	31.2(28.5)	32.8(30.1)					
ZW-CS32	42.3(37.2)	39.3(34.2)					

Figure A1.1. Plot of potential energy vs. simulated annealing cycle obtained for $[(Pro)_2H]^+$ ion.

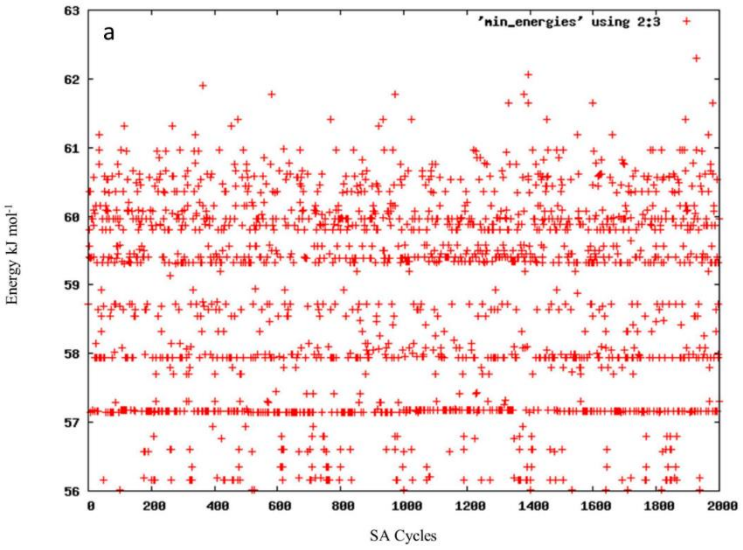

Figure A1.2. Groups of structures with similar energies obtained for $[(Pro)_2H]^+$ ion.

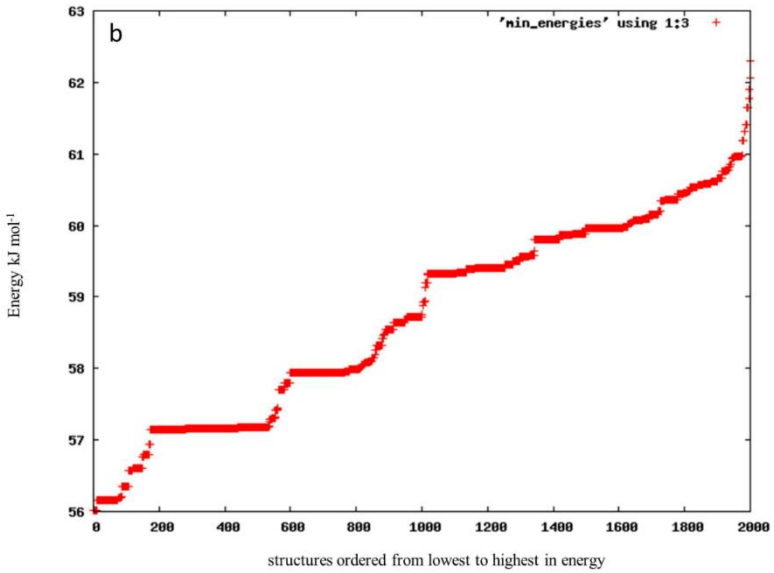

Figure A1.3a. Relative 298 K Gibbs energies and (enthalpies) computed for $[(Pro)_2H]^+$ using MP2/6-311+G(3df,3pd)//B3LYP/6-31+G(d,p). Energies are provided in kJ mol^{-1}.

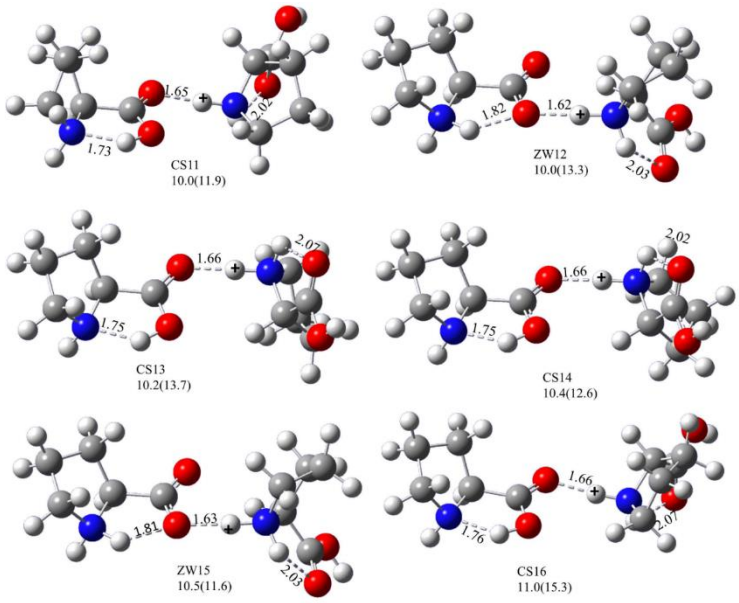

Figure A1.3b. Relative 298 K Gibbs energies and (enthalpies) computed for $[(Pro)_2H]^+$ using MP2/6-311+G(3df,3pd)//B3LYP/6-31+G(d,p). Energies are provided in kJ mol^{-1}.

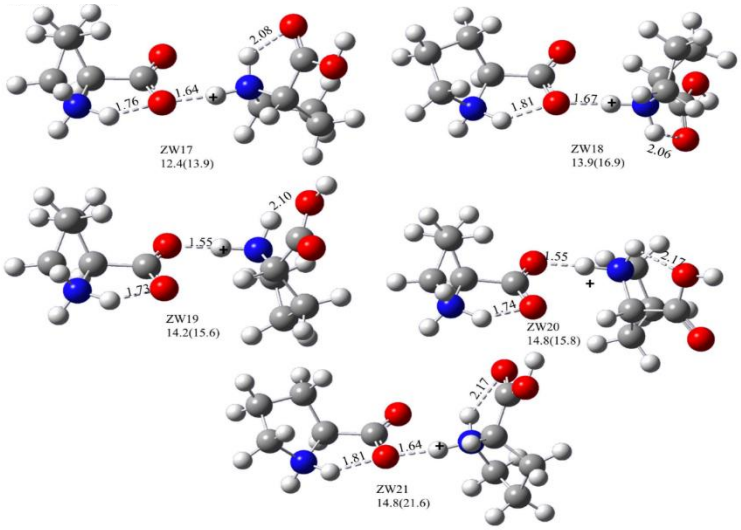

Figure A1.4. IRMPD spectrum of $(Pro)_2H^+$ investigated by McMahon and Wu between (1000-2000cm^{-1}) compared with the B3LYP/6-31+G(d,p) predicted spectra for ZW1, ZW4.

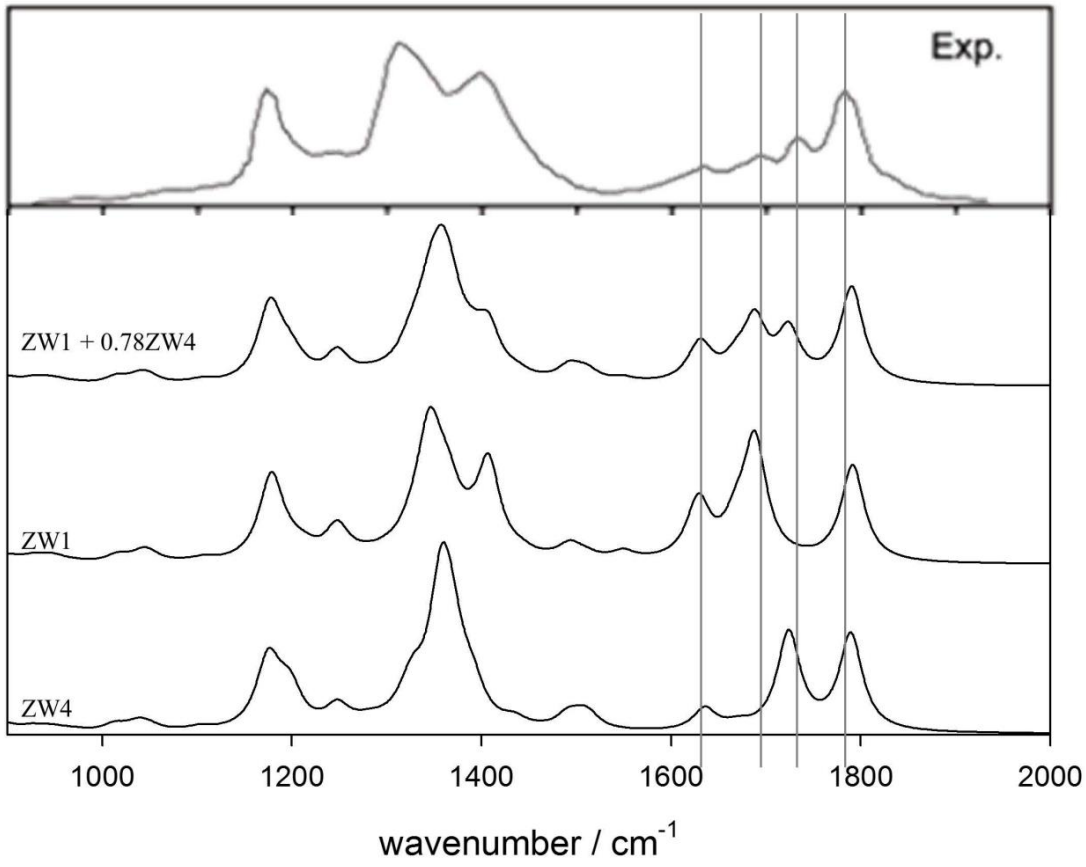

Figure A1.5a. Relative 298 K Gibbs energies and (enthalpies) computed for $[(Pro)_2Na]^+$ using B3LYP/6-311+G(3df,3pd)//B3LYP/6-31+G(d,p)). Energies are provided in kJ mol^{-1}.

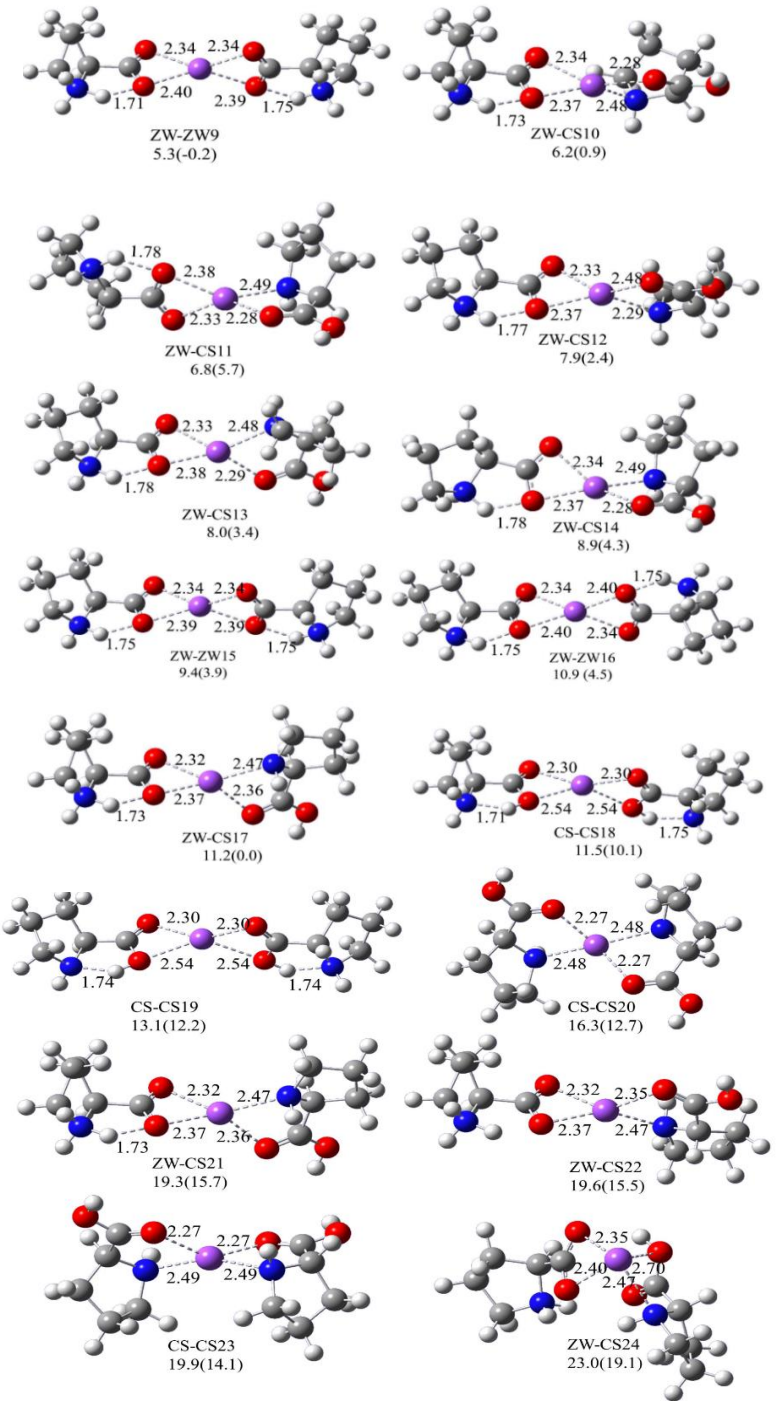

Figure A1.5b. Relative 298 K Gibbs energies and (enthalpies) computed for $[(Pro)_2Na]^+$ using B3LYP/6-311+G(3df,3pd)//B3LYP/6-31+G(d,p)). Energies are provided in kJ mol^{-1}.

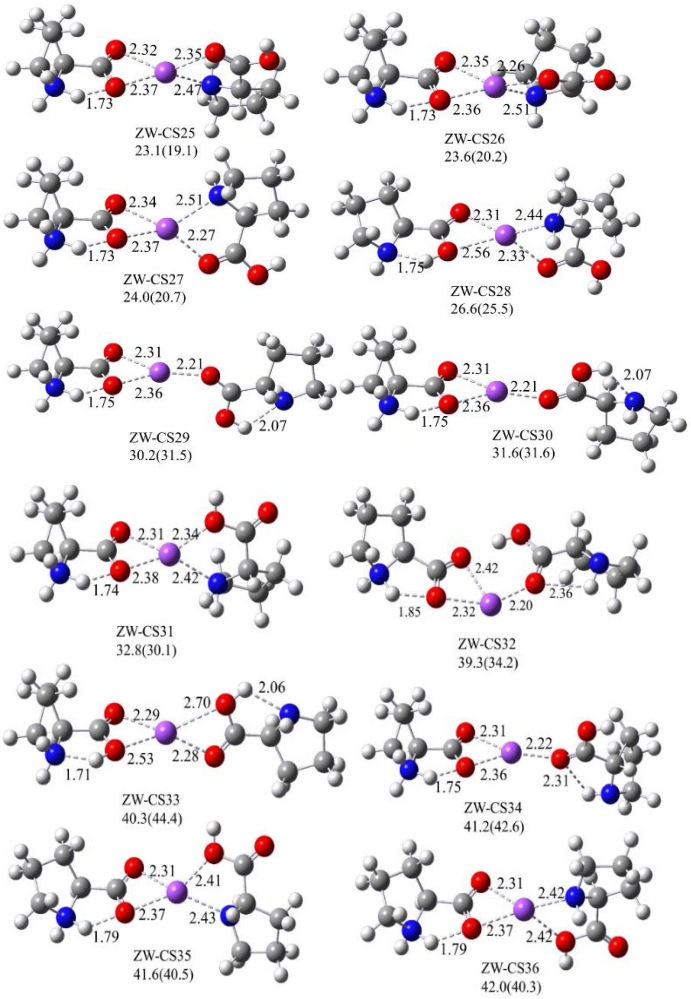

Appendix B – Supporting Information for Chapter 4

Figure A2.1. SORI/CID MS/MS spectra of $[Mn(Pro\text{-}H)(Pro)]^+$.

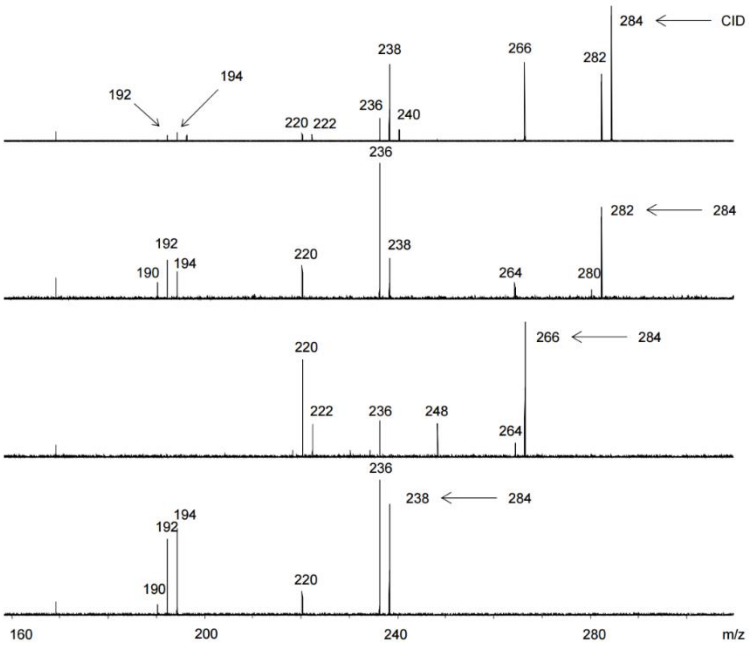

Figure A2.2. SORI/CID MS/MS spectra of $[Fe(Pro\text{-}H)(Pro)]^+$.

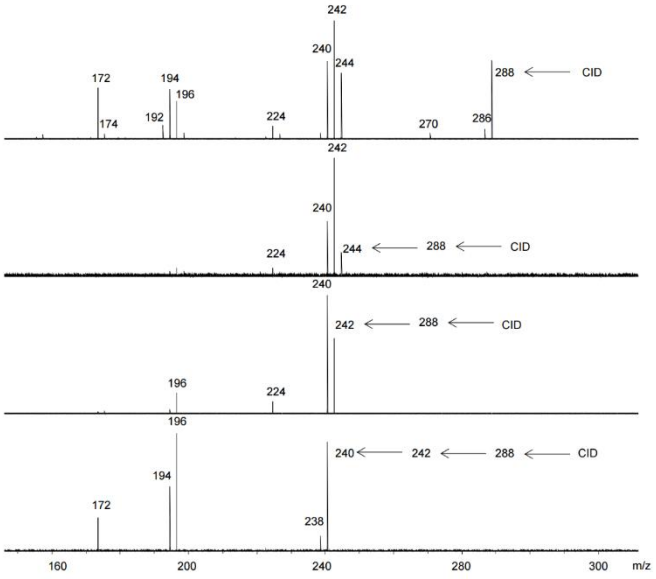

Figure A2.3. SORI/CID MS/MS spectra of $[Co(Pro\text{-}H)(Pro)]^+$.

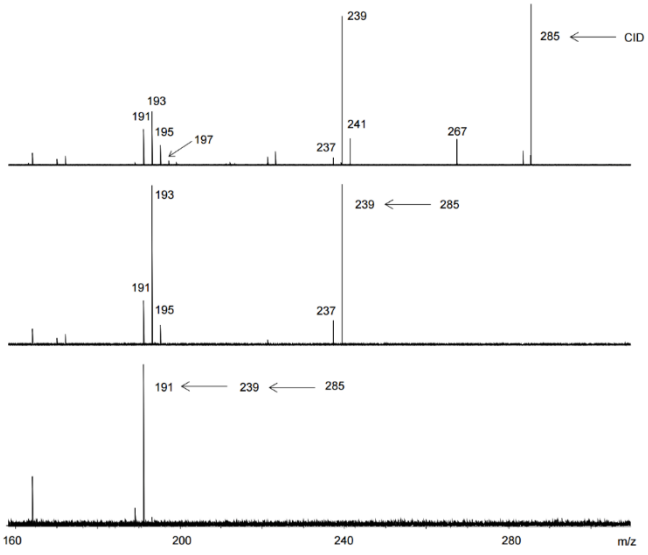

Figure A2.4. SORI/CID MS/MS spectra of $[Fe(Pro\text{-}H)(Pro)]^+$.

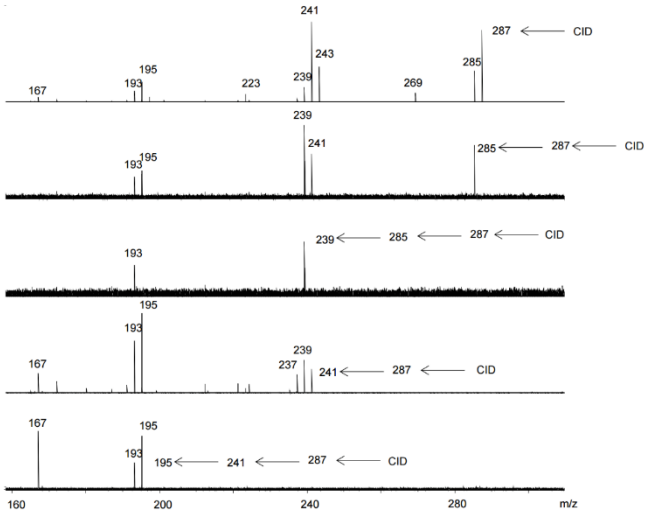

Figure A2.5. SORI/CID spectra of the $[Cu(Pro\text{-}H)(Pro)]^+$.

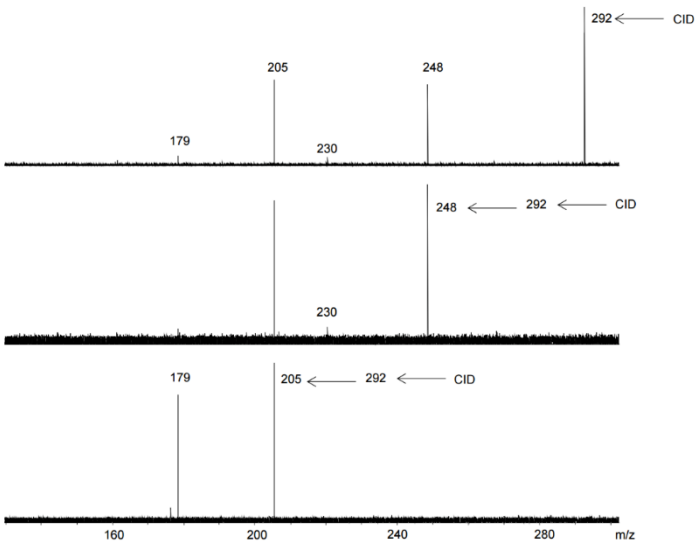

Figure A2.6. SORI/CID spectra of the $[Mg(Pro\text{-}H)(Pro)]^+$.

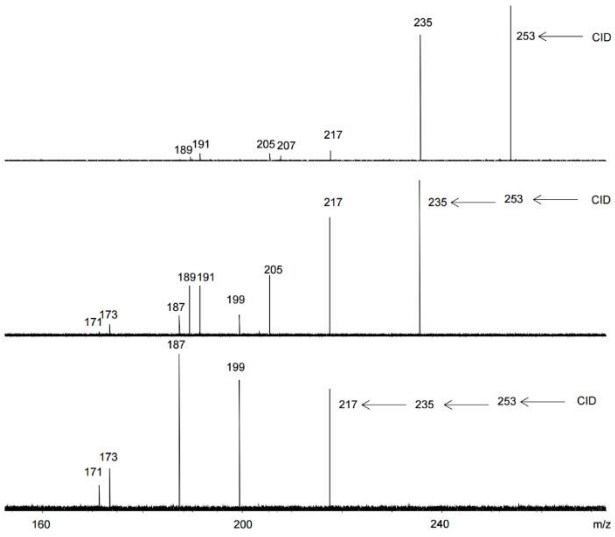

Figure A2.7. SORI/CID spectra of the $[Ca(Pro\text{-}H)(Pro)]^+$.

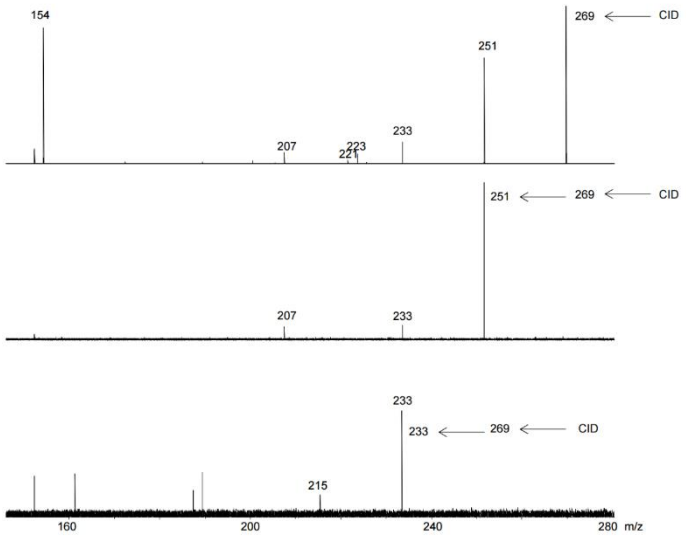

Figure A2.10. IRMPD spectra for $[Cu(Pro_2\text{-}H)]^+$ and $[Ni(Pro_2\text{-}H)]^+$ compared with the computed spectra for the four NO-NO-CS structures. Structures can be seen in Figure A.2.12a) and A 2.13a).

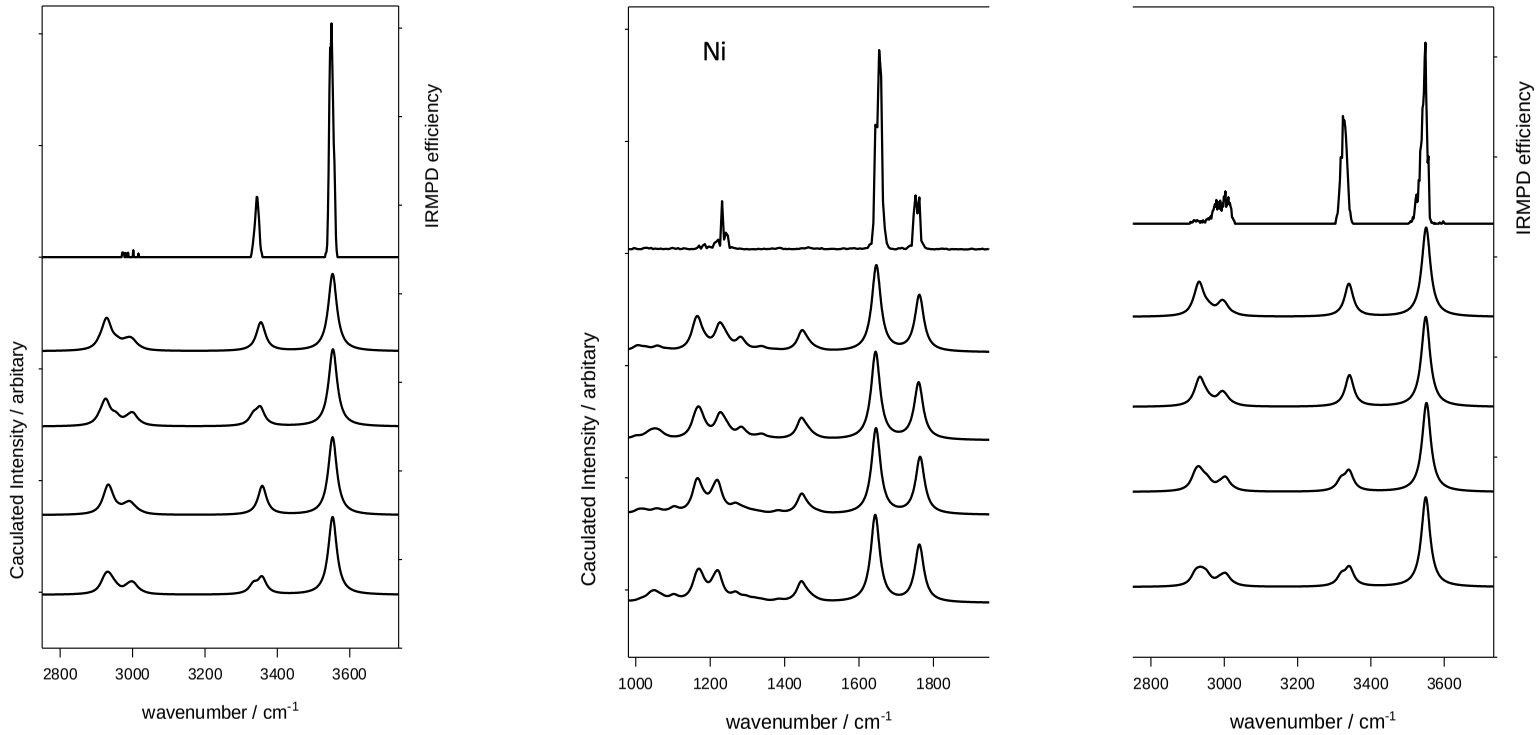

Figure A2.11a. Relative 298 K Gibbs energies (and enthalpies) computed at the B3LYP/6-311++G(3df,3pd)//6-31+G(d,p) (black) and B3LYP/6-31+G(d,p) (red) are reported for the NO-NO-CS $[Zn(Pro)_2\text{-}H]^+$ complexes.

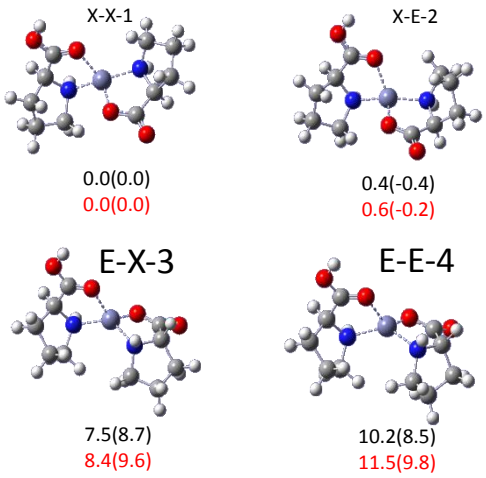

Figure A2.11b. Relative 298 K Gibbs energies (and enthalpies) computed at the B3LYP/6-311++G(3df,3pd)//6-31+G(d,p) (black) and B3LYP/6-31+G(d,p) (red) are reported for the OO-NO-ZW $[Zn(Pro)_2\text{-}H]^+$ complexes.

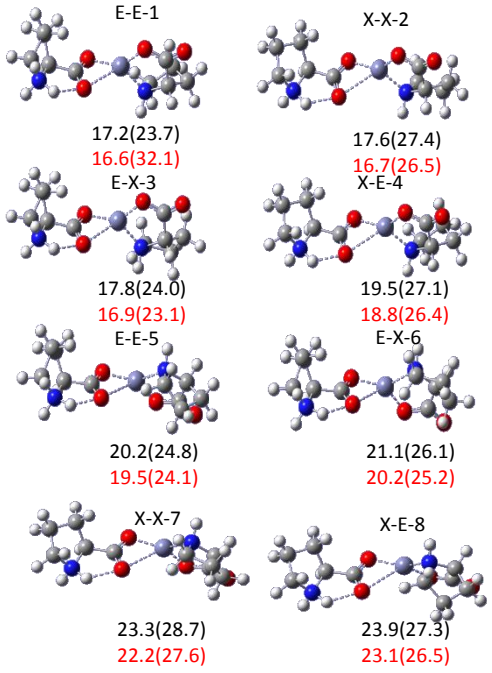

Figure A2.11c. Relative 298 K Gibbs energies (and enthalpies) computed at the B3LYP/6-311++G(3df,3pd)//6-31+G(d,p) (black) and B3LYP/6-31+G(d,p) (red) are reported for the OO-OO-ZW $[Zn(Pro)_2\text{-}H]^+$ complexes.

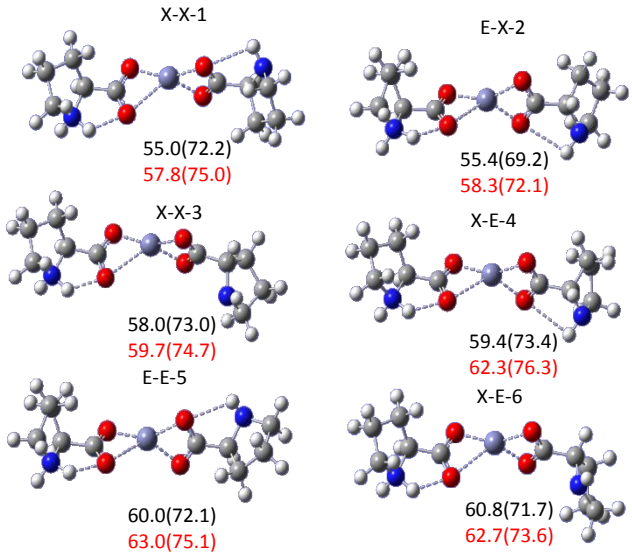

Figure A2.11d. Relative 298 K Gibbs energies (and enthalpies) computed at the B3LYP/6-311++G(3df,3pd)//6-31+G(d,p) (black) and B3LYP/6-31+G(d,p) (red) are reported for the NO-OO-CS [Zn(Pro)2-H]+ complexes.

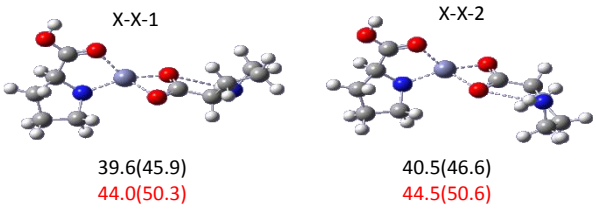

Figure A2.12a. Relative 298 K Gibbs energies and (enthalpies) computed using B3LYP/6-311++G(3df,3pd)//6-31+G(d,p) (black) and B3LYP/6-31+G(d,p) (red) for conformers of the NO-NO-CS isomers of the $[Cu(Pro)_2\text{-}H]^+$ complex. The structures are all doublets.

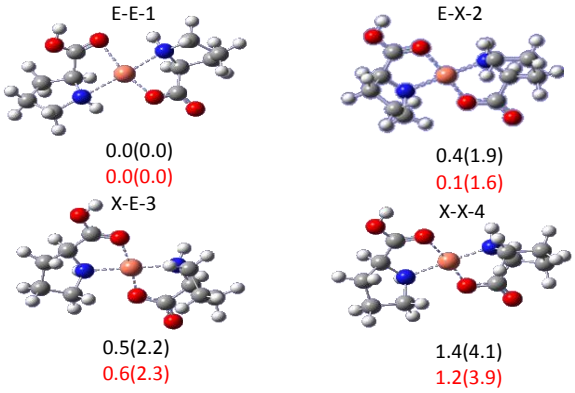

Figure A2.12b. Relative 298 K Gibbs energies and (enthalpies) computed using B3LYP/6-311++G(3df,3pd)//6-31+G(d,p) (black) and B3LYP/6-31+G(d,p) (red) for conformers of the OO-NO-ZW isomers of the $[Cu(Pro)_2\text{-}H]^+$ complex. The structures are all doublets.

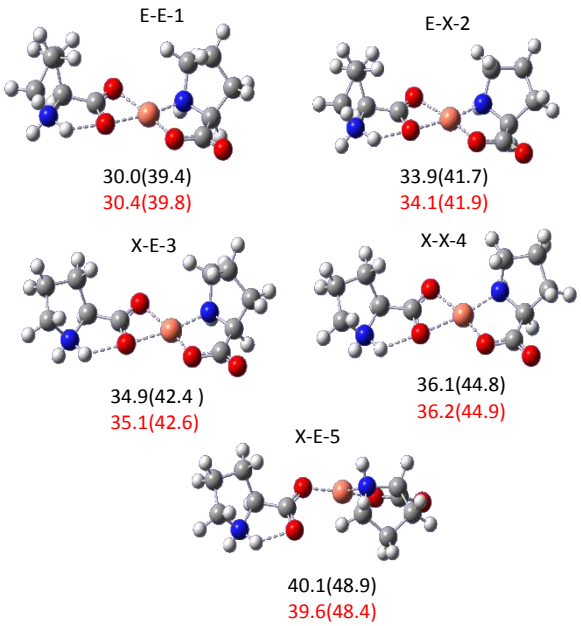

Figure A2.12c. Relative 298 K Gibbs energies and (enthalpies) computed using B3LYP/6-311++G(3df,3pd)//6-31+G(d,p) (black) and B3LYP/6-31+G(d,p) (red) for conformers of the NO-OO-CS isomers of the $[Cu(Pro)_2\text{-}H]^+$ complex. The structures are all doublets.

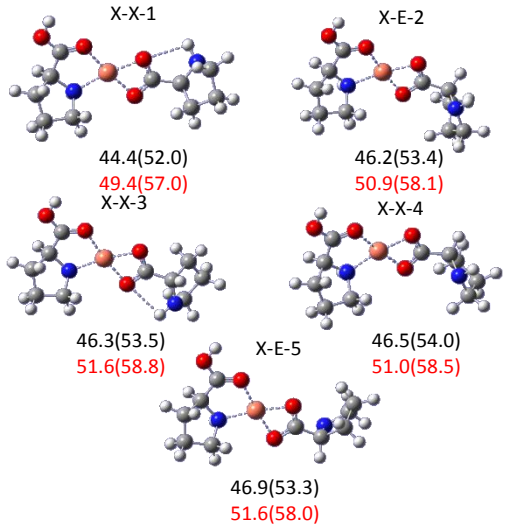

Figure A2.12d. Relative 298 K Gibbs energies and (enthalpies) computed using B3LYP/6-311++G(3df,3pd)//6-31+G(d,p) (black) and B3LYP/6-31+G(d,p) (red) for conformers of the OO-OO-ZW isomers of the $[Cu(Pro)_2\text{-}H]^+$ complex. The structures are all doublets.

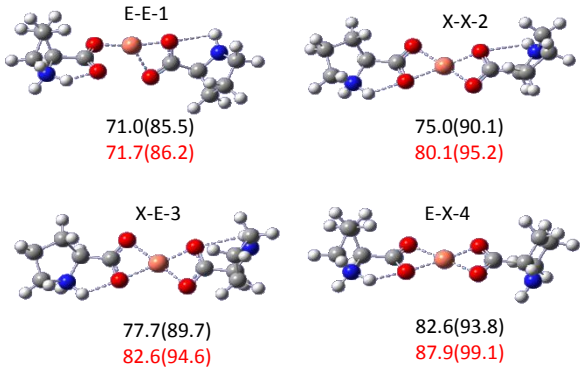

Figure A2.13a. Relative 298 K Gibbs energies and (enthalpies) computed using B3LYP/6-311++G(3df,3pd)//6-31+G(d,p) (black) and B3LYP/6- 31+G(d,p) (red) for conformers of the NO-NO-CS isomers of the $[Ni(Pro)_2\text{-}H]^+$ complex. The structures are all singlets.

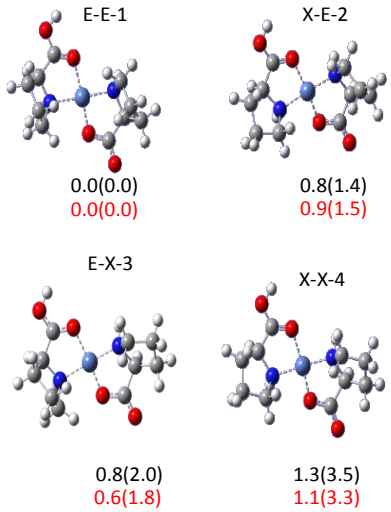

Figure A2.13b. Relative 298 K Gibbs energies and (enthalpies) computed using B3LYP/6-311++G(3df,3pd)//6-31+G(d,p) (black) and B3LYP/6- 31+G(d,p) (red) for conformers of the OO-NO-ZW isomers of the $[Ni(Pro)_2\text{-}H]^+$ complex. The structures are all triplets.

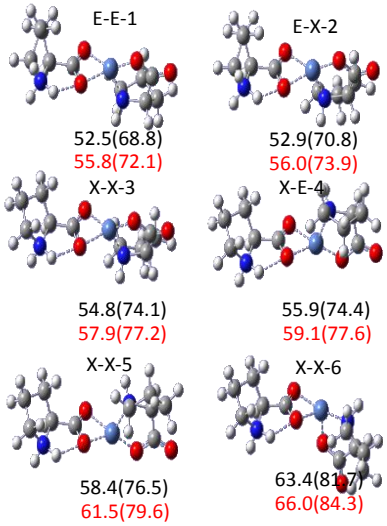

Figure A2.13c. Relative 298 K Gibbs energies and (enthalpies) computed using B3LYP/6-311++G(3df,3pd)//6-31+G(d,p) (black) and B3LYP/6-31+G(d,p) (red) for conformers of the NO-OO-CS isomers of the $[Ni(Pro)_2\text{-}H]^+$ complex. The structures are all singlets.

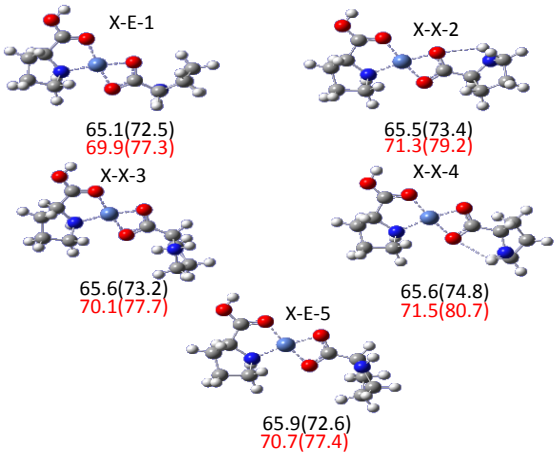

Figure A2.13d. Relative 298 K Gibbs energies and (enthalpies) computed using B3LYP/6-311++G(3df,3pd)//6-31+G(d,p) (black) and B3LYP/6-31+G(d,p) (red) for conformers of the OO-OO-ZW isomers of the $[Ni(Pro)_2\text{-}H]^+$ complex. The structures are all triplets.

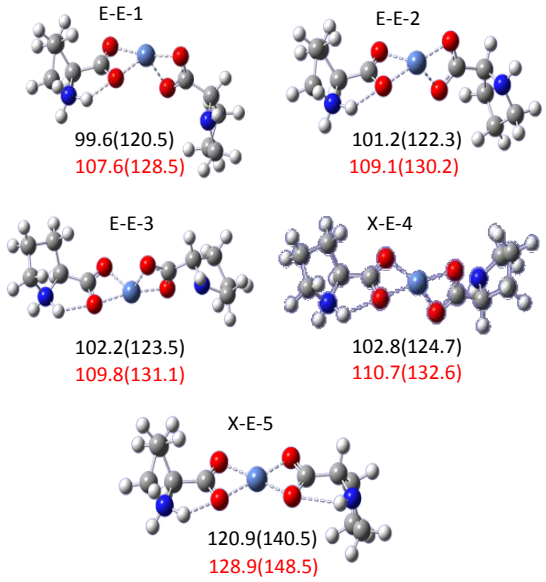

Figure A2.14a. Relative 298 K Gibbs energies and (enthalpies) computed using B3LYP/6-311++G(3df,3pd)//6-31+G(d,p) (black) and B3LYP/6-31+G(d,p) (red) for conformers of the NO-NO-CS isomers of the $[Co(Pro)_2\text{-}H]^+$ complex. The structures are all doublets.

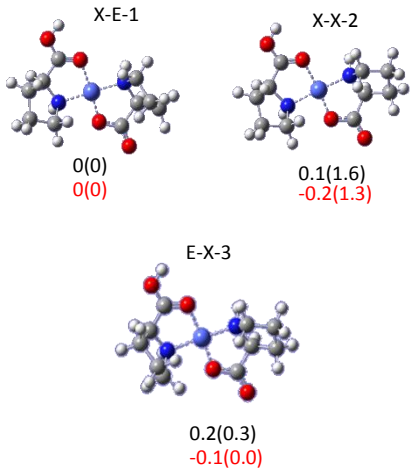

Figure A2.14b. Relative 298 K Gibbs energies and (enthalpies) computed using B3LYP/6-311++G(3df,3pd)//6-31+G(d,p) (black) and B3LYP/6-31+G(d,p) (red) for conformers of the OO-NO-ZW isomers of the $[Co(Pro)_2\text{-}H]^+$ complex. The structures are all quartets.

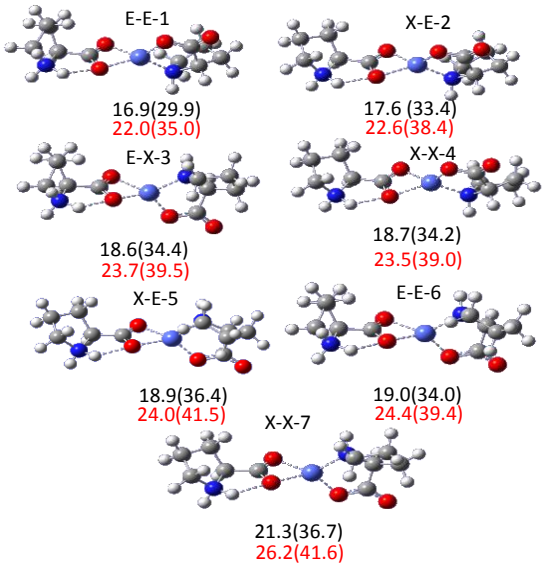

Figure A2.14c. Relative 298 K Gibbs energies and (enthalpies) computed using B3LYP/6-311++G(3df,3pd)//6-31+G(d,p) (black) and B3LYP/6-31+G(d,p) (red) for conformers of the NO-OO-CS isomers of the $[Co(Pro)_2\text{-}H]^+$ complex. The structures are all quartets.

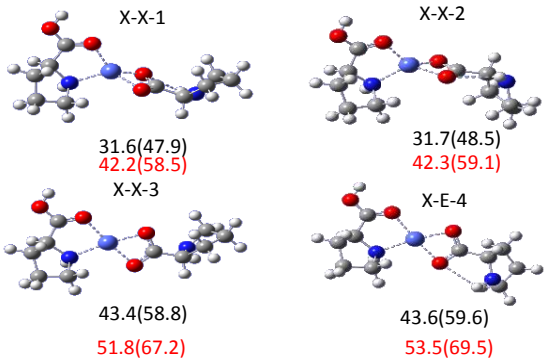

Figure A2.14d. Relative 298 K Gibbs energies and (enthalpies) computed using B3LYP/6-311++G(3df,3pd)//6-31+G(d,p) (black) and B3LYP/6-31+G(d,p) (red) for conformers of the OO-OO-ZW isomers of the $[Co(Pro)_2\text{-}H]^+$ complex. The structures are all quartets.

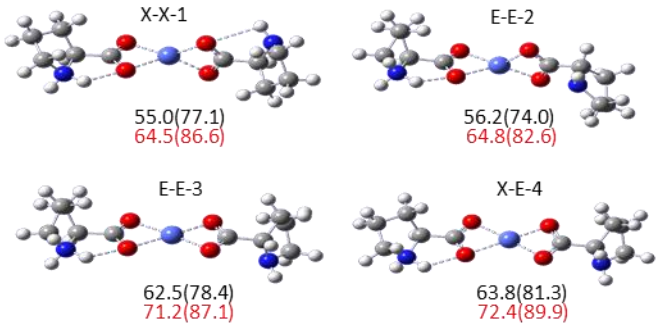

Figure A2.15a. Relative 298 K Gibbs energies and (enthalpies) computed using B3LYP/6-311++G(3df,3pd)//6-31+G(d,p) (black) and B3LYP/6-31+G(d,p) (red) for conformers of the NO-NO-CS isomers of the $[Fe(Pro)_2\text{-}H]^+$ complex. The structures are all quintets.

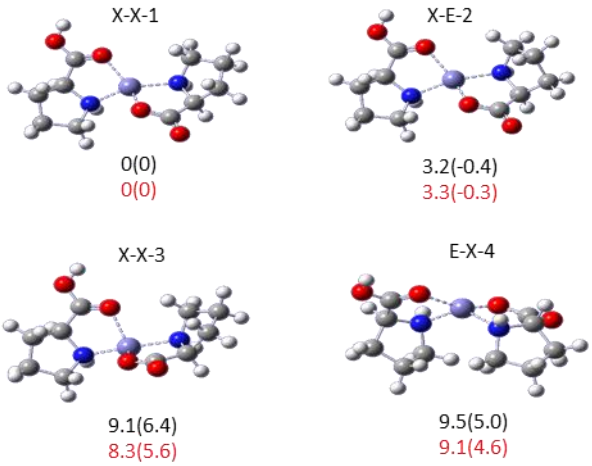

Figure A2.15b. Relative 298 K Gibbs energies and (enthalpies) computed using B3LYP/6-311++G(3df,3pd)//6-31+G(d,p) (black) and B3LYP/6-31+G(d,p) (red) for conformers of the OO-NO-ZW isomers of the $[Fe(Pro)_2\text{-}H]^+$ complex. The structures are all quintets.

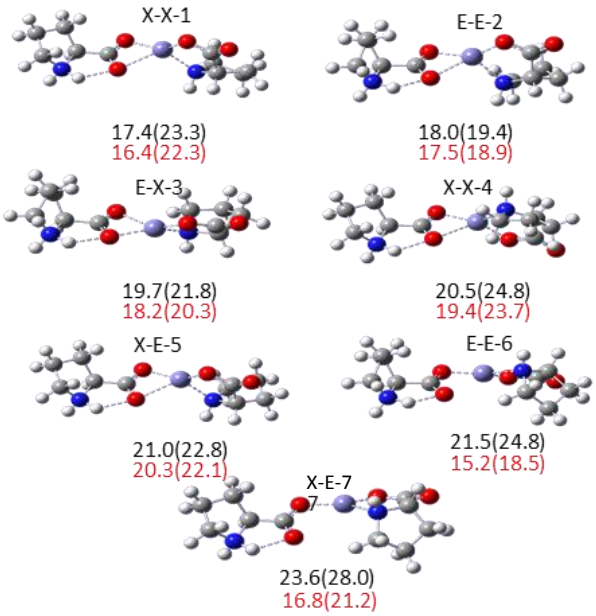

Figure A2.15c. Relative 298 K Gibbs energies and (enthalpies) computed using B3LYP/6-311++G(3df,3pd)//6-31+G(d,p) (black) and B3LYP/6- 31+G(d,p) (red) for conformers of the NO-OO-CS isomers of the $[Fe(Pro)_2\text{-}H]^+$ complex. The structures are all quintets.

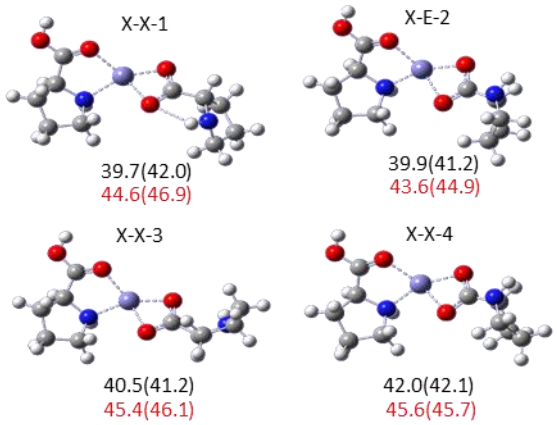

Figure A2.15d. Relative 298 K Gibbs energies and (enthalpies) computed using B3LYP/6-311++G(3df,3pd)//6-31+G(d,p) (black) and B3LYP/6- 31+G(d,p) (red) for conformers of the OO-OO-ZW isomers of the $[Fe(Pro)_2\text{-}H]^+$ complex. The structures are all quintets.

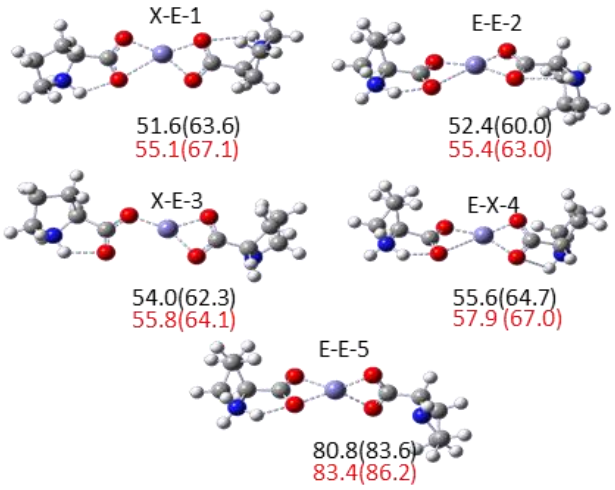

Figure A2.16a. Relative 298 K Gibbs energies and (enthalpies) computed using B3LYP/6-311++G(3df,3pd)//6-31+G(d,p) (black) and B3LYP/6-31+G(d,p) (red) for conformers of the NO-NO-CS isomers of the $[Mn(Pro)_2\text{-}H]^+$ complex. The structures are all sextets.

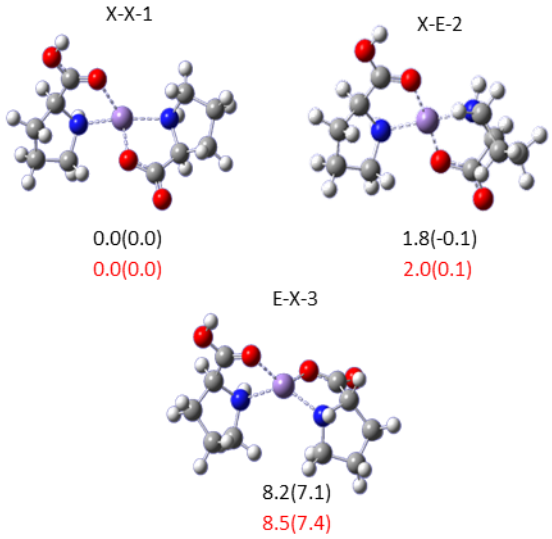

Figure A2.16b. Relative 298 K Gibbs energies and (enthalpies) computed using B3LYP/6-311++G(3df,3pd)//6-31+G(d,p) (black) and B3LYP/6-31+G(d,p) (red) for conformers of the OO-OO-ZW isomers of the $[Mn(Pro)_2\text{-}H]^+$ complex. The structures are all sextets.

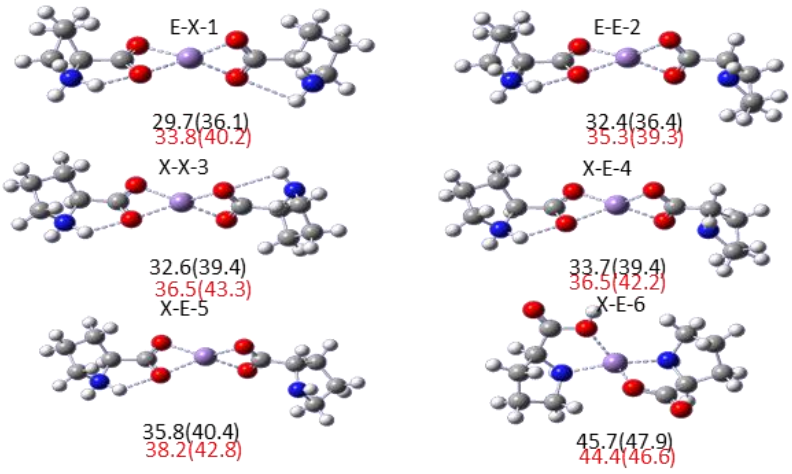

Figure A2.16c. Relative 298 K Gibbs energies and (enthalpies) computed using B3LYP/6-311++G(3df,3pd)//6-31+G(d,p) (black) and B3LYP/6-31+G(d,p) (red) for conformers of the OO-NO-ZW isomers of the $[Mn(Pro)_2\text{-}H]^+$ complex. The structures are all sextets.

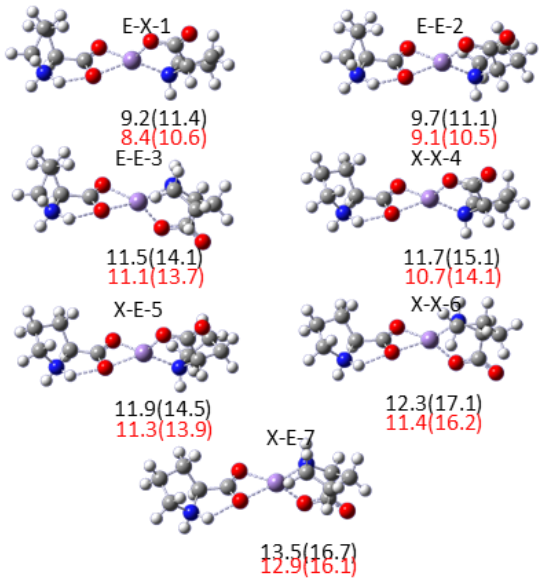

Figure A2.16d. Relative 298 K Gibbs energies and (enthalpies) computed using B3LYP/6-311++G(3df,3pd)//6-31+G(d,p) (black) and B3LYP/6-31+G(d,p) (red) for conformers of the NO-OO-CS isomers of the $[Mn(Pro)_2\text{-}H]^+$ complex. The structures are all sextets.

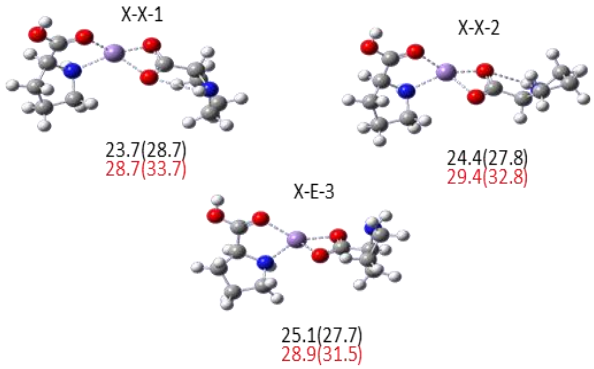

Figure A2.17. Comparison of the experimental IRMPD spectrum and calculated absorbance spectra of the lowest energy structures of each form of the $[Fe(Pro)_2\text{-}H]^+$ in a) 1000 to 2000 cm^{-1} region and b) 2800 to 3800 cm^{-1} region.

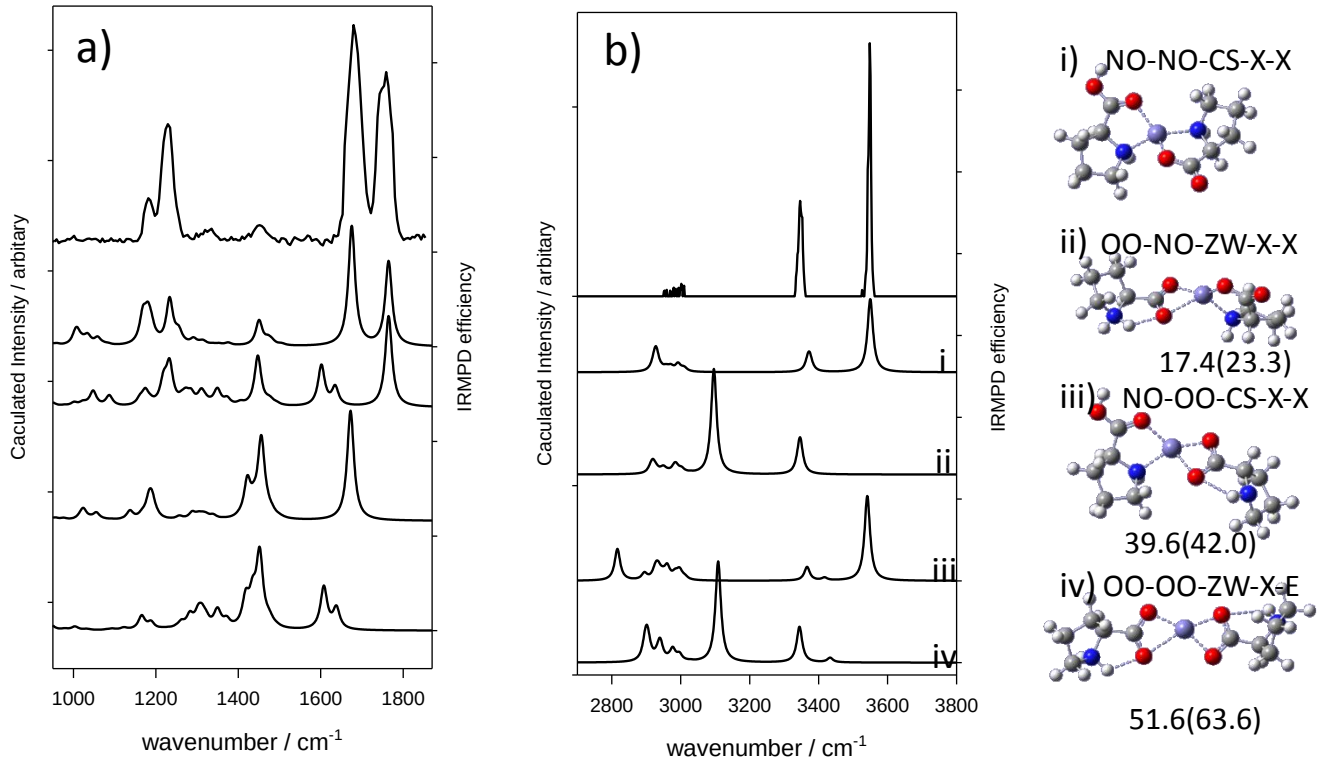

Figure A2.18. Comparison of the experimental IRMPD spectrum and calculated absorbance of the lowest energy structures of each form of the $[Ni(Pro)_2\text{-}H]^+$ in a) 1000 to 2000 cm^{-1} region and b) 2800 to 3800 cm^{-1} region.

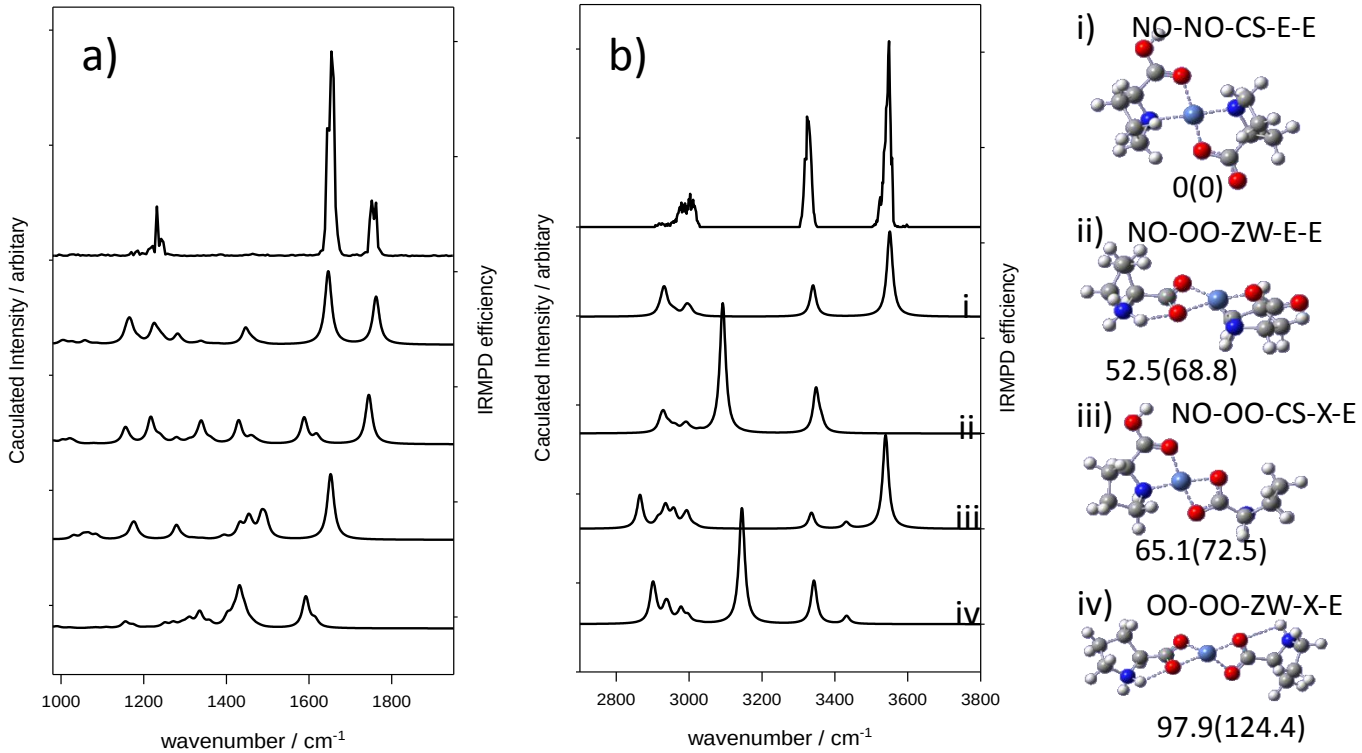

Figure A2.19. IRMPD spectra relative 298 K Gibbs energies and (enthalpies) computed using B3LYP/6- 31+G(d,p) for the lowest energy conformers of the $[Mn(Pro)_2 -H]^+$ complex (black color) along with same complexes containing two explicit water molecules (red color). The structures are all sextets.

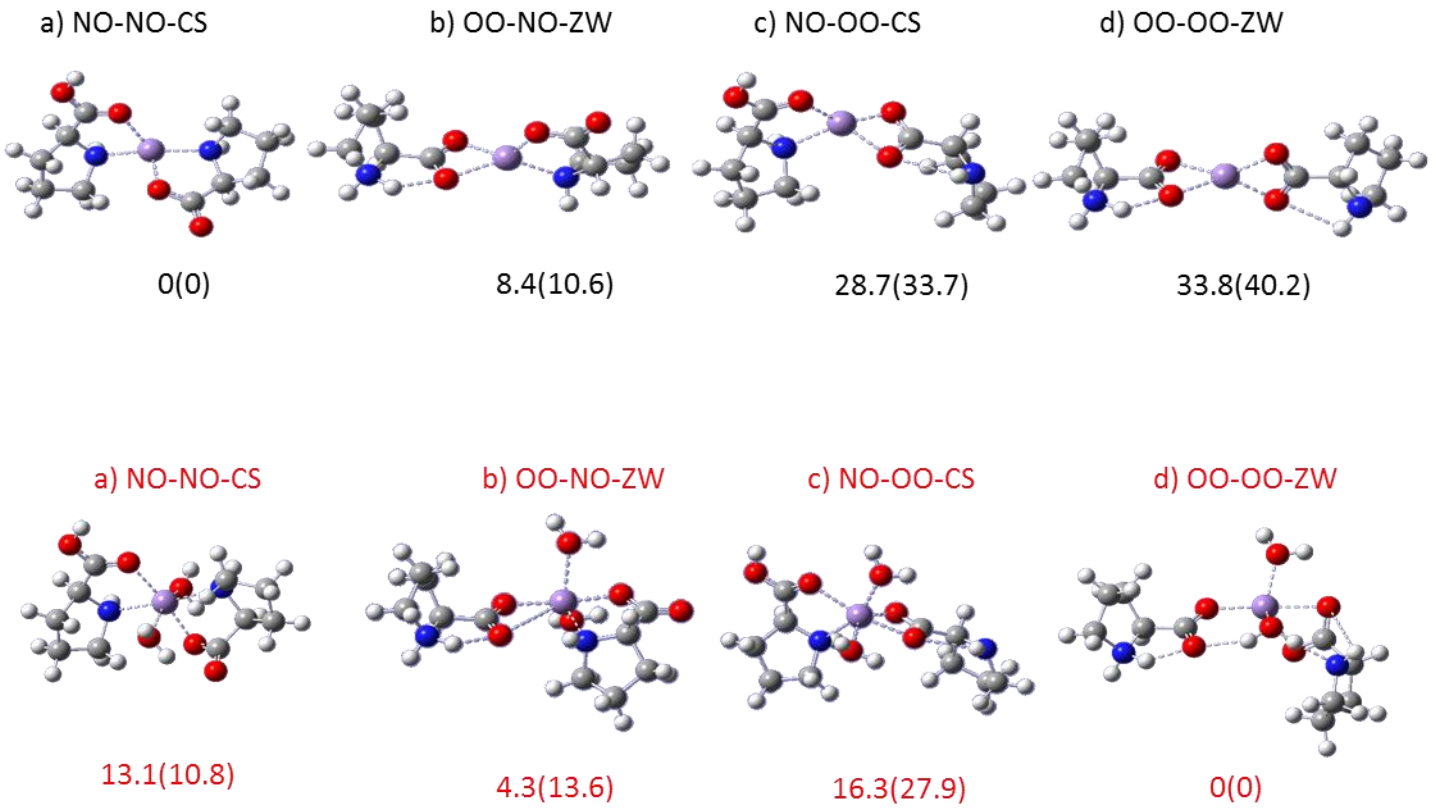

Figure A2.20. IRMPD spectra relative 298 K Gibbs energies and (enthalpies) computed using B3LYP/6- 31+G(d,p) for the lowest energy conformers of the $[Cu(Pro)_2 - H]^+$ complex (black color) along with same complexes containing two explicit water molecules (red color). The structures are all doublets.

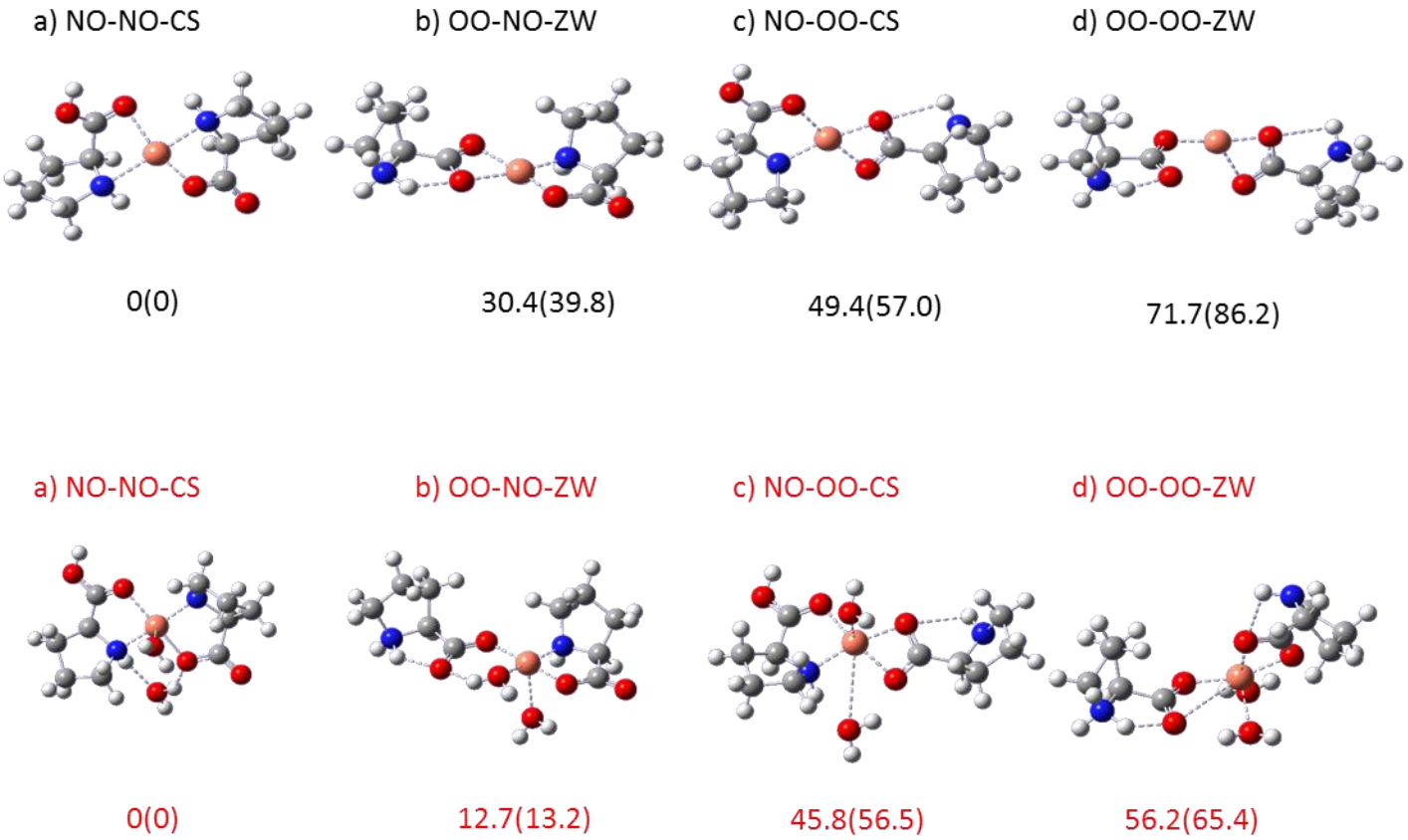

Figure A2.21a. Relative 298 K Gibbs energies and (enthalpies) computed using B3LYP/6-311++G(3df,3pd)//6-31+G(d,p) for conformers of the NO-NO-CS isomers of the $[Mg(Pro)_2\text{-}H]^+$ complex.

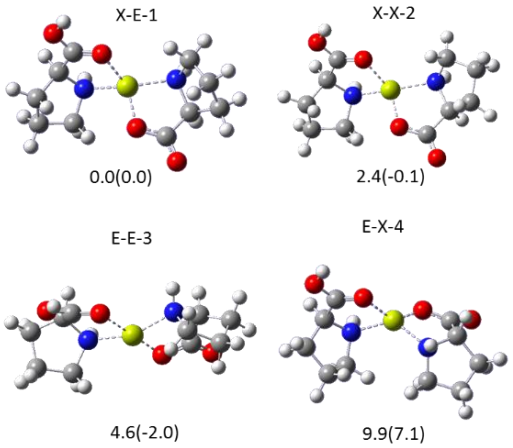

Figure A2.21b. Relative 298 K Gibbs energies and (enthalpies) computed using B3LYP/6-311++G(3df,3pd)//6-31+G(d,p) for conformers of the OO-NO-ZW isomers of the $[Mg(Pro)_2\text{-}H]^+$ complex.

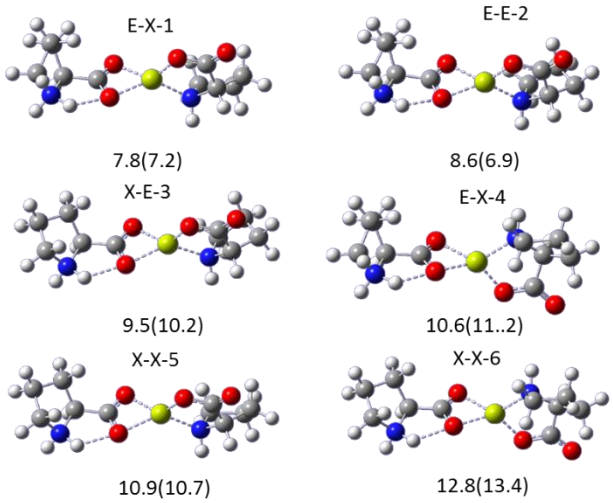

Figure A2.21c. Relative 298 K Gibbs energies and (enthalpies) computed using B3LYP/6-311++G(3df,3pd)//6-31+G(d,p) for conformers of the NO-OO-CS isomers of the $[Mg(Pro)_2\text{-}H]^+$ complex.

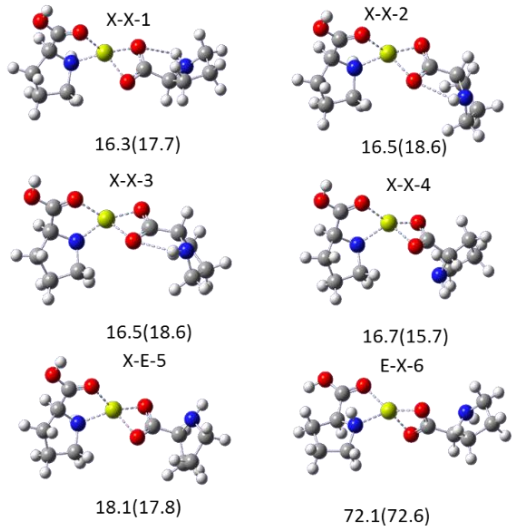

Figure A2.21d. Relative 298 K Gibbs energies and (enthalpies) computed using B3LYP/6-311++G(3df,3pd)//6-31+G(d,p) for conformers of the OO-OO-ZW isomers of the $[Mg(Pro)_2\text{-}H]^+$ complex.

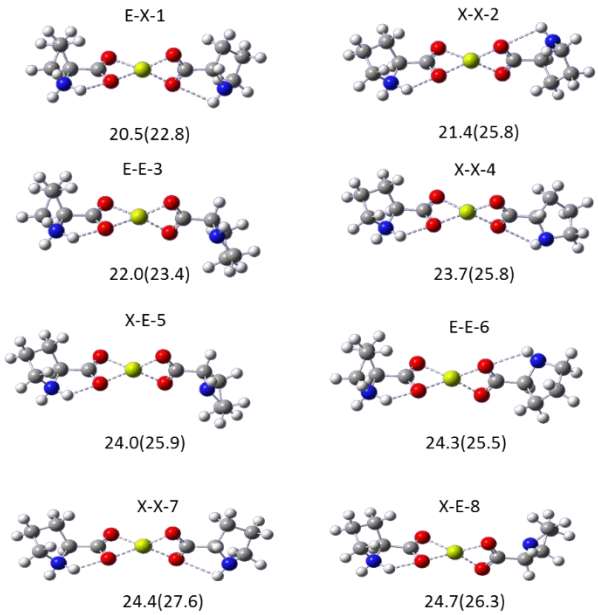

Figure A2.22a. Relative 298 K Gibbs energies and (enthalpies) computed using B3LYP/6-311++G(3df,3pd)//6-31+G(d,p) for conformers of the OO-OO-ZW isomers of the $[Ca(Pro)_2\text{-}H]^+$ complex.

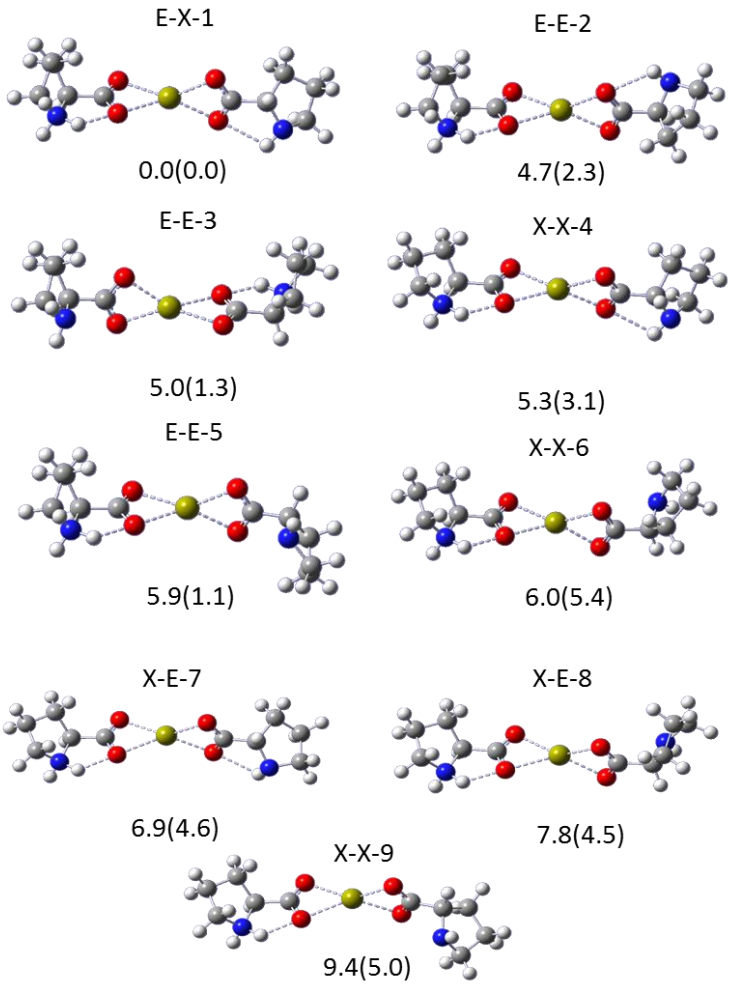

Figure A2.22b. Relative 298 K Gibbs energies and (enthalpies) computed using B3LYP/6-311++G(3df,3pd)//6-31+G(d,p) for conformers of the OO-NO-ZW isomers of the $[Ca(Pro)_2\text{-}H]^+$ complex.

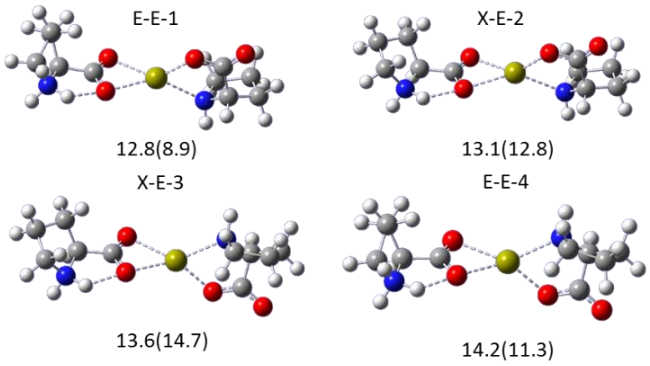

Figure A2.22c. Relative 298 K Gibbs energies and (enthalpies) computed using B3LYP/6-311++G(3df,3pd)//6-31+G(d,p) for conformers of the NO-OO-CS isomers of the $[Ca(Pro)_2\text{-}H]^+$ complex.

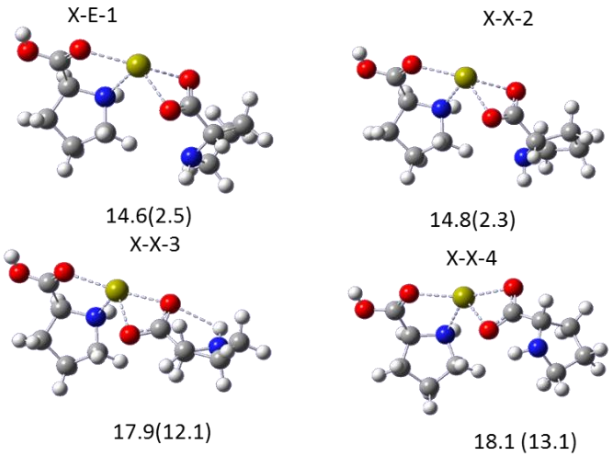

Figure A2.22d. Relative 298 K Gibbs energies and (enthalpies) computed using B3LYP/6-311++G(3df,3pd)//6-31+G(d,p) for conformers of the NO-NO-CS isomers of the $[Ca(Pro)_2\text{-}H]^+$ complex.

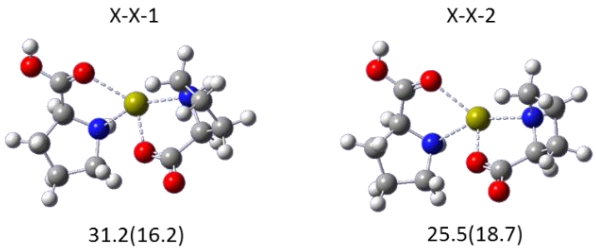

Figure A2.23a. Relative 298 K Gibbs energies and (enthalpies) computed using B3LYP/6-311++G(3df,3pd)//6-31+G(d,p) for conformers of the OO-NO-ZW isomers of the $[Sr(Pro)_2\text{-}H]^+$ complex.

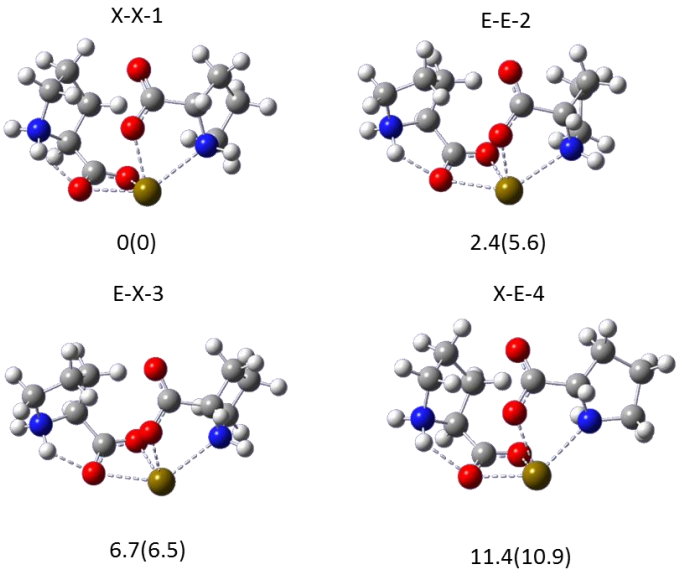

Figure A2.23b. Relative 298 K Gibbs energies and (enthalpies) computed using B3LYP/6-311++G(3df,3pd)//6-31+G(d,p) for conformers of the OO-OO-ZW isomers of the $[Sr(Pro)_2\text{-}H]^+$ complex.

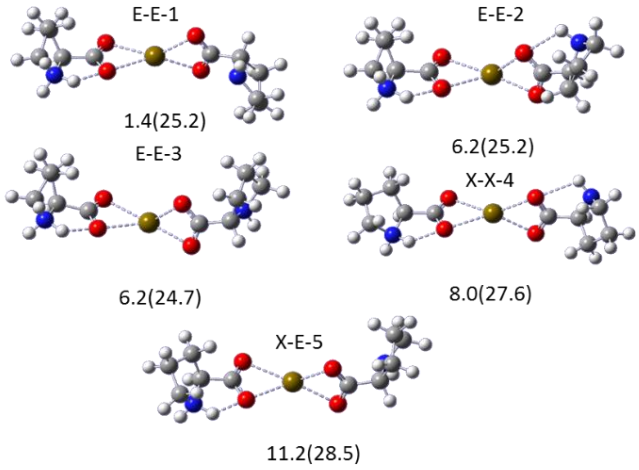

Figure A2.23c. Relative 298 K Gibbs energies and (enthalpies) computed using B3LYP/6-311++G(3df,3pd)//6-31+G(d,p) for conformers of the NO-OO-CS isomers of the $[Sr(Pro)_2\text{-}H]^+$ complex.

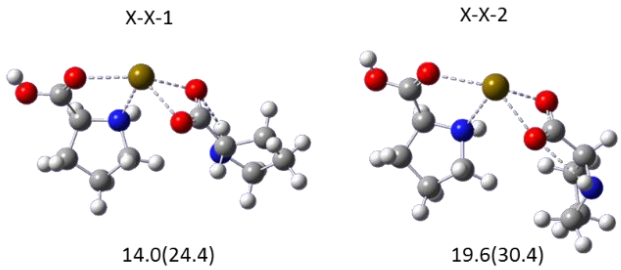

Figure A2.23d. Relative 298 K Gibbs energies and (enthalpies) computed using B3LYP/6-311++G(3df,3pd)//6-31+G(d,p) for conformers of the NO-NO-CS isomers of the $[Sr(Pro)_2\text{-}H]^+$ complex.

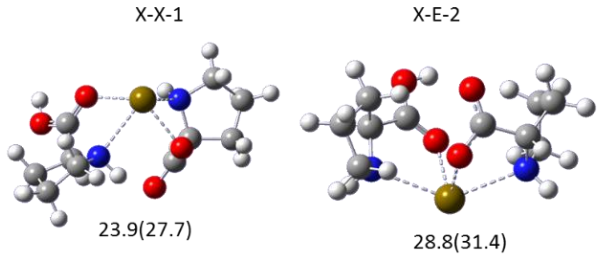

Figure A2.24a. Relative 298 K Gibbs energies and (enthalpies) computed using B3LYP/6-311++G(3df,3pd)//6-31+G(d,p) for conformers of the OO-NO-ZW isomers of the $[Ba(Pro)_2\text{-}H]^+$ complex.

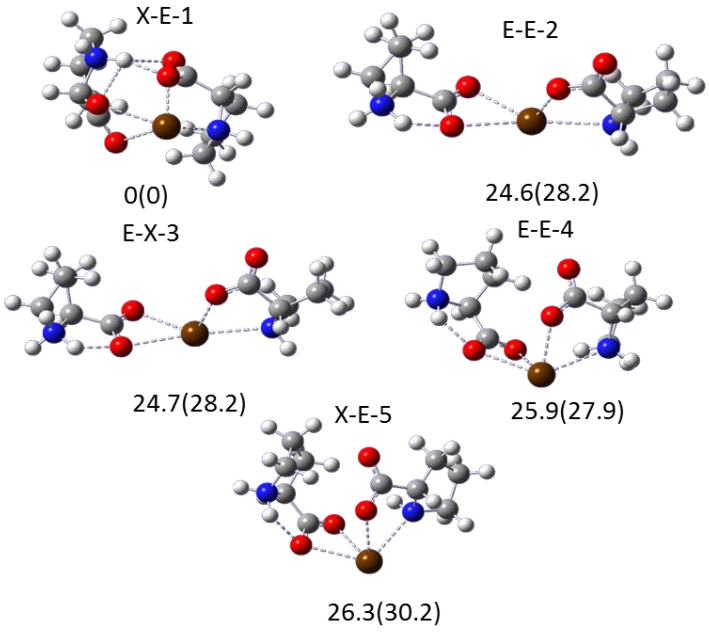

Figure A2.24b. Relative 298 K Gibbs energies and (enthalpies) computed using B3LYP/6-311++G(3df,3pd)//6-31+G(d,p) for conformers of the OO-OO-ZW isomers of the $[Ba(Pro)_2\text{-}H]^+$ complex.

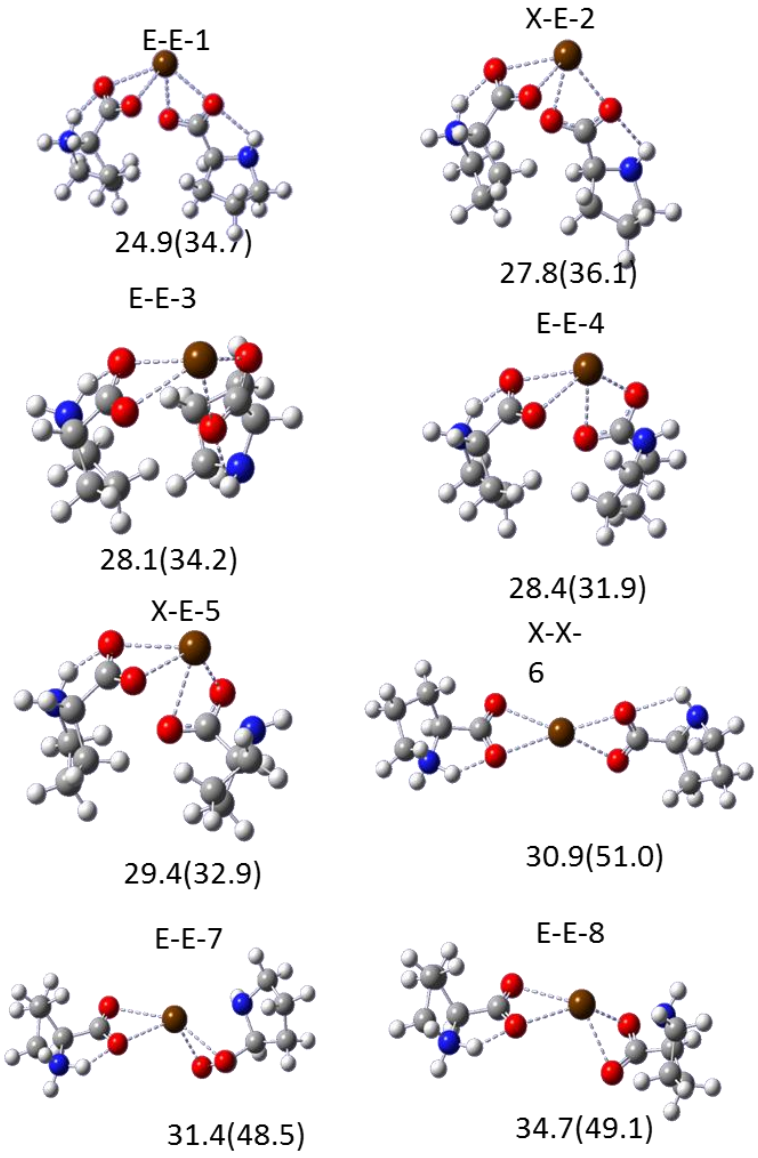

Figure A2.24c. Relative 298 K Gibbs energies and (enthalpies) computed using B3LYP/6-311++G(3df,3pd)//6-31+G(d,p) for conformers of the NO-OO-CS isomers of the $[Ba(Pro)_2\text{-}H]^+$ complex.

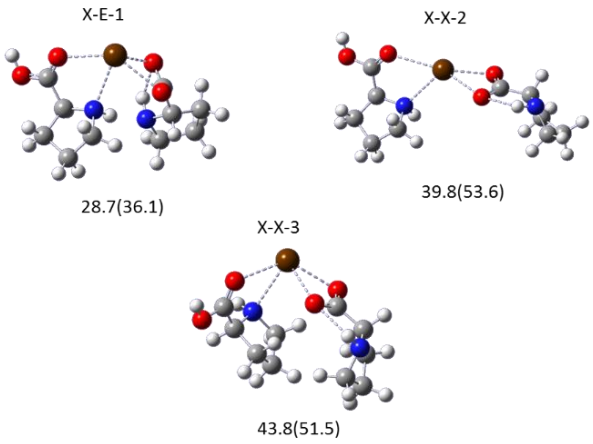

Figure A2.24d. Relative 298 K Gibbs energies and (enthalpies) computed using B3LYP/6-311++G(3df,3pd)//6-31+G(d,p) for conformers of the NO-NO-CS isomers of the $[Ba(Pro)_2\text{-}H]^+$ complex.

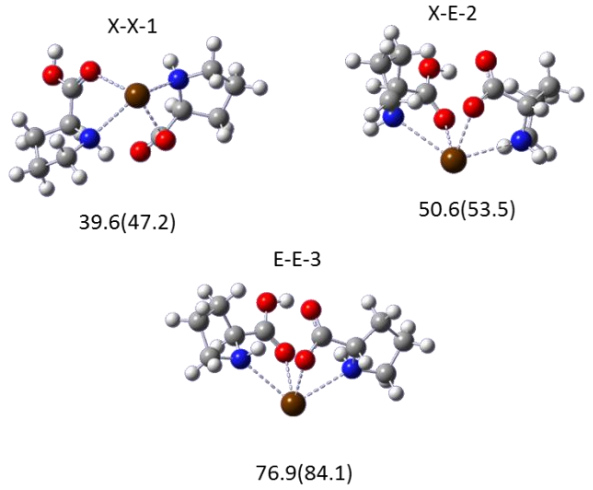

Figure A2.25. Relative 298 K Gibbs energies and (enthalpies) computed using B3LYP/6-31+G(d,p) for the lowest energy conformers of the $[Mg(Pro)_2\text{-}H]^+$ complex (black color) along with same complexes containing two explicit water molecules (red color).

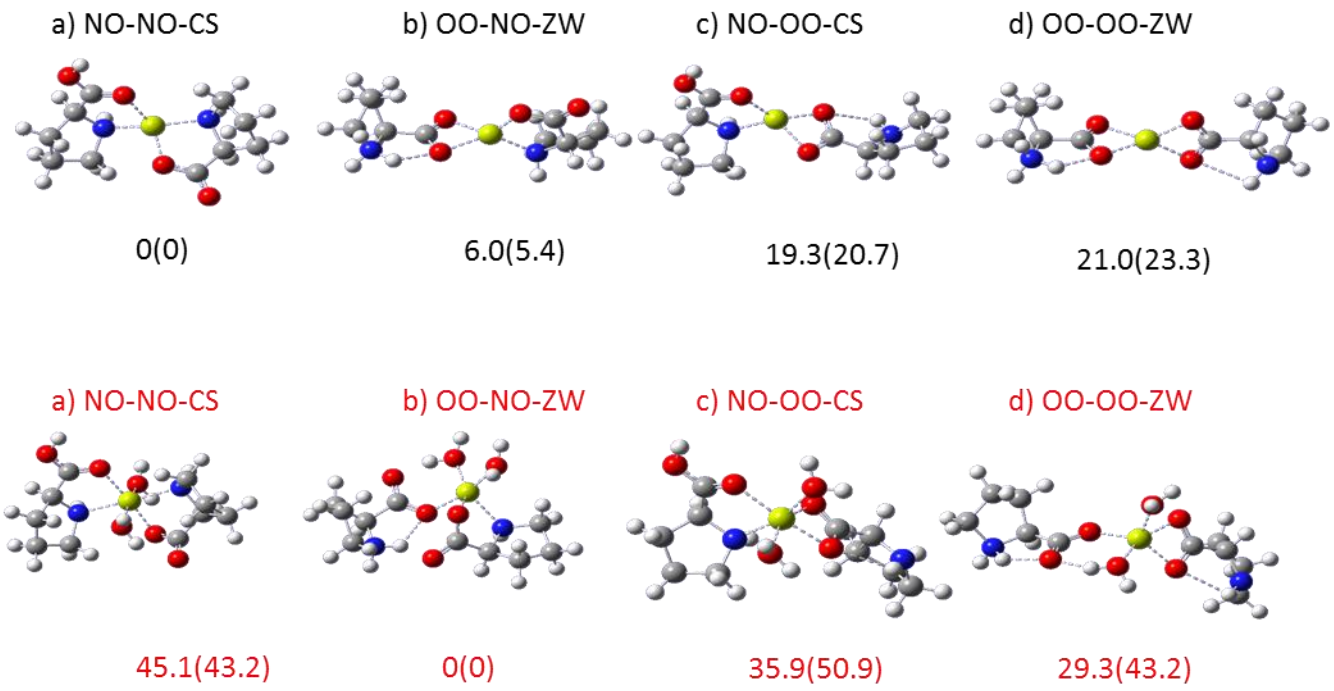

Figure A2.26. Plot of standard reduction potentials and 2-electron ionization energies for the transition metals of topic to this study.

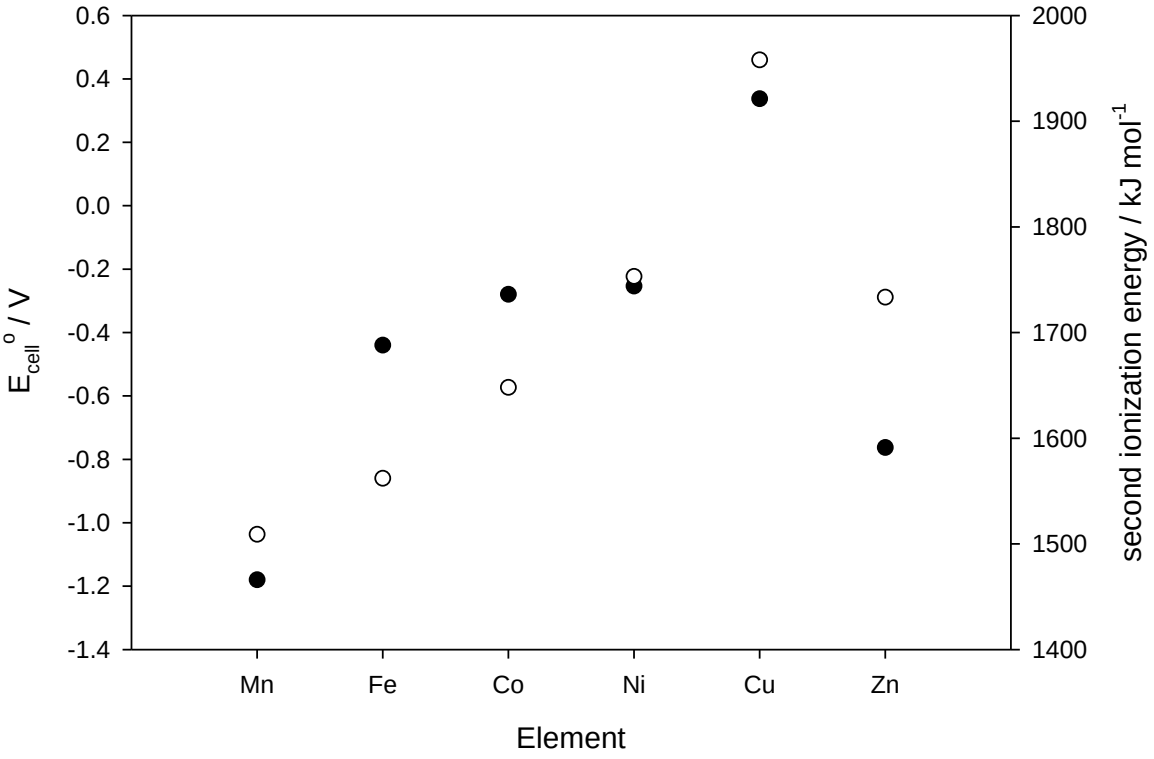

Figure A2.27. Comparison of the experimental IRMPD spectrum and calculated IR spectra of the lowest energy structures of each form of the $[Mg(Pro)_2\text{-}H]^+$ complexes in the 2700 to 3800 cm^{-1} region. Energies are B3LYPD3/cc-PVTZ 298 K Gibbs energies (and enthalpies) and in kJ mol^{-1}.

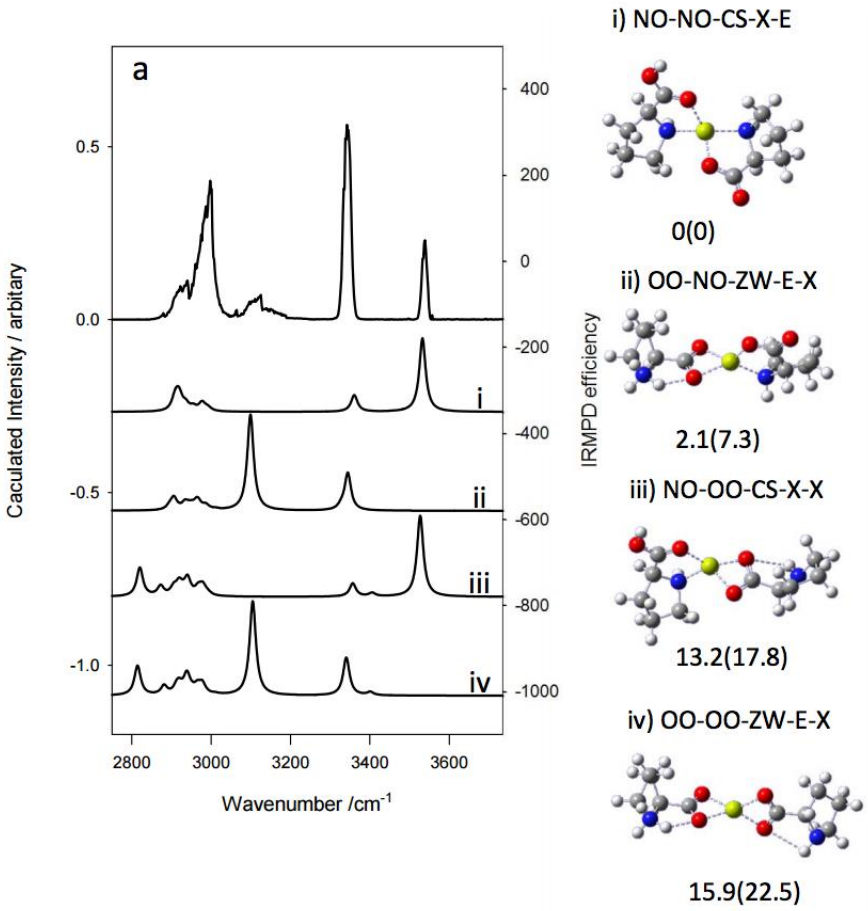

Figure A2.28. Comparison of the experimental IRMPD spectrum and calculated IR spectra for the lowest energy structures of each form of the $[Co(Pro)_2\text{-}H]^+$ complex in the a) 1000 to 2000 cm^{-1} region and b) 2800 to 3800 cm^{-1} region. Energies are UB3LYPD3/cc-pVTZ 298 K Gibbs energies (and enthalpies) and in kJ mol^{-1}.

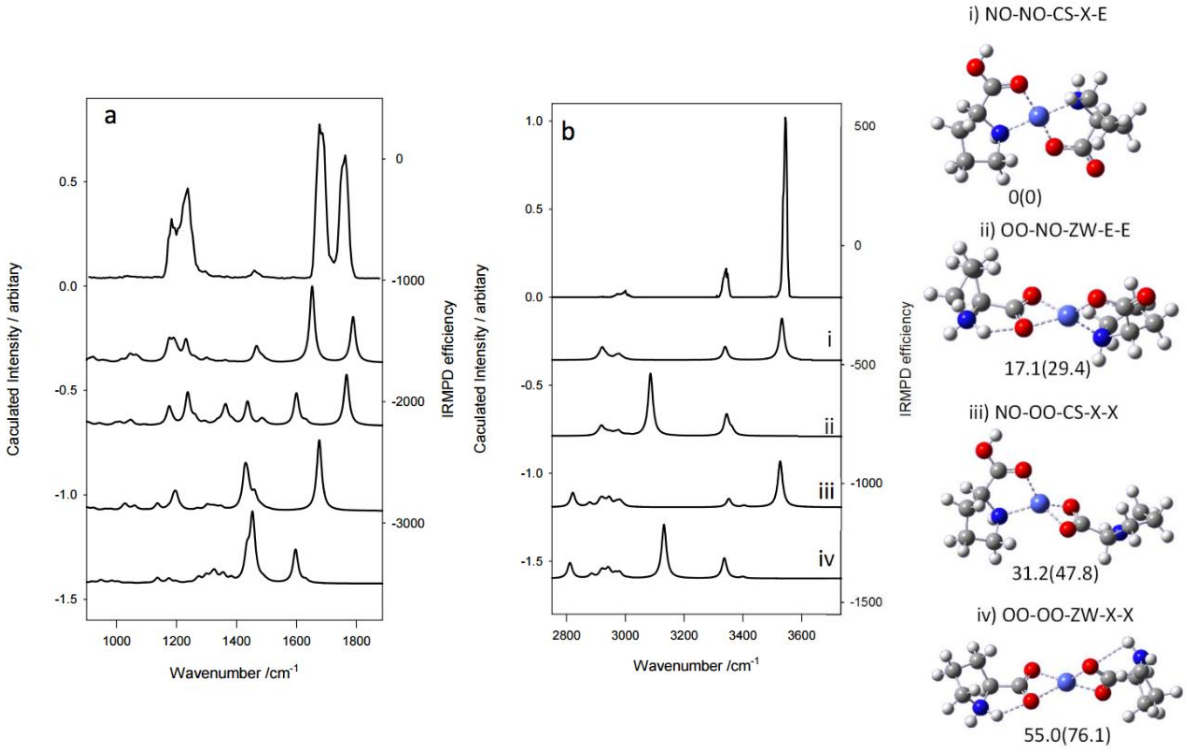

Figure A2.29. Comparison of the experimental IRMPD spectrum and calculated IR spectra for the lowest energy structures of each form of the $[Mn(Pro)_2\text{-}H]^+$ complex in the a) 1000 to 2000 cm^{-1} region and b) 2800 to 3800 cm^{-1} region. Energies are UB3LYPD3/cc-pVTZ 298 K Gibbs energies (and enthalpies) and in kJ mol^{-1}.

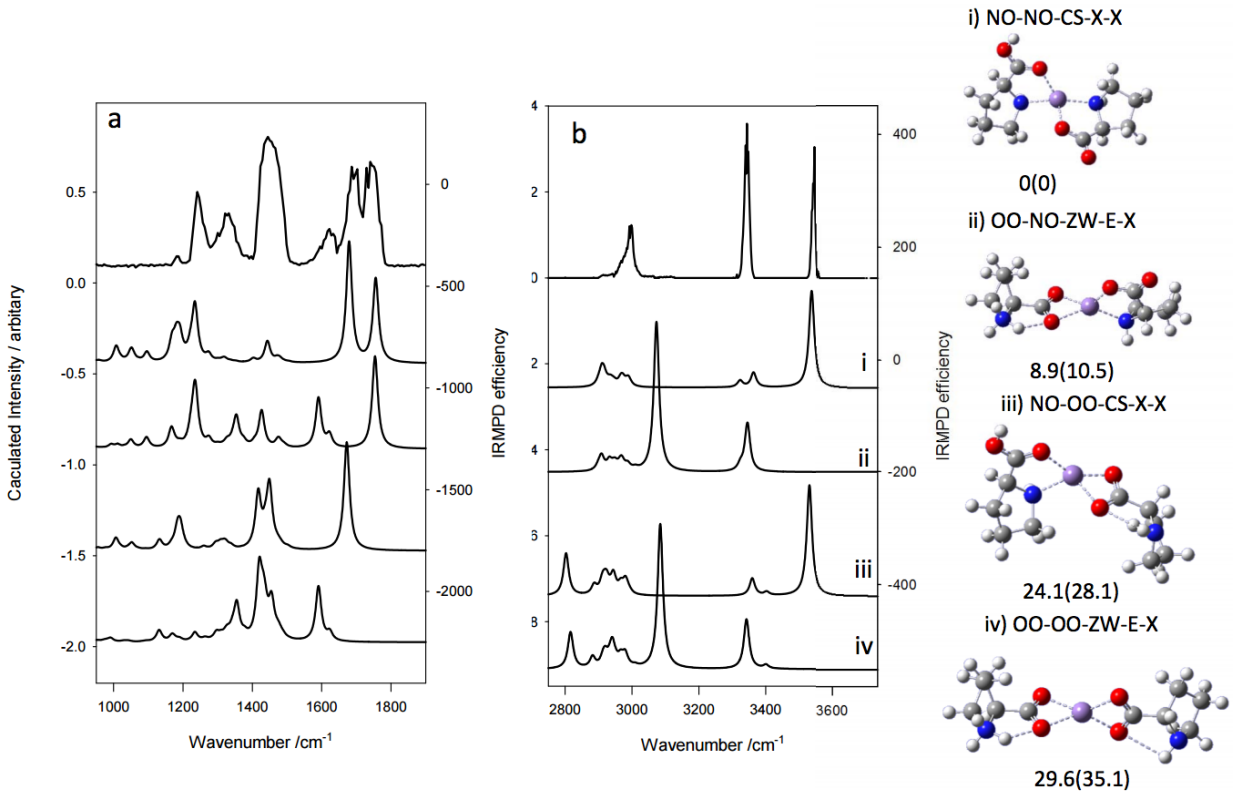

Table A2.1. UB3LYP/6-31+G(d,p) relative Gibbs energies (and enthalpies) at 298 K for quartet and doublet $[Mn(Pro)_2\text{-}H]^+$ complexes corresponding. All energies are relative to the lowest energy sextet complex in Figure A2.16.

Structure	$\Delta_{rel}G(\Delta_{rel}H)$/kJ mol^{-1} Quartet	$\Delta_{rel}G(\Delta_{rel}H)$/kJ mol^{-1} Doublet
OO-OO-ZW	165.4(164.4)	313.0(314.3)
OO-OO-ZW	166.5(160.4)	316.6(314.4)
OO-NO-ZW	122.2(113.9)	206.5(197.3)
OO-NO-ZW	122.8(115.3)	206.9(195.8)
OO-NO-ZW	124.3(116.9)	208.5(200.4)
OO-NO-ZW	125.1(118.4)	260.5(252.8)
OO-NO-ZW	133.7(127.9)	275.4(264.7)
NO-OO-CS	137.3(133.5)	329.8(320.6)
NO-NO-CS	85.0(74.4)	222.2(210.0)
NO-NO-CS	85.4(76.1)	225.8(213.6)
NO-NO-CS	86.8(74.4)	238.4(226.7)
NO-NO-CS	146.6(135.7)	247.8(238.8)
NO-NO-CS	167.2(160.7)	261.4(251.7)

Table A2.2. UB3LYP/6-31+G(d,p) relative Gibbs energies (and enthalpies) at 298 K for quartet and doublet $[Fe(Pro)_2\text{-}H]^+$ complexes corresponding. All energies are relative to the lowest energy quintent complex in Figure A2.15.

Structure	$\Delta_{rel}G(\Delta_{rel}H)$/kJ mol^{-1} Triplet	$\Delta_{rel}G(\Delta_{rel}H)$/kJ mol^{-1} Singlet
OO-OO-ZW	122.2(120.1)	261.5(175.6)
OO-OO-ZW	123.8(120.1)	284.0(278.8)
OO-OO-ZW	121.3(115.2)	309.2(300.9)
OO-NO-ZW	78.0(70.5)	205.6(16.7)
OO-NO-ZW	77.5(65.7)	207.3(197.2)
OO-NO-ZW	79.4(68.7)	189.1(171.2)
OO-NO-ZW	77.5(65.7)	209.9(200.8)
OO-NO-ZW	79.4(68.7)	207.2(197.7)
NO-OO-CS	83.5(78.5)	240.0(228.2)
NO-OO-CS	80.7(75.0)	217.2(205.3)
NO-OO-CS	90.6(82.7)	238.5(228.6)
NO-NO-CS	29.8(15.8)	157.5(138.9)
NO-NO-CS	33.0(19.5)	156.9(136.0)
NO-NO-CS	33.3(19.4)	149.7(134.0)
NO-NO-CS	91.4(79.4)	280.4(265.6)
NO-NO-CS	101.8(92.1)	188.9(175.6)
NO-NO-CS	112.0(102.5)	204.6(185.3)

Table A2.3. UB3LYP/6-31+G(d,p) relative Gibbs energies (and enthalpies) at 298 K for quartet and doublet $[Co(Pro)_2\text{-}H]^+$ complexes corresponding. All energies are relative to the lowest energy quintent complex in Figure A2.14.

Structure	$\Delta_{rel}G(\Delta_{rel}H)$/kJ mol^{-1} Quartet	$\Delta_{rel}G(\Delta_{rel}H)$/kJ mol^{-1} Doublet
OO-OO-ZW	64.5(86.6)	111.6(122.0)
OO-OO-ZW	64.8(82.6)	116.1 (124.2)
OO-OO-ZW	71.2(87.1)	125.3(129.8)
OO-OO-ZW	72.4(89.9)	124.2(129.5)
OO-NO-ZW	22.0(35.0)	50.4(52.1)
OO-NO-ZW	22.6(38.4)	50.4(53.9)
OO-NO-ZW	23.7(39.5)	52.4(55.1)
NO-OO-CS	42.2(58.5)	62.2(66.7)
NO-OO-CS	42.3(59.1)	64.3(70.3)
NO-OO-CS	51.8(67.2)	64.4(69.0)
NO-NO-CS	9.1(19.2)	0(0)
NO-NO-CS	10.0(20.0)	-0.2(1.3)
NO-NO-CS	40.5(52.4)	-0.1(0)

Table A2.4. UB3LYP/6- 31+G(d,p) relative Gibbs energies (and enthalpies) at 298 K for quartet and doublet $[Co(Pro)_2\text{-}H]^+$ complexes corresponding. All energies are relative to the lowest energy singlet complex in Figure A2.13.

Structure	$\Delta_{rel}G(\Delta_{rel}H)$/kJ mol^{-1} Triplet	$\Delta_{rel}G(\Delta_{rel}H)$/kJ mol^{-1} Singlet
OO-OO-ZW	107.6(128.5)	125.8(137.9)
OO-OO-ZW	109.1(130.2)	126.7(136.8)
OO-OO-ZW	109.8(131.1)	127.6(137.0)
OO-OO-ZW	110.7(132.6)	128.3(140.6)
OO-OO-ZW	128.9(148.5)	128.3(150.9)
OO-NO-ZW	55.8(72.1)	59.8(64.6)
OO-NO-ZW	56.0(73.9)	61.3(66.9)
OO-NO-ZW	57.9(77.2)	61.9(67.6)
OO-NO-ZW	59.1(77.6)	63.7(70.0)
OO-NO-ZW	61.5(79.6)	104.6(117.9)
NO-OO-CS	75.8(94.1)	69.9(77.3)
NO-OO-CS	88.8(107.0)	70.1(77.7)
NO-OO-CS	90.3(108.2)	70.7(77.4)
NO-OO-CS	91.1(107.6)	71.3(79.2)
NO-NO-CS	27.6(36.1)	0(0)
NO-NO-CS	27.6(40.2)	0.6(1.8)
NO-NO-CS	28.2(34.6)	0.9(1.5)
NO-NO-CS	65.0(80.8)	1.1(3.3)

Table A2.5. Topological Analysis of the lowest energy $[Mn(Pro)_2-H]^+$ structures.

$[Mn(Pro)_2-H]^+$

Electron densities ρ(e a.u.$^{-3}$), Laplacian of the charge density $\nabla^2\rho$ (e a.u.$^{-5}$) and ellipticity ε at the bond critical points, computed for geometries optimized at the B3LYP/6-31+G(d,p) level.

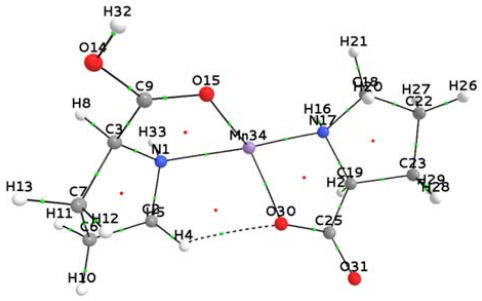

Bond	ρ	$\nabla^2\rho$	ε
N(1) – H(33)	0.342	-1.796	0.0332
O(14) – H(32)	0.350	-2.098	0.0129
C(25) – O(31)	0.414	0.075	0.1207
C(25) – O(30)	0.321	-0.454	0.0058
C(23) – H(29)	0.282	-0.997	0.0082
C(23) – H(28)	0.282	-0.993	0.0127
C(22) – H(26)	0.280	-0.981	0.0022
C(19) – C(25)	0.248	-0.584	0.0937
H(4) – O(30)	0.011	0.037	0.2549
O(30) – Mn(34)	0.099	0.559	0.0867
C(19) – H(24)	0.284	-1.014	0.0381
C(19) – C(23)	0.237	-0.521	0.0329
C(22) – H(27)	0.278	-0.952	0.0080
C(18) – H(21)	0.284	-1.018	0.0268
C(22) – C(23)	0.241	-0.537	0.0033
C(18) – H(20)	0.283	-0.998	0.0301
C(18) – C(22)	0.249	-0.576	0.0188
N(17) – C(19)	0.231	-0.531	0.0266
N(17) – C(18)	0.242	-0.605	0.0366
H(16) – N(17)	0.341	-1.779	0.0282
N(17) – Mn(34)	0.071	0.271	0.0288
C(9) – O(14)	0.327	-0.359	0.0065
C(9) – O(15)	0.391	-0.068	0.0591
O(15) – Mn(34)	0.058	0.281	0.0762
C(7) – H(13)	0.283	-1.010	0.0086
C7() – H(12)	0.280	-0.973	0.0119
C(6) – H(11)	0.279	-0.963	0.0090
C6() – H(10)	0.281	-0.995	0.0008
C(3) – C(9)	0.265	-0.678	0.1125
C(3) – H(8)	0.285	-1.024	0.0303
C(3) – C(7)	0.234	-0.509	0.0165
C(2) – H(5)	0.285	-1.029	0.0321
C(6) – C(7)	0.243	-0.548	0.0013
C(2) – H(4)	0.289	-1.071	0.0317
C(2) – C(6)	0.249	-0.577	0.0223
N(1) – C(3)	0.251	-0.625	0.0155
N(1) – Mn(34)	0.059	0.211	0.0447
N(1) – C(2)	0.230	-0.540	0.0364

Table A2.6. Topological Analysis of the lowest energy $[Fe(Pro)_2 -H]^+$ structures.

$[Fe(Pro)_2 -H]^+$

Electron densities ρ(e a.u.$^{-3}$), Laplacian of the charge density $\nabla^2 \rho$ (e a.u.$^{-5}$) and ellipticity ε at the bond critical points, computed for geometries optimized at the B3LYP/6-31+G(d,p) level.

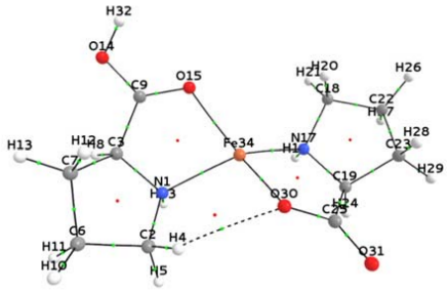

Bond	ρ	$\nabla^2\rho$	ε
N(1) – Fe(34)	0.065	0.210	0.1184
N(1) – C(2)	0.231	-0.548	0.0332
N(1) – C(3)	0.253	-0.640	0.0159
C(2) – C(6)	0.249	-0.577	0.0230
C(2) – H(4)	0.289	-1.064	0.0325
C(6) – C(7)	0.243	-0.546	0.0014
C(2) – H(5)	0.286	-1.038	0.0309
C(6) – H(11)	0.279	-0.964	0.0092
C(3) – C(7)	0.234	-0.509	0.0154
C(3) – H(8)	0.284	-1.024	0.0295
C(3) – C(9)	0.266	-0.681	0.1126
C(6) – H(10)	0.281	-0.994	0.0011
C(7) – H(12)	0.280	-0.968	0.0122
C(7) – H(13)	0.283	-1.011	0.0086
O(15) – Fe(34)	0.065	0.321	0.1874
C(9) – O(15)	0.388	-0.078	0.0581
C(9) – O(14)	0.328	-0.348	0.0055
O(14) – H(32)	0.349	-2.099	0.0128
N(17) – Fe(34)	0.076	0.260	0.0745
H(16) – N(17)	0.342	-1.791	0.0293
N(17) – C(18)	0.242	-0.601	0.0343
N(17) – C(19)	0.232	-0.533	0.0269
C(18) – H(20)	0.283	-0.997	0.0309
C(22) – C(23)	0.243	-0.545	0.0032
C(18) – H(21)	0.284	-1.020	0.0267
C(22) – H(27)	0.278	-0.953	0.0073
C(18) – C(22)	0.249	-0.576	0.0196
C(19) – C(23)	0.238	-0.527	0.0281
C(19) – H(24)	0.286	-1.024	0.0386
H(4) – O(30)	0.010	0.036	0.3789
O(30) – Fe(34)	0.115	0.629	0.0867
C(19) – C(25)	0.253	-0.605	0.0959
C(22) – H(26)	0.280	-0.981	0.0026
C(23) – H(28)	0.281	-0.975	0.0125
C(23) – H(29)	0.283	-1.004	0.0060
C(25) – O(30)	0.315	-0.464	0.0054
C(25) – O(31)	0.416	0.091	0.1236
N(1) – (H33)	0.343	-1.802	0.0330

Table A2.7. Topological Analysis of the lowest energy $[Co(Pro)_2-H]^+$ structures.

$[Co(Pro)_2-H]^+$

Electron densities ρ(e a.u.$^{-3}$), Laplacian of the charge density $\nabla^2 \rho$ (e a.u.$^{-5}$) and ellipticity ε at the bond critical points, computed for geometries optimized at the B3LYP/6-31+G(d,p) level.

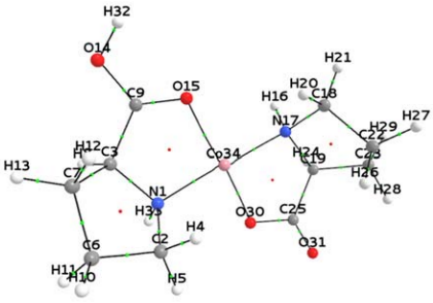

Bond	ρ	$\nabla^2\rho$	ε
N(1) – Co(34)	0.0928	0.482	0.116
N(1) – C(2)	0.2386	-0.591	0.019
N(1) – C(3)	0.2536	-0.639	0.014
C(2) – C(6)	0.2501	-0.581	0.022
C(2) – H(4)	0.2851	-1.020	0.033
C(6) – C(7)	0.2417	-0.540	0.003
C(2) – H(5)	0.2886	-1.071	0.025
C(6) – H(11)	0.2791	-0.965	0.009
C(3) – C(7)	0.2320	-0.500	0.014
C(3) – H(8)	0.2837	-1.022	0.027
C(3) – C(9)	0.2671	-0.691	0.108
C(7) – H(13)	0.2833	-1.012	0.010
C(6) – H(10)	0.2807	-0.992	0.002
C(7) – H(12)	0.2802	-0.972	0.013
O(15) – Co(34)	0.0811	0.459	0.685
C(9) – O(15)	0.3859	-0.160	0.057
C(9) – O(14)	0.3305	-0.331	0.003
N(17) – Co(34)	0.1013	0.497	0.116
H(16) – N(17)	0.3419	-1.800	0.024
N(17) – C(18)	0.2364	-0.572	0.005
N(17) – C(19)	0.2362	-0.562	0.027
C(18) – H(21)	0.2843	-1.013	0.030
C(18) – H(20)	0.2847	-1.018	0.032
C(18) – C(22)	0.2484	-0.575	0.017
C(22) – C(23)	0.2428	-0.544	0.001
C(19) – C(23)	0.2450	-0.557	0.022
C(19) – H(24)	0.2844	-1.021	0.035
O(30) – Co(34)	0.1338	0.743	0.434
C(19) – C(25)	0.2540	-0.612	0.095
C(23) – H(28)	0.2831	-1.016	0.003
C(22) – H(26)	0.2785	-0.957	0.009
C(22) – H(27)	0.2805	-0.985	0.004
C(23) – H(29)	0.2793	-0.964	0.012
N(1) – H(33)	0.3410	-1.811	0.028
C(25) – O(30)	0.3145	-0.542	0.002
C(25) – O(31)	0.4175	0.123	0.116
O(14) – H(32)	0.3487	-2.098	0.012

Table A2.8. Topological Analysis of the lowest energy $[Ni(Pro)_2-H]^+$ structures.

$[Ni(Pro)_2-H]^+$

Electron densities ρ(e a.u.$^{-3}$), Laplacian of the charge density $\nabla^2 \rho$ (e a.u.$^{-5}$) and ellipticity ε at the bond critical points, computed for geometries optimized at the B3LYP/6-31+G(d,p) level.

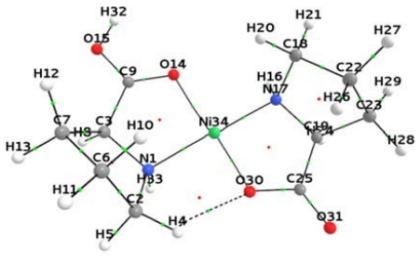

Bond	ρ	$\nabla^2\rho$	ε
N(1) – C(2)	0.237	-0.584	0.014
N(1) – Ni(34)	0.091	0.376	0.101
N(1) – C(3)	0.251	-0.629	0.009
C(2) – H(4)	0.291	-1.099	0.026
C(2) – H(5)	0.284	-1.008	0.033
C(2) – C(6)	0.252	-0.591	0.022
C(7) – H(13)	0.283	-0.999	0.014
C(3) – C(7)	0.228	-0.486	0.019
C(6) – C(7)	0.241	-0.539	0.002
C(3) – H(8)	0.285	-1.036	0.028
C(3) – C(9)	0.267	-0.690	0.110
C(6) – H(10)	0.278	-0.954	0.010
C(6) – H(11)	0.281	-0.996	0.002
C(7) – H(12)	0.282	-0.996	0.013
O(14) – Ni(34)	0.076	0.458	0.037
C(9) – O(14)	0.387	-0.107	0.075
C(9) – O(15)	0.329	-0.342	0.003
N(17) – Ni(34)	0.107	0.430	0.100
H(16) – N(17)	0.342	-1.805	0.022
N(17) – C(18)	0.235	-0.566	0.003
N(17) – C(19)	0.235	-0.556	0.026
C(18) – H(21)	0.284	-1.014	0.031
C(18) – H(20)	0.286	-1.027	0.032
C(18) – C(22)	0.249	-0.577	0.017
C(22) – C(23)	0.243	-0.543	0.001
C(23) – H(29)	0.279	-0.965	0.012
C(19) – C(23)	0.245	-0.558	0.022
C(19) – H(24)	0.285	-1.024	0.036
O(30) – Ni(34)	0.130	0.709	0.077
H(4) – O(30)	0.013	0.050	0.416
C(19) - C25)	0.255	-0.616	0.095
C(23) – H(28)	0.283	-1.016	0.003
C(22) – H(26)	0.279	-0.958	0.009
C(22) – H(27)	0.281	-0.987	0.004
N(1) – H(33)	0.340	-1.806	0.024
C(25) – O(30)	0.316	-0.498	0.015
C(25) – O(31)	0.417	0.104	0.114
O(15) – H(32)	0.349	-2.098	0.013

Table A2.9. Topological Analysis of the lowest energy $[Cu(Pro)_2 -H]^+$ structures.

$[Cu(Pro)_2 -H]^+$

Electron densities ρ(e a.u.$^{-3}$), Laplacian of the charge density $\nabla^2 \rho$ (e a.u.$^{-5}$) and ellipticity ε at the bond critical points, computed for geometries optimized at the B3LYP/6-31+G(d,p) level.

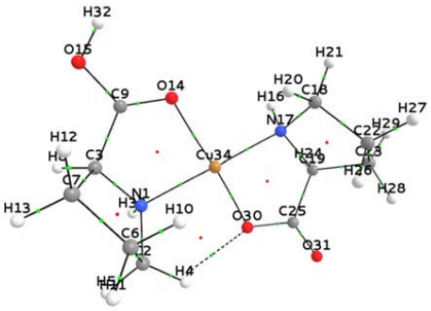

Bond	ρ	$\nabla^2\rho$	ε
N(1) – C(2)	0.239	-0.592	0.0163
N(1) – Cu(34)	0.081	0.233	0.0089
N(1) – C(3)	0.255	-0.655	0.0147
C(2) – H(4)	0.290	-1.097	0.0266
C(2) – H(5)	0.283	-1.007	0.0329
C(2) – C(6)	0.252	-0.590	0.0222
C(3) – C(7)	0.228	-0.483	0.0191
C(6) – C(7)	0.241	-0.538	0.0012
C(3) – H(8)	0.285	-1.035	0.0278
C(3) – C(9)	0.265	-0.678	0.1095
C(6) – H(10)	0.277	-0.944	0.0108
C(7) – H(13)	0.283	-1.000	0.0138
C(6) – H(11)	0.281	-0.997	0.0018
C(7) – H(12)	0.282	-0.995	0.0129
O(14) – Cu(34)	0.070	0.290	0.0102
C(9) – O(14)	0.391	-0.089	0.0598
C(9) - O(15)	0.327	-0.351	0.0093
N(17) – Cu(34)	0.094	0.268	0.0195
H(16) – N(17)	0.342	-1.801	0.0262
N(17) – C(18)	0.236	-0.573	0.0065
N(17) – C(19)	0.237	-0.571	0.0302
C(18) – H(21)	0.285	-1.015	0.0301
C(18) – H(20)	0.285	-1.017	0.0333
C(18) – C(22)	0.248	-0.573	0.0171
C(22) – C(23)	0.243	-0.543	0.0011
C(19) – C(23)	0.245	-0.557	0.0226
C(19) – H(24)	0.284	-1.021	0.0358
O(30) – Cu(34)	0.115	0.489	0.0121
H(4) – O(30)	0.013	0.048	0.2998
C(19) – C(25)	0.251	-0.596	0.0954
C(23) – H(28)	0.283	-1.019	0.0032
C(22) – H(26)	0.278	-0.955	0.0093
C(22) – H(27)	0.281	-0.986	0.0044
C(23) – H(29)	0.279	-0.963	0.0120
C(25) – O(30)	0.321	-0.464	0.0060
C(25) – O(31)	0.414	0.083	0.1099
O(15) – H(32)	0.350	-2.099	0.0130
N(1) – H(33)	0.340	-1.800	0.0278

Table A2.10. Topological Analysis of the lowest energy $[Zn(Pro)_2 -H]^+$ structures.

$[Zn(Pro)_2 -H]^+$

Electron densities ρ(e a.u.$^{-3}$), Laplacian of the charge density $\nabla^2 \rho$ (e a.u.$^{-5}$) and ellipticity ε at the bond critical points, computed for geometries optimized at the B3LYP/6-31+G(d,p) level.

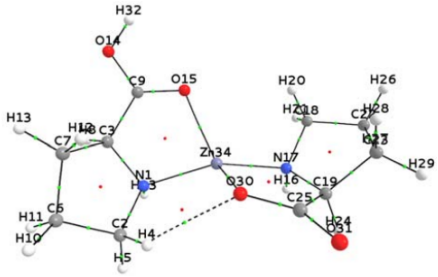

Bond	ρ	$\nabla^2\rho$	ε
N(1) – Zn(34)	0.0792	0.227	0.0191
N(1) – C(2)	0.2267	-0.522	0.0353
N(1) – C(3)	0.2500	-0.629	0.0088
C(2) – H(4)	0.2904	-1.083	0.0321
C(2) – H(5)	0.2859	-1.034	0.0338
C(2) – C(6)	0.2486	-0.576	0.0222
C(6) – C(7)	0.2433	-0.547	0.0006
C(3) – C(7)	0.2354	-0.515	0.0176
C(3) – H(8)	0.2852	-1.030	0.0307
C(3) – C(9)	0.2643	-0.673	0.1114
C(6) – H(10)	0.2813	-0.998	0.0016
C(6) – H(11)	0.2794	-0.966	0.0098
C(7) - H(12)	0.2804	-0.978	0.0116
C(7) – H(13)	0.2831	-1.012	0.0087
O(15) – Zn(34)	0.0644	0.259	0.0268
C(9) – O(15)	0.3930	-0.068	0.0619
C(9) – O(14)	0.3271	-0.359	0.0066
N(17) – Zn(34)	0.0896	0.247	0.0074
H(16) – N(17)	0.3425	-1.800	0.0260
N(17) – C(18)	0.2378	-0.583	0.0320
N(17) – C(19)	0.2274	-0.511	0.0258
C(18) – H(20)	0.2849	-1.015	0.0316
C(22) – C(23)	0.2435	-0.547	0.0033
C(18) – H(21)	0.2846	-1.022	0.0286
C(18) – C(22)	0.2495	-0.579	0.0201
C(19) – C(23)	0.2396	-0.533	0.0298
C(19) – H(24)	0.2858	-1.026	0.0409
O(30) – Zn(34)	0.1061	0.429	0.0427
H(4) – O(30)	0.0115	0.040	0.4892
C(19) – C(25)	0.2470	-0.577	0.0919
C(23) – H(29)	0.2829	-1.008	0.0055
C(22) – H(26)	0.2799	-0.981	0.0031
C(22) – H(27)	0.2780	-0.954	0.0075
C(23) – H(28)	0.2802	-0.973	0.0131
C(25) – O(30)	0.3247	-0.448	0.0127
C(25) – O(31)	0.4131	0.053	0.1218
O(14) – H(32)	0.3494	-2.100	0.0129
N(1) – H(33)	0.3425	-1.806	0.0295

Table A2.11. Topological Analysis of the lowest energy $[Mg(Pro)_2-H]^+$ structures.

$[Mg(Pro)_2-H]^+$

Electron densities ρ(e a.u.$^{-3}$), Laplacian of the charge density $\nabla^2\rho$ (e a.u.$^{-5}$) and ellipticity ε at the bond critical points, computed for geometries optimized at the B3LYP/6-31+G(d,p) level.

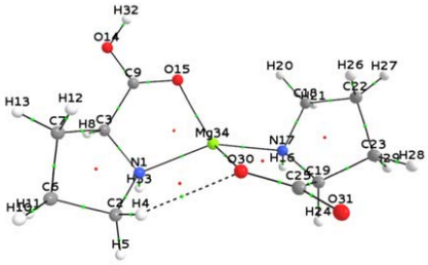

Bond	ρ	$\nabla^2\rho$	ε
N(1) – C(2)	0.229	-0.531	0.0372
N(1) – C(3)	0.251	-0.626	0.0168
N(1) – Mg(34)	0.036	0.213	0.0357
C(2) – H(4)	0.289	-1.074	0.0317
C(6) – C(7)	0.243	-0.547	0.0011
C(2) – H(5)	0.286	-1.032	0.0323
C(2) – C(6)	0.249	-0.577	0.0228
C(3) – C(7)	0.233	-0.506	0.0158
C(3) – H(8)	0.285	-1.028	0.0300
C(3) – C(9)	0.265	-0.678	0.1135
C(6) – H(10)	0.281	-0.997	0.0009
C(6) – H(11)	0.279	-0.964	0.0094
C(7) – H(12)	0.280	-0.972	0.0124
C(7) – H(13)	0.283	-1.012	0.0090
C(9) – O(15)	0.388	-0.100	0.0473
C(9) – O(14)	0.329	-0.343	0.0074
O(15) – Mg(34)	0.040	0.288	0.0115
N(17) – Mg(34)	0.043	0.267	0.0397
H(16) – N(17)	0.342	-1.785	0.0318
N(17) – C(18)	0.232	-0.541	0.0140
N(17) – C(19)	0.230	-0.524	0.0378
C(18) – H(21)	0.285	-1.018	0.0298
C(18) – H(20)	0.283	-0.999	0.0345
C(18) – C(22)	0.245	-0.558	0.0164
C(22) – C(23)	0.243	-0.545	0.0010
C(19) – C(23)	0.247	-0.567	0.0230
C19) – H(24)	0.283	-1.006	0.0372
O(30) – Mg(34)	0.061	0.513	0.0573
H(4) – O(30)	0.011	0.039	0.2571
C(19) – C(25)	0.242	-0.553	0.0923
C(22) – H(26)	0.279	-0.965	0.0103
C(22) – H(27)	0.280	-0.981	0.0062
C(23) – H(28)	0.284	-1.025	0.0018
C(23) – H(29)	0.278	-0.952	0.0116
C(25) – O(30)	0.327	-0.438	0.0071
C(25) – O(31)	0.412	0.060	0.1177
O(14) – H(32)	0.349	-2.100	0.0125
N(1) – H(33)	0.342	-1.790	0.0348

Table A2.12. Topological Analysis of the lowest energy $[Ca(Pro)_2 - H]^+$ structures.

$[Ca(Pro)_2 - H]^+$

Electron densities ρ(e a.u.$^{-3}$), Laplacian of the charge density $\nabla^2 \rho$ (e a.u.$^{-5}$) and ellipticity ε at the bond critical points, computed for geometries optimized at the B3LYP/6-31+G(d,p) level.

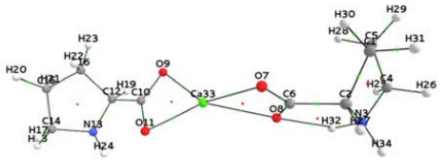

Bond	ρ	$\nabla^2\rho$	ε
C(1) – C(2)	0.242	-0.544	0.0242
C(2) – N(3)	0.227	-0.522	0.0187
N(3) – C(4)	0.224	-0.515	0.0123
C(1) – C(5)	0.242	-0.540	0.0015
C(4) – C(5)	0.249	-0.579	0.0194
C(2) – C(6)	0.254	-0.616	0.0953
O(8) – Ca(33)	0.030	0.142	0.0032
C(6) – O(7)	0.380	-0.238	0.0613
C(6) – O(8)	0.362	-0.333	0.0332
O(7) – Ca(33)	0.032	0.155	0.0342
N(3) – H(32)	0.323	-1.751	0.0022
O(9) – Ca(33)	0.043	0.225	0.0487
O(9) – C(10)	0.357	-0.361	0.0102
C(10) – O(11)	0.355	-0.341	0.0052
C(10) – C(12)	0.261	-0.651	0.0997
O(11) – Ca(33)	0.042	0.219	0.0448
N(13) – C(14)	0.263	-0.714	0.0412
C(12) – N(13)	0.272	-0.733	0.0629
C(14) – H(18)	0.283	-1.005	0.0273
C(12) – C(16)	0.232	-0.502	0.0166
C(15) – H(21)	0.279	-0.958	0.0039
C(14) – C(15)	0.248	-0.575	0.0212
C(15) – C(16)	0.243	-0.543	0.0033
C(14) – H(17)	0.276	-0.936	0.0264
C(12) – H(19)	0.282	-0.988	0.0351
C(15) – H(20)	0.279	-0.961	0.0014
C(16) – H(22)	0.277	-0.941	0.0076
C(16) – H(23)	0.281	-0.984	0.0056
N(13) – H(24)	0.343	-1.785	0.0502
C(4) – H(25)	0.288	-1.067	0.0330
C(4) – H(26)	0.288	-1.053	0.0346
C(2) – H(27)	0.287	-1.056	0.0384
C(5) – H(28)	0.280	-0.973	0.0125
C(5) – H(29)	0.282	-1.003	0.0047
C(1) – H(30)	0.283	-1.021	0.0073
C(1) – H(31)	0.281	-0.985	0.0146
O(8) – H(32)	0.035	0.111	0.1071
N(3) – H(34)	0.340	-1.852	0.0029

Table A2.13. Topological Analysis of the lowest energy $[Sr(Pro)_2-H]^+$ structures.

$[Sr(Pro)_2-H]^+$

Electron densities ρ(e a.u.$^{-3}$), Laplacian of the charge density $\nabla^2\rho$ (e a.u.$^{-5}$) and ellipticity ε at the bond critical points, computed for geometries optimized at the B3LYP/6-31+G(d,p) level.

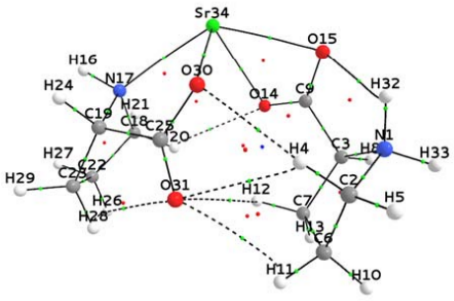

Bond	ρ	$\nabla^2\rho$	ε
C(25) – O(30)	0.336	-0.342	0.003
H(28) – O(31)	0.016	0.065	2.574
C(25) – O(31)	0.395	0.090	0.085
N(1) – H(32)	0.327	-1.782	0.004
O(14) – Sr(34)	0.036	0.154	0.040
O(15) – Sr(34)	0.032	0.139	0.035
O(30) – Sr(34)	0.055	0.256	0.082

Bond	ρ	$\nabla^2\rho$	ε
N(1) – (C2)	0.224	-0.502	0.0356
N(1) – (C3)	0.230	-0.547	0.0042
C(2) – (H4)	0.290	-1.113	0.0291
C(2) – (H5)	0.286	-1.045	0.0376
C(2) – (C6)	0.252	-0.597	0.0199
C(3) – (C7)	0.238	-0.535	0.0306
C(6) – (C7)	0.239	-0.534	0.0076
C(3) – (C9)	0.254	-0.621	0.0847
C(3) – (H8)	0.285	-1.036	0.0365
N(1) – H(33)	0.342	-1.850	0.0013
C(6) – H(10)	0.278	-0.955	0.0155
C(6) – H(11)	0.284	-1.031	0.0014
H(12) – O(31)	0.008	0.029	0.2886
C(7) – H(12)	0.286	-1.029	0.0120
C(7) – H(13)	0.282	-0.996	0.0139
C(9) – O(14)	0.374	-0.150	0.0564
O(15) – H(32)	0.031	0.101	0.1825
C(9) – O(15)	0.363	-0.219	0.0405
N(17) – Sr(34)	0.031	0.109	0.0223
H(16) – N(17)	0.340	-1.746	0.0351
O(14) – H(20)	0.008	0.028	0.1539
N(17) – C(18)	0.249	-0.646	0.0413
N(17) – C(19)	0.243	-0.595	0.0286
C(18) – H(20)	0.284	-1.014	0.0272
C(18) – H(21)	0.282	-0.998	0.0267
C(18) – C(22)	0.247	-0.570	0.0185
C(22) – C(23)	0.236	-0.519	0.0028
C(19) – C(23)	0.241	-0.539	0.0273
C(19) – C(25)	0.246	-0.579	0.0754
C(19) – H(24)	0.283	-0.999	0.0253
H(4) – O(31)	0.010	0.036	0.1792
H(11) – O(31)	0.009	0.033	0.3380
C(22) – H(26)	0.280	-0.974	0.0020
C(22) – H(27)	0.278	-0.954	0.0084
C(23) – H(28)	0.284	-1.012	0.0071
C(23) – H(29)	0.280	-0.970	0.0127
H(4) – O(30)	0.009	0.030	0.1771

Table A2.14. Topological Analysis of the lowest energy $[Ba(Pro)_2 - H]^+$ structures.

$[Ba(Pro)_2 - H]^+$

Electron densities ρ(e a.u.$^{-3}$), Laplacian of the charge density $\nabla^2 \rho$ (e a.u.$^{-5}$) and ellipticity ε at the bond critical points, computed for geometries optimized at the B3LYP/6-31+G(d,p) level.

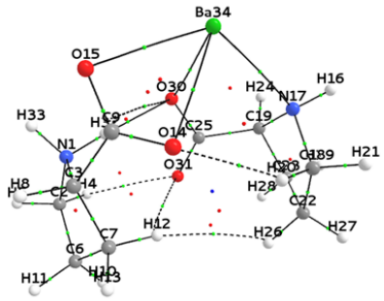

Bond	ρ	$\nabla^2\rho$	ε
C(25) – O(31)	0.395	0.076	0.087
N(1) – H(32)	0.310	-1.659	0.002
N(1) – H(33)	0.341	-1.852	0.005
O(14) – Ba(34)	0.034	0.132	0.037
O(15) – Ba(34)	0.036	0.138	0.046
N(17) – Ba(34)	0.028	0.090	0.023
O(30) – Ba(34)	0.043	0.173	0.072

Bond	ρ	$\nabla^2\rho$	ε
N(1) – C(2)	0.228	-0.544	0.026
N(1) – C(3)	0.232	-0.554	0.010
C(2) – H(4)	0.292	-1.106	0.029
C(2) – H(5)	0.287	-1.040	0.037
C(2) – C(6)	0.241	-0.549	0.022
C(3) – C(7)	0.252	-0.598	0.024
C(6) – C(7)	0.241	-0.539	0.004
C(3) – C(9)	0.257	-0.639	0.054
C(3) – H(8)	0.285	-1.027	0.028
C(9) – O(30)	0.011	0.039	0.748
C(6) – H(10)	0.282	-1.003	0.007
C(6) – H(11)	0.281	-0.974	0.013
C(7) - H(12)	0.283	-0.999	0.010
C(7) – H(13)	0.281	-0.993	0.005
C(9) - O(14)	0.370	-0.159	0.061
C(9) - O(15)	0.365	-0.225	0.053
H(16) – N(17)	0.341	-1.756	0.038
O(14) – H(20)	0.009	0.030	0.093
N(17) – C(18)	0.242	-0.602	0.035
N(17) – C(19)	0.249	-0.628	0.038
C(18) – H(20)	0.286	-1.024	0.030
C(18) – H(21)	0.283	-1.003	0.029
H(12) – H(26)	0.002	0.007	0.520
C(18) – C(22)	0.237	-0.527	0.019
C(22) – C(23)	0.240	-0.535	0.002
C(19) – C(23)	0.249	-0.578	0.017
C(19) – C(25)	0.249	-0.600	0.072
C(19) – H(24)	0.281	-0.991	0.023
H(4) – O(31)	0.012	0.041	0.231
H(12) – O(31)	0.007	0.026	0.208
C(22) – H(26)	0.281	-0.977	0.010
C(22) – H(27)	0.280	-0.977	0.007
C(23) – H(28)	0.283	-1.010	0.001
C(23) – H(29)	0.278	-0.951	0.010
O(30) – H(32)	0.041	0.105	0.050
C(25) – O(30)	0.333	-0.345	0.003

Table A2.15. Comparison of the three levels calculations, UB3LYPD3/6-311++G(3df,3pd)//6- 31+G(d,p), UB3LYPD3/6-31+G(d,p), and UB3LYPD3/cc-PVTZ, relative Gibbs energies (and enthalpies) of the lowest energy structures of each forms of the $[Co(Pro)_2\text{-}H]^+$ complex at 298 K.

Structure	$\Delta_{rel}G(\Delta_{rel}H)$/kJ mol^{-1} B3LYP/6-311++G(3d,3p)// 6-31+G(d,p	$\Delta_{rel}G(\Delta_{rel}H)$/kJ mol^{-1} B3LYP/6-31+G(d,p)	$\Delta_{rel}G(\Delta_{rel}H)$/kJ mol^{-1} UB3LYP/cc-PVTZ
Co-NO-NO-CS-X-E	0(0)	0(0)	0(0)
Co-OO-NO-ZW-E-E	16.9(29.9)	22.0(35.0)	17.1(29.4)
Co- NO-OO-CS-X-X	31.6(47.9)	42.2(58.5)	31.2(47.8)
Co- OO-OO-ZW-E-X	55.0(77.1)	64.5(86.6)	55.0(76.1)

Table A2.16. Comparison of the three levels calculations, UB3LYPD3/6-311++G(3df,3pd)//6- 31+G(d,p), UB3LYPD3/6-31+G(d,p), and UB3LYPD3/cc-PVTZ, relative Gibbs energies (and enthalpies) of the lowest energy structures of each forms of the $[Mn(Pro)_2\text{-}H]^+$ complex at 298 K.

Structure	$\Delta_{rel}G(\Delta_{rel}H)$/kJ mol^{-1} B3LYP/6-311++G(3d,3p)// 6-31+G(d,p	$\Delta_{rel}G(\Delta_{rel}H)$/kJ mol^{-1} B3LYP/6-31+G(d,p)	$\Delta_{rel}G(\Delta_{rel}H)$/kJ mol^{-1} UB3LYP/cc-PVTZ
Mn-NO-NO-CS-X-X	0(0)	0(0)	0(0)
Mn- OO-NO-ZW-E-X	9.2(11.4)	8.4(10.6)	8.9(10.5)
Mn- NO-OO-CS-X-X	23.6(28.7)	28.6(33.7)	24.1(28.1)
Mn- OO-OO-ZW-E-X	29.7(36.1)	33.8(40.2)	29.6(35.1)

Table A2.17. Comparison of the three levels calculations, B3LYPD3/6-311++G(3df,3pd)//6-31+G(d,p), B3LYPD3/6-31+G(d,p), and B3LYPD3/cc-PVTZ, relative Gibbs energies (and enthalpies) of the lowest energy structures of each forms of the $[Mg(Pro)_2\text{-}H]^+$ complex at 298 K.

Structure	$\Delta_{rel}G(\Delta_{rel}H)$/kJ mol^{-1} B3LYP/6-311++G(3d,3p)// 6-31+G(d,p	$\Delta_{rel}G(\Delta_{rel}H)$/kJ mol^{-1} B3LYP/6-31+G(d,p)	$\Delta_{rel}G(\Delta_{rel}H)$/kJ mol^{-1} UB3LYP/cc-PVTZ
Mg-NO-NO-CS-X-E	0(0)	0(0)	0(0)
Mg-OO-NO-ZW-E-X	7.8(7.2)	6.0(5.4)	2.1(7.3)
Mg-NO-OO-CS-X-X	16.3(17.7)	19.3(20.7)	13.2(17.8)
M-OO-OO-ZW-E-X	20.5(22.8)	21.0(23.3)	15.9(22.5)

Table A2.18. xyz Cartesian geometry of each complex in Chapter 4.

Mn-NO-NO-CS-X-X

1 6

N	-1.96482300	-0.38702200	-1.08455200
C	-2.16409700	-1.86462100	-0.76489900
C	-3.01720900	0.37758900	-0.33424100
H	-1.40055000	-2.16429900	-0.04270600
H	-2.02663700	-2.44826600	-1.67713300
C	-3.56582600	-1.95375400	-0.16009600
C	-3.66978000	-0.64561400	0.63393400
H	-3.77480900	0.77010600	-1.02092800
C	-2.40887500	1.55041000	0.40020000
H	-3.68449000	-2.83635600	0.47273800
H	-4.33215100	-1.98919300	-0.94290900
H	-3.08747200	-0.71512100	1.56002000
H	-4.68878900	-0.35273000	0.89093400
O	-3.30193900	2.33957400	0.95773400
O	-1.19100000	1.74598000	0.49500100
H	2.35318700	0.58331100	-1.89999100
N	2.12047800	0.52703100	-0.90814900
C	2.74771800	1.72752800	-0.24799300
C	2.85798000	-0.68519400	-0.33955000
H	2.27750400	1.86029100	0.73367300
H	2.55728000	2.62064600	-0.84802800
C	4.21952900	1.34419400	-0.09561200
C	4.14623500	-0.13308300	0.33031900
H	3.09261500	-1.35018300	-1.17585000
C	1.98973400	-1.51122400	0.64251800
H	4.74092200	1.97002700	0.63310900
H	4.73164500	1.45510600	-1.05900500
H	4.05847300	-0.22579100	1.41606000
H	5.02605700	-0.70508100	0.03191100
O	0.70914300	-1.18933300	0.69364200
O	2.52036000	-2.39949000	1.27718600
H	-2.86701700	3.06150800	1.44937200
H	-2.12950500	-0.24997900	-2.07984200
Mn	0.05436700	0.26098800	-0.41074000

Mn-OO-NO-ZW-E-X

1 6

N	4.18395800	-0.29959200	-1.05811500
C	4.95201500	0.92084200	-0.54442800
C	3.50802200	-0.97716500	0.13613900
H	4.84454000	1.73084700	-1.26657700
H	6.00282500	0.63292800	-0.47213800
C	4.33535200	1.18119200	0.83048900
C	4.05947600	-0.23328300	1.36539400
H	3.73527700	-2.04541400	0.13062200
C	2.00156400	-0.78107300	-0.05366900
H	3.40595900	1.75289200	0.73450800
H	5.01478800	1.75086000	1.46766600
H	3.33889200	-0.26201800	2.18415100
H	4.98442900	-0.70948500	1.70515100
O	1.21637500	-1.13396600	0.86383500
O	1.59501200	-0.22836900	-1.12527800
H	-2.60418500	-1.26300000	-1.51231400
N	-2.46210900	-0.80812000	-0.61008900
C	-3.08462000	-1.69881700	0.43034200
C	-3.29640300	0.46911600	-0.60669100
H	-2.69427500	-1.40039700	1.41072000
H	-2.80098700	-2.73795800	0.24640800
C	-4.58144300	-1.40277700	0.33086200
C	-4.61695700	0.12403400	0.13548800
H	-3.47854100	0.74774300	-1.64880800
C	-2.55046800	1.66596600	0.03725200
H	-5.13195400	-1.72996000	1.21671600
H	-5.00355300	-1.92446000	-0.53669700
H	-4.63732300	0.64455400	1.09639200
H	-5.49013500	0.45871300	-0.42677500
O	-1.26048700	1.49221400	0.25688700
O	-3.17846000	2.67746300	0.27745700
H	3.39535000	-0.01833000	-1.67308700
H	4.78573000	-0.93795900	-1.58118900
Mn	-0.44234100	-0.20010000	-0.15790400

Mn-NO-OO-CS-X-X

1 6

N	-1.92929200	0.71325700	0.89620800
C	-1.58808700	2.05518800	0.27758600
C	-3.31680900	0.35643100	0.44447900
H	-1.00683800	1.88044100	-0.63382700
H	-0.96510100	2.62230000	0.97144700
C	-2.94038300	2.69072600	-0.04442400
C	-3.76607100	1.48891700	-0.52337100
H	-3.99457600	0.30264700	1.30272000
C	-3.31660100	-1.00188300	-0.22184400
H	-2.86382200	3.47400700	-0.80228200
H	-3.38332500	3.13100900	0.85615400
H	-3.50240000	1.23412000	-1.55605300
H	-4.84556100	1.63994500	-0.48048700
O	-4.51074400	-1.41593900	-0.57710100
O	-2.28874500	-1.65983000	-0.43368100
H	3.32595300	-0.26644400	-2.07176100
N	3.96652600	-0.20706300	-1.28784600
C	4.44835900	1.15334500	-1.01430400
C	3.42803100	-0.77264300	-0.05825100
H	3.63726300	1.90321400	-0.98979200
H	5.17244800	1.45865900	-1.77489300
C	5.06464400	0.99298100	0.37768700
C	4.04485300	0.09000600	1.09862100
H	3.72048000	-1.82519100	0.05329600
C	1.92037100	-0.76606100	0.04551600
H	5.21525900	1.94530500	0.89316600
H	6.03182100	0.48760600	0.29643400
H	3.26816400	0.69840500	1.57495200
H	4.48473700	-0.53928000	1.87412300
O	1.17409400	-0.16323800	-0.80908400
O	1.33506900	-1.38799700	1.01118600
H	-4.46287600	-2.28731800	-1.01485400
H	-1.94780800	0.82820000	1.90849700
Mn	-0.46766800	-0.83747900	0.26055600

Mn-OO-OO-ZW-E-X

1 6

C	-4.60008500	1.03773200	-0.83407700
C	-3.90660400	-0.33890500	-0.84757700
N	-4.54541600	-1.10598100	0.31281600
C	-5.50254500	-0.16217300	1.04056900
C	-5.00414900	1.22521100	0.63755600
C	-2.40893700	-0.26423700	-0.55235900
O	-1.65719900	0.35572900	-1.35072700
O	-1.96473400	-0.82350000	0.50026800
O	1.53783400	0.91351100	0.86308000
C	2.37254000	0.01573300	0.47227100
O	1.91985800	-0.93617700	-0.26362900
C	3.82540700	0.09202300	0.88367100
N	4.63441700	-1.06260200	0.51244400
C	5.41597200	-0.72286700	-0.68556600
C	5.80572000	0.73040600	-0.40470100
C	4.51207300	1.32056800	0.18976700
H	4.82705600	-0.78779100	-1.61739000
H	6.27693900	-1.39108400	-0.77743300
H	3.81042800	0.22813800	1.97333000
H	6.13468200	1.26647200	-1.29897200
H	6.61389000	0.75942100	0.33271400
H	3.87107200	1.71433000	-0.60599800
H	4.68469400	2.13267400	0.89819100
H	4.08859100	-1.91173900	0.41173400
H	-5.46954200	-0.38290400	2.10803000
H	-6.50528200	-0.36098900	0.65656500
H	-4.05471600	-0.89012700	-1.77855600
H	-4.14324700	1.51706500	1.24867100
H	-5.78158900	1.98027900	0.77034900
H	-3.92718400	1.81025200	-1.20977600
H	-5.48328400	1.01361600	-1.47951200
H	-3.74590700	-1.37544600	0.91800300
Mn	0.05790900	-0.07427000	-0.14886000
H	-5.00974300	-1.96277800	0.00547300

Fe-NO-NO-CS-X-X

1 5

N	-1.83036800	-0.54867700	-0.91554800
C	-2.11552000	-1.96909200	-0.44781000
C	-2.96021500	0.31700400	-0.45087400
H	-1.45802600	-2.19095600	0.39594000
H	-1.87322300	-2.66622300	-1.25151700
C	-3.58844000	-1.96058400	-0.03463300
C	-3.76805200	-0.55299500	0.54923100
H	-3.60371000	0.61188500	-1.28682600
C	-2.41534700	1.57362200	0.18475800
H	-3.81750900	-2.74551400	0.68994000
H	-4.24196900	-2.09895500	-0.90341100
H	-3.32245700	-0.49454100	1.54925700
H	-4.80485700	-0.22039700	0.61790200
O	-3.33267600	2.46403500	0.48826900
O	-1.21089000	1.74434600	0.42525300
H	2.03279700	0.81341100	-1.79644100
N	1.97469300	0.66138100	-0.79077200
C	2.58638000	1.86276400	-0.11382000
C	2.86965800	-0.53191200	-0.45669400
H	2.16093700	1.94499000	0.89334500
H	2.32968400	2.76763200	-0.66949900
C	4.07948800	1.54208100	-0.04003800
C	4.07646400	0.04995900	0.32201900
H	3.19421700	-0.98645900	-1.39649800
C	2.13216200	-1.62244800	0.34351300
H	4.60369600	2.15827300	0.69491200
H	4.54819900	1.70994700	-1.01724000
H	3.92387200	-0.08216000	1.39815300
H	5.00042300	-0.46708600	0.05990100
O	0.87207100	-1.34451900	0.66227900
O	2.71651800	-2.64125400	0.64050900
H	-2.93430500	3.24077800	0.92432600
H	-1.81001800	-0.53737500	-1.93290500
Fe	0.05085900	0.17009900	-0.07267300

Fe-OO-NO-ZW-X-X

1 5

N	-4.01108300	-0.22818300	1.26648200
C	-5.02954000	0.82644700	0.84902500
C	-3.39953500	-0.82284200	-0.00349800
H	-4.49984000	1.78127300	0.82087200
H	-5.82399300	0.87355000	1.59467500
C	-5.45209200	0.36680400	-0.54488100
C	-4.13243100	-0.11687200	-1.16820300
H	-3.57698300	-1.90057400	-0.00226800
C	-1.90115500	-0.54059500	0.04905700
H	-5.91311800	1.17911200	-1.11104600
H	-6.18019400	-0.44951100	-0.47700600
H	-3.53933900	0.73172500	-1.52291200
H	-4.27150500	-0.79788700	-2.00865400
O	-1.19411400	-0.92772100	-0.93550100
O	-1.43461800	0.09530100	1.02565700
H	2.12802800	-1.26063500	1.40487100
N	2.28562300	-0.81570800	0.50078800
C	3.09193400	-1.76837400	-0.33438900
C	3.18869800	0.38639200	0.73441100
H	3.00486200	-1.45519400	-1.38145500
H	2.68687700	-2.77888500	-0.24048700
C	4.52548100	-1.59176700	0.16850600
C	4.63051000	-0.06957300	0.37911400
H	3.10015200	0.67181500	1.78672900
C	2.73392100	1.61505700	-0.08468100
H	5.26767500	-1.97403200	-0.53695200
H	4.65407500	-2.13168900	1.11448000
H	4.95543600	0.43462900	-0.53470200
H	5.33996000	0.20127500	1.16270600
O	1.53055300	1.51801400	-0.64201000
O	3.45747900	2.58348900	-0.16262400
H	-3.21115600	0.17018500	1.79534800
H	-4.44605700	-0.95246100	1.84082200
Fe	0.53823800	-0.03446900	-0.40872500

Fe-NO-OO-CS-X-X

1 5

N	-1.81080100	0.72951400	0.82885200
C	-1.56347200	2.04596000	0.11921400
C	-3.24006500	0.34854000	0.57516700
H	-1.10466800	1.83429600	-0.85090500
H	-0.85269600	2.63640300	0.69864400
C	-2.95143700	2.66424800	-0.04130600
C	-3.82416600	1.44321600	-0.36481400
H	-3.80218600	0.31546000	1.51399500
C	-3.28898800	-1.02940700	-0.04225500
H	-2.98287200	3.42019700	-0.82952000
H	-3.27643300	3.13467000	0.89364200
H	-3.69696500	1.15251500	-1.41366900
H	-4.88984300	1.59093500	-0.18449500
O	-4.49987100	-1.49429100	-0.23286300
O	-2.26994800	-1.66039800	-0.36333500
H	3.18319800	0.98020500	-1.82128900
N	3.86224600	0.54962700	-1.20327300
C	4.43235300	1.46374900	-0.20501000
C	3.35972000	-0.63262700	-0.52009000
H	3.66501100	2.04458000	0.33797900
H	5.11805400	2.16779800	-0.68448500
C	5.13209900	0.48869100	0.74521400
C	4.12372000	-0.67347200	0.85120400
H	3.56425300	-1.54272200	-1.10023600
C	1.86938100	-0.64626600	-0.28061700
H	5.36171700	0.92906000	1.71907100
H	6.06665700	0.14281900	0.29360800
H	3.42814900	-0.50617300	1.68015900
H	4.59223500	-1.64536500	1.01421700
O	1.10986300	0.34999600	-0.55231800
O	1.29522800	-1.69681200	0.20637000
H	-4.47610600	-2.37820700	-0.64718000
H	-1.69147600	0.87785700	1.82943000
Fe	-0.45935300	-0.80508000	0.10341900

Fe-OO-OO-ZW-X-E

1 5

N	4.52672200	0.86928700	-0.56351400
C	5.46625500	1.02185400	0.62893000
C	3.81462000	-0.47916000	-0.43875800
H	4.91906300	1.57999400	1.39166300
H	6.34421400	1.59164800	0.32278600
C	5.72749300	-0.42201800	1.05421500
C	4.35677100	-1.09364600	0.87150100
H	4.07173400	-1.08865000	-1.30794900
C	2.31777300	-0.19709800	-0.43215300
H	6.09064200	-0.47592200	2.08287500
H	6.48194500	-0.88413600	0.40761100
H	3.69287300	-0.84612600	1.70602700
H	4.40845300	-2.18054700	0.79716600
O	1.52754700	-1.19929900	-0.38176200
O	1.91508200	0.98767700	-0.45158200
N	-4.86426800	-0.21281100	-0.82688600
C	-5.44419400	-0.93157300	0.33634900
C	-3.93607300	0.80595100	-0.37741500
H	-5.21910700	-2.00313600	0.30139000
H	-6.53450500	-0.81951700	0.32363800
C	-4.83064900	-0.25656400	1.57969100
C	-4.41112200	1.12900400	1.06196300
H	-3.96646000	1.70444000	-1.00901400
C	-2.47997700	0.37893100	-0.36216000
H	-3.94818400	-0.81210100	1.91972500
H	-5.52910000	-0.19981100	2.41848500
H	-3.64031500	1.62114900	1.65908500
H	-5.27355200	1.79860300	0.99266900
O	-2.11291300	-0.81749300	-0.66411300
O	-1.54507000	1.20873600	-0.06093300
H	5.03683300	0.93399000	-1.44656800
Fe	-0.21659000	-0.24763000	-0.37636400
H	3.77284200	1.58215100	-0.57776400
H	-4.47576100	-0.83001900	-1.52942600

Co-NO-NO-CS-X-E

1 2

N	1.61116000	0.95008700	-0.40237600
C	1.77883100	1.83986800	0.80638300
C	2.81225000	0.05234400	-0.45802900
H	1.28768000	1.35434100	1.65472500
H	1.27384400	2.78700200	0.61909200
C	3.29113500	1.91114200	1.01184500
C	3.73684300	0.46768700	0.72466500
H	3.33262400	0.16974300	-1.41459500
C	2.32625900	-1.37169100	-0.37805500
H	3.56242100	2.23806100	2.01836300
H	3.74481000	2.60709000	0.29694100
H	3.54896200	-0.16848000	1.59621900
H	4.79023800	0.36754000	0.45964400
O	3.26549800	-2.28460500	-0.38249200
O	1.11616000	-1.65967800	-0.30666000
H	-1.74192300	-1.78449900	-1.11111600
N	-1.74723600	-1.08306700	-0.37092900
C	-2.01765100	-1.77493900	0.95309300
C	-2.88920100	-0.10887200	-0.61484700
H	-1.08119900	-1.90682000	1.50005700
H	-2.44116300	-2.76409200	0.75267400
C	-3.03737700	-0.87482600	1.65264700
C	-3.91736900	-0.39546700	0.48859800
H	-3.28979100	-0.26205000	-1.62065700
C	-2.35308500	1.33125500	-0.55406700
H	-2.53666300	-0.02344200	2.12847800
H	-3.59364900	-1.41219600	2.42386000
H	-4.50312800	0.49815100	0.71140700
H	-4.60357000	-1.18918800	0.17454000
O	-1.02024500	1.42708300	-0.53355200
O	-3.09483600	2.28582200	-0.53863600
H	2.88475300	-3.18206200	-0.33208700
H	1.59627000	1.54815400	-1.22911700
Co	-0.06645900	-0.09460600	-0.40437000

Co-OO-NO-ZW-E-E

1 4

N	4.08117500	-0.19049900	-1.03631100
C	4.92376600	0.89458900	-0.36188000
C	3.34434400	-0.97095700	0.05583300
H	4.89826300	1.79218600	-0.98062300
H	5.94723200	0.51818100	-0.30514300
C	4.28887100	1.03146000	1.02199400
C	3.90698600	-0.41478500	1.37711400
H	3.51589300	-2.04132700	-0.07711500
C	1.85607500	-0.67415000	-0.12869500
H	3.40189700	1.67263800	0.97768800
H	4.98674600	1.47313900	1.73615600
H	3.16329300	-0.49158600	2.17183300
H	4.78913000	-0.98912600	1.67625600
O	1.02559200	-1.10271400	0.71154700
O	1.49833700	0.03851300	-1.12411600
H	-2.30646600	-1.15394400	-1.74380000
N	-2.27669700	-0.80052400	-0.78965100
C	-2.74223500	-1.90562400	0.14783800
C	-3.27183200	0.35126400	-0.66937400
H	-1.89103200	-2.29782300	0.70937800
H	-3.16549700	-2.71790400	-0.45066200
C	-3.81339300	-1.25028700	1.02535500
C	-4.47529500	-0.24552400	0.07197900
H	-3.52292400	0.70609100	-1.67303800
C	-2.66651100	1.56381100	0.08783000
H	-3.35202800	-0.72389800	1.86899000
H	-4.50947000	-1.98768500	1.43181400
H	-5.04428700	0.53633400	0.57709400
H	-5.13911900	-0.76124500	-0.63105600
O	-1.35596700	1.53912600	0.28298200
O	-3.39805200	2.46630100	0.43770600
H	3.32527900	0.22337000	-1.61521500
H	4.64479000	-0.79572400	-1.63600600
Co	-0.46803600	0.00618200	-0.27732300

Co-NO-OO-CS-X-X

1 4

N	-2.14988100	-0.72767700	-0.75236000
C	-2.38834800	-2.01816300	0.00976300
C	-3.32470300	0.17430700	-0.47953700
H	-1.83896600	-1.96453300	0.95432000
H	-1.98870300	-2.85320900	-0.56780500
C	-3.89749500	-2.05436300	0.24703900
C	-4.22410200	-0.58266200	0.53785600
H	-3.87767700	0.36672000	-1.40452300
C	-2.83591100	1.50321700	0.05057300
H	-4.17232000	-2.71433100	1.07316000
H	-4.42326700	-2.39756800	-0.65116900
H	-3.93811900	-0.32493100	1.56376500
H	-5.27496800	-0.32134100	0.40608100
O	-3.78853000	2.38206300	0.25076300
O	-1.64335600	1.74042300	0.29499800
H	3.61408700	-0.46369000	-1.89575700
N	4.12889400	-0.52776000	-1.02421900
C	4.92314200	0.67015600	-0.71340200
C	3.29025300	-0.84481000	0.12302200
H	4.35224000	1.60764200	-0.82994100
H	5.80067000	0.71972100	-1.36390700
C	5.27345700	0.43990200	0.75869000
C	3.95750100	-0.11178200	1.34126600
H	3.25560200	-1.92823600	0.30161100
C	1.84945600	-0.41535400	-0.00124000
H	5.60249400	1.34933700	1.26809200
H	6.06899900	-0.30740000	0.83648300
H	3.31955200	0.70802500	1.68795800
H	4.09959200	-0.79119900	2.18337300
O	1.42371700	0.29781600	-0.98464400
O	0.97491200	-0.76184400	0.87943000
H	-3.42610900	3.21763400	0.60312900
H	-2.13960100	-0.94375100	-1.74849800
Co	-0.38370600	0.22217900	-0.17588400

Co-OO-OO-ZW-X-X

1 4

C	4.44429200	-0.11039600	1.14154300
C	3.80419600	-0.39890300	-0.23464300
N	4.13400700	0.83179400	-1.08457400
C	4.98277300	1.77934900	-0.23866100
C	5.59347700	0.85656200	0.81457800
C	2.29197800	-0.54831500	-0.20456200
O	1.57431400	0.33998900	-0.75800400
O	1.77695800	-1.53527100	0.39185600
O	-1.67273400	-0.07874600	0.89493700
C	-2.42349000	-0.60766100	-0.00339400
O	-1.81528600	-1.27924100	-0.91854400
C	-3.92283100	-0.46682400	-0.00447500
N	-4.48555400	0.11950000	1.20642800
C	-4.83782700	1.52116100	0.93923900
C	-5.36345000	1.44519800	-0.49633000
C	-4.36610900	0.48473300	-1.17161100
H	-3.97098900	2.20284300	0.99372800
H	-5.58905300	1.86459900	1.65614200
H	-4.31218700	-1.48017300	-0.17064600
H	-5.40198500	2.41936200	-0.99109600
H	-6.37004000	1.01560900	-0.49892100
H	-3.50458200	1.04124300	-1.55599500
H	-4.78945000	-0.07864700	-2.00492700
H	-3.89980200	-0.00763900	2.02462100
H	4.29804300	2.50676500	0.20255200
H	5.69331200	2.29551000	-0.88509300
H	4.24987200	-1.27560600	-0.71003400
H	5.93385200	1.41791200	1.68744600
H	6.45582700	0.31939200	0.40398200
H	3.71487300	0.36681200	1.80394300
H	4.77132200	-1.03617100	1.61649100
H	3.22486700	1.24450400	-1.35966600
Co	-0.10337200	-0.86448600	-0.04657000
H	4.62393200	0.56247600	-1.94018100

Ni-NO-NO-E-E

1 1

N	1.64354800	1.06511300	-0.58991600
C	1.67767400	2.16329600	0.44450400
C	2.86700000	0.21886400	-0.37461600
H	0.66608600	2.54437400	0.57924800
H	2.32873100	2.97107400	0.09152000
C	2.28134800	1.45502600	1.65094200
C	3.42078600	0.62708000	1.03104000
H	3.61577600	0.38213300	-1.15542500
C	2.44824500	-1.22841200	-0.41763400
H	1.53012100	0.80553100	2.11600400
H	2.64064000	2.15313800	2.40965100
H	3.71244300	-0.24013100	1.62719900
H	4.31269200	1.24189200	0.88796900
O	1.25397600	-1.57331400	-0.43256800
O	3.43336200	-2.09559100	-0.41197500
H	-1.56933300	-1.81055600	-1.16086200
N	-1.60876400	-1.12634500	-0.40519200
C	-1.78259200	-1.85703200	0.91534000
C	-2.82401100	-0.22899000	-0.59253600
H	-0.81817000	-1.94283400	1.41952700
H	-2.15515600	-2.86475900	0.70651000
C	-2.82598500	-1.03159000	1.66878700
C	-3.78258400	-0.59262000	0.54955100
H	-3.25230100	-0.40002200	-1.58370900
C	-2.37041200	1.23770500	-0.53179800
H	-2.35933500	-0.15757900	2.13791600
H	-3.31523500	-1.61398500	2.45257400
H	-4.40916900	0.26255700	0.80999600
H	-4.43479900	-1.42127500	0.25411800
O	-1.04865100	1.40429100	-0.55092200
O	-3.15880000	2.15372200	-0.47792400
H	3.09591900	-3.01100800	-0.42208200
H	1.64287000	1.47251500	-1.52627700
Ni	0.00102900	-0.05840200	-0.49116100

Ni-OO-NO-ZW-E-E

1 3

N	3.88071200	-0.29491900	-1.18917400
C	4.96588700	0.63073900	-0.63514300
C	3.17713800	-0.96794900	-0.00710000
H	5.00667000	1.53002000	-1.25065400
H	5.91434400	0.09453000	-0.70797000
C	4.54320400	0.84576900	0.81817000
C	3.98409300	-0.52644000	1.22791200
H	3.16375300	-2.04987000	-0.15594500
C	1.74053900	-0.44436700	-0.00419400
H	3.77136400	1.62019000	0.88379400
H	5.38776000	1.16110900	1.43416500
H	3.34459500	-0.49614500	2.11157500
H	4.79460300	-1.23707700	1.41623500
O	0.96395100	-0.74997900	0.93371200
O	1.36691800	0.31952500	-0.95230100
H	-1.59501300	-0.93504000	-1.73091700
N	-1.87127900	-0.71073300	-0.77692300
C	-2.11987300	-1.99117200	-0.00677100
C	-3.17023300	0.07879600	-0.79890900
H	-1.26280000	-2.20599600	0.63527200
H	-2.24213500	-2.81537800	-0.71737700
C	-3.42215600	-1.72929200	0.75466800
C	-4.23038500	-0.87948700	-0.23664000
H	-3.38465100	0.39291100	-1.82423700
C	-3.05109300	1.37041800	0.04458100
H	-3.22235700	-1.16027600	1.67012900
H	-3.92154600	-2.65829600	1.03878400
H	-5.05144000	-0.32352300	0.21879700
H	-4.63864500	-1.50788600	-1.03589600
O	-1.82225500	1.68454700	0.44756500
O	-4.03753300	2.03105800	0.28471400
H	3.13149400	0.24249300	-1.66644100
H	4.25837900	-0.97105400	-1.85536700
Ni	-0.49256300	0.49127000	0.09463400

Ni-NO-OO-CS-X-E

1 1

N	1.98502700	0.77085300	-0.59099000
C	2.39632400	1.93662400	0.28431700
C	3.13717300	-0.20342500	-0.60989400
H	2.00875200	1.75728700	1.29057100
H	1.93964500	2.84849400	-0.10106500
C	3.92447700	1.90149800	0.26608800
C	4.22650700	0.39546200	0.32004300
H	3.51927300	-0.31696000	-1.62946600
C	2.60493900	-1.53462400	-0.15124500
H	4.36145700	2.44503100	1.10693700
H	4.31175400	2.34227700	-0.65962300
H	4.10330500	0.01945600	1.34130700
H	5.22814900	0.12751400	-0.01886200
O	3.47367800	-2.51505200	-0.12118200
O	1.41869700	-1.67596200	0.18703300
H	-3.90889900	1.45082000	-1.60421000
N	-3.73237800	0.61000100	-1.06793300
C	-4.89197800	-0.30488600	-0.98116600
C	-3.23008700	0.89561800	0.29323400
H	-4.92180500	-0.95876900	-1.85729900
H	-5.84345000	0.24575700	-0.92795700
C	-4.64617400	-1.06635800	0.32483100
C	-4.07622200	0.02549600	1.24811300
H	-3.26337700	1.96231100	0.54499400
C	-1.77975400	0.49239500	0.25037400
H	-3.90296800	-1.85510100	0.17025600
H	-5.55614800	-1.52222600	0.72236900
H	-3.49673100	-0.37239400	2.08458000
H	-4.88317000	0.64156800	1.65678800
O	-0.84608900	1.30276600	-0.12912900
O	-1.34676300	-0.68442100	0.51363200
H	3.05716300	-3.34217600	0.18891100
H	1.83105600	1.11971000	-1.53801700
Ni	0.35928800	-0.10371500	-0.00817000

Ni-OO-OO-ZW-E-E

1 3

C	-4.62274000	-0.46351500	0.48695000
C	-3.38813100	0.33142100	0.95698300
N	-3.53234500	1.70255100	0.29097900
C	-4.76352600	1.66748000	-0.61349200
C	-4.97149400	0.17498300	-0.86783100
C	-2.06920800	-0.25286200	0.46271300
O	-1.69845400	-1.39046600	0.85890300
O	-1.36132300	0.42292100	-0.34808100
O	1.66219600	-0.48613700	0.76954700
C	2.30884300	-0.70172600	-0.31259100
O	1.63115700	-1.21841100	-1.27900300
C	3.76016300	-0.31597200	-0.50208600
N	3.71573300	1.05789200	-1.04844300
C	4.54693300	1.94553100	-0.21038900
C	4.48753200	1.28028900	1.16792100
C	4.55555500	-0.21642300	0.81708700
H	4.13837400	2.96057800	-0.21418600
H	5.58862500	1.99245700	-0.56498300
H	4.19454100	-1.03666700	-1.20440400
H	3.53520400	1.50870800	1.65743600
H	5.30057500	1.59907000	1.82501000
H	4.15398600	-0.86335300	1.60032900
H	5.59110400	-0.51611300	0.62673000
H	3.93484100	1.09323800	-2.03661300
H	-4.56556200	2.27271100	-1.49883500
H	-5.59095500	2.10332700	-0.04957800
H	-3.33542600	0.45215100	2.04093000
H	-4.29685900	-0.17793000	-1.65520900
H	-5.99545000	-0.03511400	-1.18341200
H	-4.39396600	-1.52892700	0.42689400
H	-5.44093300	-0.33220000	1.20139800
H	-2.66141000	1.81956000	-0.26186700
Ni	0.04293600	-1.15772900	-0.16792300
H	-3.57476300	2.46333700	0.97194900

Cu-NO-NO-CS-E-E

1 2

N	1.874572	-0.730016	1.188541
C	2.145719	-1.832157	0.198940
C	2.901497	0.332304	0.969301
H	1.234824	-2.415518	0.065662
H	2.943995	-2.480331	0.578426
C	2.605468	-1.050946	-1.026356
C	3.538704	0.016163	-0.426854
H	3.663763	0.336314	1.754165
C	2.219842	1.681503	0.975312
H	1.741533	-0.587568	-1.519599
H	3.110645	-1.680866	-1.761160
H	3.643089	0.908944	-1.047036
H	4.540069	-0.390761	-0.267720
O	0.989826	1.819588	0.926841
O	3.048914	2.701728	1.005618
H	-2.033612	1.484735	1.468842
N	-1.857809	0.819946	0.717056
C	-2.039380	1.515411	-0.618069
C	-2.859191	-0.316386	0.788790
H	-1.065311	1.779895	-1.036430
H	-2.604479	2.439116	-0.459553
C	-2.840986	0.518583	-1.458399
C	-3.780266	-0.119118	-0.423769
H	-3.393850	-0.268753	1.741484
C	-2.133632	-1.679201	0.749271
H	-2.180038	-0.241344	-1.891979
H	-3.368365	1.011337	-2.278140
H	-4.210195	-1.070914	-0.740392
H	-4.598907	0.564978	-0.175614
O	-0.818331	-1.636516	0.893242
O	-2.761391	-2.707214	0.606880
H	2.563194	3.547383	0.981645
H	1.919117	-1.093116	2.140828
Cu	-0.022833	0.046876	0.941830

Cu-OO-NO-ZW-E-E

1 2

N	4.02794400	0.96135600	-0.34179200
C	4.85796200	0.67607300	0.90724500
C	3.33052000	-0.33522400	-0.76283900
H	4.83038500	1.55292100	1.55512200
H	5.88400800	0.49428300	0.58042900
C	4.21079100	-0.58506500	1.47907400
C	3.85741100	-1.39763700	0.22216900
H	3.56314000	-0.55663900	-1.80636400
C	1.83086800	-0.07426200	-0.62762700
H	3.31092700	-0.32905800	2.04857600
H	4.89341600	-1.11393600	2.14726800
H	3.10537500	-2.16956900	0.39380900
H	4.74845900	-1.87837900	-0.19285400
O	1.00466900	-0.98658100	-0.90152300
O	1.45042000	1.06590500	-0.22481400
H	-2.21633100	-0.94284800	-1.81972800
N	-2.19202200	-0.75757300	-0.81791400
C	-2.24581400	-2.05629500	-0.04930900
C	-3.38324100	0.08749200	-0.40312600
H	-1.23220700	-2.39521100	0.17702000
H	-2.73461500	-2.81606000	-0.66864600
C	-3.10154400	-1.71584800	1.17080600
C	-4.17868600	-0.79560900	0.57563600
H	-3.96402700	0.35939200	-1.28831500
C	-2.91605000	1.40718600	0.25092500
H	-2.50644800	-1.17780800	1.91878800
H	-3.51076600	-2.61030100	1.64569800
H	-4.69810700	-0.18073400	1.31260700
H	-4.92510300	-1.38684800	0.03480200
O	-1.61617700	1.64047800	0.22492500
O	-3.73013100	2.16188900	0.74223200
H	3.24529400	1.61447400	-0.13394400
H	4.58767300	1.36762800	-1.09387400
Cu	-0.54055400	0.29047700	-0.41368100

Cu-NO-NO-CS-E-E

1	2			
N		1.874572	-0.730016	1.188541
C		2.145719	-1.832157	0.198940
C		2.901497	0.332304	0.969301
H		1.234824	-2.415518	0.065662
H		2.943995	-2.480331	0.578426
C		2.605468	-1.050946	-1.026356
C		3.538704	0.016163	-0.426854
H		3.663763	0.336314	1.754165
C		2.219842	1.681503	0.975312
H		1.741533	-0.587568	-1.519599
H		3.110645	-1.680866	-1.761160
H		3.643089	0.908944	-1.047036
H		4.540069	-0.390761	-0.267720
O		0.989826	1.819588	0.926841
O		3.048914	2.701728	1.005618
H		-2.033612	1.484735	1.468842
N		-1.857809	0.819946	0.717056
C		-2.039380	1.515411	-0.618069
C		-2.859191	-0.316386	0.788790
H		-1.065311	1.779895	-1.036430
H		-2.604479	2.439116	-0.459553
C		-2.840986	0.518583	-1.458399
C		-3.780266	-0.119118	-0.423769
H		-3.393850	-0.268753	1.741484
C		-2.133632	-1.679201	0.749271
H		-2.180038	-0.241344	-1.891979
H		-3.368365	1.011337	-2.278140
H		-4.210195	-1.070914	-0.740392
H		-4.598907	0.564978	-0.175614
O		-0.818331	-1.636516	0.893242
O		-2.761391	-2.707214	0.606880
H		2.563194	3.547383	0.981645
H		1.919117	-1.093116	2.140828
Cu		-0.022833	0.046876	0.941830

Cu-OO-NO-ZW-E-E

1	2			
N		4.02794400	0.96135600	-0.34179200
C		4.85796200	0.67607300	0.90724500
C		3.33052000	-0.33522400	-0.76283900
H		4.83038500	1.55292100	1.55512200
H		5.88400800	0.49428300	0.58042900
C		4.21079100	-0.58506500	1.47907400
C		3.85741100	-1.39763700	0.22216900
H		3.56314000	-0.55663900	-1.80636400
C		1.83086800	-0.07426200	-0.62762700
H		3.31092700	-0.32905800	2.04857600
H		4.89341600	-1.11393600	2.14726800
H		3.10537500	-2.16956900	0.39380900
H		4.74845900	-1.87837900	-0.19285400
O		1.00466900	-0.98658100	-0.90152300
O		1.45042000	1.06590500	-0.22481400
H		-2.21633100	-0.94284800	-1.81972800
N		-2.19202200	-0.75757300	-0.81791400
C		-2.24581400	-2.05629500	-0.04930900
C		-3.38324100	0.08749200	-0.40312600
H		-1.23220700	-2.39521100	0.17702000
H		-2.73461500	-2.81606000	-0.66864600
C		-3.10154400	-1.71584800	1.17080600
C		-4.17868600	-0.79560900	0.57563600
H		-3.96402700	0.35939200	-1.28831500
C		-2.91605000	1.40718600	0.25092500
H		-2.50644800	-1.17780800	1.91878800
H		-3.51076600	-2.61030100	1.64569800
H		-4.69810700	-0.18073400	1.31260700
H		-4.92510300	-1.38684800	0.03480200
O		-1.61617700	1.64047800	0.22492500
O		-3.73013100	2.16188900	0.74223200
H		3.24529400	1.61447400	-0.13394400
H		4.58767300	1.36762800	-1.09387400
Cu		-0.54055400	0.29047700	-0.41368100

Zn-NO-NO-CS-X-X

1 1

N	-1.87602700	-0.31082000	-1.08631700
C	-2.19903200	-1.79246600	-0.88574500
C	-2.84668600	0.48057000	-0.25933000
H	-1.41066100	-2.22706000	-0.26738600
H	-2.20385800	-2.28980600	-1.85720300
C	-3.54589400	-1.80781000	-0.15998900
C	-3.47601300	-0.54854200	0.71333900
H	-3.62635400	0.92136800	-0.88913400
C	-2.13784000	1.60178000	0.46845100
H	-3.67803500	-2.71726800	0.43046500
H	-4.37920800	-1.73639900	-0.86801100
H	-2.81073500	-0.71339400	1.56878100
H	-4.44174000	-0.20328500	1.08519200
O	-2.95975400	2.43995500	1.06135200
O	-0.90817800	1.70874000	0.52828700
H	2.13584800	0.30824400	-1.96471100
N	1.96129500	0.41257400	-0.96662500
C	2.54466100	1.73905400	-0.53289400
C	2.74700200	-0.68512000	-0.23711900
H	1.98162600	2.09097700	0.33718400
H	2.42812000	2.46869100	-1.33749100
C	3.98666200	1.40926700	-0.15008100
C	3.83330700	0.06303500	0.57079300
H	3.20072100	-1.32711600	-0.99660000
C	1.87921300	-1.60032700	0.66575500
H	4.43573600	2.18276900	0.47827900
H	4.60381300	1.30543200	-1.05067100
H	3.49221400	0.21623600	1.60026200
H	4.75386800	-0.51974000	0.61841600
O	0.59080000	-1.32969000	0.73381500
O	2.44518300	-2.49940100	1.25498900
H	-2.46502100	3.12132600	1.55443700
H	-2.00861500	-0.06885700	-2.06621900
Zn	0.04462400	0.09207100	-0.39305400

Zn-OO-NO-ZW-E-E

1 1

N	4.28596900	-0.39450100	-1.02456100
C	5.17044100	0.72702900	-0.48308500
C	3.43431900	-0.93293800	0.12460600
H	5.26052700	1.50201800	-1.24505300
H	6.15330700	0.29567600	-0.28175800
C	4.45984600	1.14886100	0.80264700
C	3.94494100	-0.18414000	1.37007300
H	3.54403300	-2.01724500	0.19099100
C	1.98177100	-0.58664800	-0.24197900
H	3.62979500	1.82737100	0.57858900
H	5.14118800	1.66444800	1.48240700
H	3.14661400	-0.07025800	2.10481800
H	4.75877100	-0.74847600	1.83601400
O	1.10487400	-0.89167200	0.64322300
O	1.74906500	-0.02769600	-1.32664600
H	-2.14774900	-1.27842200	-1.60584300
N	-2.29110800	-0.87869200	-0.68074300
C	-3.00257200	-1.90118200	0.19369800
C	-3.19824300	0.34180200	-0.79982900
H	-2.29706200	-2.34902800	0.89803200
H	-3.39956500	-2.69507000	-0.44580400
C	-4.13343600	-1.11332700	0.86067100
C	-4.54866400	-0.11938800	-0.23250000
H	-3.25818700	0.63230800	-1.85221700
C	-2.64700600	1.58824800	-0.03897400
H	-3.76265100	-0.57611900	1.74154900
H	-4.94526600	-1.76823800	1.18519300
H	-5.12317500	0.73093800	0.13653900
H	-5.13565500	-0.62548500	-1.00709500
O	-1.41147600	1.52136300	0.42346800
O	-3.37518100	2.55434700	0.06332900
H	3.57785400	-0.03107800	-1.69788500
H	4.82841300	-1.12364300	-1.49040000
Zn	-0.57472900	-0.11726600	0.12166900

Zn-NO-OO-CS-X-X

1 1

N	-2.19895500	-0.74373900	-0.76113000
C	-2.41149900	-2.02043800	0.03796000
C	-3.33482300	0.18583000	-0.43580500
H	-1.79633700	-1.96642200	0.94077800
H	-2.07300800	-2.87150500	-0.55499100
C	-3.90113300	-2.01507200	0.37724100
C	-4.17443800	-0.53095100	0.65875300
H	-3.94466600	0.36326500	-1.32719300
C	-2.79761700	1.52397300	0.02857200
H	-4.13266300	-2.65257900	1.23369000
H	-4.49446200	-2.36329300	-0.47575400
H	-3.81088800	-0.25912500	1.65606600
H	-5.22616900	-0.24853200	0.59542300
O	-3.73430800	2.41308000	0.25873100
O	-1.59367700	1.75594000	0.19656700
H	3.65070200	-0.62928500	-1.79749500
N	4.15732600	-0.63661800	-0.91933700
C	5.01090600	0.54563500	-0.72256700
C	3.29179800	-0.80143300	0.24344100
H	4.50486600	1.49124600	-0.98343700
H	5.91601600	0.46276000	-1.33082100
C	5.28813700	0.49168200	0.78146500
C	3.91466000	0.10663000	1.35988100
H	3.27432900	-1.84826700	0.57503800
C	1.84477900	-0.42534600	0.03201600
H	5.65834400	1.43852600	1.18337800
H	6.02648700	-0.28762400	0.99544400
H	3.30299100	1.00426100	1.50270800
H	3.96352500	-0.41399000	2.31791300
O	1.44726200	0.18450400	-1.02897500
O	0.96107900	-0.71233500	0.91841400
H	-3.35041300	3.25534300	0.56988500
H	-2.24223900	-0.97221500	-1.75336200
Zn	-0.39875000	0.15557800	-0.28358800

Zn-OO-OO-ZW-X-X

1 1

C	4.43316000	-0.40556300	1.09734100
C	3.83519600	-0.32871300	-0.32447700
N	4.41432300	0.95424100	-0.92238400
C	5.35103200	1.57931900	0.10692000
C	5.74118800	0.39476000	0.98982400
C	2.31379200	-0.19327200	-0.37070700
O	1.80568900	0.86584800	-0.76619000
O	1.66207500	-1.22384200	0.04130300
O	-1.83364900	-0.32858700	0.94144200
C	-2.51574700	-0.60288000	-0.10971700
O	-1.87034100	-1.01806000	-1.14269100
C	-4.02308100	-0.46401100	-0.15806600
N	-4.65848600	-0.15958500	1.11464700
C	-4.87380000	1.29155600	1.18900100
C	-5.33453200	1.60882900	-0.23629500
C	-4.41166100	0.72783400	-1.10464800
H	-3.95322600	1.85200800	1.43018400
H	-5.62577800	1.52407300	1.94819900
H	-4.38750200	-1.41613000	-0.56398100
H	-5.25133000	2.66979700	-0.48677800
H	-6.37837900	1.30563600	-0.36039200
H	-3.51780600	1.28244000	-1.40732300
H	-4.88996700	0.36543800	-2.01625200
H	-4.16263500	-0.54172700	1.91284500
H	4.76759200	2.32235200	0.65486600
H	6.17336400	2.07442300	-0.41059300
H	4.15198300	-1.17197200	-0.94209900
H	6.11566500	0.72608600	1.96088200
H	6.52788600	-0.19957100	0.51161000
H	3.75420100	0.06232900	1.81767500
H	4.57883700	-1.44308200	1.40069800
H	3.59224900	1.55044900	-1.13831500
Zn	-0.19638800	-0.84326700	-0.09745000
H	4.90214200	0.76286900	-1.79954500

Mg-NO-NO-CS-X-E

1 1

N	1.90240500	0.48798000	-1.06522300
C	2.11649000	1.93346500	-0.62250300
C	2.94079500	-0.35001100	-0.37836400
H	1.34130100	2.18777100	0.10517500
H	2.00491600	2.59089200	-1.48662300
C	3.50889300	1.95038000	0.00963600
C	3.58818300	0.57651600	0.68763700
H	3.70491900	-0.68929300	-1.08541500
C	2.30259600	-1.57154000	0.24280600
H	3.62753200	2.77185000	0.71997800
H	4.28843500	2.04476800	-0.75488900
H	2.99213900	0.57111700	1.60782800
H	4.60000700	0.25064400	0.93317600
O	3.16493500	-2.44277300	0.71059800
O	1.07541600	-1.72789900	0.33089200
H	-2.15964500	-0.68905400	-2.06101000
N	-1.99730200	-0.59578600	-1.06060900
C	-2.58842600	-1.83114500	-0.38507300
C	-2.81017800	0.60652800	-0.57900500
H	-1.80072700	-2.39936100	0.11966300
H	-3.02268200	-2.47539800	-1.15420400
C	-3.65917100	-1.30117200	0.58193400
C	-4.12568500	0.00335700	-0.07785900
H	-2.94973600	1.28688000	-1.42504600
C	-2.07733300	1.43241100	0.52844400
H	-3.22036300	-1.08751400	1.56292000
H	-4.46346200	-2.02595700	0.72798800
H	-4.62811600	0.68540800	0.60915200
H	-4.79593000	-0.20521100	-0.91976700
O	-0.78824600	1.20776700	0.65558900
O	-2.72902600	2.24167900	1.15979600
H	2.70912600	-3.19357700	1.13638300
H	2.06599100	0.43160500	-2.06848900
Mg	-0.04925400	-0.18532100	-0.38224300

Mg-OO-NO-ZW-E-X

1 1

N	4.02700600	-0.31938900	-1.08509700
C	4.86882100	0.83826400	-0.53861300
C	3.33147500	-1.00219800	0.09447400
H	4.80410000	1.67563500	-1.23412600
H	5.90118900	0.48664700	-0.48437000
C	4.27682700	1.08797000	0.84862900
C	3.92962300	-0.32599200	1.34181200
H	3.50709200	-2.07944300	0.05349200
C	1.83440700	-0.73442800	-0.06619300
H	3.37971900	1.71267900	0.77922800
H	4.99079200	1.59922800	1.49747000
H	3.21504100	-0.34300300	2.16616000
H	4.83025600	-0.86125400	1.65762100
O	1.03945900	-1.07930500	0.84414600
O	1.43537200	-0.12635300	-1.11577100
H	-2.49199600	-1.23264400	-1.58856200
N	-2.35963100	-0.81238400	-0.66901200
C	-2.91187800	-1.78698200	0.33662300
C	-3.26983300	0.41749400	-0.59757100
H	-2.51051600	-1.52728500	1.32393400
H	-2.58577200	-2.80039000	0.08940900
C	-4.42262500	-1.55826500	0.29416500
C	-4.52926400	-0.02708200	0.19515000
H	-3.52186200	0.69744500	-1.62451900
C	-2.58668600	1.66396400	0.03713300
H	-4.93321800	-1.96447700	1.17126300
H	-4.84463100	-2.04417800	-0.59424200
H	-4.51342900	0.43185000	1.18751600
H	-5.44548400	0.30642400	-0.29440400
O	-1.29638900	1.57605600	0.26204600
O	-3.29352000	2.62873300	0.26261100
H	3.25270300	0.02710000	-1.68233300
H	4.58718700	-0.97062000	-1.63811300
Mg	-0.45811500	-0.05173500	-0.18371500

Mg-NO-OO-CS-X-X

1 1

N	-2.15590200	-0.68632500	-0.80756900
C	-2.25873400	-1.98767600	-0.03249200
C	-3.39861200	0.10369900	-0.51543500
H	-1.70023600	-1.88237800	0.90353400
H	-1.79339000	-2.78749700	-0.61084400
C	-3.75371500	-2.16600900	0.23018400
C	-4.21754500	-0.73057800	0.51386800
H	-3.98261900	0.25523300	-1.42887700
C	-3.02483400	1.46794400	0.02282500
H	-3.95307000	-2.84140400	1.06549100
H	-4.25619300	-2.56621000	-0.65771700
H	-3.95330800	-0.44023500	1.53710800
H	-5.28924600	-0.57138000	0.38696600
O	-4.04797400	2.26056400	0.22486300
O	-1.85615800	1.80278800	0.27314700
H	3.49357600	-0.29753900	-1.88660100
N	4.03474100	-0.49971000	-1.05333600
C	5.02793700	0.54137100	-0.73945700
C	3.19701100	-0.73416600	0.11961600
H	4.63536100	1.56413600	-0.87333400
H	5.90898500	0.42789100	-1.37755900
C	5.31846200	0.27950500	0.74015700
C	3.91740900	-0.00951700	1.30578200
H	3.11687100	-1.80875500	0.33597800
C	1.77276100	-0.24765900	0.00103700
H	5.80405400	1.12345600	1.23727000
H	5.96259000	-0.59987000	0.84390800
H	3.40764800	0.93183800	1.54090200
H	3.91622200	-0.61947500	2.21093000
O	1.37996600	0.46532900	-0.99707300
O	0.90864400	-0.55320700	0.90554400
H	-3.76207600	3.12113100	0.58742000
H	-2.14931100	-0.91127100	-1.80143700
Mg	-0.42619900	0.44160800	-0.17626300

Mg-OO-OO-ZW-E-X

1 1

C	-4.47826400	1.06225100	-0.84335100
C	-3.80060200	-0.32248200	-0.87747300
N	-4.45150800	-1.10173700	0.26734200
C	-5.40125100	-0.15838000	1.00808900
C	-4.88606800	1.22956700	0.62963900
C	-2.30358600	-0.26605900	-0.58223000
O	-1.53871600	0.35845100	-1.36043000
O	-1.86325900	-0.85045300	0.46521700
O	1.43157300	0.85999100	0.87678900
C	2.27223800	-0.02133400	0.46201400
O	1.83491600	-0.97827100	-0.27865000
C	3.72939400	0.07794000	0.85731000
N	4.55766400	-1.05888100	0.46820200
C	5.35672700	-0.68040200	-0.70682000
C	5.70785100	0.77649400	-0.39559100
C	4.38600100	1.32613200	0.17263800
H	4.78918500	-0.74182600	-1.65216700
H	6.23441900	-1.32756100	-0.79232100
H	3.72411000	0.20330700	1.94836900
H	6.04775200	1.33282200	-1.27333800
H	6.49589100	0.81254800	0.36328900
H	3.74807000	1.69318200	-0.63861100
H	4.51677300	2.14755200	0.87939600
H	4.01706100	-1.90582800	0.32895900
H	-5.37417000	-0.39760800	2.07170300
H	-6.40453200	-0.34043400	0.61729700
H	-3.95102800	-0.85558100	-1.81867900
H	-4.02515600	1.50300200	1.24926900
H	-5.65600400	1.99070100	0.77124500
H	-3.79551400	1.83328200	-1.20413000
H	-5.35873600	1.05818600	-1.49281400
H	-3.66183000	-1.39420500	0.87279600
Mg	0.03551000	-0.15006300	-0.10754200
H	-4.92626200	-1.94656100	-0.05733400

Ca-OO-OO-ZW-E-X

1 1

C	-4.93059900	1.00355700	-0.76598500
C	-4.23456700	-0.37054600	-0.77519000
N	-4.77012700	-1.08368000	0.46742500
C	-5.66872200	-0.11273700	1.22884400
C	-5.21587600	1.25706900	0.72354800
C	-2.70889000	-0.28529200	-0.61118800
O	-2.04694300	0.29921300	-1.50160400
O	-2.19899300	-0.81419000	0.43372400
O	1.78063900	0.98374200	0.68607400
C	2.58997000	0.04323700	0.36038100
O	2.18263600	-0.96833000	-0.31692700
C	4.03792400	0.14771900	0.79952200
N	4.84402100	-1.05362000	0.56433600
C	5.90433700	-0.74579100	-0.41183900
C	6.18047100	0.73904100	-0.15833500
C	4.76458600	1.30167500	0.04321200
H	5.57929800	-0.89254100	-1.45645400
H	6.77937900	-1.37965700	-0.23771200
H	3.99893700	0.38326600	1.87224700
H	6.71559100	1.22105200	-0.98135300
H	6.77341800	0.85947400	0.75508800
H	4.29142100	1.47157900	-0.93169500
H	4.72718000	2.24100100	0.59850600
H	4.26708300	-1.83795200	0.28035700
H	-5.54574300	-0.28348400	2.29898600
H	-6.69931300	-0.33090100	0.94076500
H	-4.45796000	-0.96293800	-1.66473100
H	-4.31061300	1.57943100	1.24935000
H	-5.98529000	2.01468000	0.88552500
H	-4.29365600	1.75858300	-1.22953900
H	-5.86383600	0.95207000	-1.33505200
H	-3.90964600	-1.31385500	1.00560200
Ca	0.03075800	-0.12159600	-0.32621900
H	-5.24918300	-1.95785100	0.24422400

Ca-OO-NO-ZW-E-E

1 1

N	4.44604200	-0.17432000	-1.10749800
C	5.26616400	0.99171800	-0.55941800
C	3.82393400	-0.92224100	0.07235700
H	5.16609600	1.84131700	-1.23586800
H	6.30905000	0.66895000	-0.53083400
C	4.69644900	1.19737100	0.84418400
C	4.41149000	-0.23692500	1.31980000
H	4.06708100	-1.98460100	0.00505700
C	2.30102000	-0.75196000	-0.05459400
H	3.77556400	1.78906500	0.80214100
H	5.40408400	1.72522600	1.48666700
H	3.71034300	-0.29511900	2.15375700
H	5.33771500	-0.73732400	1.61864500
O	1.57329700	-1.22164900	0.85177700
O	1.86450400	-0.11897100	-1.07459000
H	-2.99785200	-1.49069500	-1.46838500
N	-2.76086700	-0.91991900	-0.65698900
C	-3.38603400	-1.59946800	0.53810200
C	-3.54740300	0.36621100	-0.81213700
H	-2.78285700	-1.38233800	1.42884200
H	-3.36823000	-2.68169900	0.38444100
C	-4.81743900	-1.01496900	0.70313100
C	-4.98562300	-0.03937100	-0.48125000
H	-3.43115700	0.71810000	-1.84418800
C	-2.99835800	1.50971000	0.11080800
H	-4.89533000	-0.47392300	1.64948900
H	-5.57741300	-1.80014300	0.70589300
H	-5.58968700	0.83232100	-0.22732300
H	-5.43929500	-0.54361500	-1.34260200
O	-1.71396600	1.46610300	0.32792800
O	-3.78312500	2.35531000	0.51139100
H	3.61939700	0.15777100	-1.64602100
H	4.99942700	-0.78284600	-1.71292700
Ca	-0.41070200	-0.23737900	-0.14466600

Ca-NO-OO-CS-X-E

1 1

N	-1.22971100	-0.55514500	-0.50928400
C	-0.75181800	-1.43136200	0.61968700
C	-2.68630700	-0.81838400	-0.67117200
H	-0.87420900	-0.88716000	1.56488400
H	0.31777400	-1.62501800	0.49727900
C	-1.68333900	-2.64246300	0.57949900
C	-3.04948000	-2.00000900	0.28822000
H	-2.91567000	-1.09017100	-1.70764000
C	-3.48548700	0.43447500	-0.36806000
H	-1.68265800	-3.21254000	1.51200600
H	-1.39092700	-3.31925800	-0.23188500
H	-3.49325900	-1.61715200	1.21363300
H	-3.77470900	-2.67438500	-0.16957400
O	-4.78662500	0.26278500	-0.49388900
O	-2.98769700	1.51718500	-0.03165600
H	2.82731900	-1.53468300	1.54608500
N	2.76932400	-1.11079000	0.62627200
C	3.62569000	-1.80344700	-0.36468700
C	3.17457100	0.32769400	0.67877500
H	3.08373900	-2.64310700	-0.81257900
H	4.54775400	-2.19757600	0.08941900
C	3.96652900	-0.69953300	-1.36823900
C	4.20643400	0.51166900	-0.45116400
H	3.57571200	0.59670200	1.66155600
C	1.88259600	1.11546800	0.48822000
H	3.11209900	-0.50638200	-2.02588100
H	4.83152300	-0.94690500	-1.98888000
H	4.08911100	1.46792100	-0.96443000
H	5.21563600	0.46997500	-0.02805700
O	1.53716100	1.52449900	-0.67498300
O	1.11021000	1.26781300	1.49948300
H	-5.26453900	1.08735800	-0.28713400
H	-0.74927100	-0.86307500	-1.35301900
Ca	-0.62067200	1.83070500	0.08435900

Ca-NO-NO-CS-X-X

1 1

N	-2.25520400	-0.56101800	-1.06202400
C	-2.14601300	-1.97196300	-0.50401900
C	-3.35443700	0.12889400	-0.31362100
H	-1.29005100	-2.02438600	0.17700600
H	-1.95873200	-2.66909800	-1.32357200
C	-3.46193800	-2.21118100	0.23758700
C	-3.75625500	-0.83273300	0.84219800
H	-4.22180100	0.29939900	-0.96079800
C	-2.91614100	1.47761100	0.21662400
H	-3.37463700	-2.99051200	0.99837900
H	-4.25718000	-2.50060600	-0.45917400
H	-3.12027300	-0.66074900	1.71888200
H	-4.79438800	-0.68115600	1.14174000
O	-3.91365300	2.18101500	0.71658600
O	-1.74885500	1.88453500	0.21929700
H	2.94022200	1.23511100	-1.69688200
N	2.50014200	0.86686800	-0.85327600
C	3.02048800	1.69720100	0.29329000
C	3.11751900	-0.49946700	-0.62941100
H	2.27709900	1.68977300	1.10113900
H	3.13746300	2.73249300	-0.03748200
C	4.34162300	1.03663900	0.77917200
C	4.53467200	-0.18887900	-0.14166300
H	3.10523700	-1.04168600	-1.58249200
C	2.28787200	-1.36376000	0.38293200
H	4.24173900	0.71816200	1.81954100
H	5.18406000	1.73019500	0.72362900
H	4.96452400	-1.04457500	0.37998100
H	5.17593200	0.05983300	-0.99492800
O	0.99858600	-1.15849300	0.34876200
O	2.87840000	-2.17418500	1.07763800
H	-3.58874800	3.02553000	1.08051100
H	-2.55022200	-0.63422100	-2.03303100
Ca	0.03475200	0.55592000	-0.62610700

Sr-OO-NO-ZW-X-X

1 1

N	3.46531200	0.16237500	-0.23996600
C	2.93498600	1.35293300	-1.02583000
C	2.66733800	0.12222200	1.05777200
H	1.99611700	1.03587000	-1.48810500
H	3.66638900	1.63436000	-1.78504700
C	2.67887600	2.38024700	0.07032000
C	2.06795200	1.54246700	1.21357700
H	3.34527500	-0.15136900	1.87077400
C	1.63424300	-1.00489900	0.88606700
H	3.61349600	2.86260900	0.38023900
H	1.98389000	3.14372400	-0.28222700
H	0.98515100	1.49069400	1.09913200
H	2.28611100	1.95382500	2.20043600
O	0.58673100	-0.97752200	1.58295900
O	1.86742300	-1.87190100	-0.01631400
H	-3.54400700	-0.54332300	-0.13764100
N	-2.58108900	-0.24902700	0.03282900
C	-2.55616200	0.35398200	1.40391300
C	-2.32180300	0.92813700	-0.87858600
H	-1.50734600	0.48921800	1.69013800
H	-3.01667400	-0.32894900	2.12406900
C	-3.27747200	1.70115200	1.26147100
C	-2.90839700	2.17388300	-0.16910800
H	-2.80114900	0.72560500	-1.84222200
C	-0.79737000	1.02357600	-1.18023300
H	-2.97516100	2.41409500	2.03317300
H	-4.35907800	1.55344400	1.35786700
H	-2.15506200	2.96389600	-0.15998200
H	-3.78268200	2.55670700	-0.70127600
O	-0.23862200	-0.11176500	-1.48816000
O	-0.20749400	2.10214200	-1.12280200
H	3.29126900	-0.74407300	-0.70855900
H	4.46571700	0.26208300	-0.05912500
Sr	-0.64419200	-2.03372900	-0.30587700

Sr-OO-OO-ZW-E-E

1 1

C	5.09999500	-0.70992600	0.47888500
C	4.26088500	-0.26130300	-0.73020800
N	4.55649100	1.23101000	-0.87494600
C	5.44192200	1.66197000	0.28880100
C	5.21733500	0.56519500	1.33128100
C	2.74014000	-0.38226800	-0.50427300
O	2.06402000	0.70104100	-0.53952400
O	2.26833100	-1.52366600	-0.29971300
O	-2.45435200	-0.86159200	-0.64983300
C	-2.78276900	-0.53466000	0.54447200
O	-1.90674400	-0.48827100	1.48177900
C	-4.20157600	-0.07513700	0.85526300
N	-4.16214000	1.40374800	0.68857800
C	-5.26297000	1.81459600	-0.20611100
C	-5.43496700	0.59991100	-1.12224400
C	-5.26615400	-0.57536600	-0.14306800
H	-4.99139200	2.72698700	-0.74700900
H	-6.19900000	2.00831300	0.34303800
H	-4.42431300	-0.36839400	1.88758900
H	-4.63765000	0.57807600	-1.87225800
H	-6.39912700	0.59275100	-1.63784500
H	-4.96742800	-1.50341800	-0.63515200
H	-6.20382400	-0.75775400	0.39297200
H	-4.16792400	1.88533700	1.58013700
H	5.15569400	2.66818300	0.59782500
H	6.47264800	1.67196100	-0.07248800
H	4.51996700	-0.77999800	-1.65544300
H	4.29316900	0.75102500	1.88941200
H	6.03975400	0.52408500	2.04848400
H	4.61473700	-1.54168800	0.99228000
H	6.08769700	-1.04521700	0.14714100
H	3.60597200	1.65901400	-0.82096600
Sr	-0.13595000	-0.63733900	-0.10662100
H	4.96558200	1.46814000	-1.78002200

Sr-NO-NO-CS-X-X

1 1

N	1.79580400	-0.77195600	-0.26653900
C	2.97309000	-1.31342700	-1.00783700
C	2.33298600	0.05751600	0.84574700
H	3.25060000	-0.61433200	-1.80834300
H	2.71100000	-2.27099400	-1.46471700
C	4.09346300	-1.39742600	0.03514300
C	3.88417500	-0.10676600	0.84190100
H	1.90231100	-0.30067600	1.78957800
C	1.88807500	1.49763300	0.71300900
H	5.09047400	-1.45944200	-0.40878800
H	3.94579200	-2.27865800	0.66935400
H	4.35714200	0.74102500	0.33429900
H	4.28521800	-0.14858300	1.85574000
O	2.46135600	2.30608300	1.59010000
O	1.05578700	1.90354500	-0.10732400
H	-2.14996900	1.67065000	0.83187800
N	-2.25662600	0.83496500	0.26049000
C	-3.60850600	0.89520600	-0.38625200
C	-2.27389200	-0.35867600	1.20942800
H	-3.57803900	0.32919100	-1.32748200
H	-3.86862400	1.93215500	-0.61747500
C	-4.55769800	0.20333800	0.59546400
C	-3.69410600	-0.96055600	1.10697500
H	-2.05608600	-0.01138300	2.22213700
C	-1.16001200	-1.32435400	0.77214300
H	-5.48647100	-0.12866700	0.12355200
H	-4.81781600	0.88790700	1.41184400
H	-3.69342400	-1.77630400	0.37695300
H	-4.02885500	-1.36099000	2.06633600
O	-1.15528600	-1.58081900	-0.50363700
O	-0.29715700	-1.69310100	1.57951100
H	2.12536700	3.21385500	1.48008800
H	1.28931100	-1.54805900	0.17344800
Sr	-0.31145300	0.31688500	-1.48656800

Sr-NO-OO-CS-X-X

1 1

N	-1.17400500	-0.79836400	-0.49069700
C	-0.48088800	-1.64930500	0.54519800
C	-2.59030400	-1.25495100	-0.55997500
H	-0.50402000	-1.12385800	1.50662600
H	0.56536700	-1.78662500	0.25702500
C	-1.30640500	-2.93501400	0.60865700
C	-2.74355700	-2.41401000	0.47422700
H	-2.83069300	-1.62368800	-1.56403200
C	-3.54479600	-0.11320700	-0.27710500
H	-1.14861600	-3.49410100	1.53459200
H	-1.05246200	-3.59200100	-0.23150800
H	-3.09533500	-2.02119100	1.43520700
H	-3.46635500	-3.15772800	0.13486500
O	-4.81474700	-0.47185400	-0.35842900
O	-3.19710600	1.03766200	0.00820700
H	2.67562100	-0.73961100	-1.44408200
N	2.84577400	-1.18336900	-0.54116600
C	4.21256000	-1.74987300	-0.53481300
C	2.91199700	-0.10348800	0.45945500
H	4.40894900	-2.26210900	-1.48026600
H	4.26830200	-2.49881600	0.26297100
C	5.19461400	-0.57418900	-0.24752400
C	4.28881800	0.58618300	0.25105300
H	2.86381600	-0.54604200	1.46029100
C	1.72587600	0.82204700	0.31085300
H	5.73978800	-0.28005600	-1.14896600
H	5.93864800	-0.85607500	0.50305800
H	4.19137300	1.36189900	-0.51583000
H	4.65615200	1.05865700	1.16596700
O	1.35770200	1.17343100	-0.86535400
O	1.07155300	1.19035100	1.34627900
H	-5.39521500	0.28555400	-0.15979400
H	-0.72490800	-0.99358100	-1.38385800
Sr	-0.79314500	1.81630600	-0.00881600

Ba-OO-NO-ZW-X-E

1 1

N	-2.56023400	-0.92729000	0.82460300
C	-3.73185700	0.03008200	0.97496700
C	-2.37259500	-1.20209200	-0.65988100
H	-3.40548800	0.82249700	1.64646500
H	-4.57113100	-0.51571100	1.40865600
C	-4.01349500	0.54537000	-0.45580400
C	-2.78894900	0.12104000	-1.29005900
H	-3.05805700	-2.01266900	-0.92924300
C	-0.92777100	-1.68200100	-0.83808100
H	-4.15438100	1.62769600	-0.45919500
H	-4.92453000	0.08507100	-0.85048300
H	-1.97644000	0.84385700	-1.18582200
H	-3.01086600	0.00501700	-2.35243700
O	-0.16520200	-1.09210100	-1.65313000
O	-0.54296900	-2.58485500	-0.03027400
H	2.91924100	1.92396700	0.03675100
N	1.99236400	1.51888600	-0.09102800
C	1.50159000	1.96257500	-1.44909600
C	1.09891600	2.21478600	0.89421700
H	0.88428400	1.16921700	-1.88206800
H	2.36396700	2.11376600	-2.10402600
C	0.66456300	3.25514200	-1.23320300
C	0.82239300	3.58402600	0.26546600
H	1.61615000	2.27705200	1.85888800
C	-0.18480200	1.38293000	1.13378100
H	-0.38684700	3.06312800	-1.46368300
H	1.00024100	4.07260900	-1.87565200
H	-0.06539100	4.05448700	0.69028800
H	1.68251300	4.24132500	0.43568200
O	-0.00006400	0.10257000	1.32157200
O	-1.29307100	1.91935100	1.13806300
H	-1.66921200	-0.48326700	1.17297200
H	-2.66988500	-1.80012200	1.34225600
Ba	1.76791800	-1.31535600	0.16271300

Ba-OO-OO-ZW-E-E

1 1

C	-2.181653	1.505129	-0.768182
C	-3.171614	0.334565	-0.886768
N	-3.861648	0.275028	0.475031
C	-3.174181	1.270291	1.405924
C	-1.826612	1.523164	0.728061
C	-2.475870	-1.030678	-1.065588
O	-1.705386	-1.173196	-2.044697
O	-2.693553	-1.908670	-0.168431
O	0.302048	-1.070736	0.755837
C	1.481321	-0.930798	0.274240
O	1.928465	-1.724043	-0.619578
C	2.319936	0.240717	0.738159
N	3.753235	0.028083	0.528914
C	4.308122	1.335602	0.147878
C	3.225781	2.004475	-0.722445
C	1.912188	1.553090	-0.049363
H	5.268189	1.209860	-0.359844
H	4.488645	1.926255	1.055856
H	2.109344	0.383474	1.803706
H	3.283791	1.611581	-1.744005
H	3.319182	3.093936	-0.774843
H	1.116121	1.366924	-0.777863
H	1.543703	2.305726	0.654918
H	3.870388	-0.636067	-0.233783
H	-3.117056	0.834743	2.404417
H	-3.795787	2.168213	1.434208
H	-3.917284	0.464926	-1.673860
H	-1.114685	0.725030	0.964547
H	-1.396364	2.474606	1.048558
H	-1.321399	1.338260	-1.417946
H	-2.665570	2.439471	-1.071263
H	-3.691492	-0.712723	0.769270
Ba	-0.277675	-3.059124	-0.802227
H	-4.868619	0.430507	0.417301

Ba-NO-OO-CS-X-E

1 1

N	-0.61445700	-0.96684600	0.43095100
C	-0.74770200	-1.34322000	1.86928100
C	-1.50448500	-1.86601700	-0.34081400
H	-1.53358300	-0.73514800	2.34369600
H	0.19123800	-1.13603100	2.38671900
C	-1.16873000	-2.81641800	1.85944100
C	-2.14592800	-2.86492600	0.67585000
H	-0.92192500	-2.41863000	-1.08800100
C	-2.55960500	-1.09087800	-1.10187800
H	-1.62628200	-3.14213400	2.79741900
H	-0.29615400	-3.45031300	1.66523300
H	-3.13561700	-2.51060800	0.98700900
H	-2.27341900	-3.85670500	0.23900200
O	-3.32570400	-1.86944900	-1.85360300
O	-2.71937900	0.13118500	-1.04114800
H	2.06048400	-0.80729500	-1.41647500
N	2.27387000	-1.18593800	-0.49107700
C	3.44729200	-2.08504900	-0.62538200
C	2.80561600	-0.03891000	0.29016500
H	3.32380000	-2.72794900	-1.50086700
H	3.48545700	-2.73164400	0.25744200
C	4.70833900	-1.16968100	-0.69720200
C	4.19377200	0.24704900	-0.31772300
H	2.90127100	-0.34839900	1.33608500
C	1.78097600	1.07930400	0.22811300
H	5.15027000	-1.17177600	-1.69738600
H	5.47938300	-1.51499100	-0.00260900
H	4.06969100	0.87304300	-1.20760600
H	4.85440200	0.77182900	0.37731900
O	1.32870600	1.41646500	-0.92100200
O	1.28898700	1.54187000	1.30602000
H	-3.99414900	-1.33366200	-2.31751200
H	0.35699800	-1.17779900	0.14465700
Ba	-0.98474800	1.86463600	0.10992000

Ba-NO-NO-CS-X-X

1 1

N	-1.87432900	0.15791000	-0.80258300
C	-3.03577800	-0.33736400	-1.59619000
C	-2.42590400	0.95652500	0.32349600
H	-3.33444900	-1.32836600	-1.22700300
H	-2.74930600	-0.43661600	-2.64644200
C	-4.15570200	0.67933100	-1.34422800
C	-3.97417700	0.99544300	0.14757900
H	-2.00492500	1.96894700	0.27497000
C	-1.99640600	0.40307400	1.66432900
H	-5.15087900	0.29049400	-1.57581100
H	-3.98782100	1.57577700	-1.95160900
H	-4.44912400	0.22173700	0.76133200
H	-4.38868700	1.95792800	0.45139600
O	-2.57428300	1.01974200	2.68658600
O	-1.17906600	-0.50862400	1.82762200
H	2.21375400	0.52406400	1.88136400
N	2.31270400	0.25144600	0.90572000
C	3.69229100	-0.30214000	0.72517100
C	2.23282700	1.52317500	0.07473400
H	3.68355500	-1.02285400	-0.10480800
H	4.00957200	-0.82751600	1.63077500
C	4.56558700	0.89782500	0.34673900
C	3.62675700	1.69539600	-0.57182600
H	1.98879000	2.36279500	0.73002400
C	1.09841900	1.36165200	-0.95012500
H	5.49829500	0.60581000	-0.14376400
H	4.82039700	1.47438100	1.24424200
H	3.62088900	1.25640400	-1.57467300
H	3.89878100	2.74930200	-0.66215100
O	1.13474400	0.24419100	-1.61295100
O	0.19308700	2.20444300	-1.01726300
H	-2.25065700	0.64679200	3.52598300
H	-1.32736600	0.81300400	-1.37155600
Ba	0.32995000	-1.54666200	-0.14204000

Appendix C – Supporting Information for Chapter 5

Figure A3.1. SORI/CID MS/MS spectra of $[Li(ProLeu)]^+$

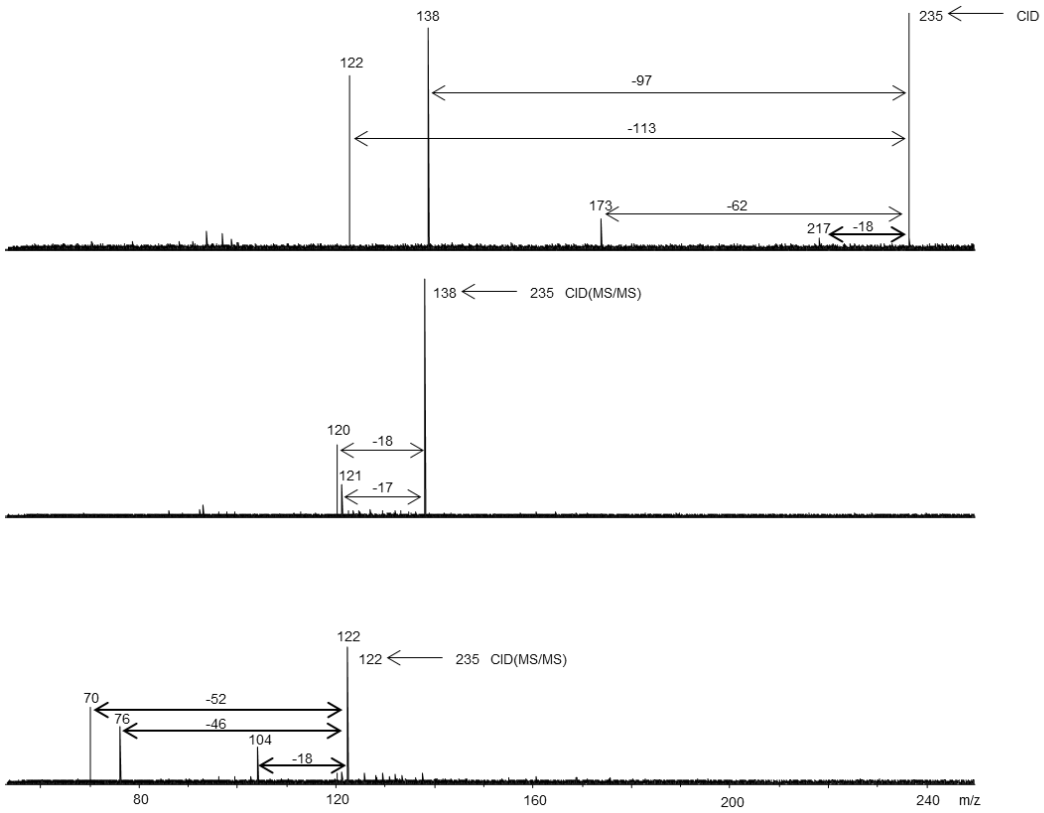

Figure A3.2. SORI/CID MS/MS spectra of $[Li(LeuPro)]^+$

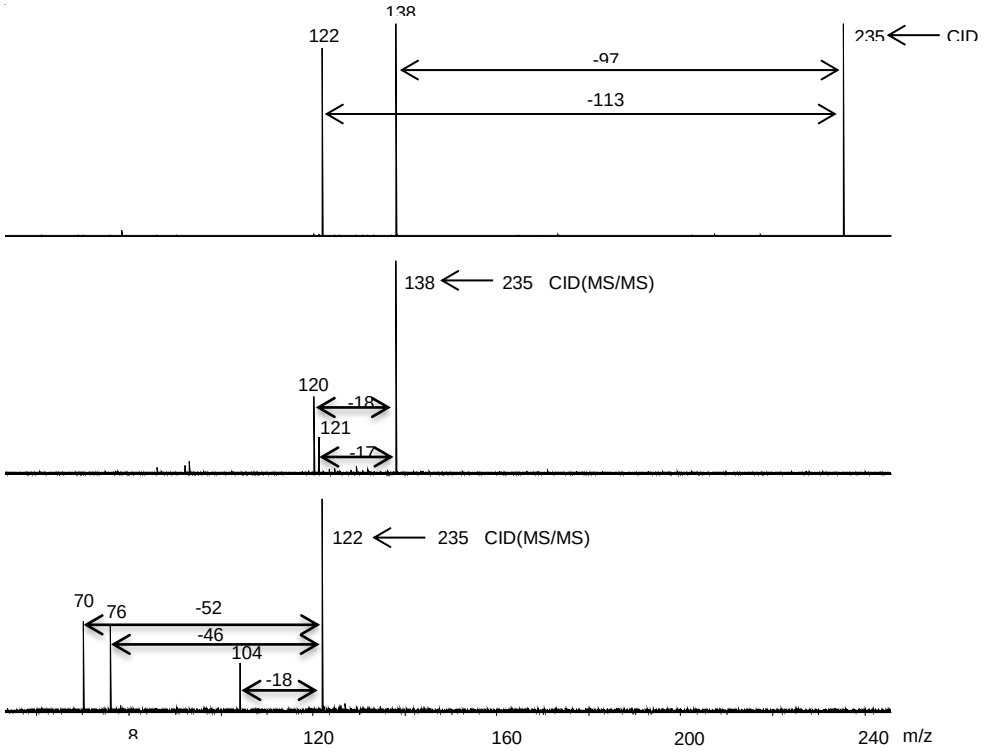

Figure A3.3 Comparison of the experimental IRMPD spectra of the a) m/z 122 and b) m/z 138 fragment ions from CID of (ProLeu)-Li^+ and (LeuPro)-Li^+ with the calculated spectra of proline-Li^+ and leucine-Li^+. Energies are M06-2XD3/6-31+G(d,p) 298 K Gibbs energies (and enthalpies) and in kJ mol^{-1}.

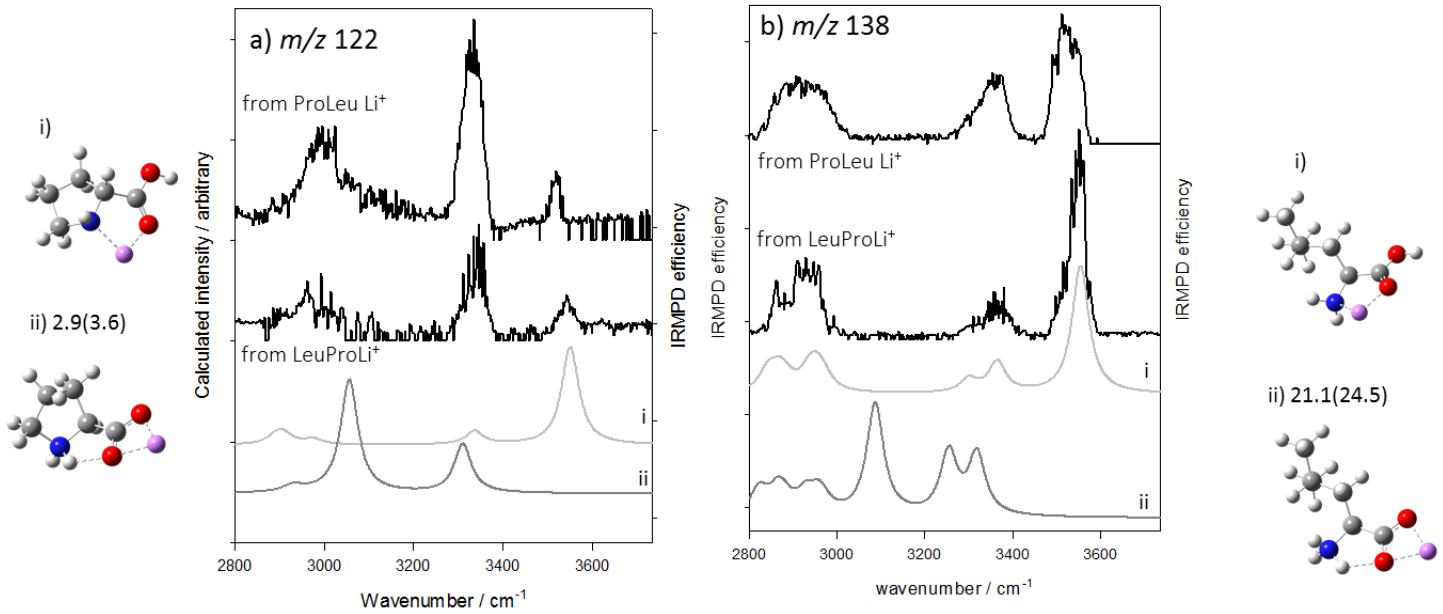

Figure A3.4. Proposed mechanism for the dissociation of (ProLeu)Li^+ and (LeuPro)Li^+ forming (Pro)Li^+ (m/z 122) and (Leu)Li^+ (m/z 138).

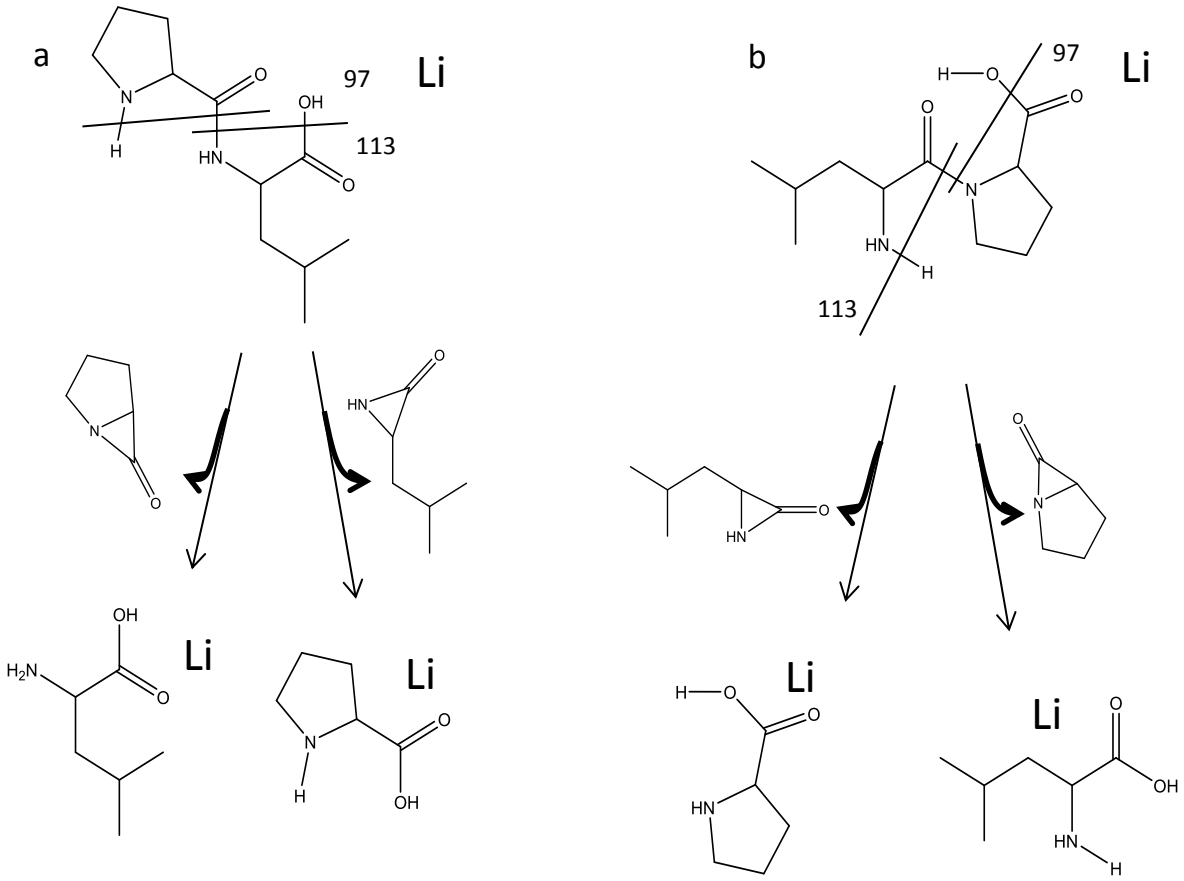

Figure A3.5. Comparison of the experimental IRMPD spectrum and calculated IR spectra of the lowest energy structures of each form of the (ProLeu)-Li^+ complex a) from 1000 to 1900 cm^{-1}, b) from 2700 to 3800 cm^{-1}.
Energies are M06-2XD3/6-311++G(3df,3pd)//6-31+G(d,p), 298 K Gibbs energies (and enthalpies) and in kJ mol^{-1}.

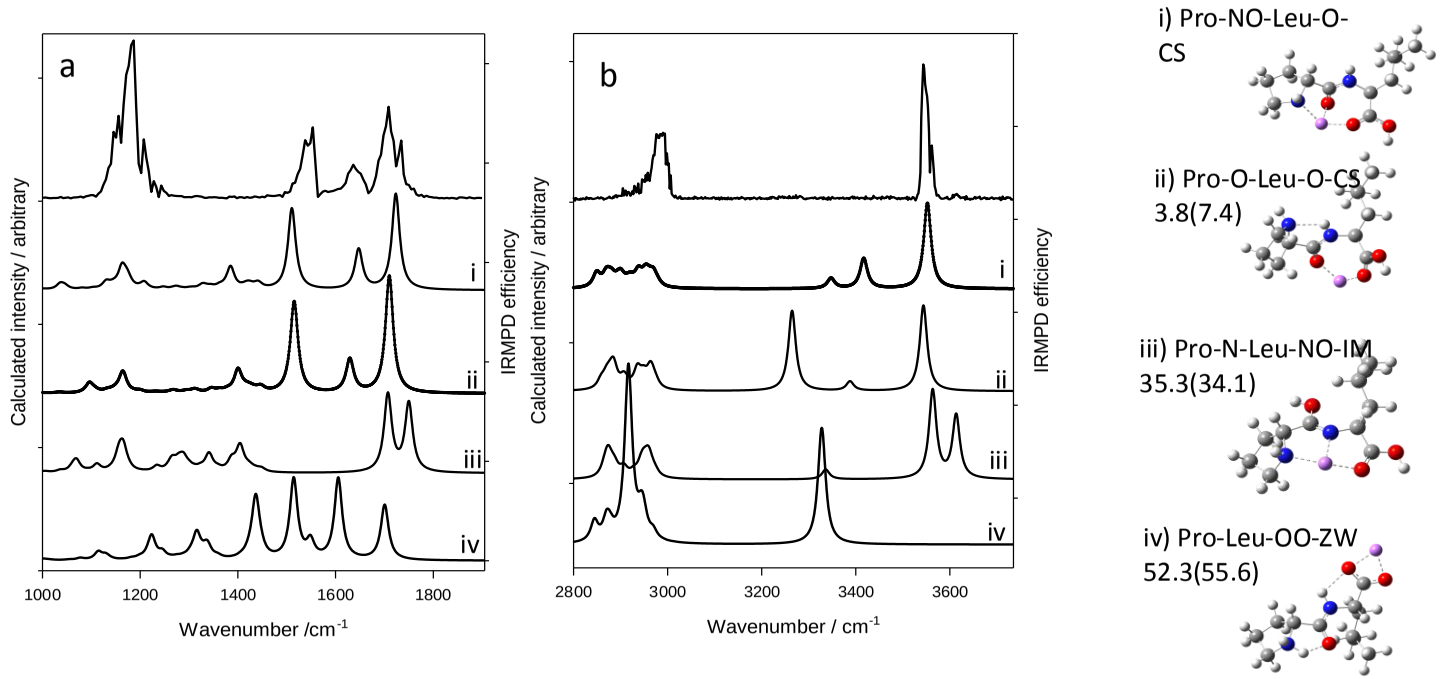

Figure A3.6. Comparison of the experimental IRMPD spectrum and calculated IR spectra of the lowest energy structures of each form of the (ProLeu)-Na^+ complex from 2700 to 3800 cm^{-1}. Energies are M06-2X/6-311++G(3df,3pd)//6-31+G(d,p), 298 K Gibbs energies (and enthalpies) and in kJ mol^{-1}.

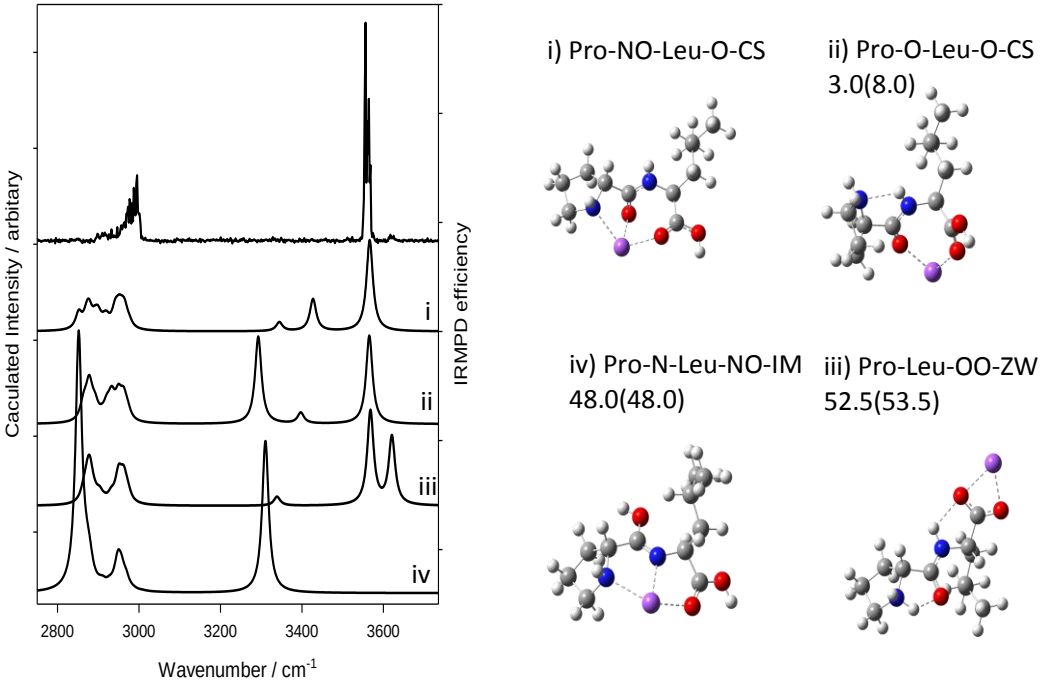

Figure A3.7. Comparison of the experimental IRMPD spectrum and calculated IR spectra of the lowest energy structures of each form of the (ProLeu)-Rb^+ complex a) from 1000 to 1900 cm^{-1}, b) from 2700 to 3800 cm^{-1}.
Energies are M06-2X/6-311++G(3df,3pd)//6-31+G(d,p), 298 K Gibbs energies (and enthalpies) and in kJ mol^{-1}.

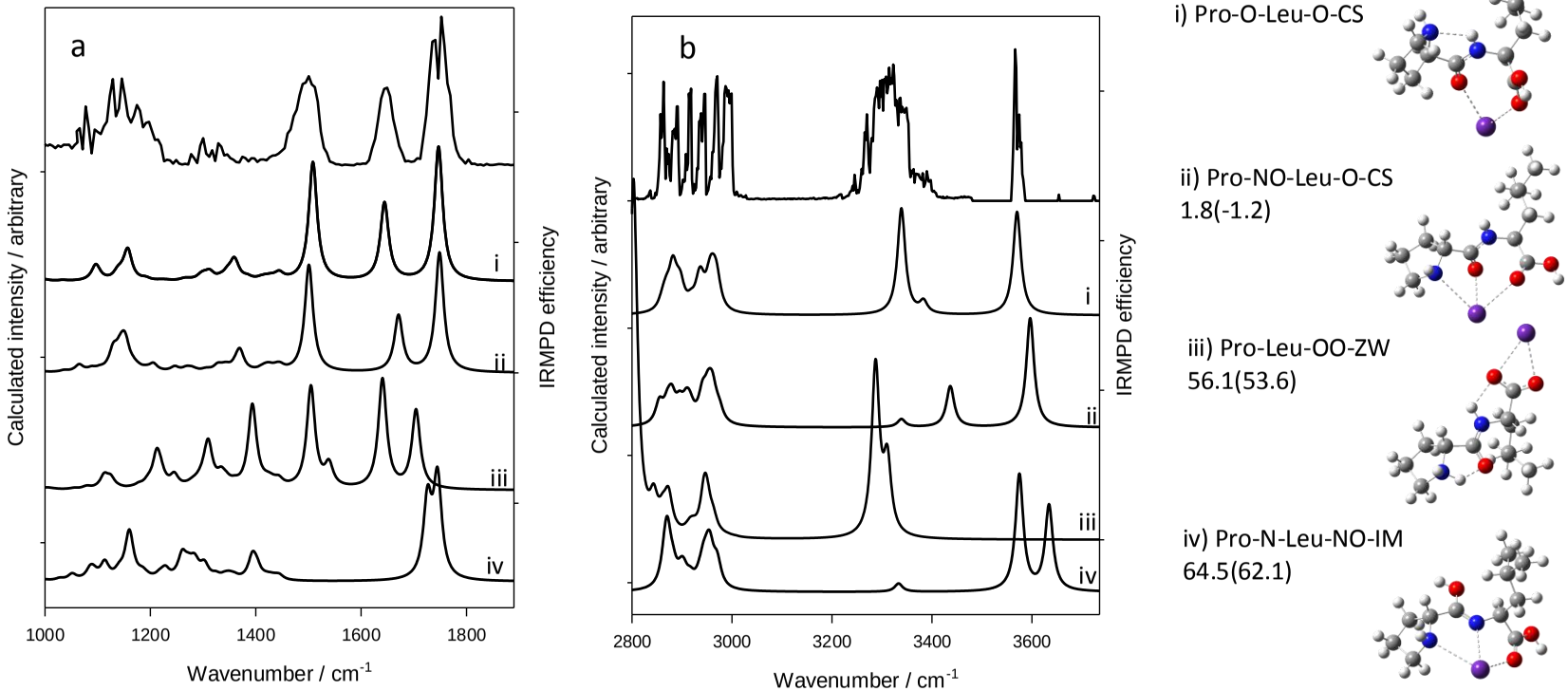

Figure A3.8. Comparison of the experimental IRMPD spectrum and calculated IR spectra of the lowest energy structures of each form of the (ProLeu)-Cs^+ complex a) from 1000 to 1900 cm^{-1}, b) from 2700 to 3800 cm^{-1}.
Energies are M06-2X/6-311++G(3df,3pd)//6-31+G(d,p), 298 K Gibbs energies (and enthalpies) and in kJ mol^{-1}.

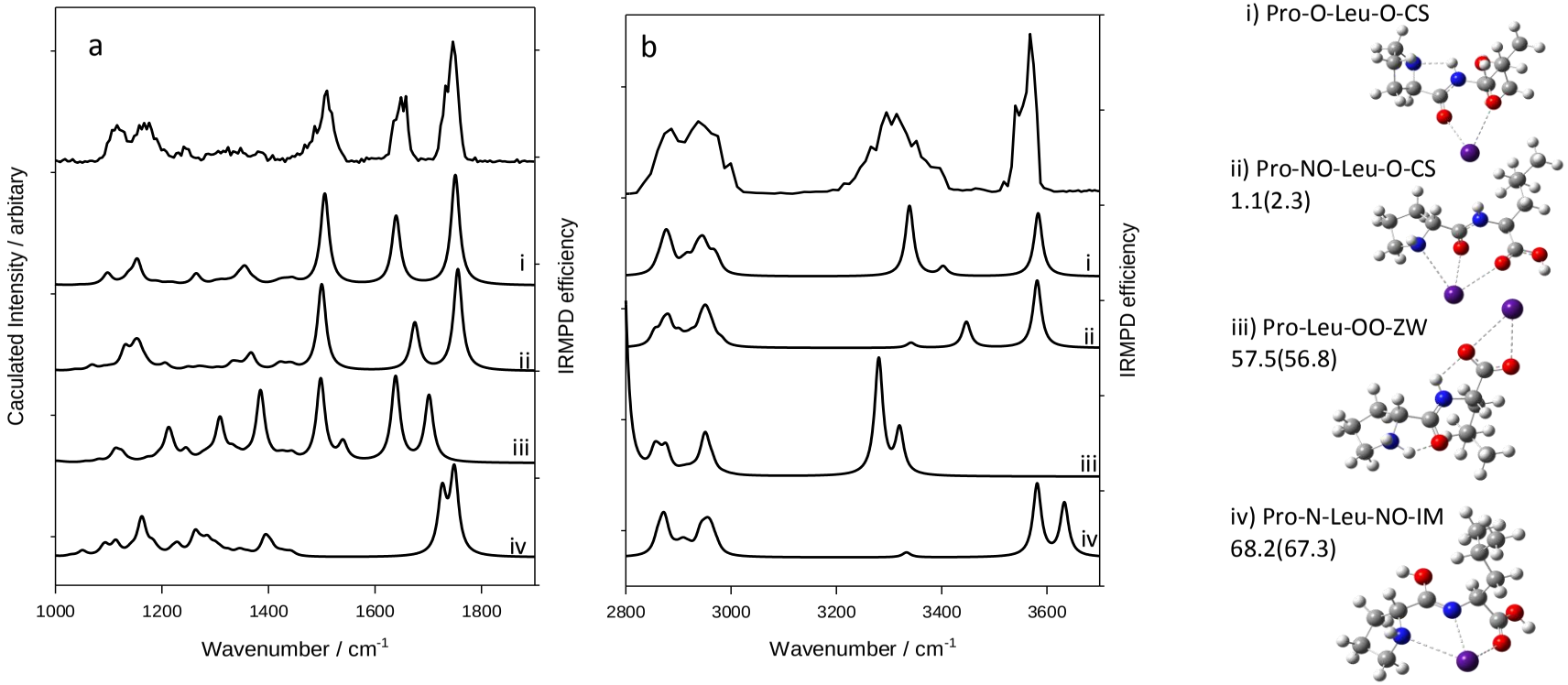

Figure A3.9. Comparison of the experimental IRMPD spectrum and calculated IR spectra of the lowest energy structures of each form of the (LeuPro)-Li^+ complex a) from 1000 to 1900 cm^{-1}, b) from 2700 to 3800 cm^{-1}.
Energies are M06-2X/6-311++G(3df,3pd)//6-31+G(d,p), 298 K Gibbs energies (and enthalpies) and in kJ mol^{-1}.

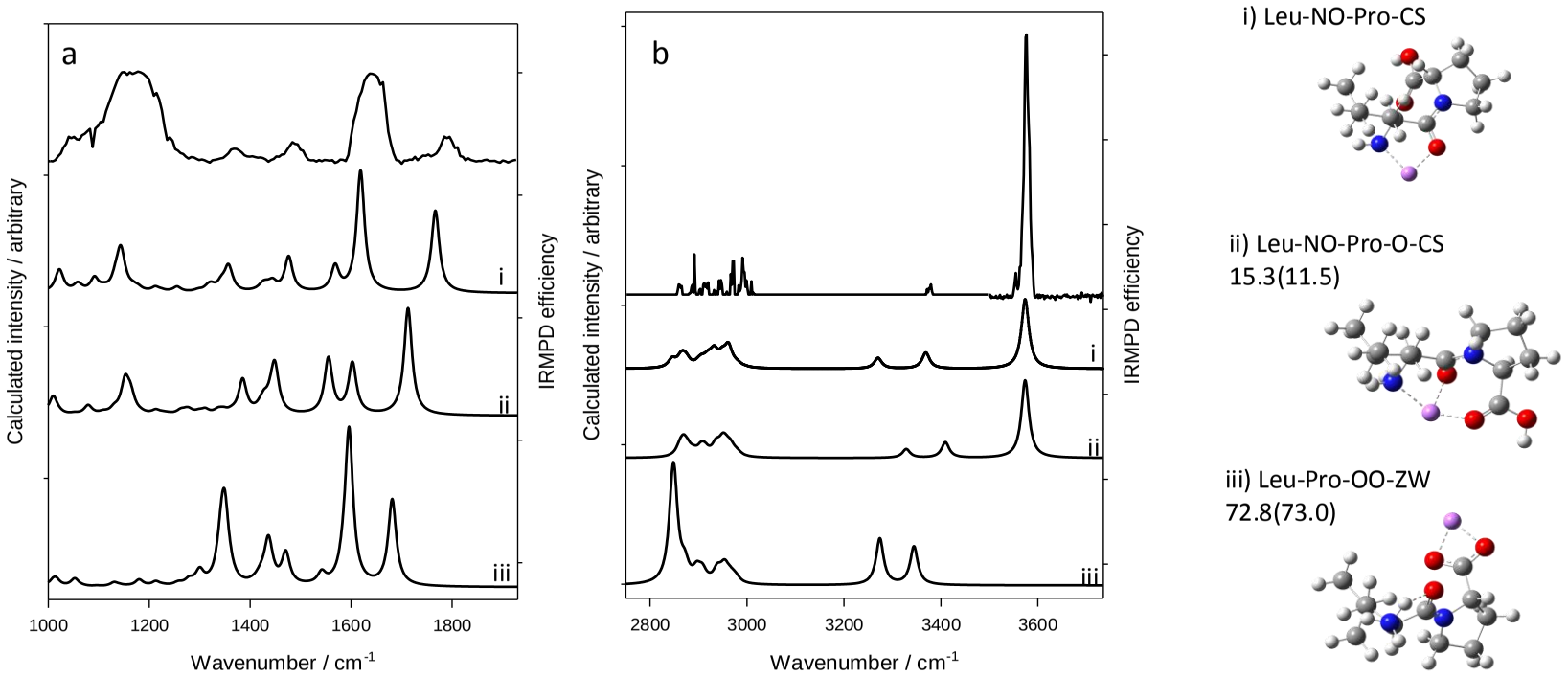

Figure A3.10. Comparison of the experimental IRMPD spectrum and calculated IR spectra of the lowest energy structures of each form of the (LeuPro)-Na^+ complex a) from 1000 to 1900 cm^{-1}, b) from 2700 to 3800 cm^{-1}.
Energies are M06-2X/6-311++G(3df,3pd)//6-31+G(d,p), 298 K Gibbs energies (and enthalpies) and in kJ mol^{-1}.

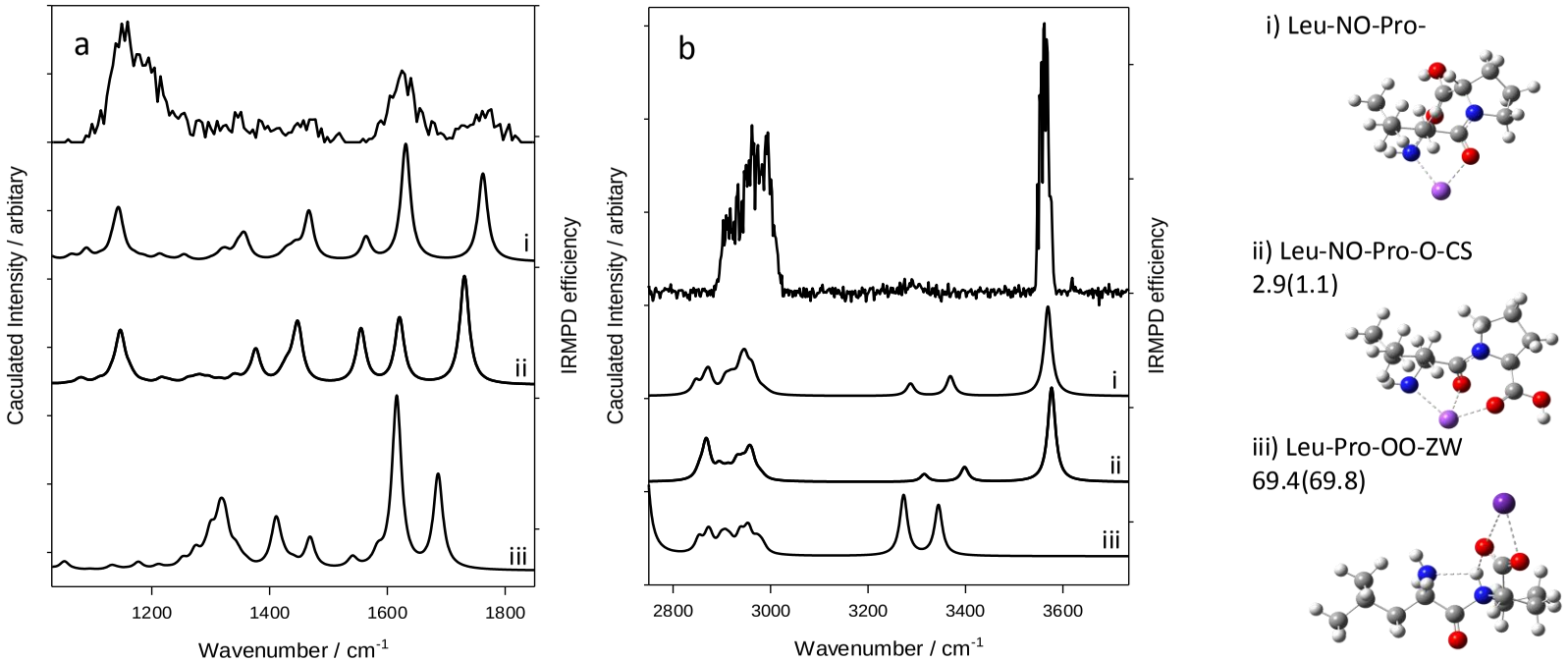

Figure A3.11. Comparison of the experimental IRMPD spectrum and calculated IR spectra of the lowest energy structures of each form of the (LeuPro)-Rb^+ complex a) from 1000 to 1900 cm^{-1}, b) from 2700 to 3800 cm^{-1}.
Energies are M06-2X/6-311++G(3df,3pd)//6-31+G(d,p), 298 K Gibbs energies (and enthalpies) and in kJ mol^{-1}.

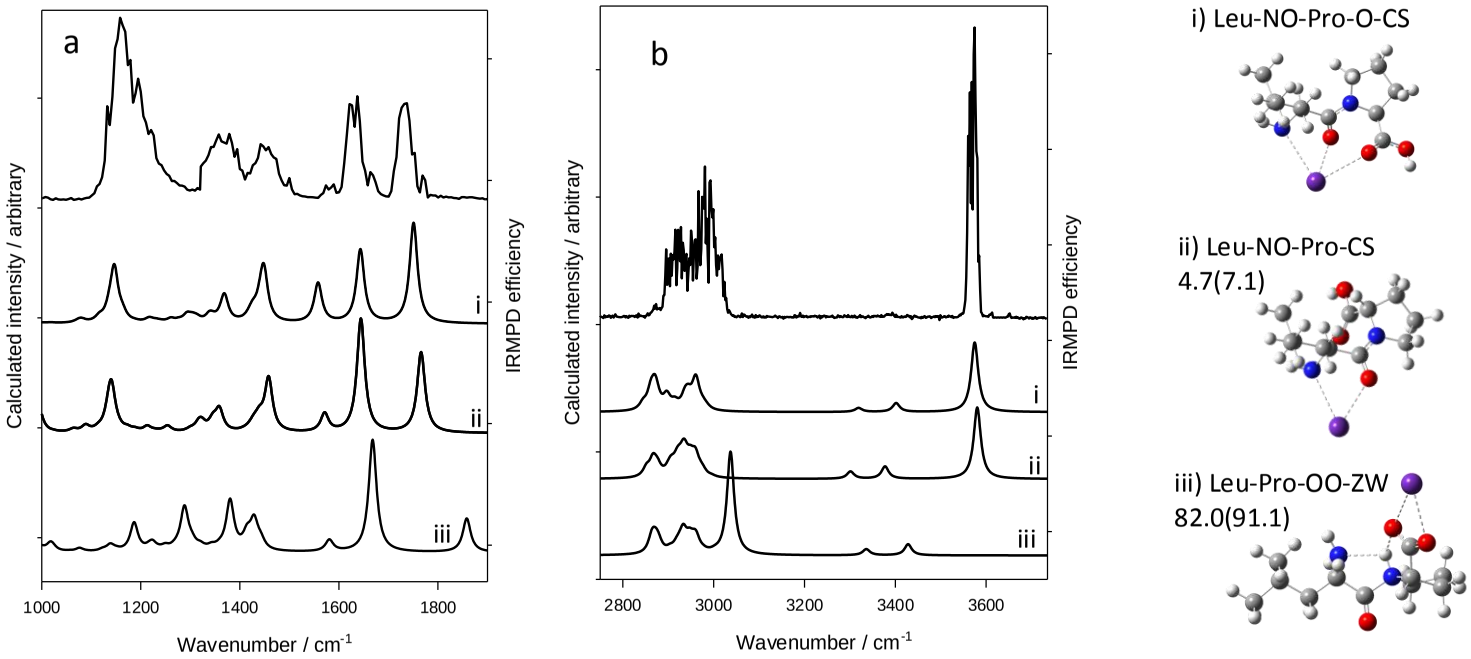

Figure A3.12. Comparison of the experimental IRMPD spectrum and calculated IR spectra of the lowest energy structures of each form of the (LeuPro)-Cs^+ complex a) from 1000 to 1900 cm^{-1}, b) from 2700 to 3800 cm^{-1}.
Energies are M06-2X/6-311++G(3df,3pd)//6-31+G(d,p), 298 K Gibbs energies (and enthalpies) and in kJ mol^{-1}.

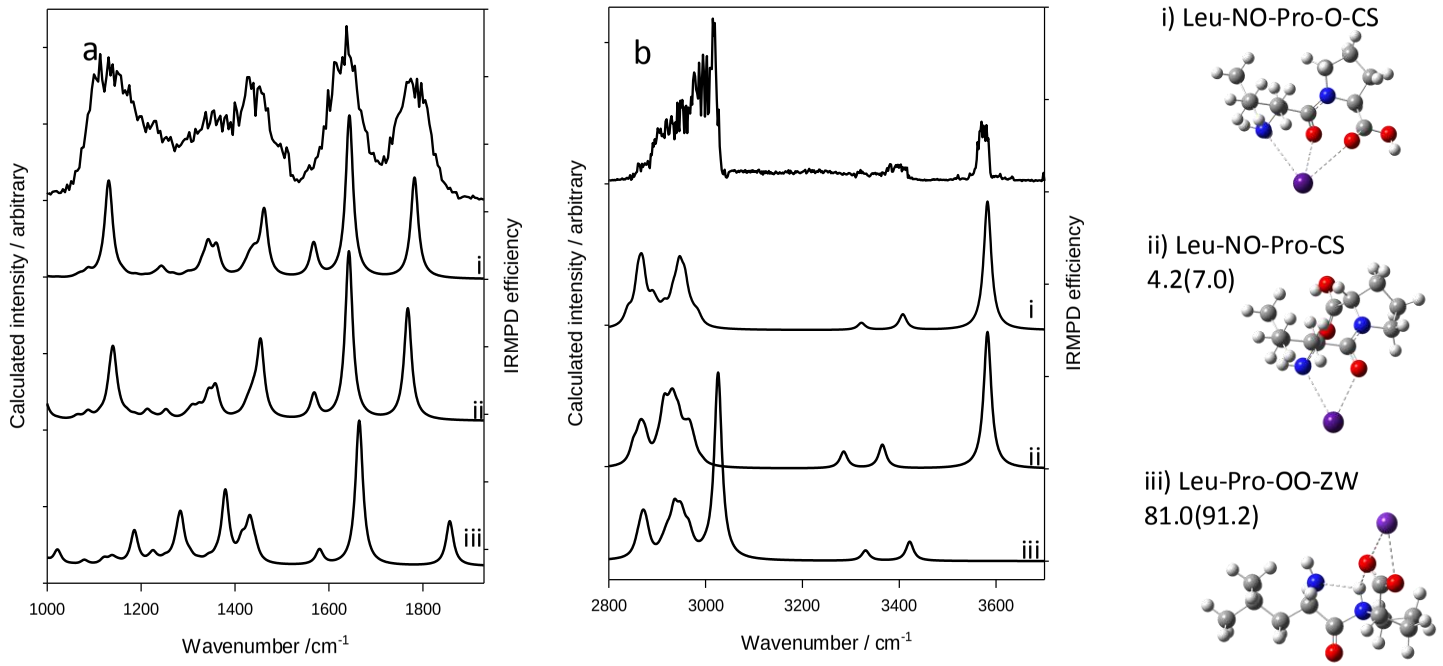

Figure A3.13. Comparison of the experimental IRMPD from 2700 to 3800 cm^{-1} of the a)(pro)Li^+ and b)(Leu)Li^+ complex resulted from i) cleavage of ProLeu and ii) cleavage of LeuPro dipeptides using CID experiment.

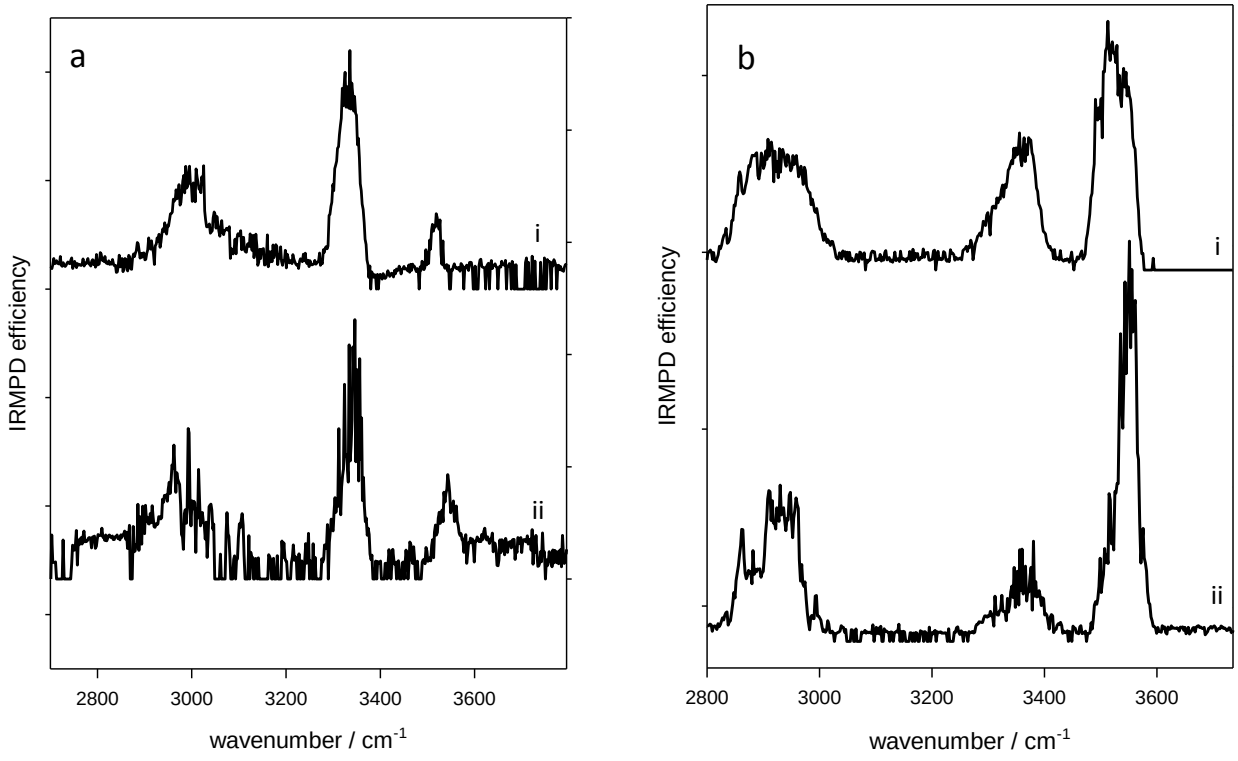

Table A3.1. Comparison of M06-2X/6-31+G(d,p) and M06-2X/6-311++G(3df,3pd)//6-31+G(d,p), relative Gibbs energies (and enthalpies) of the lowest energy structures of each forms of the $[M(ProLeu)]^+$complex at 298 K.

Structure	$\Delta_{rel}G(\Delta_{rel}H)$/kJ mol^{-1} M06-2X/6-31+G(d,p)	$\Delta_{rel}G(\Delta_{rel}H)$/kJ mol^{-1} M06-2X/6-311++G(3df,3pd)//6-31+G(d,p)	$\Delta_{rel}G(\Delta_{rel}H)$/kJ mol^{-1} B3LYP/6-31+G(d,p)	$\Delta_{rel}G(\Delta_{rel}H)$/kJ mol^{-1} B3LYP/6-311++G(3df,3pd)//6-31+G(d,p)
Li-Pro-NO-Leu-O-CS	0(0)	0(0)	2.6(-1.3)	4.1(0.1)
Li-Pro-O-Leu-O-CS	4.7(8.2)	3.8(7.4)	0(0)	0(0)
Li-Pro-Leu-OO-ZW	53.3(56.6)	52.3(55.6)	39.9(39.6)	41.0(40.8)
Li-Pro-N-Leu-NO-IM	35.0(33.8)	35.3(34.1)	41.0(36.6)	42.2(37.7)
Na-Pro-NO-Leu-O-CS	0(0)	0(0)	0(0)	0(0)
Na-Pro-O-Leu-O-CS	3.7(8.7)	3.0(8.0)	2.1(4.1)	1.1(3.1)
Na-Pro-Leu-OO-ZW	51.4(52.5)	52.5(53.5)	40.2(40.1)	42.4(42.4)
Na-Pro-N-Leu-NO-IM	48.2(48.3)	48.0(48.0)	57.4(54.1)	56.6(53.4)
Rb-Pro-O-Leu-O-CS	0(0)	0(0)	0(0)	0(0)
Rb-Pro-NO-Leu-O-CS	2.9(-0.1)	1.8(-1.2)	6.2(2.4)	4.9(1.2)
Rb-Pro-Leu-OO-ZW	54.7(52.2)	56.1(53.6)	50.9(46.9)	53.5(49.4)
Rb-Pro-N-Leu-NO-IM	66.3(63.9)	64.5(62.1)	78.0(72.3)	75.9(70.3)
Cs-Pro-O-Leu-O-CS	0(0)	0(0)	0(0)	0(0)
Cs-Pro-NO-Leu-O-CS	3.0(4.1)	1.1(2.3)	9.9(5.7)	8.2(3.9)
Cs-Pro-Leu-OO-ZW	58.0(57.4)	57.5(56.8)	56.1(51.6)	56.5(52.0)
Cs-Pro-N-Leu-NO-IM	71.7(70.9)	68.2(67.3)	86.5(78.5)	82.9(74.8)

Table A3.2. Comparison of M06-2X/6-31+G(d,p) and M06-2X/6-311++G(3df,3pd)//6-31+G(d,p), relative Gibbs energies (and enthalpies) of the lowest energy structures of each forms of the $[M(LeuPro)]^+$complex at 298 K.

Structure	$\Delta_{rel}G(\Delta_{rel}H)$/kJ mol^{-1} M06-2X/6-31+G(d,p)	$\Delta_{rel}G(\Delta_{rel}H)$/kJ mol^{-1} M06-2X/6-311++G(3df,3pd)//6-31+G(d,p)	$\Delta_{rel}G(\Delta_{rel}H)$/kJ mol^{-1} B3LYP/6-31+G(d,p)	$\Delta_{rel}G(\Delta_{rel}H)$/kJ mol^{-1} B3LYP/6-311++G(3df,3pd)//6-31+G(d,p)
Li-Leu-NO-Pro-CS	0(0)	0(0)	0(0)	0(0)
Li-Leu-O-Pro-O-CS	14.1(15.8)	12.1(13.8)	10.7(11.2)	9.3(9.8)
Li-Leu-Pro-OO-ZW	74.8(74.9)	72.8(73.0)	66.0(63.8)	65.6(63.4)
Na-Leu-NO-Pro-CS	0(0)	0(0)	0(0)	0(0)
Na-Leu-O-Pro-O-CS	12.0(14.9)	9.8(12.7)	7.8(10.1)	6.2(8.6)
Na-Leu-Pro-OO-ZW	70.4(70.8)	69.4(69.8)	64.1(61.2)	64.8(61.9)
Rb-Leu-NO-Pro-O-CS	0(0)	0(0)	0(0)	0(0)
Rb-Leu-NO-Pro-CS	3.2(5.7)	4.7(7.1)	1.1(3.2)	1.8(4.0)
Rb-Leu-Pro-OO-ZW	79.3(88.5)	82.0(91.1)	73.0(81.4)	75.6(84.0)
Cs-Leu-NO-Pro-O-CS	0(0)	0(0)	0(0)	0(0)
Cs-Leu-NO-Pro-CS	3.3(8.9)	2.8(8.4)	2.1(7.7)	1.1(6.6)
Cs-Leu-Pro-OO-ZW	79.1(89.3)	81.0(91.2)	75.9(83.1)	77.4(84.6)

Appendix D – Supporting Information for Chapter 6

Figure A4.1. The number of degrees of freedom vs 298 K rate constants for. In general for complexes that lie in the large molecule kinetics region, master equation modeling is not necessary, whereas if they lay in the small molecule region, master equation modeling is necessary to extract the dissociation thresholds. The blue dots correspond to uracil/Ca^{2+} complexes where the 14-mer resulted in larger dissocation thresholds than the BIRD activation energies. The red dots correspond to quadruplexes (octomers) of 9-ethylguanine bound by metal cations where only the Na complex resulted in larger dissocation thresholds than the BIRD activation energies. The green dot corresponds to the $Na(LeuPro)_3^+$ complex which is seen to be on the border between large- and small-molecule kinetics.

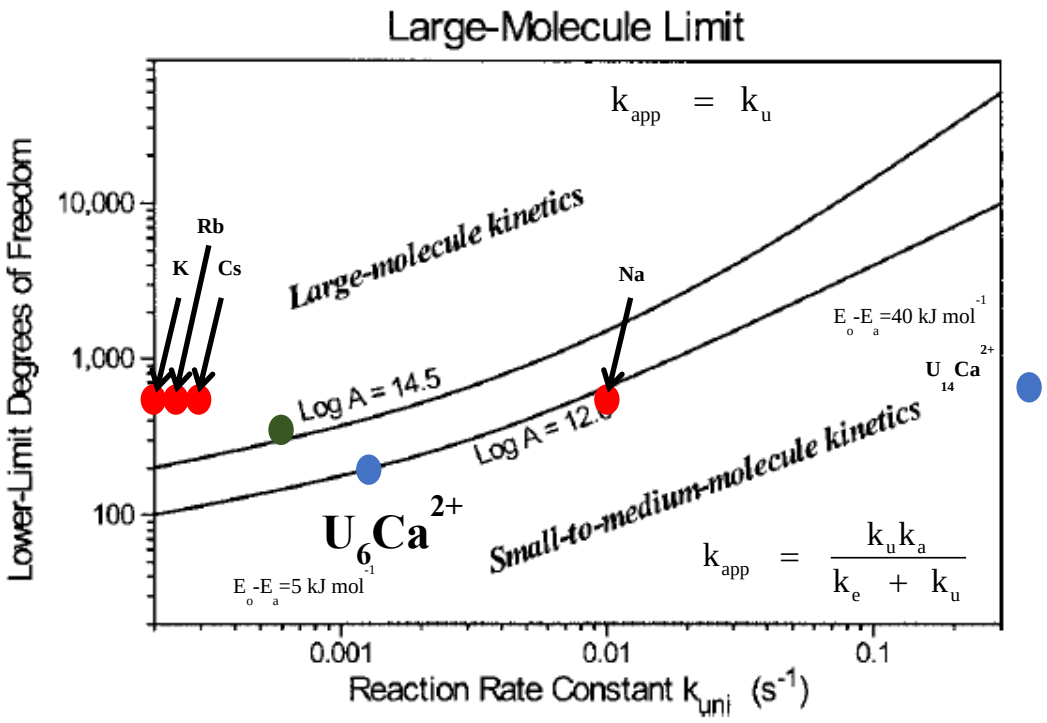

Dunbar, R.C. *Mass Spectrom. Rev.* **2004**, *23*, 127.

E.A.L. Gillis, M. Demireva, K. Nanda, G.J.O. Beran, E. Williams, and T.D. Fridgen *Phys. Chem. Chem. Phys*. **2012**, *14*, 3304.

M. Azargun, Y. Jami-Alahmadi, and T. D. Fridgen, *Phys. Chem. Chem. Phys*. **2017**, *19*, 1281-1287.

Figure A4.2. Structures and relative 298 K Gibbs energies (and enthalpies), in kJ mol^{-1} computed at the B3LYPD3/6-31+G(d,p) for the $Na^+(ProLeu)_3$.

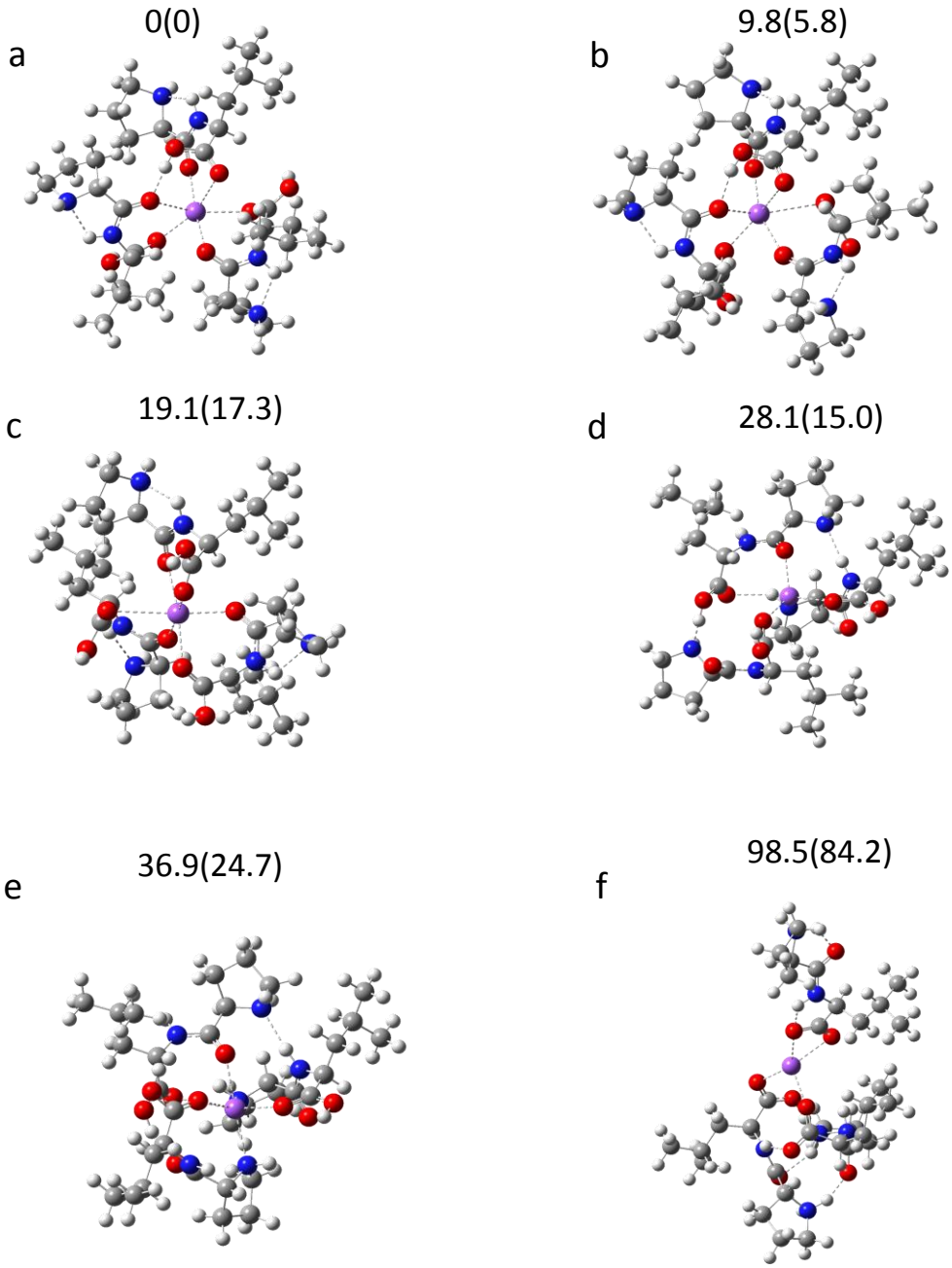

Figure A4.3. Structures and relative 298 K Gibbs energies (and enthalpies), in kJ mol^{-1} computed at the B3LYPD3/6-31+G(d,p) for the $Na^+(LeuPro)_3$.

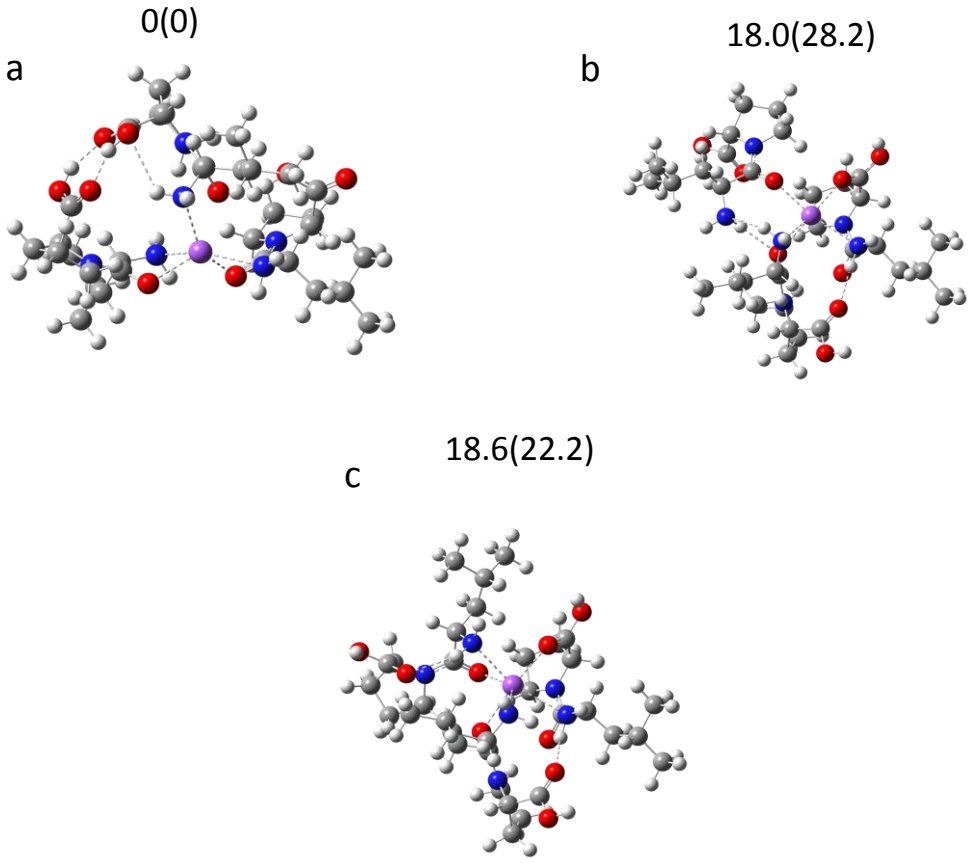

Figure A4.4. Comparison of the experimental IRMPD spectrum and calculated IR spectra of the different isomers shown in Figure A4.2 for the $Na^+(ProLeu)_3$ complex in the 2800 to 3800 cm^{-1} region using B3LYPD3/6-31+G(d,p) 298 K.

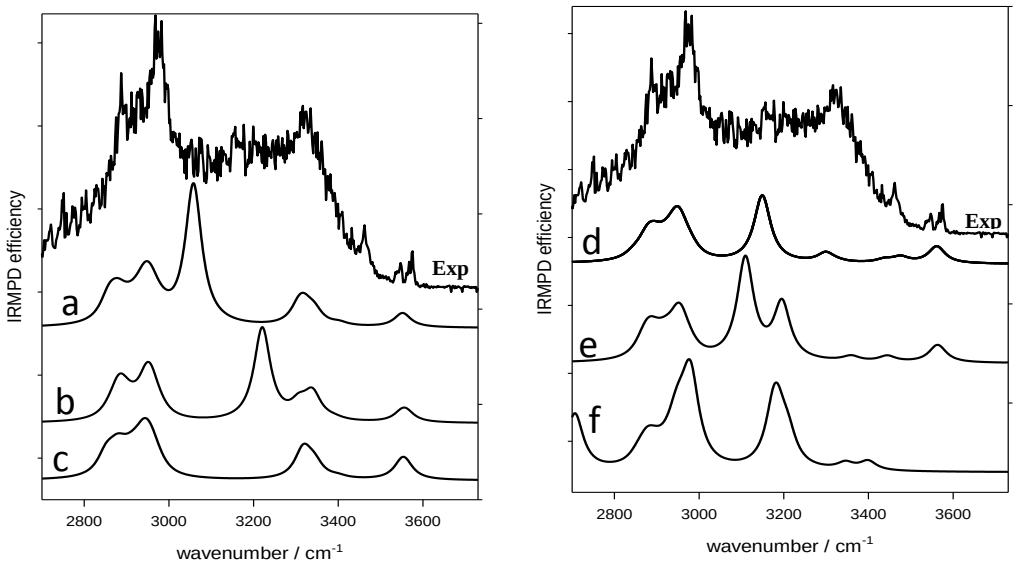

Figure A4.5. Comparison of the experimental IRMPD spectrum and calculated IR spectra of the different isomers shown in Figure A4.3 for the $Na^+(LeuPro)_3$ complex, in the 2800 to 3800 cm^{-1} region using B3LYPD3/6-31+G(d,p) 298 K.

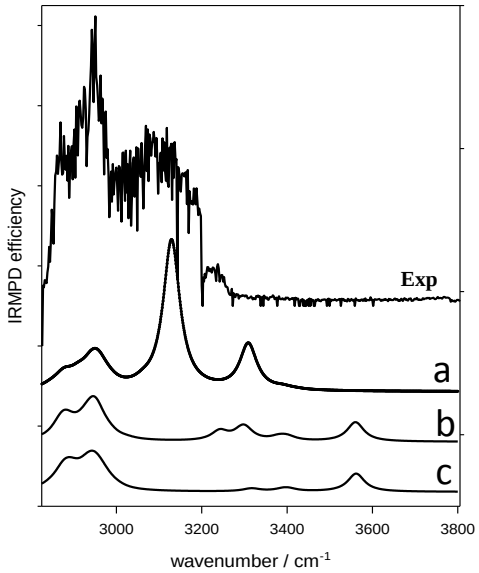

Figure A4.6. Master equation modeling results for $Na^+(LeuPro)_3$ using $A=10^{14}$, the best fit when E_0=0.9 - 1.00 eV

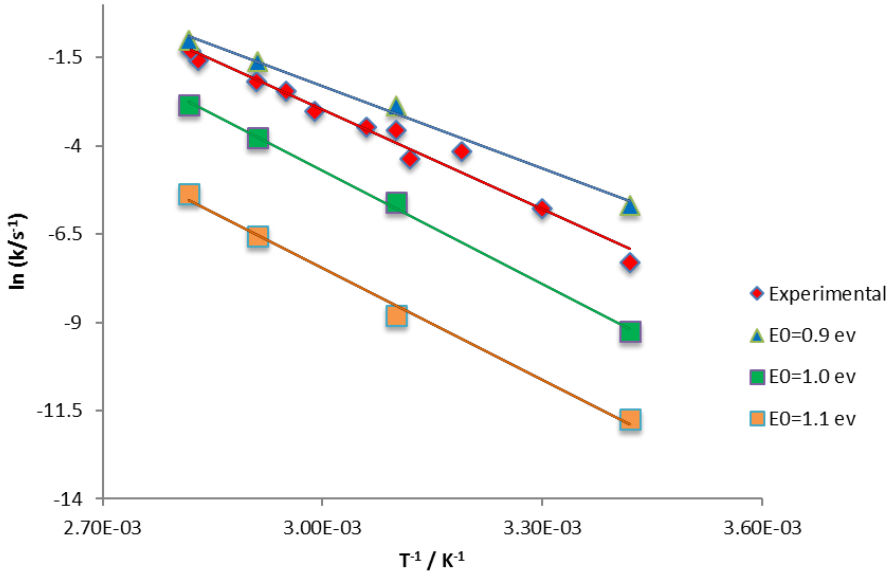

Figure A4.7. Master equation modeling results for $Na^+(LeuPro)_3$ using $A=10^{15}$, the best fit when E_0=1.00 eV.

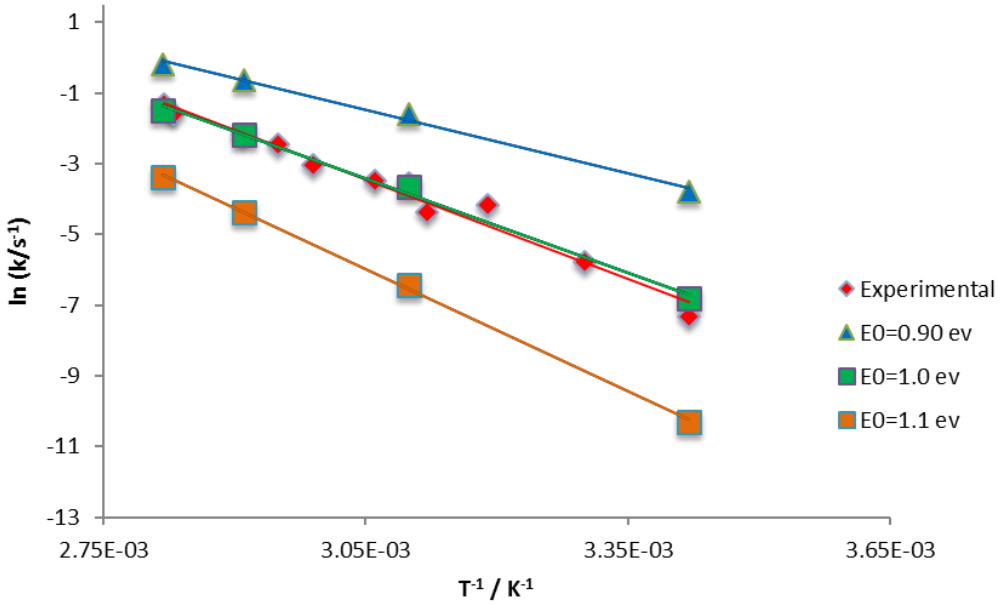

Figure A4.8. Master equation modeling results for $Na^+(LeuPro)_3$ using $A=10^{18}$, the best fit when E_0=1.10 eV.

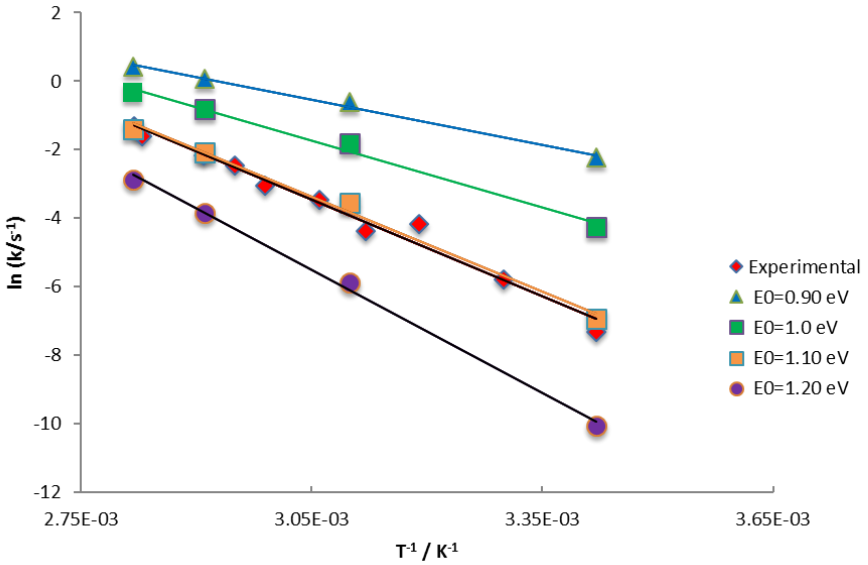

Figure A4.9. Master equation modeling results for $Na^+(LeuPro)_3$ using $A=10^{20}$, the best fit when E_0=1.20 eV.

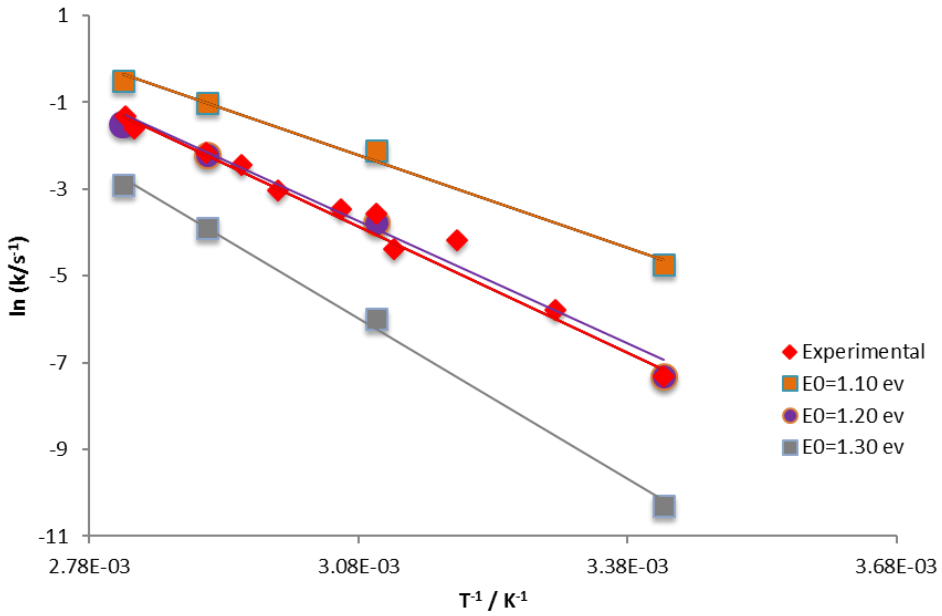

Figure A4.10. Master equation modeling results for $Na^+(ProLeu)_3$ using $A=10^{14}$, the best fit when E_0=1.00 eV.

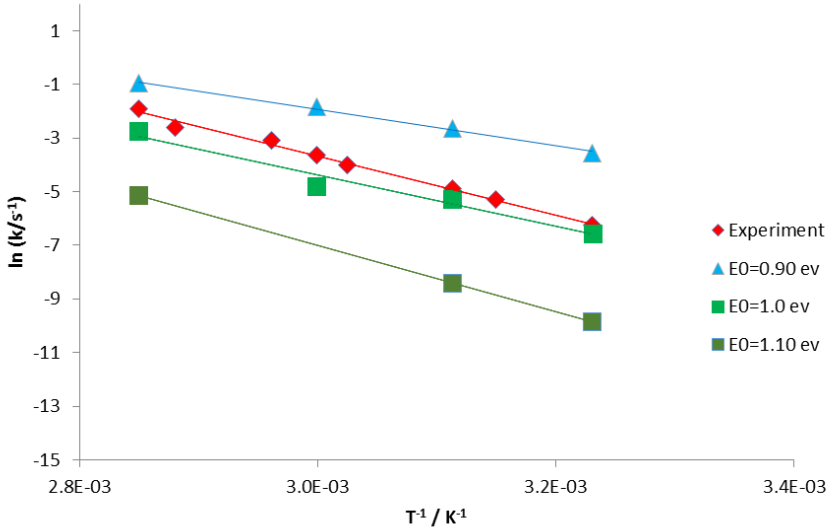

Figure A4.11. Master equation modeling results for $Na^+(ProLeu)_3$ using $A=10^{15}$, the best fit when E_0=1.0 – 1.1 eV.

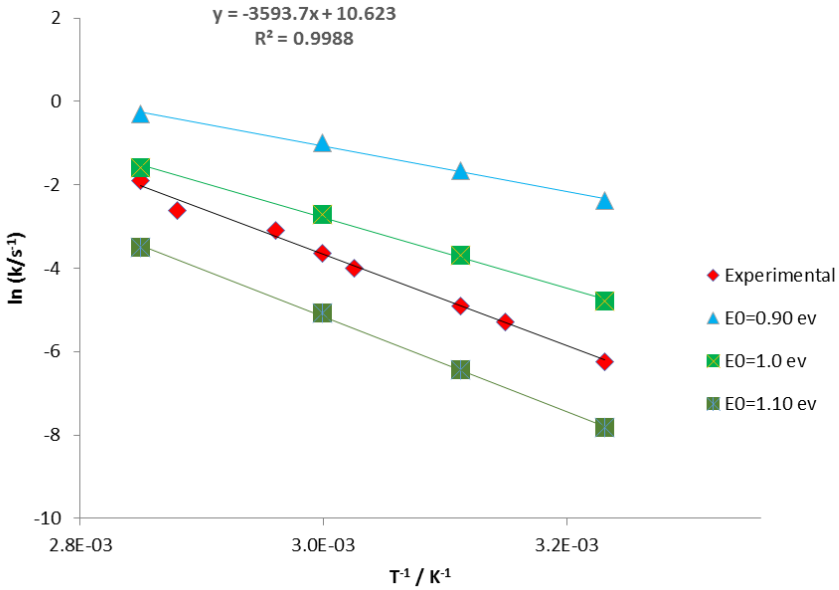

Figure A4.12. Master equation modeling results for $Na^+(ProLeu)_3$ using $A=10^{18}$, the best fit when E_0=1.20 eV.

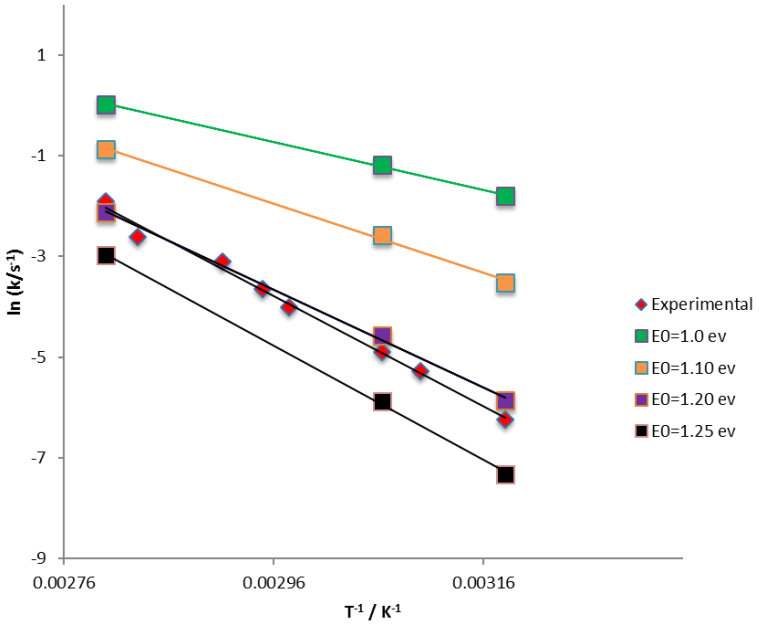

Figure A4.13. Master equation modeling results for $Na^+(ProLeu)_3$ using $A=10^{20}$, the best fit when E_0=1.25-1.3 eV.